Mathematical Modelling of Wrinkle Formation in Bacterial Biofilms

By

Heather A. Wallace

A Thesis submitted for the degree of Doctor of Philosophy

Division of Mathematics

University of Dundee

Dundee

November 2016

Contents

List of figures

List of tables

Acknowledgements

Firstly, I would like to express profound gratitude to my supervisor, Prof. Fordyce Davidson. Always on hand for discussions throughout my PhD, his thoughtful insight, knowledge, enthusiasm and patient guidance have simply made this thesis possible. I have learned a great deal from him.

I am also very much obliged to all of the staff in the Division of Mathematics at the University of Dundee for many helpful discussions and for making my time here enjoyable. In particular, thanks must go to Mr Nick Dawes, whose expertise helped to resolve many technical difficulties.

Special thanks must also go to Dr. Laoshen Li for permitting me to include photographs of some of her experimental results in this thesis. In addition, I would also like to thank Prof. Gürol Süel, Prof. Jordi Garcia-Ojalvo and Dr. Pau Rué for kindly providing me with the C code implemented in Chapter 2.

Last, but not least, a big thank you to all of my friends and family, especially my mum, who has supported and encouraged me and spent many hours proofreading. Without all of you, I'm sure that I would not have been able to complete this thesis. Your support has been much appreciated.

Declaration

I declare that the following thesis is my own composition and that it has not been submitted before in application for a higher degree.

Heather Wallace

Certification

This is to certify that Heather Wallace has complied with all the requirements for the submission of this Doctor of Philosophy thesis to the University of Dundee.

Prof. Fordyce Davidson

Abstract

Biofilms are matrix-producing communities of bacterial cells that adhere to surfaces and adopt a multicellular lifestyle. As the predominant life-form of bacteria (estimates suggest that 99% of all bacteria exist in biofilm communities), biofilms play a crucial role in the Earth's ecosystems, where their existence is known to contribute both beneficial and detrimental effects.

One of the defining characteristics of biofilms is heterogeneity in their structure. Indeed, it is commonly observed that biofilms of certain species of bacteria grown under certain conditions can display an unusual wrinkled structure, the pattern of which can vary at different locations throughout the biofilm. It is known that the type of wrinkle morphology displayed can be partially attributed to the expression of particular genes, which also have an effect on the mechanical properties observed in biofilms. Although the functions of wrinkles in biofilms, and the mechanisms controlling their formation, are not fully understood, it is believed that the presence of wrinkles enhances antimicrobial resistance (a property often associated with biofilms).

In this thesis we investigate cellular processes and mechanical mechanisms that may contribute to biofilm wrinkle formation. Some emphasis is directed towards the development of wrinkling patterns in biofilms of the *Bacillus subtilis* bacterium. Particular focus on the role of cell death in initiating pattern formation is explored through the analysis and numerical simulations of mathematical models. In addition we investigate whether classical mathematical tools and techniques that were originally designed to be applied to non-biological structures, and which take into account the mechanical properties of materials, can be implemented and used to explain biofilm wrinkling patterns. Using a mixture of mathematical modelling, analysis and numerical simulations, we conclude that a model description that incorporates the interplay between both biological and mechanical effects may be a useful tool for gaining a better understanding of the biofilm wrinkling process, and thus in the future, may enhance our knowledge of how these complex communities function.

Chapter 1

Introduction

In this introductory chapter the overall struture of the thesis is outlined, and a short summary of the chapter contents is given. First, to motivate the work undertaken, a brief biological and mathematical background of topics relating to the project are presented.

1.1 Biological Background

Microorganisms, whose small size make them invisible to the naked eye, can be found living and thriving everywhere from high in the Earth's atmosphere to deep on the ocean floor and within the Earth's crust, in a wide range of temperatures, pressures and other environmental conditions that can be either moderate or extreme [28, 39, 129]. Despite their small size, the total mass of microorganisms is estimated to account for more than half of the Earth's total biomass. Ranging from their involvement in natural recycling processes to their participation in the carbon and nitrogen cycles, microorganisms play essential roles in supporting the Earth's ecosystems and sustaining life on Earth. Both prokaryotes and eukaryotes can fall under the umbrella of microorganisms, with prokaryotic microorganisms being split into two domains; bacteria and archaea. In this thesis the focus is on bacteria which, aside from contributing to the Earth's ecosystems in the aforementioned ways, are most commonly associated with causing disease in plants and animals.

1.1.1 What are Biofilms?

Bacteria may exist in two distinct forms: *planktonic* and *biofilm* states. The most common perception of bacteria is that the majority exist in the planktonic state, where they are a motile, free-flowing and isolated entity within a bulk fluid. However, it has been estimated that 99% of bacteria in their natural habitat actually live in close-knit communtities called biofilms. Bacterial biofilms differ from their planktonic counterparts in several different ways. The key identifying features of biofilms are summarised by the following points, which are explained further in the succeeding paragraphs:

- Biofilms are close-knit communities of cells that adhere to surfaces
- Biofilms may comprise either a single bacterial species or multiple bacterial species
- Biofilms are encased in a self-produced extracellular matrix
- Most biofilms exhibit some degree of heterogeneity within their structure

Biofilms can be found growing on almost all surfaces, whether they be artificial or natural, living or inert, and the interface at which they grow may be either solid-air, liquid-air or liquid-solid depending on the environmental conditions they are exposed to [29, 64, 158]. To distinguish between biofilms growing on solid surfaces, which are sometimes referred to as 'solid-surface-associated biofilms' (or more commonly

(a) biofilm coated rock (b) biofilm colonised pipe

Figure 1.1: Examples of two commonly found naturally occurring biofilms growing on solid surfaces. Figure (a): Rock taken from the Molalla River in Oregon. The slime like material covering the previously submerged rock is an example of a biofilm. Image reproduced from [19]. Figure (b): Biofilm colonisation of a stainless steel pipe. Image reproduced from [172].

simply ‘biofilms’), floating biofilms growing on liquid-air interfaces are referred to as ‘pellicles’ [4]. Examples of some biofilms growing in different environments can be seen in Figures 1.1 and 1.2.

Environmental conditions are also important in determining whether single-species biofilms or multi-species biofilms are more likely to grow. While most biofilms in nature comprise multiple species, the majority of biofilm research focuses on single-species biofilms that tend to exist in specific infection sites, for example on the surface of medical implants [29, 52, 121]. While multi-species biofilms can display co-aggregation of species (where species are thoroughly mixed), it is also possible that multi-species biofilms comprise single-species microcolonies that align side-by-side, or in distinct layers [46].

Perhaps the single most recognisable characteristic feature of biofilms is the presence of a self-produced extracellular matrix which encases the bacterial cells, transiently immobilising them [51]. The matrix commonly comprises lipids, proteins and nucleic acids, however the primary component is extracellular polymeric substances (EPS)

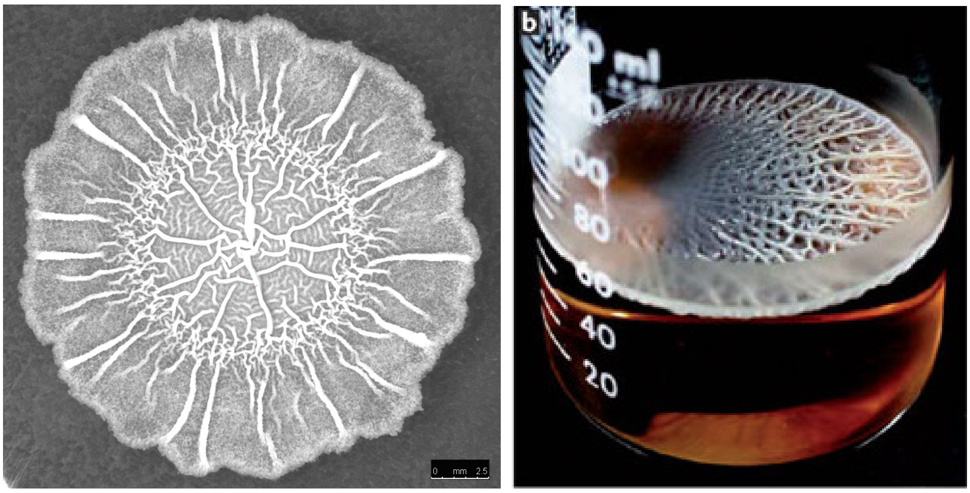

(a) Wildtype *Bacillus subtilis* biofilm (b) Wildtype *Bacillus subtilis* pellicle

Figure 1.2: Examples of two biofilm structures growing on different surfaces *in vitro*. Figure (a): Mature wildtype *Bacillus subtilis* biofilm grown on solid agar substrate. Photograph courtesy of L. Li. Figure (b): Mature wildtype *Bacillus subtilis* pellicle grown on liquid medium. Image reproduced from [14].

[71]. Within biofilms, it is estimated that only a small percentage of mass is cellular material; the remaining proportion consists of extracellular components (EPS is estimated to account for 50-90% of the total biofilm matter [57, 159]). The sliminess and stickiness that is often associated with the biofilm phenotype can be attributed to the presence of the extracellular matrix, which acts as a glue [83] and helps to provide structure and structural stability to the biofilm [51]. Production of EPS involves a significant investment of energy and thus it is assumed that matrix must be beneficial for growth by offering protection from environmental effects [104]. In particular, EPS is thought to contribute to the increased antimicrobial resistance that is displayed in wildtype biofilms in comparison to *eps* mutants.

One final biofilm characteristic is heterogeneity; most biofilms display some degree of heterogeneity within their structure [28, 34, 43, 96]. Furthermore, the heterogeneity of many species of biofilms may be exhibited through the formation of striking marcroscopic patterns. The presence of the extracellular matrix is thought to be an important contributing factor to the spatial heterogeneity, as the matrix provides architectural structure to the biofilm [51]. In many ways, biofilms resemble multicellular organisms [97]. Some of these multicellular characteristics stem from the presence of the extracellular matrix and increased heterogeneity, which increases structural complexity and the organisation and cooperation between cells. The cellular differentiation exhibited in biofilms is one of the main factors suggesting a multicellular existence [157].

1.1.2 The Colonisation Process of Biofilms

The biofilm colonisation of a surface is a multi-stage process which is described through the schematic shown in Figure 1.3. Although the details occurring during each colonisation phase vary depending on the strain of bacteria and environmental conditions considered, the overall stages in the colonisation process are common to all biofilms. First, free-flowing 'motile' bacteria in the planktonic state sense their proximity to, and attach to, surfaces [122]. Initially attachment is reversible, allowing bacteria to break away from the surface and rejoin the planktonic bacteria in the bulk fluid. Irreversible attachment occurs when the attached bacterial cells undergo a phenotypic change to become slow growing 'matrix-producing' cells. Thereafter, these cells can begin to produce EPS, which acts to anchor the bacterial cells more firmly to their attached surface [122]. Once in this biofilm state bacteria divide and replicate, whilst continuing to produce EPS, in order to construct microcolonies which eventually differentiate to form a mature biofilm [29]. The last stage in the biofilm colonisation process is detachment; some bacteria in the biofilm may detach from the main biofilm body to return to the planktonic state where they are free to begin the colonisation process again. In the case of endospore forming bacteria, some matrix-producing cells may sporulate at this stage [158].

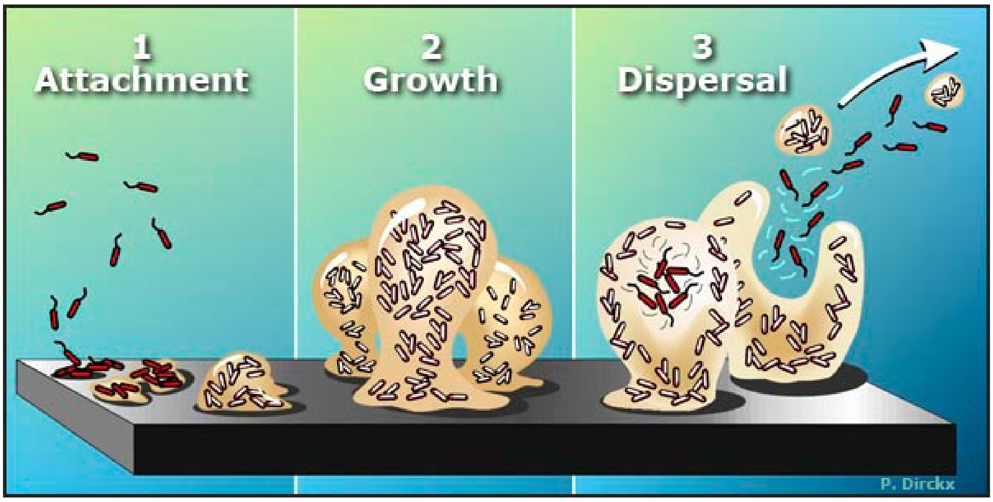

Figure 1.3: Stages in biofilm colonisation of a surface. Image reproduced from [172].

1.1.3 The Importance of Biofilms in Everyday Life

Because of their abundance in everday life, biofilms are recognised as extremely important. In particular, biofilms are considered of great significance in human health, as it has been estimated that upwards of 80% of bacterial infections in humans are biofilm related [130]. The chronic nature of biofilm infections is largely attributed to the increased antimicrobial resistance that they have come to be associated with [29]. It is thought that antimicrobial resistance in biofilms may be explained by the presence of a small population of ‘persister’ cells that are in the dormant state, which are unaffected by antimicrobial treatment and are protected from the immune response by the extracellular matrix [98, 99].While the majority of cells in the biofilm population are killed by antimicrobials, complete eradication is avoided by the presence of these persister cells which survive. Upon removal of the antimicrobial treatment, persisters are free to repopulate a population [170].

One classic example of a biofilm associated infection present in humans is caused by biofilms of the bacterial species *Pseudomonas aeruginosa*. These biofilms infect the lungs of cystic fibrosis sufferers, leading to chronic infections which can cause irreparable damage to the lungs and invariably prove fatal [29, 57]. Other examples of harmful biofilms present in humans include those growing on the surface of medical implants, in non-healing wounds, and on the surface of teeth in the form of dental plaque [17, 29, 122].

Despite the above, not all biofilms have a detrimental effect on their surroundings. In fact, the presence of many have proven to be advantageous, especially within the area of bioremediation. In particular, the utilisation of biofilms in the purification processes at water-treatment plants is well known, as is their use in the clean-up of oil spills [126, 137]. The effect of biofilms may also be environmentally dependant. For example, it has been shown that biofilms of *Paenibacillus polymyxa* growing on the roots of *Arabidopsis thaliana* increase the plant's drought resistance and its presence is therefore advantageous in dry conditions. In the absence of an extreme climate, however, the presence of *P. polymyxa* has a negative affect on the plant, reducing growth [144]. In general, whether good or bad, biofilms can be regarded as holding great consequence in our everyday lives.

1.1.4 The Role of Cell Death in Biofilm Formation

Experimental discoveries show that cell death is an important process in biofilms. Perhaps surprisingly, it has been proposed that controlled, localised cell death in biofilms may be advantageous for the community as a whole, as the lysing of cells reduces competition and provides an extra nutrient source that can be utilised by surviving cells [166]. Specifically, the energy-intensive sporulation process, that is triggered in response to nutrient limited conditions in some species of bacteria, may be delayed by localised cell death [63, 105]. For example, in *Bacillus subtilis* biofilms, cannibal cells release toxins that they themselves have resistance to, killing some of their sister cells [9]. In this situation, the bacterial community may be thought of as cutting its losses;

the cost of losing the lysed cells may be less than the energy expenditure required to enter into the sporulation process, especially in the case where nutrient depletion is only temporary [63]. Complete population suicide or eradication is avoided by the presence of persister cells which, as previously mentioned, persist in the presence of external threats that either kill or induce self-programmed cell death in the rest of the bacterial population. The sole purpose of these persister cells is survival.

It has also been discovered that the structure of bacterial communities may be influenced by cell death. For example, the creation of void spaces in areas of localised cell death in *Pseudomonas aeruginosa* and *Pseudoalteromonas tunicata* biofilms has been shown in [106, 167]. In addition, recent work has highlighted the role that localised cell death may play in inducing wrinkling patterns in biofilms. Asally et al. [6] identified that wrinkle formation and cell death are correlated in space, with cell death preceding and facilitating wrinkle formation. It is proposed that cell death may act as a precursor to buckling, leading to the formation of wrinkles.

1.1.5 Pattern Formation in Biofilms

As already noted, the heterogeneous nature of biofilms is one of their defining characteristics. Experiments have shown that different strains of bacteria, grown in a range of different conditions, may form a range of unusual patterns. Some examples of these patterns may be seen in Figures 1.2 and 1.4.

In this thesis we investigate biofilm models of a generic nature, however particular focus is on single-species biofilms of the bacterium *Bacillus subtilis*. *B. subtilis* is a rod-shaped, gram-positive endospore forming bacterium that is regarded as a model organism in bacterial studies because it is relatively easy to genetically manipulate, easy

(a) *Paenibacillus vortex* colony

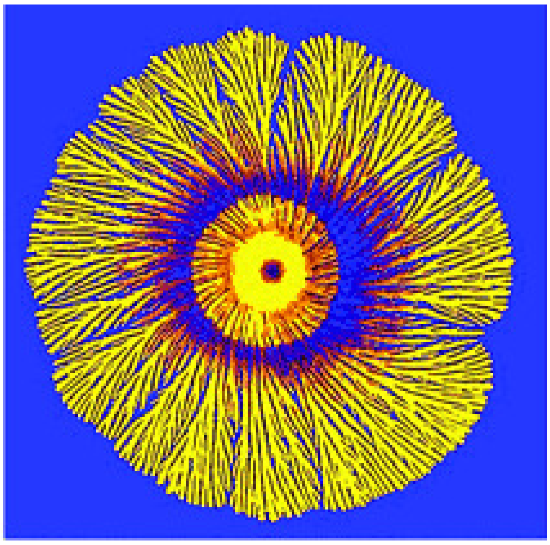

(b) *Paenibacillus dendritiformis* colony

Figure 1.4: Examples of types of patterns exhibited in bacterial colonies of different strains of bacteria. Figure (a): Patterning caused by swarming behaviour in *Paenibacillus vortex*. Figure shows petri dish with 88 mm diameter. Figure (b): Typical branching pattern formed by *Paenibacillus dendritiformis* bacteria grown on a nutrient depleted agar substrate. Colony shown is approximately 5 cm in diameter. Both images reproduced from [12].

to grow in a laboratory setting and is widely recognised as safe to work with. Agriculturally, *B. subtilis* has been shown to act effectively as a soil inoculant [36], while it is also an important industrial enzyme and protein producer [38, 152]. In addition, its ability to produce antimicrobial peptides with potential antibiotic properties is noted [139, 142]. Our specific interest lies in *B. subtilis* biofilms because of the unusual wrinkling patterns that they develop when grown *in vitro*. Particular focus is on the unique wrinkling patterns observed in mature wildtype *B. subtilis* biofilms grown on agar. Grown under certain specific conditions, the formation of a 'coffee-ring' structure is observed. Within the coffee-ring region, a cluster of overlapping wrinkles is observed to develop. Outside the coffee-ring, radial wrinkles extend from the ring's boundary towards the outer edge of the biofilm [48] (see Figure 1.2(a)).

The function of the wrinkles in *B. subtilis* patterns is as yet unknown, though it has been suggested that the wrinkles may act as channels delivering nutrients to those areas of the biofilm under increased environmental pressures [168]. However, it is unknown if the wrinkles actually form with this function intended, or whether the transport system is a circumstantial by-product of the wrinkles that form because of other factors. For example, it has also been suggested that wrinkling may enhance the potential of biofilms to utilise oxygen [40].

1.2 Mathematical Background

Biofilms are complex structures. The diverse range of phenotypes and behaviour exhibited by biofilms of different species, and under different environmental conditions, only increases the number of possible areas of study. While advances in microbiology provide an ever expanding catalogue of data and information that helps us to understand more about these interesting communities, there is still a lot that is yet to be understood. The implementation of mathematical models to describe biofilm communities has proved useful in building up knowledge of these fascinating structures. In this section we give an overview of various mathematical modelling approaches that have been used to describe biofilm behaviour over the last 30-40 years, with particular emphasis on pattern formation models. These models consider biofilm behaviour over a range of scales, from microscopic to macroscopic. We catergorise the different model approaches into two separate classes: discrete and continuum models. Several reviews of biofilm mathematical models exist in the literature, and we direct the reader to two of these for further information [73, 160].

1.2.1 Discrete Models

Discrete modelling may be thought of as implementing a traditional ‘bottom-up’ approach; individuals within the community are modelled with the aim that their combined behaviour may help to predict behaviour of the entire population. In the context of biofilms, discrete models typically describe the behaviour of the individual microscopic bacterial cells in order to infer the collective behaviour of the macroscopic population as a whole.

Cellular automaton (CA) models consider both space and time discretely. The cellular automaton set-up consists of a regular grid of cells, where each cell is initially assigned one of a number of finite states. A governing set of model rules acts to control the development of each cell at each new generation (time $t+1$), by considering a specific neighbourhood around the cell in question at time t. While each cell is considered individually at each time-step, the rules governing all cells are the same and so can be thought of as global. One example of a biofilm model implementing a CA approach describes the growth and division of bacterial cells in the presence of a diffusing substrate [169]. This model assumes a random distribution of substrate molecules within an array. An initial population of bacterial cells is placed along the bottom of the array where the substratum would be located. At each iteration, cells can ‘grow’ when the site they occupy has a sufficient level of nutrients, and at least one neighbouring site is unoccupied. Upon the removal of substrate from the original grid location, a new cell grows in a neighbouring location. In order that the simulation may continue, substrate molecules diffuse into a neighbouring cell at each iteration. The simulation results from the above model show that the application of different substrate concentrations generate different types of patterns that are similar to those observed in biofilms. Thus the authors hypothesise that substrate concentration is an important factor in determining biofilm structure. Other examples of biofilm models implementing a cellular automata approach are [95, 143].

Another type of discrete model framework used in biofilm modelling is diffusion-limited aggregation (DLA) models. The DLA approach considers a single initial (seed) particle placed at the origin of a square lattice. A second particle is released far from the origin and follows a random path around the lattice until it comes into contact with the seed. Upon its arrival in a neighbouring site the particle becomes irreversibly stuck to the site, forming a cluster with the original seed, and another particle is released. This newly released particle can then follow another random path until it becomes stuck in a neighbouring site of the cluster. On repeating the process, the cluster continues to grow in size. DLA models have proved popular in modelling the branching patterns in bacterial colonies because of the fractal patterns they reproduce. In [54, 55, 110], the branch-like patterns observed in some *B. subtilis* colonies are modelled using the DLA approach.

Individual-based modelling (IbM) represents bacterial cells as spheres with variable volume and mass, and also takes into consideration substrate diffusion and reaction. Growth of cells occurs as cells consume substrate, while division of cells is induced when cells reach a pre-determined volume. As the number of bacterial cells increase, the shifting of cells occurs to minimise overlap between neighbouring cells. This shifting determines the direction of movement of the bacterial cells as time passes. In individual-based models, concentration of substrate is determined through a reaction-diffusion equation, and thus IbM is an example of a discrete-continuum approach to modelling. The first individual-based models applied to the biofilm context were formulated by Kreft et al. [89–92]. Further individual based models applied to biofilms include those discussed in [3, 60, 123, 124, 171].

1.2.2 Continuum Models

While discrete biofilm models focus on the behaviour of each bacterial cell separately, continuum models take no account of individual cells and instead consider the bacterial population as a whole. Continuum models represent the most traditional way to describe biological systems, and in particular the behaviour of bacterial populations. When using a continuum approach, differential equations are used to describe the time evolution of the densities of particular biofilm components.

Ordinary differential equation (ODE) models are used to describe the behaviour of variables over space or time. It is known that bacteria can display density-dependent behaviour via quorum sensing, a strategy allowing cell-cell communication [131]. ODE models are used to represent quorum sensing mechanisms and behaviours in biofilms. In Ward et al. [165], a bacterial population is split into different kinds of cells; up-regulated cells producing many quorum sensing molecules and down-regulated cells producing these molecules more slowly. In the well-mixed population, an ODE model is formulated to describe how the fraction of up-regulated and down-regulated cells vary over time. Other ODE models implementing an ODE approach to modelling quorum sensing in bacteria include [42, 81]. Another interesting ODE model describing a bacterial population is presented in [26]. This ODE model predicts the effect that antibiotics will have on a bacterial population by dividing it into two subpopulations; antimicrobial susceptible cells and persister (antimicrobial resistant) cells.

Perhaps the most commonly used method for modelling biofilm development, especially in the area of biofilm pattern formation, is through the use of partial differential equation (PDE) models. In comparison to ODE models, PDEs model variables as functions of both space and time.

Reaction-diffusion systems are one example of a PDE approach to modelling biofilms. The general set-up used when implementing such an approach is to formulate equations which describe the net rate of accumulation of mass for each biofilm component;

$$\begin{pmatrix}\text{Net rate}\\ \text{of mass}\\ \text{accumulation}\end{pmatrix} = \begin{pmatrix}\text{Mass flow}\\ \text{of component}\\ \text{entering}\end{pmatrix} - \begin{pmatrix}\text{Mass flow}\\ \text{of component}\\ \text{exiting}\end{pmatrix} + \begin{pmatrix}\text{net rate of}\\ \text{creation/loss}\\ \text{of component}\end{pmatrix}. \tag{1.1}$$

Reaction-diffusion models make up a large proportion of biofilm PDE models, and many examples of reaction-diffusion biofilms in the literature exist, including [11, 44, 53, 62, 84, 87, 113, 164] . For example in [111], bacterial cells are split into two subpopulations and represented by two separate variables; active and inactive cells. While it is assumed that active cells may diffuse, grow and multiply, inactive cells do none of these things. A total of three coupled differential equations represent the biofilm system, as a third variable represents a nutrient source. Numerical simulations of this model have shown that a range of different patterns can be formed by altering the initial nutrient concentration, and also the diffusion coefficient of the active cells (as cells are assumed more likely to be able to diffuse on softer substrates, this corresponds to varying the firmness of the agar substrate). These patterns correspond well with experimental results. While the model is relatively simple, numerical results are biologically relevant to the biofilm pattern formation problem.

The recent model of Asally et al. [6] uses a reaction-diffusion approach to model cell death patterns in *B. subtilis* biofilms. Experimental results showed that localised cell death could initiate wrinkling in biofilms. These results were used to formulate a model whereby the evolution of cell density was described using a reaction-diffusion equation (where diffusion was dependent on extracellular matrix). Cell death was linked to cell density through a density dependent ODE. While the proposed model predicted heterogeneity of cell death in biofilms, the model did not incorporate mechanical forces, and the buckling mechanism, that was hypothesised to be significant in the development of wrinkle structures.

While the above models take into account different cellular processes which transpire within biofilms, they do not generally incorporate physical processes that may occur. These may include, for example, external forces acting on the biofilm and changes in pressure gradients within and around it. The implementation of a fluid dynamics approach has been used to address this oversight in several biofilm models including [7, 25, 32, 61, 125, 174]. Of particular relevance here is the model formulated by Dockery and Klapper [41], which models a substrate limited biofilm layer as an incompressible fluid whose growth and expansion is governed using a Darcy's law-type relationship. The biofilm grows into a static aqueous environment and the evolution of the biofilm is tracked via a moving front. This model is investigated further in Chapter 4.

Increasingly in recent years, a more mechanical-focussed approach to modelling wrinkling in biofilms has been undertaken. In these models, physical properties of the biofilm and their environment are described explicitly through physical parameters, such as Young's modulus. While the literature available on such parameters is limited, such models have proved effective in modelling biofilm wrinkling patterns. For example, an ODE model implemented in [149] considers biofilm pellicles of *B. subtilis* which have been shown to wrinkle when grown in confined spaces. The pellicles are modelled as growing elastic plates and the ODE model uses force balance equations to determine pellicle displacement and predict wrinkle wavelength as forces in the system increase during growth. Again, in [48, 119], biofilms are modelled using equations describing thin elastic plates. In [48], a mechanical approach to wrinkling is used in conjunction with cellular automata to describe the growth of the biofilm, in order to model the wrinkling patterns of *B. subtilis* grown on agar.

1.3 Thesis Outline

The aim of this thesis is to better understand the mechanisms by which wrinkling may occur in bacterial biofilms. The structure of the thesis is as follows.

In Chapter 2, we carry out analysis of the model of [6] which uses a reaction diffusion approach to model cell density and death patterns in *B. subtilis* biofilms grown on agar. Our work investigates if there is a singular driving force that initiates or causes the patterning that is observed in numerical simulations of the model. By first simplifying and then reconstructing the full model in [6], we use a combination of analysis and numerics to determine the emergence of heterogeneity in model solutions. In particular, we explore the effect that a non-constant diffusion term has on the spatial results of the model. Finally we investigate the consequences of using a random growth rate to describe heterogeneity in cell density.

In Chapter 3 we use a cross-diffusion set-up to investigate whether a two-species cross-diffusion model may be a (biologically relevant) method of modelling pattern formation in biofilms. First we derive the cross-diffusion model using a random walk process. We then formulate a general two-species cross-diffusion model to represent bacterial cells, u, and the extracellular matrix component, v, in a biofilm. The model set-up we use takes the following form:

$$
\begin{aligned}
\frac{\partial u}{\partial t} &= F(u,v) + \nabla \cdot \left[D_{11}(u,v)\nabla u + D_{12}(u,v)\nabla v \right], \\
\frac{\partial v}{\partial t} &= G(u,v) + \nabla \cdot \left[D_{21}(u,v)\nabla u + D_{22}(u,v)\nabla v \right].
\end{aligned} \tag{1.2}
$$

While D_{ij} are diffusion terms, F and G represent reaction terms which are formulated by considering basic processes that occur within the biofilm. We perform a stability analysis on system (1.2) and determine conditions under which the possibility of pattern formation exists for different combinations of diffusion terms. We present a simple example model to highlight certain features.

In Chapter 4 we present an extension of the model proposed by Dockery and Klapper [41]. It is assumed the biofilm is a viscous, homogeneous, incompressible fluid of constant density which expands due to a pressure gradient in the biofilm, which in turn is caused by bacterial growth. While the model in [41] considers biofilm growing into a static aqueous environment, we consider a biofilm growing on agar into the air above (oxygen is assumed to be a growth limiting substrate). We extend the model of [41] by introducing cell death terms. The new system describing susbtrate S and pressure P in the biofilm ($0 < z < h$) and air ($h < z < h + L$) regions is

$$
\nabla^2 S = 0; \qquad h(\mathbf{x},t) < z < h(\mathbf{x},t) + L, \tag{1.3}
$$

$$
\begin{cases}
\nabla^2 S = GS; \\
\nabla^2 P = -D_\mu S + \mu;
\end{cases} \qquad 0 < z < h(\mathbf{x},t), \tag{1.4}
$$

where μ and L are positive constants. Constant and substrate dependent cell death are represented by $D_\mu = 1$ or $D_\mu = 1 + \mu$, respectively. We investigate planar solutions of the problem, and compare the differences in behaviour for different cases of cell death.

Next, stability of planar solutions to non-planar perturbations is investigated. We linearise around non-planar perturbations and derive a dispersion relation describing the non-planar evolution of the biofilm front at a steady state solution. We determine that biofilm height is important in determining whether non-planar perturbations grow or decay. In addition, we explore the effect that varying cell death has on the stability of planar steady state solutions to non-planar perturbations.

Chapter 5 considers the relevance of a purely mechanical model applied to the biofilm wrinkling context. The model explored is that formulated by Huang and Im in [76], which describes the evolution of wrinkles in an elastic-viscoelastic bilayer subject to axial compressive forces. We describe the model set-up and the different wrinkling morphologies that are observed in the results of numerical simulations. We note the striking similarity between the wrinkles that develop in *B. subtilis* biofilms grown on agar and the wrinkles that emerge in the results of the model describing an equibiaxially compressed bilayer. We proceed to determine if the model can realistically be applied to the biofilm context. First we compile a list of some estimated values of physical parameters that describe biofilms. We then consider that the elastic-viscoelastic bilayer may represent two different biological set-ups. The first set-up considers the possibility that the bilayer may represent an elastic biofilm growing on a viscoelastic agar substrate. The second set-up considers the possibility that the bilayer may describe two different component parts of the biofilm; a viscoelastic bulk and an elastic coating. We use a combination of numerical simulations and analytical results presented in [76] to determine whether the model can be used to realistically describe wrinkling in biofilms.

In the concluding chapter we summarise key results of this thesis, and discuss the possible implications in our understanding of the process of biofilm wrinkling. A discussion of possible future work that may be undertaken is also given.

Chapter 2

Investigating Heterogeneity in a Reaction-Diffusion Biofilm Model

2.1 Introduction

Experimental data and results show that wildtype biofilms of the soil bacterium *Bacillus subtilis*, grown on agar, form spatially heterogeneous biofilms and display complex structural patterns. However *eps* mutants, which lack the gene controlling EPS matrix production, do not display these spatial patterns. We aim to understand more about the mechanisms controlling pattern formation in *B. subtilis* biofilms and also try to understand more about the effect that the production of extracellular matrix has on these mechanisms.

In this chapter we outline the link that has been discovered between the heterogeneous nature of cell death and the wrinkling process in *B. subtilis* biofilms. We explain the concept of the ‘coffee-ring’ effect and investigate the reaction-diffusion model of Asally et al. [6] that models the heterogeneous pattern of cell death within the central coffee-ring area of *B. subtilis* biofilms. We recreate model simulation results from [6] and determine which features of the proposed model are essential for pattern formation to occur. Turing instability analysis is carried out to establish if a simpler model with fewer variables and terms is capable of producing instabilities that can lead to pattern formation. We discuss the role that a non-constant diffusion term and a random growth rate have on the spatial patterns exhibited. Finally we determine if the heterogeneous patterns observed in numerical simulations capture some underlying process or are simply a result of the model input or formulation.

2.2 Coffee-ring Effect

Wildtype *B. subtilis* bacteria form biofilms displaying a ‘coffee-ring’ structure when grown on some surfaces [6, 47, 135]. The coffee-ring is a commonly occurring phenomena observed when a liquid with suspended particles (for example, coffee grounds or bacterial cells) dries on a surface. As the liquid dries it leaves a ring around the perimeter of the original drop. This ring is thought to form as a consequence of capillary flow [135]. Liquid at the edge of the drop dries first and is replaced by liquid from the interior, pulling the suspended particles (cells) towards the perimeter of the original droplet [37], leaving a ring outline. In biofilms grown on agar, coffee-ring formation occurs at the initial perimeter of bacterial inoculation. The coffee-ring persists and remains detectable throughout the growth and development of the biofilm [135], as can be seen in Figure 2.1(b) (where the coffee-ring outline is highlighted in yellow). Inside the coffee-ring of wildtype *B. subtilis* biofilms, a rope-like structure of wrinkles form in a knotted pattern. A close-up of this intricate pattern is shown in Figure 2.1(c). Outside of the coffee-ring radial wrinkles extend from the perimeter of the coffee-ring to the edge of the biofilm. The coffee-ring appears to act as a barrier between these two distinct areas of the biofilm.

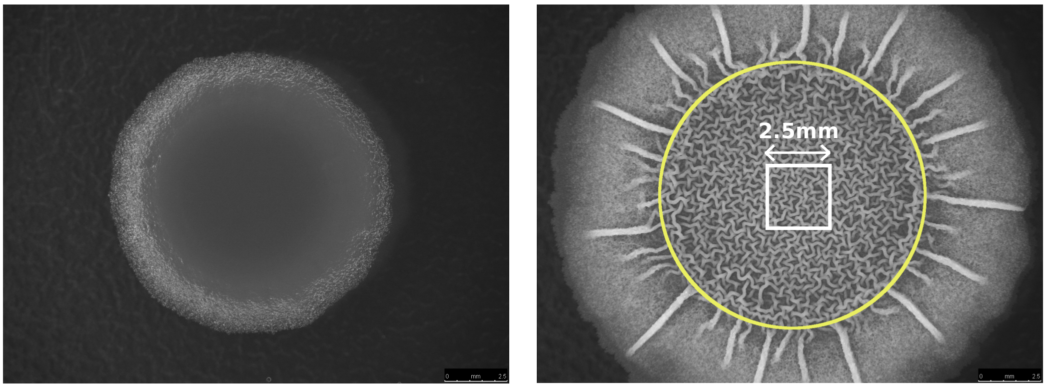

(a) *B. subtilis eps* mutant biofilm at $t = 48\,\text{h}$ (b) Wildtype *B. subtilis* biofilm at $t = 48\,\text{h}$

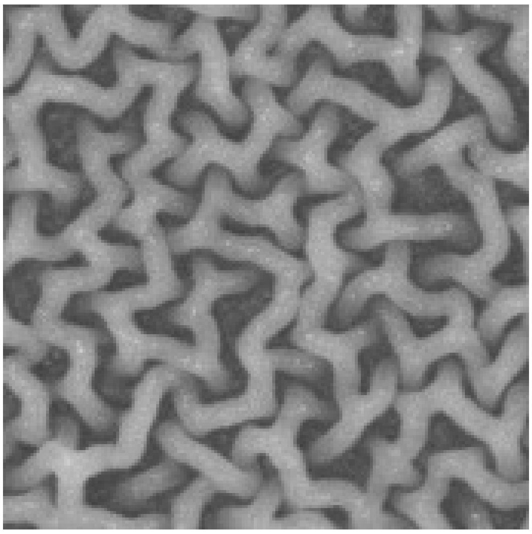

(c) Close-up of wrinkles in coffee-ring area

Figure 2.1: Morphology of *Bacillus subtilis* biofilms grown at 30°C on 1.5% agar substrate. Figures shown are at $t = 48\,\text{h}$ after initial inoculation. Figure (a): *eps* mutant shows homogeneity. Figure (b): Wildtype biofilm shows complex heterogeneous pattern within the coffee-ring region (yellow outline). A close-up of the intricate wrinkle structure in the highlighted white square can be seen in Figure (c). Photographs courtesy of L. Li.

In *eps* mutants, a coffee-ring will also form at the initial point of inoculation and will remain visible throughout development, though it is not as clear as in wildtype strains. In the case of an *eps* mutant, a homogeneous structure is observed and no obvious structural difference can be seen between the areas inside and outside of the coffee-ring. It is also noted that wildtype *B. subtilis* biofilms show faster radial expansion than *eps* mutants [134], with the diameter of wildtype biofilms being significantly larger compared to *eps* mutants at later time steps. The differences between *eps* and wildtype *B. subtilis* biofilm structure are illustrated in Figures 2.1(a) and 2.1(b), which show the different strains grown in identical conditions, 48 hours after initial inoculation.

2.3 Localised Cell Death Model

Experimental results by Asally et al. presented in [6] showed that wrinkle formation and the localisation of bacterial cell death in *B. subtilis* biofilms grown on agar were correlated in space, with cell death preceding the formation of wrinkles. It was also shown that localised cell death occurs first at areas of high initial cell density, which is hypothesised to be due to increased environmental stresses in these areas. It follows that where there is a higher density of living cells there is more competition for resources such as nutrients, space and oxygen, which results in increased cell death in these areas. The hypothesis of the authors is that as the biofilm grows, mechanical forces build up within the biofilm. Cell death occurs at the bottom of the biofilm (the interface closest to the agar) at areas of high cell density due to increased environmental pressures, thus providing a release for some of these mechanical forces. As a result, neighbouring living cells push into the area of cell death from all directions. As the cells meet in the region of cell death, a buckling phenomena is thought to occur (as illustrated in Figure 2.2). This buckling is hypothesised as being the cause of wrinkle formation. It is important to note that it is localisation of cell death that is taken as an

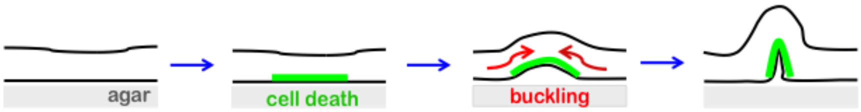

Figure 2.2: Schematic showing the buckling process in a biofilm, as hypothesised in [6]. The figure shows a side-view of the biofilm as cell death occurs. Grey area represents agar while the white area is the biofilm. The green region represents an area of cell death and the red arrows show the buckling mechanism that has been proposed to occur in these areas. Figure reproduced from [6].

indicator to show that wrinkling can occur, as homogeneous cell death does not result in wrinkle patterns developing. One result of the conclusion that localised high cell density and death cause wrinkle formation is that it is possible for biofilms with predetermined, manually induced wrinkle patterns to be grown on agar. These patterns can be obtained by either purposely killing bacterial cells in specific regions of the domain, or by increasing cell density in areas where wrinkle formation is envisioned.

The mathematical model published in [6] uses a reaction-diffusion approach to predict the behaviour of bacterial cells and reproduce the cell death pattern observed in *B. subtilis* biofilms inside the central coffee-ring structure where a complex rope-like wrinkling pattern is observed (see Figure 2.1(c)). The implementation of reaction-diffusion equations to model pattern formation in biofilms has been widely used. The model in [6] centres around one reaction-diffusion equation describing the dynamics of the density of living bacterial cells, $\rho(\mathbf{r},t)$, where $\mathbf{r} = (x,y)$ is 2-D space and t is time. Ω is the complete domain of integration. Other variables in the system are modelled using other partial differential equations (PDEs). The components in the system are bacterial cell density $\rho(\mathbf{r},t)$, extracellular matrix component $m(\mathbf{r},t)$, waste products $w(\mathbf{r},t)$, and cell death reporter $s(\mathbf{r},t)$. Carrying capacity is modelled by both a local term $k(\mathbf{r},t)$ and a non-local term $K(t)$, and cell diffusivity $D(m)$ is non-constant and dependent on extracellular matrix production. Growth rate of bacterial cells is described

Parameter	Value		Parameter	Value
α_0	1 h^{-1}		k_0	5 cells µm^{-2}
k_1	1.5 cells µm^{-2}		γ_K	0.05 h^{-1}
k_k	50 cells h µm^{-2}		n_k	2
D_0	2500 µm^2 h^{-1}		λ_m	10 h^{-1}
k_m	0.05 cells µm^{-2}		n_m	2
α_s	20 molecules h^{-1}		k_s	3.75 cells µm^{-2}
n_s	3		λ_s	20 h^{-1}

Table 2.1: Table of default parameter values as given in [6] to be used in conjunction with system (2.1). For further details, please refer to [6].

by a spatially correlated random function $\alpha(\mathbf{r})$. The full model is given below:

$$\begin{aligned}
\frac{\partial \rho(\mathbf{r},t)}{\partial t} =& \alpha(\mathbf{r})\rho(\mathbf{r},t)\left(1-\frac{\rho(\mathbf{r},t)}{k(\mathbf{r},t)}\right)+\nabla\cdot\big(D(m(\mathbf{r},t))\nabla\rho(\mathbf{r},t)\big)\\
k(\mathbf{r},t) =& \frac{K(t)+k1\cdot(w(\mathbf{r},t)/k_k)^{n_k}}{1+(w(\mathbf{r},t)/k_k)^{n_k}}\\
\frac{dK(t)}{dt} =& -\frac{\gamma_K}{\Omega}\int_\Omega \rho(\mathbf{r},t)d\mathbf{r}, \qquad K(0)=k_0\\
\frac{\partial w(\mathbf{r},t)}{\partial t} =& \rho(\mathbf{r},t)\\
\frac{\partial m(\mathbf{r},t)}{\partial t} =& \lambda_m\frac{(\rho(\mathbf{r},t)/k_m)^{n_m}}{1+(\rho(\mathbf{r},t)/k_m)^{n_m}}\\
D(m) =& D_0\exp(-m)\\
\frac{\partial s(\mathbf{r},t)}{\partial t} =& \alpha_s\frac{(\rho(\mathbf{r},t)/k_s)^{n_s}}{1+(\rho(\mathbf{r},t)/k_s)^{n_s}}-\lambda_s s(\mathbf{r},t)\\
\alpha(\mathbf{r}) =& \alpha_0\cdot\left(\phi+\frac{1-\phi}{1+\exp(-a_0-a_1\eta(\mathbf{r}))}\right)
\end{aligned} \tag{2.1}$$

Note that $\eta(\mathbf{r})$ is a spatial correlation term that influences the spatially dependent random growth function $\alpha(\mathbf{r})$ (where a_0, a_1 and ϕ are constants), which is described in more detail in Section 2.6. Default parameter values as used for system (2.1) in [6] are shown in Table 2.1. For further details of parameters refer to [6].

A brief description of the model terms are given here: Bacterial cell density, ρ, has carrying capacity, k, and the cell population grows in a logistic manner with a random, spatially correlated growth rate, α. Bacterial cells can diffuse, but their diffusion is limited with increasing matrix production. The local carrying capacity, k, is a decreasing function which falls as waste builds up within the system, while the rate at which waste is produced increases with an increase in cell density. Extracellular matrix production increases slowly and is activated at a threshold value, k_m, of cell density, while the rate of cell-death is modelled by a death reporter, s. This reporter is also activated at a threshold value, k_s, of cell density, but in addition shows degradation over time (as observed experimentally). It can be seen that the rate equation for the cell death reporter, s, does not feed back into system (2.1). Thus, having found the solution for ρ, the behaviour of s over time and space can be directly calculated from this. It follows that where heterogeneity or homogeneity is observed in cell density results, it is expected that the same type of behaviour will be observed in cell death results.

2.3.1 Numerical Simulation of Results

In the original paper [6], numerical computation of system (2.1) was carried out over a square domain representing an area measuring 5 mm x 5 mm. Periodic boundary conditions were imposed. The initial condition for ρ comprised randomly placed colonies inside a circle of diameter 2.5 mm located in the centre of the square domain. The majority of the colonies were concentrated at the circumference of the circle, producing a high density ring with numerous small randomly distributed microcolonies inside. This is representative of the coffee-ring effect explained in section 2.2; the central circle represents the area of initial bacterial inoculation on agar. Outside of the coffee-ring area the initial cell density ρ was set to zero. All other variables in the system had zero initial condition across the full domain. It is noted that system (2.1) was proposed as a method of predicting cell density and cell death patterns only in the central coffee-ring area of the biofilm and so the focus of interest is in the central circle with diameter

2.5 mm. The behaviour outwith this region can be discounted.

Simulation results of system (2.1) in [6] reproduced the heterogeneous nature of cell density and corresponding cell death within the coffee-ring structure in wildtype strain. Homogeneity of cell density and cell death is observed in the *eps* mutant with zero matrix production. These results are in agreement with experimental results which show a heterogeneous cell death pattern and wrinkle formation in wildtype strains and global homogeneous cell death and flat biofilms with no wrinkling in *eps* mutants that have drastically reduced matrix production.

As an alternative to a square domain, we propose that system (2.1) could be solved on a circular domain with a diameter equal to the diameter of the coffee-ring, i.e. 2.5 mm. Although this will not allow us to witness the persistence of the coffee-ring outline through time, it does allow us to focus purely on the behaviour within the coffee-ring structure which is the main purpose of our investigation. A small random initial condition of cell density throughout the circular domain is used to represent the bacterial microcolonies inside the coffee-ring. Again, all other variables in the system are set to zero initially. As previously noted, photographic images of wildtype and mutant strains of *B. subtilis* (Figure 2.1) show a distinct difference between wrinkling inside and outside of the coffee-ring. We hypothesise that the coffee-ring therefore acts as a boundary between the two separate areas and that biofilm contents that are inside the coffee-ring region after it has dried are trapped inside and cannot escape. The boundary conditions we choose to represent this behaviour in our new domain are no-flux conditions. This differs from the original boundary conditions used in simulations of model (2.1) in [6], where periodic boundary conditions are implemented on the large square domain, and no boundary conditions are applied to the coffee-ring region.

Having carried out a suitable non-dimensionalisaton of the model, COMSOL multiphysics software was used to carry out numerical simulations of system (2.1) on the new circular domain with the alternative (no-flux) boundary conditions. We used the General Form PDE package of COMSOL for numerical simulations, which implements a finite element method. Results can be seen in Figure 2.3. The results obtained using a circular domain were comparable to those observed inside the coffee-ring area in simulations of [6], with the same phenotypic behaviour in ρ and s being displayed. We use this new circular domain, with no-flux boundary conditions, for numerical simulation results throughout the rest of the chapter unless otherwise stated. As we are unable to define a spatially correlated random growth rate $\alpha(\mathbf{r})$ in COMSOL, we instead use a random growth rate where $\alpha(\mathbf{r})$ is normally distributed in $[0.25, 1]$. Again, results were comparable to those observed inside the coffee-ring area in simulations of [6] and thus this is the growth rate we use unless otherwise stated.

As an aside, we note that K (the global carrying capacity) in system (2.1) is a decreasing function in time. As such, it appears that it may be possible that $K < 0$ as time proceeds. This is not biologically plausible. However, it was checked that for all numerical simulation results included in this chapter, $K \geq 0$. It is noted that some numerical difficulties were encountered when running simulations for longer time periods i.e. running simulations for longer than approximately 100 hours. It is possible that these difficulties may arise as a result of the formulation of K.

2.4 Causes of Heterogeneity

It can be seen from simulation results of system (2.1) in Figure 2.3 that heterogeneity in cell density materialises when extracellular matrix production occurs (see left column of Figure 2.3). In the absence of matrix production, patterns do not emerge (see right column of Figure 2.3). Whilst not shown here, the same behaviour is also observed in simulations of cell death.

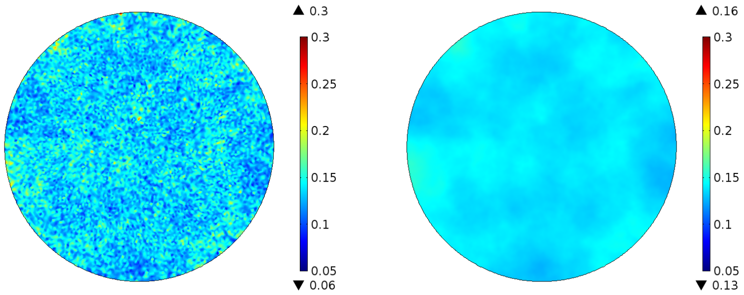

(a) WT at $t = 10\,\mathrm{h}$ (b) *eps* mutant at $t = 10\,\mathrm{h}$

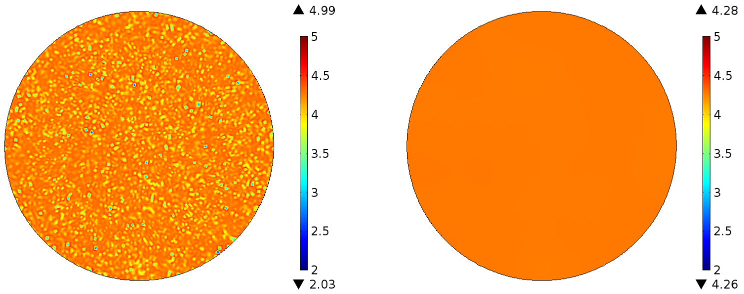

(c) WT at $t = 20\,\mathrm{h}$ (d) *eps* mutant at $t = 20\,\mathrm{h}$

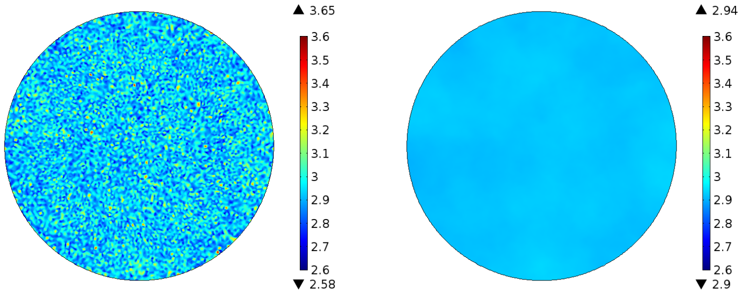

(e) WT at $t = 30\,\mathrm{h}$ (f) *eps* mutant at $t = 30\,\mathrm{h}$

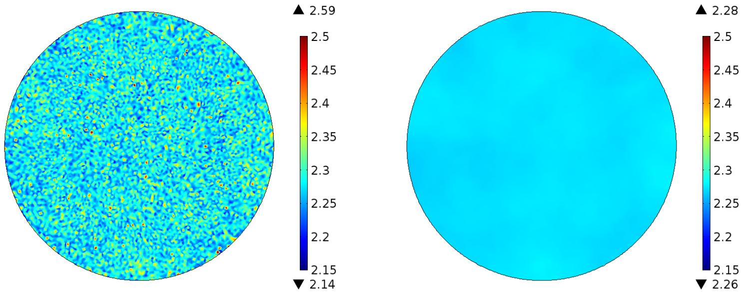

(g) WT at $t = 40\,\mathrm{h}$ (h) *eps* mutant at $t = 40\,\mathrm{h}$

Figure 2.3: Numerical simulations of cell density, ρ (in cells $\mu\mathrm{m}^{-2}$), for wildtype (WT) and *eps* mutant strains, using system (2.1) calculated on a circular domain representing the coffee-ring region (diameter 2.5 mm). No-flux boundary conditions are implemented. Wildtype (left column) and *eps* mutant strains (right column) are shown at times t=10, 20, 30 and 40 h. Higher cell density is represented by red and lower cell density is represented by blue. Parameter values are as given in [6] (see Table 2.1), with $\lambda_m = 10\,\mathrm{h}^{-1}$ in wildtype and $\lambda_m = 0\,\mathrm{h}^{-1}$ in *eps* mutant. Initial condition for ρ is a small random function everywhere in the domain. Other variables are set to 0 initially. Simulations created in COMSOL.

As system (2.1) is quite complex the driving force behind the pattern formation is not clear. Asally et al. [6] have stated that the random growth rate is a crucial feature of their model and they also note that the degree of heterogeneity displayed can be attributed to the parameter k_m. This parameter is described as the matrix accumulation density threshold and controls the value of cell density at which matrix production is switched on for different strains of *B. subtilis* biofilms. We aim to understand if random growth rate α is the only crucial term within system (2.1) that allows pattern formation to develop, and ask whether any of the other terms are also vital. We also determine if the parameter k_m is the only term which can be used as a means of controlling the degree of heterogeneity displayed.

2.4.1 Simplification of the Model

The complexity of system (2.1) makes it difficult to determine what is driving the pattern formation in numerical simulations. A simplification of model (2.1) is analysed to determine whether heterogeneous patterns can be retained in the absence of some of the model features.

First we set the growth rate $\alpha = \alpha_0$, diffusion term $D = D_0$, and local carrying capacity $k = k_0$, to be constant. By fixing $k = k_0$ to be constant, it follows that variables w and K are no longer necessary and system (2.1) therefore becomes

$$\begin{aligned}
\frac{\partial \rho(\mathbf{r},t)}{\partial t} &= \alpha_0 \rho(\mathbf{r},t)\left(1-\frac{\rho(\mathbf{r},t)}{k_0}\right) + \nabla\cdot\left(D_0 \nabla \rho(\mathbf{r},t)\right),\\
\frac{\partial m(\mathbf{r},t)}{\partial t} &= \lambda_m \frac{(\rho(\mathbf{r},t)/k_m)^{n_m}}{1+(\rho(\mathbf{r},t)/k_m)^{n_m}},\\
\frac{\partial s(\mathbf{r},t)}{\partial t} &= \alpha_s \frac{(\rho(\mathbf{r},t)/k_s)^{n_s}}{1+(\rho(\mathbf{r},t)/k_s)^{n_s}} - \lambda_s s(\mathbf{r},t),
\end{aligned} \tag{2.2}$$

where reaction terms are unchanged from the original system. A single steady state given by $(\rho^*, m^*, s^*) = (0, m^*, 0)$ exists for this system. It can be seen that in system

(2.2), variable ρ positively feeds forward into the equations for m and s, however the equation for ρ is now dependent on no variable other than itself. The equation describing ρ has become a stand alone equation, recognisable as Fisher's equation, which is known to produce no patterns when coupled with Neumann boundary conditions. It is concluded that if the variables α, D and k in the original model of Asally et al. [6] (system (2.1)) are set as constants, no pattern formation will occur.

2.4.2 A Two-Variable Model Analysis

It is known that a system of two reaction-diffusion equations can produce patterns via Turing instabilities provided certain conditions are satisfied. Having determined that a simplified form of the model of Asally et al. [6] (system (2.2)) cannot produce patterns, we investigate whether it is possible for any two-variable model consisting of a single reaction-diffusion equation coupled to a second PDE (without explicit spatial terms) to produce patterns through Turing instabilities.

We consider the model set-up,

$$\begin{aligned} \frac{\partial u}{\partial t} &= F(u,v) + \nabla \cdot \left(D(u,v) \nabla u \right), \\ \frac{\partial v}{\partial t} &= G(u,v), \end{aligned} \tag{2.3}$$

where $u = u(\mathbf{x},t)$ and $v = v(\mathbf{x},t)$ are (non-dimensional) variables, and $\mathbf{x} \in \mathbb{R}^n$. This is the generic form of system (2.2), where the two new variables, u and v, represent cell density and matrix respectively, and cell death is ignored. It is assumed that (u^*, v^*) is a steady state associated with the system and that $D > 0$ for all (u,v).

Four possibilities for the form of reaction terms in system (2.3) are reviewed here and are as follows:

$$
\begin{array}{lcc}
\text{Case A:} & F = F(u), & G = G(u); \\
\text{Case B:} & F = F(u,v), & G = G(u); \\
\text{Case C:} & F = F(u), & G = G(u,v); \\
\text{Case D:} & F = F(u,v), & G = G(u,v);
\end{array}
$$

These possibilities only consider the cases where F and G are dependent on u, the cell density. $G = G(v)$ is not considered as it is unlikely that matrix exclusively controls its own production. Similarly, $F = F(v)$ is not considered.

Next we consider a solution to system (2.3) of the form

$$
u(\mathbf{x},t) = u^* + \hat{u}(\mathbf{x},t), \quad v(\mathbf{x},t) = v^* + \hat{v}(\mathbf{x},t), \tag{2.4}
$$

where $|\hat{u}| \ll 1$ and $|\hat{v}| \ll 1$ are small perturbations. Using Taylor series to expand F around the steady state (u^*, v^*) yields

$$
\begin{aligned}
F(u) = F(u^* + \hat{u}) = F^* + F_u^* \hat{u} + \text{H.O.T.}, \\
F(u,v) = F(u^* + \hat{u}, v^* + \hat{v}) = F^* + F_u^* \hat{u} + F_v^* \hat{v} + \text{H.O.T.},
\end{aligned}
\tag{2.5}
$$

where higher order terms (H.O.T.) will be subsequently ignored, and $F^* = F(u^*, v^*)$. Similarly, $F_u^* = F_u(u^*, v^*)$ and $F_v^* = F_v(u^*, v^*)$ denote the derivatives of F with respect to u and v evaluated at the steady state. Similar results are found for the expansion of G around (u^*, v^*). Substituting the results of the expansions in equation (2.5) into system (2.3) results in four generic systems corresponding to the four cases of F and G investigated (for example, see equation (2.8) relating to Case A below). For each case, solutions are assumed to be separable and of the form

$$
\hat{\mathbf{W}}(\mathbf{x},t) = \sum_k \Psi_k(t) \Phi_k(\mathbf{x}), \tag{2.6}
$$

where $\Phi_k(\mathbf{x})$ satisfies the related eigenvalue problem

$$\begin{aligned} \nabla^2\Phi_k + k^2\Phi_k = 0 \quad \text{on } B, \\ \mathbf{n}\cdot\nabla\Phi_k = 0 \quad \text{on } \partial B. \end{aligned} \tag{2.7}$$

Here, $\hat{\mathbf{W}}(\mathbf{x},t) = \begin{bmatrix} \hat{u}(\mathbf{x},t) & \hat{v}(\mathbf{x},t) \end{bmatrix}^T$, $\Phi_k = \begin{bmatrix} \tilde{u}_k(\mathbf{x}) & \tilde{v}_k(\mathbf{x}) \end{bmatrix}^T$, B is the n-dimensional bounded spatial domain, $\mathbf{n}$ is the normal to the boundary ∂B, and k is the wave number. We assume zero-flux boundary conditions.

Case A

The linearised form of system (2.3) becomes

$$\begin{aligned} \hat{u}_t &= F_u^*\hat{u} + D^*\nabla^2\hat{u} \\ \hat{v}_t &= G_u^*\hat{u}, \end{aligned} \tag{2.8}$$

where $D^* = D(u^*, v^*)$. Substituting the ansatz (2.6) into (2.8) gives the associated Jacobian matrix

$$J_A = \begin{pmatrix} F_u^* - k^2D^* & 0 \\ G_u^* & 0 \end{pmatrix}. \tag{2.9}$$

The corresponding characteristic polynomial for the calculation of the eigenvalues, λ, of J_A is given by

$$\lambda^2 + (k^2D^* - F_u^*)\lambda = 0. \tag{2.10}$$

Similarly, the corresponding Jacobian matrices and characteristic polynomials in Cases B-D are shown below:

Case B

$$\text{Jacobian:} \quad J_B = \begin{pmatrix} F_u^* - k^2D^* & F_v^* \\ G_u^* & 0 \end{pmatrix} \tag{2.11}$$

$$\text{Characteristic polynomial:} \quad \lambda^2 + (k^2D^* - F_u^*)\lambda - F_v^*G_u^* = 0 \tag{2.12}$$

Case C

$$\text{Jacobian:} \quad J_C = \begin{pmatrix} F_u^* - k^2 D^* & 0 \\ G_u^* & G_v^* \end{pmatrix} \tag{2.13}$$

$$\text{Characteristic polynomial:} \quad \lambda^2 + (k^2 D^* - F_u^* - G_v^*)\lambda + (F_u^* - k^2 D^*)G_v^* = 0 \tag{2.14}$$

Case D

$$\text{Jacobian:} \quad J_D = \begin{pmatrix} F_u^* - k^2 D^* & F_v^* \\ G_u^* & G_v^* \end{pmatrix} \tag{2.15}$$

$$\text{Characteristic polynomial:} \quad \lambda^2 + (k^2 D^* - F_u^* - G_v^*)\lambda + (F_u^* - k^2 D^*)G_v^* - F_v^* G_u^* = 0 \tag{2.16}$$

It is noted that in these calculations the diffusion term D can be either constant or dependent on the variables u, v or both. The form of D has no bearing on the results of these calculations as the linearised systems, and resulting characteristic polynomials, in Cases A-D are the same regardless, and depend only on the value D^*. However, it is assumed that D is positive for all u and v, i.e. the standard Fickian assumption.

Turing instability analysis is used to determine whether any diffusion-driven patterns can be formed in system (2.3). By first assuming that a steady state is stable in the absence of diffusion, it is determined if it can be made unstable when diffusion is added into the system. If instability can occur in the presence of diffusion, then pattern formation is a possible outcome. The stability of the steady state is determined by computing the eigenvalues, λ, in both the presence and absence of diffusion. The conditions required for Turing instability to occur are

$$\text{tr}(\tilde{J}) < 0, \quad \det(\tilde{J}) > 0, \quad \text{tr}(J) < 0, \quad \det(J) < 0, \tag{2.17}$$

where $\tilde{J}$ and J are the Jacobian matrices in the absence and presence of diffusion respectively. All four inequalities in (2.17) must be satisfied in order for the classic Turing instability to occur.

In Cases A, B and C it is found that Turing instabilities cannot occur as the inequalities (2.17) are not satisfied. In case D it is necessary to impose the following conditions in order for all inequalities in (2.17) to be satisfied:

$$\begin{aligned} G_v^* &> 0, \\ F_u^* &< 0, \\ F_v^* G_u^* &< 0, \\ F_u^* G_v^* &> F_v^* G_u^* \\ k^2 &> \frac{F_u^* G_v^* - F_v^* G_u^*}{G_v^* D^*}. \end{aligned} \tag{2.18}$$

It is noted that the last inequality in (2.18) is a linear function of k^2 because only one diffusion term exists in system (2.3). It suggests that pattern formation can occur for all values of k^2 above a threshold value. This differs from the quadratic inequality in k^2 that is normally found in Turing analysis when two reaction-diffusion equations are analysed. In that case, patterns can only emerge for values of k^2 bounded in a specific finite interval.

Examining conditions (2.18) it can be seen that a necessary condition for Turing instability to occur is $G_v(u^*, v^*) > 0$. Applying this condition to a system (2.3) where u and v represent cell density and matrix production respectively, it is found that Turing instability can only occur if matrix is facilitating its own production at the steady state, (u^*, v^*). We suggest that this unchecked production of matrix would be unrealistic in the biofilm context and instead suggest that either matrix production will slow down, or matrix will be degraded at higher densities. In both of these cases, $G_v^* < 0$. Overall it is unlikely that the matrix production rate will continue to increase unchecked throughout biofilm development. As such, we conclude that Turing instabilities cannot occur in a system (2.3) where u represents cell density and v represents extracellular matrix.

2.4.3 Drivers of Heterogeneity

It is clear that pattern formation does not occur in the most simplified version (system (2.2)) of the model presented by Asally et al. [6]. It is also now clear that a general two variable system (2.3) of one reaction-diffusion equation representing cell density coupled to another PDE representing matrix production will not produce patterns. We now build on the simplified form given in system (2.2) and reconstruct the full model of Asally et al. [6] (system (2.1)) in stages to ascertain the driver(s) of heterogeneity (via numerical simulations). A summary of results is presented in Table 2.2 and a brief description of these results is given below. It is noted that the same phenotypic behaviour is observed in simulations using both random and constant initial conditions for cell density throughout a circular domain. Consequently, it can be concluded that heterogeneity, where observed, is not a result of heterogeneous initial conditions and is indeed an emergent property of the system.

Simulation results of system (2.1) show that pattern formation cannot be observed in any case where either a constant growth rate, $\alpha = \alpha_0 = 0.625\,\mathrm{h}^{-1}$, or constant diffusion term, $D = D_0 = 2500\,\mu\mathrm{m}^2\,\mathrm{h}^{-1}$, is observed. Conversely, in simulations with a random growth rate and non-constant diffusion, heterogeneity is always observed, regardless of the form of w, k and K. Some simulation results are shown in Figure 2.4. Despite the above result, we note that on reduction of D_0, phenotypic behaviour can

	w, K and k all constant	w constant, K and k varying	K constant, w and k varying	w, K and k all varying
constant α, constant D	✗	✗	✗	✗
random α, constant D	✗	✗	✗	✗
constant α, non-constant D	✗	✗	✗	✗
random α, non-constant D	✓	✓	✓	✓

Table 2.2: Table showing cases where heterogeneous (✓) and homogeneous (✗) patterns are observed in cell density, ρ, and cell death, s, for different forms of growth rate α, diffusion D, waste w, global carrying capacity K, and local carrying capacity k. In the case of constant terms, $\alpha = \alpha_0 = 0.625\,\mathrm{h}^{-1}$ and $D = D_0 = 2500\,\mu\mathrm{m}^2\,\mathrm{h}^{-1}$. All forms are substituted into system (2.1).

change. Simulation results (not included here) show that some patterning may be possible in all cases of Table 2.2 where D_0 is reduced (initial conditions are often important in these cases), however the degree of heterogeneity is less than that observed in cases including both a random growth rate and a non-constant diffusion term (row 4 of Table 2.2). With regard to the heterogeneity observed in simulations appearing in [6], where $D_0 = 2500\,\mu\mathrm{m}^2\,\mathrm{h}^{-1}$ is the default value, both random growth rate and non-constant diffusion are essential for patterning to occur in system (2.1). Thus we suggest that in cases where D_0 is sufficiently large, a random growth rate and non-constant diffusion term are both drivers of heterogeneity (as suggested by Table 2.2).

It is noted that in the case with $k = k_0$ (constant), random $\alpha = \alpha(\mathbf{r})$, and non-constant diffusion $D = D(m)$, heterogeneity is observed throughout much of the simulation time, but is lost at later times as cell density approaches the carrying capacity, k_0. In contrast, heterogeneity persists until the end of simulations for varying (decreasing) carrying capacity, k. These results can be seen in Figure 2.5. An explanation of this is as follows. No explicit death term is included in the cell density equation of system (2.1), indicating that carrying capacity is the only term limiting the overall cell

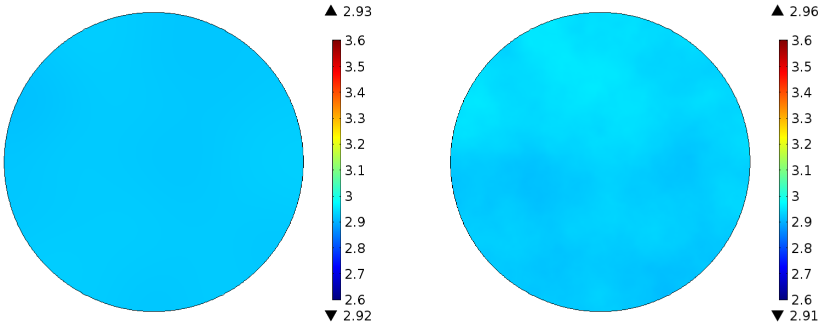

(a) Constant α and constant D (b) Random α and constant D

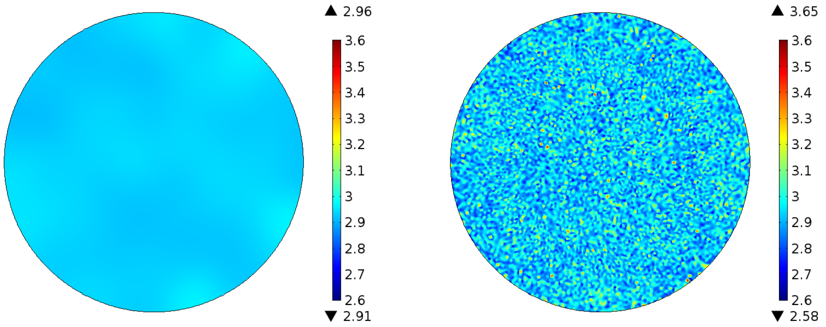

(c) Constant α and non-constant D (d) Random α and non-constant D

Figure 2.4: Simulations showing wildtype cell density ρ (in cells μm^{-2}) for different forms of growth rate, α, and diffusion, D, at $t = 30\,\text{h}$. All other terms are as described in the original model (2.1) and initial conditions are the same as those in Figure 2.3. Parameter values are $D = D_0 = 2500\,\mu\text{m}^2\,\text{h}^{-1}$ for D constant and $\alpha = \alpha_0 = 0.625\,\text{h}^{-1}$ for α constant. Non-constant diffusion $D = D(m)$ is of the same form as defined in system (2.1). All other parameter values taken from Table 2.1. Simulations are carried out in COMSOL on a circular domain (diameter 2.5 mm to represent the coffee-ring region) with no-flux boundary conditions.

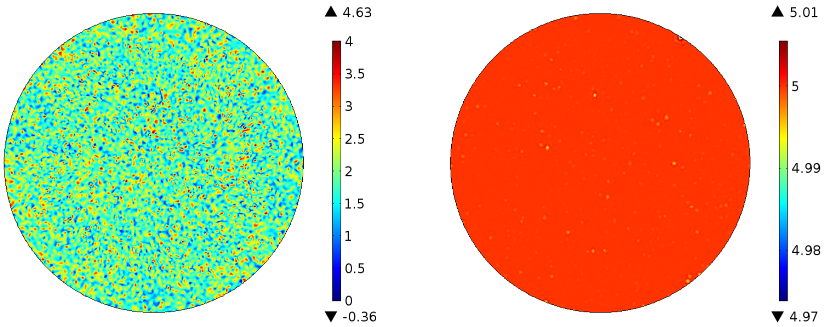

(a) Constant k, $t = 15\,\mathrm{h}$ (b) Constant k, $t = 40\,\mathrm{h}$

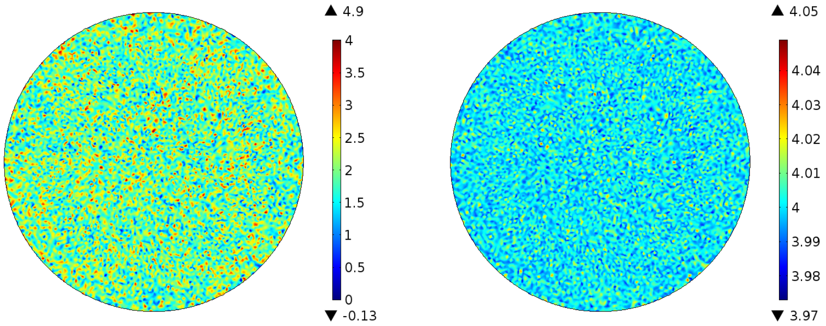

(c) Varying k, $t = 15\,\mathrm{h}$ (d) Varying k, $t = 40\,\mathrm{h}$

Figure 2.5: Wildtype cell density, ρ (in cells $\mu\mathrm{m}^{-2}$), for different forms of carrying capacity, k, at times $t = 15\,\mathrm{h}$ and $t = 40\,\mathrm{h}$. All other terms are as described in the original model (2.1) and initial conditions are the same as those in Figure 2.3. Parameter values are as given in Table 2.1, with $k = k_0 = 5\,\mathrm{cells}\ \mu\mathrm{m}^{-2}$ chosen for the k constant case. Simulations conducted in COMSOL on a circular domain (diameter 2.5 mm to represent the coffee-ring region) with no-flux boundary conditions.

density. While carrying capacity is constant ($k = k_0$), the model with random growth rate and non-constant diffusion will grow heterogeneously throughout the domain at earlier time-steps as it does for varying k. As the first peaks in cell density reach carrying capacity they must stop growing, allowing the level of cell density in the remainder of the domain to catch-up until it too reaches capacity. This results in homogeneous cell density eventually being reached everywhere in the domain. In these simulations increasing the constant carrying capacity (k_0) allows heterogeneity to be observed longer into the simulation. A similar increase in carrying capacity in simulations where either growth rate α or diffusion D is constant has no effect on results and homogeneity continues to be observed. Therefore, we can deduce from these cases that the variable k is not driving heterogeneity. It can be seen from system (2.1) that global carrying capacity, K, and waste products, w, affect only the local carrying capacity, k. Therefore it follows that both K and w can be neglected without influencing the general phenotype of the results.

We can conclude that two terms act as the driving force in producing heterogeneity in cell density and cell death: random growth rate and non-constant diffusion. The fact that both terms are needed for patterning to occur suggests that the balance between the two terms is important in the determination of heterogeneity.

2.5 Effect of Non-constant Diffusion Term

The non-constant diffusion term ($D = D(m)$) in system (2.1) has been shown above to play an important part in instigating pattern formation. Density dependent diffusion has been used to model various biological scenarios ranging from insect dispersal [115] to cancer invasion [56]. It has been commented upon that reaction-diffusion equations utilising non-constant diffusion terms present difficult mathematical challenges, and that the majority of models using non-constant diffusion terms cannot be solved analytically [112].

Disassembling the cell-density equation in system (2.1) and determining the influence of each of the separate terms can help in understanding the effect that the non-constant diffusion term contributes to the system. For ease of notation, the dependence of the variables on space and time are omitted although we note that we consider the general spatial case, $\mathbf{x} \in \mathbb{R}^n$. At this point only the effect of non-constant diffusion is of interest so we consider constant $\alpha = \alpha_0$ and constant $k = k_0$. Thus the cell density equation from system (2.1) becomes

$$\begin{aligned}\frac{\partial \rho}{\partial t} &= \alpha_0 \rho \left(1 - \frac{\rho}{k_0}\right) + \nabla \cdot \big(D(m)\nabla \rho\big) \\ &= \underbrace{\alpha_0 \rho \left(1 - \frac{\rho}{k_0}\right)}_{a} + \underbrace{D(m)\nabla^2 \rho}_{b} + \underbrace{\nabla D(m) \cdot \nabla \rho}_{c}.\end{aligned} \tag{2.19}$$

It can be seen from equation (2.19) that term (a) represents logistic growth. The behaviour of the logistic equation is well known, and it is widely used in population dynamics modelling. The steady states of the logistic equation are $\rho^* = 0$ (an unstable steady state) and $\rho^* = k_0$ (a stable steady state). From any biologically relevant initial condition ($\rho > 0$), population ρ will grow until reaching carrying capacity.

Term (b) in equation (2.19), where D is a constant, is the classical diffusion operator. Considering only terms (a) and (b) (where term (b) has constant diffusion D) reduces equation (2.19) to Fisher's equation. Fisher's equation has the same uniform steady states and stability as the logistic equation.

Expression (c) in equation (2.19) comes about as a consequence of the non-constant diffusion term. Expansion of equation (2.19) using the chain rule gives

$$\frac{\partial \rho}{\partial t} = \underbrace{\alpha_0 \rho \left(1 - \frac{\rho}{k_0}\right)}_{a} + \underbrace{D(m)\nabla^2 \rho}_{b} + \underbrace{\frac{\partial D(m)}{\partial m}\left(\nabla m \cdot \nabla \rho\right)}_{c}. \tag{2.20}$$

The general diffusion-convection equation is

$$\frac{\partial \rho}{\partial t} = \underbrace{\text{Reaction Terms}}_{a_1} + \underbrace{D_1 \nabla^2 \rho}_{b_1} \underbrace{- \mathbf{v} \cdot \nabla \rho}_{c_1}, \tag{2.21}$$

where the term (c_1) describes the collective movement of suspended particles in an incompressible fluid moving with velocity $\mathbf{v} \in \mathbb{R}^n$. Comparing term ($c$) and ($c_1$) it

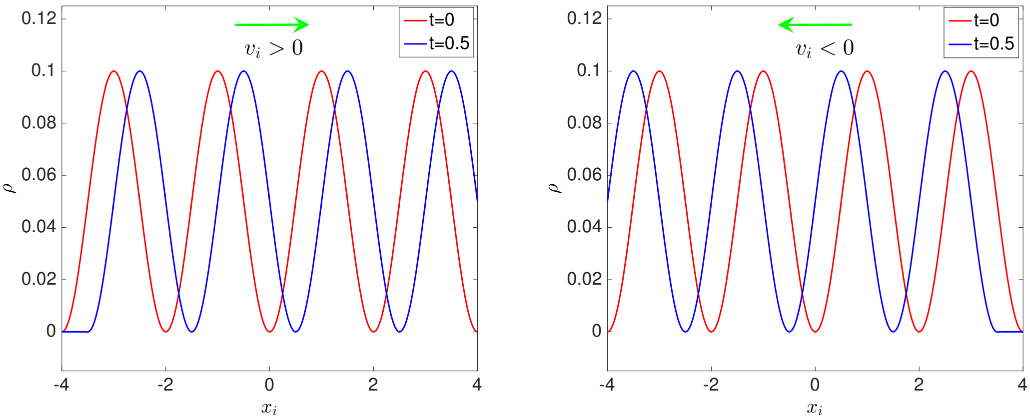

(a) $v_i > 0$ $(v_i = 1)$ (b) $v_i < 0$ $(v_i = -1)$

Figure 2.6: Direction of flow for positive and negative v_i. Simulations of cell density, ρ, in equation (2.21) where terms $(a_1) = 0$ and $(b_1) = 0$, and $v_i \neq 0$. Results show the direction of flow for positive and negative v (green arrow). Times shown are $t = 0$ (red) and $t = 0.5$ (blue). Simulations carried out using MATLAB's pdepe solver with the initial condition $\rho = 0.1\sin(\pi x_i/2)^2$ and other parameter values as given in Table 2.1.

can be seen that non-constant diffusion, D, can be thought of as contributing a non-linear convective effect (c) to Fisher's equation [115], where the velocity components v_i $(i = 1, .., n)$ are dependent on m and are given by

$$v_i = -\frac{\partial D(m)}{\partial m}\frac{\partial m}{\partial x_i}. \tag{2.22}$$

The signs of v_i give the direction of flow. Flow is along the increasing x_i-axis for $v_i > 0$ (as seen in Figure 2.6(a)) and along the decreasing x_i-axis for $v_i < 0$ (as seen in Figure 2.6(b)).

We now consider equation (2.19) including only the convective term and growth rate (expressions (c) and (a)). As the diffusion term is matrix dependent, we also consider the equation for matrix production from system (2.1). The relevant system is therefore:

$$\begin{aligned}\frac{\partial \rho}{\partial t} =& \alpha\rho\left(1-\frac{\rho}{k_0}\right)+\frac{\partial D(m)}{\partial m}\left(\nabla m\cdot\nabla\rho\right),\\ \frac{\partial m}{\partial t} =& \lambda_m\frac{(\rho/k_m)^{n_m}}{1+(\rho/k_m)^{n_m}}.\end{aligned} \tag{2.23}$$

The relationship between m and ρ suggests that they are spatially correlated i.e. local peaks and troughs of cell density and matrix density occur at the same points in domain $\mathbf{x}$. Therefore, where the gradient components of cell density are positive in domain $\mathbf{x}$, the gradient components of matrix density are also positive. Similarly, negative gradients in cell density and matrix density occur at the same points in $\mathbf{x}$. Consequently $\partial\rho/\partial x_i$ and $\partial m/\partial x_i$ have the same sign. In [6], the chosen function for D is a decreasing function of m, i.e. $\partial D/\partial m < 0$. Therefore from equation (2.22),

$$\text{sign of }(v_i) = \text{sign of }\left(\frac{\partial\rho}{\partial x_i}\right),$$

and the direction of flow at each point in the domain can be determined by considering the signs of $\partial\rho/\partial x_i$. Where ρ is increasing, $v_i > 0$ and so flow is to the right along the x_i-axis. Where ρ is decreasing, $v_i < 0$ so flow is to the left. Density is therefore expected to increase at the central region of peaks and decrease further out from peaks (i.e. a narrowing of peaks is expected). This is demonstrated in Figures 2.7(a) and 2.7(c). In contrast, if diffusion D is an increasing function in m (e.g. $D = \exp(m)$) it is surmised that the opposite will be true and a widening of peaks is expected. This effect can be seen in Figures 2.7(b) and 2.7(d). In both cases, wherever $\partial\rho/\partial x_i = 0$ in the domain, $v_i = 0$. This suggests that at minima and maxima of ρ (and consequently m), cell density (and matrix density) remains unchanged.

Results in Figure 2.7 also correlate with simulation results of the full model system (2.1) in $\mathbb{R}^2$ as seen in Figure 2.3. In system (2.1), the matrix dependent decreasing diffusion function, $D = D_0\exp(-m)$, slows spatial spread through time as m builds up

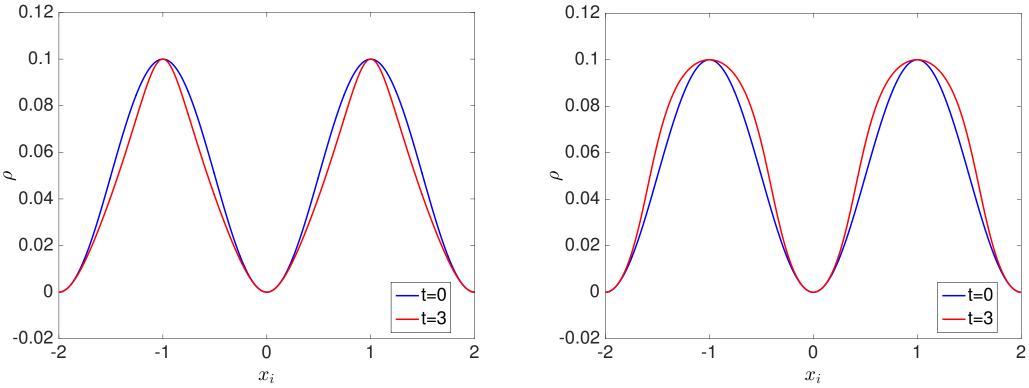

(a) $\alpha_0 = 0$, $D = \exp(-m)$ (b) $\alpha_0 = 0$, $D = \exp(m)$

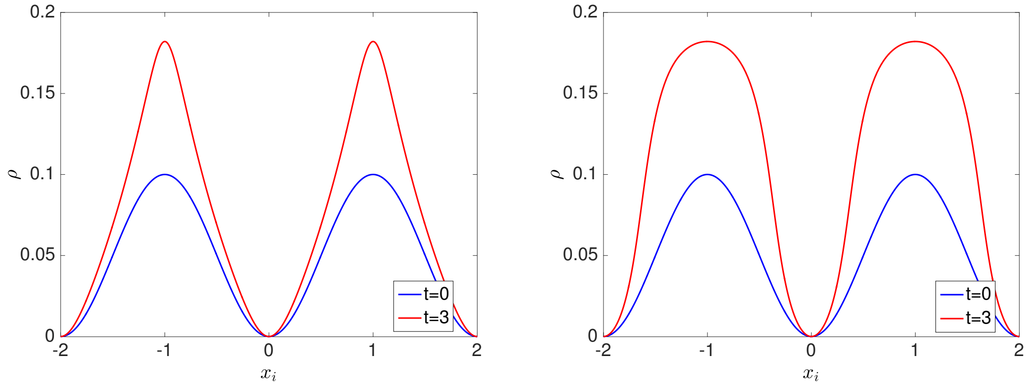

(c) $\alpha_0 = 0.2$, $D = \exp(-m)$ (d) $\alpha_0 = 0.2$, $D = \exp(m)$

Figure 2.7: Effects of non-constant diffusion rates on density distributions. Simulations of cell density, ρ, in system (2.23) conducted using MATLAB's pdepe solver. Density profile (red) shows ρ at $t = 3$. Initial conditions are $\rho = 0.1\sin(\pi x_i/2)^2$ (blue) and $m = 0$. Figures (a) and (b) show results of system (2.23) with no reaction term. Figures (c) and (d) show results with the inclusion of reaction term. Other parameter values as given in Table 2.1.

(a result of term (b) in equation (2.20)). Initial peaks of cell density remain as peaks and do not spread spatially (a result of term (c) in equation (2.20)). This leads to heterogeneity. Relating this to the biology, extracellular matrix as modelled in system (2.1) limits spatial spread, with bacterial cells that are situated within matrix in wildtype strains finding it more difficult to move than free bacteria in *eps* mutant strains.

Asally et al. [6] comment on the fact that the degree of heterogeneity observed in simulation results can be altered by varying the value of k_m. A greater degree of heterogeneity is observed for lower values of k_m, where matrix production switches on at lower values of ρ. An almost homogeneous result is observed for high k_m, where matrix production is switched on at higher values of ρ. Matrix production therefore takes longer to switch on for high k_m, which results in a larger diffusion term $D = D_0 \exp(-m)$ persisting for longer into the simulation time. This persisting diffusion term acts to even out cell density and death throughout biofilm development. For smaller values of k_m, the diffusion term D decreases quickly, limiting the spread of the cell density and death through the domain. Diffusion is therefore less dominant for low k_m than for high k_m, and so more heterogeneity can be expected to materialise for lower k_m. These findings correspond to experimental results in [6]. Different *B. subtilis* mutant strains which produce different quantities of matrix content show varying degrees of heterogeneity. The degree of heterogeneity is observed to be positively correlated to the quantity of matrix produced.

It has been shown and previously noted that *eps* mutants deficient in extracellular matrix expand considerably slower than the wildtype strain (see Figure 2.1). This suggests that, rather than limiting diffusion, matrix production actually promotes spatial spread. Although the chosen diffusion term in [6] produces simulation results to match experimental results within the coffee-ring area, we reason that the growth of the biofilm outwith the coffee-ring cannot be realistically modelled in the same way.

2.6 Effect of Random Growth Rate

Having investigated further the effect of the non-constant diffusion term in system (2.1), we now turn our attention to the other feature in the system that we propose plays an important role in the production of heterogeneous cell density and cell death patterns; the random growth rate α. The authors of [6] have described the random growth rate α as a 'crucial assumption' in their model. The growth rate term defined for system (2.1) in [6] has the spatial correlation

$$< \eta(\mathbf{r}), \eta(\mathbf{r}') > \propto \exp\left(-\left(\frac{|\mathbf{r}-\mathbf{r}'|^2}{2\lambda_c^2}\right)^2\right), \tag{2.24}$$

with

$$\alpha(\mathbf{r}) = \alpha_0 \cdot \left(\phi + \frac{1-\phi}{1+e^{-a_0-a_1\eta(\mathbf{r})}}\right), \tag{2.25}$$

where $\mathbf{r} = (x, y)$. The parameters are not explicitly defined, although they are given the values λ_c=20 µm, $a_0 = 1$, $a_1 = 1$ and $\phi = 0.25$ in the original paper. These values ensure that the growth rate α is is bounded in the range [0.25,1].

The Euclidean distance $|\mathbf{r}-\mathbf{r}'|$ between two points, $\mathbf{r} = (x_1, y_1)$ and $\mathbf{r}' = (x_2, y_2)$, in $\mathbb{R}^2$ is defined by

$$|\mathbf{r}-\mathbf{r}'| = \sqrt{(x_1-x_2)^2+(y_1-y_2)^2}. \tag{2.26}$$

Equation (2.24) ensures that for a fixed value of λ_c, correlation of α in space decays exponentially as $|\mathbf{r}-\mathbf{r}'|$ increases. Therefore, in system (2.1), neighbouring bacterial cells are more likely to have similar growth rates, while bacterial cells that are separated by some distance are less likely to have similar growth rates.

An examination of relation (2.24) shows that as well as $|\mathbf{r}-\mathbf{r}'|$, the value of the parameter λ_c also plays a part in the determination of the correlation of α. We hypothesise that the chosen value of λ_c is instrumental in determining the phenotypic nature of patterns that emerge in cell density and cell death simulations in [6].

Increasing λ_c increases the correlation $< \eta(\mathbf{r}), \eta(\mathbf{r}') >$ while a decrease in λ_c decreases $< \eta(\mathbf{r}), \eta(\mathbf{r}') >$. This suggests that growth rate α at two neighbouring points is more likely to vary for small λ_c than for large λ_c, (i.e. α varies more across a fixed domain $\mathbf{x} \in \mathbb{R}^2$ for small λ_c compared to large λ_c). As a result more local peaks of ρ and s are expected to emerge in a fixed area for small λ_c in comparison to larger λ_c. In other words, a smaller characteristic wavelength of pattern is expected for small values of λ_c compared to large values.

Simulation results of system (2.1) are run in C (code courtesy of the authors of [6]) for varying values for λ_c. The reason for using C here is that the random growth term α can be directly controlled in the code. We were unable to exert this control in COMSOL. Numerical simulations are computed over the original square domain described in [6] with periodic boundary conditions and initial condition representing the coffee-ring as described in section 2.2. Once again, the behaviour outwith the coffee-ring region can be neglected. Consequently, simulation results (shown here in Figures 2.9 and 2.10) zoom into a central square area fitting inside the coffee-ring as demonstrated in Figure 2.8.

Simulation results of system (2.1) in C immediately reveal two interesting results. Firstly, a comparison of plots of the landscape of $\alpha(\mathbf{r})$ with either $\rho(\mathbf{r},t)$ (shown here in Figure 2.9) or with $s(\mathbf{r},t)$ (not shown here) at a given time using a specific random seed and a specific value of λ_c reveal a direct correlation between the peaks/troughs in α and ρ or s. Thus the wavelength of pattern in α is also evident in simulation results of ρ and s. Secondly, the emergence of different characteristic wavelengths in ρ for differing values of λ_c is evident, as can be seen in Figure 2.10.

Visually it is clear from the results in Figure 2.10 that an increase in the value of λ_c increases the wavelength between peaks in cell density, while a decrease in λ_c decreases

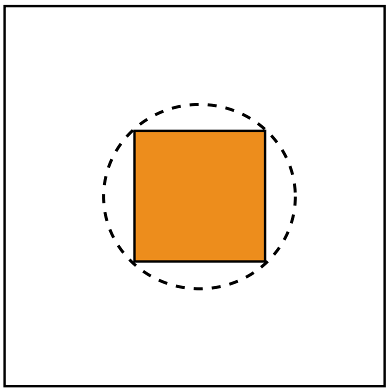

Figure 2.8: Schematic of various spatial domains considered in different simulations of system (2.1). Outer square (5 mm×5 mm) shows original domain over which the full original model system (2.1) is calculated in [6]. Circle represents coffee-ring area (diameter=2.5 mm) and the domain considered in Figures 2.3, 2.4, 2.5. Highlighted orange square is region shown in Figures 2.9 and 2.10, and is the region considered in the calculation of characteristic wavelength as seen in Figure 2.11.

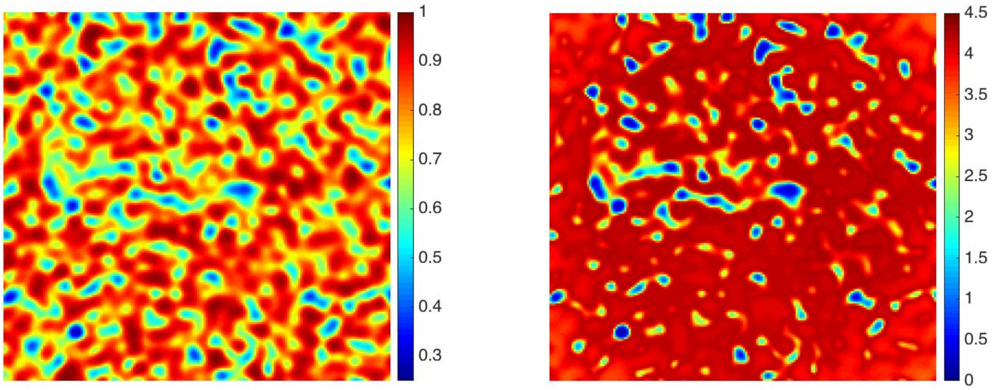

(a) $\alpha(\mathbf{r})$

(b) $\rho(\mathbf{r},t)$ at $t = 20\,\text{h}$

Figure 2.9: A comparison of the landscape of the spatially correlated growth rate $\alpha(\mathbf{r})$ with the landscape of cell density $\rho(\mathbf{r},t)$. Figure (a) shows $\alpha(\mathbf{r})$ (in h^{-1}) for a specific random seed and λ_c value ($\lambda_c = 20\,\mu\text{m}$), while Figure (b) shows the corresponding $\rho(\mathbf{r},t)$ (in cells μm^{-2}) at $t = 20\,\text{h}$ using the same random seed and λ_c value. Other parameter values are as specified in [6] (see Table 2.1). The spatial domain shown represents the highlighted orange square region as seen in Figure 2.8. Simulations from C.

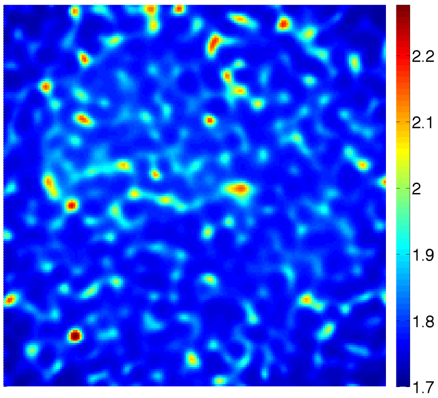

(a) $\lambda_c = 20\,\mu\text{m}$

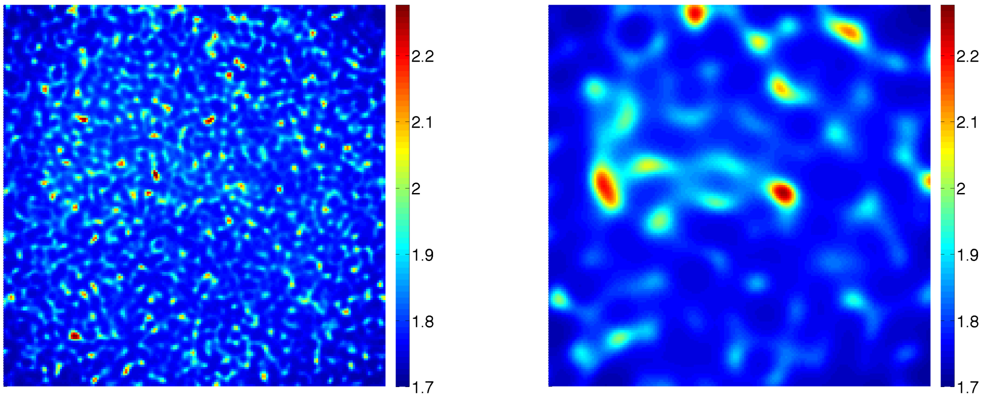

(b) $\lambda_c = 10\,\mu\text{m}$

(c) $\lambda_c = 40\,\mu\text{m}$

Figure 2.10: Effect of varying λ_c. Simulations show cell density ρ (in cells μm^{-2}) in system (2.1) for different values of λ_c in the highlighted square region of the original domain as seen in Figure 2.8. Time shown is $t = 40\,\text{h}$. Figure (a) shows the result for $\lambda_c = 20\,\mu\text{m}$, the original value for λ_c as specified in [6]. In Figure (b), $\lambda_c = 10\,\mu\text{m}$ and Figure (c) $\lambda_m = 40\,\mu\text{m}$. Other parameter values are as specified in [6] (see Table 2.1). Simulations from C.

the wavelength, as hypothesised. Similar results are also evident in simulations of the cell death reporter s (not shown here). It follows from these results that a positive correlation exists between the parameter λ_c and the corresponding wavelength that emerges from the model. As a means of quantitatively determining the degree of heterogeneity that is observed for each value of λ_c, we calculated the characteristic wavelength.

The method for calculation of the characteristic wavelength for cell density, ρ, in the domain highlighted in Figure 2.8 was as follows. A threshold value (thv_ρ) of ρ was assigned. Where $\rho > thv_\rho$ in the domain, this could be considered a peak. Values of $\rho < thv_\rho$ could be considered as background cell density. These values were disregarded and as such were set to zero. MATLAB was used to find the local peaks from the remaining data ($\rho > thv_\rho$), and a sparse matrix was formed determining the location of the regional peaks within the domain. The Euclidean distance between each local peak and its closest neighbouring peak was input into a vector, and the characteristic wavelength was defined as being the mean of these vector values. The same method was used to calculate the characteristic wavelength for cell death reporter, s, however a different threshold value, thv_s, was chosen.

Plots showing the mean characteristic wavelength observed in cell density, ρ, and cell death, s, for different values of λ_c can be seen in Figures 2.11(a) and 2.11(b) respectively. The data appears to show that characteristic wavelength is directly proportional to λ_c, with a doubling of λ_c leading to a doubling of the characteristic wavelength of the emergent pattern. An equation of the form

$$\text{wavelength} = \beta \lambda_c \tag{2.27}$$

was used in MATLAB's Curve Fitting Toolbox to fit the data with a curve of best fit. The value of β was found to vary as the values thv_ρ and thv_s were adjusted, however the linear relationship was always retained providing the threshold values were chosen

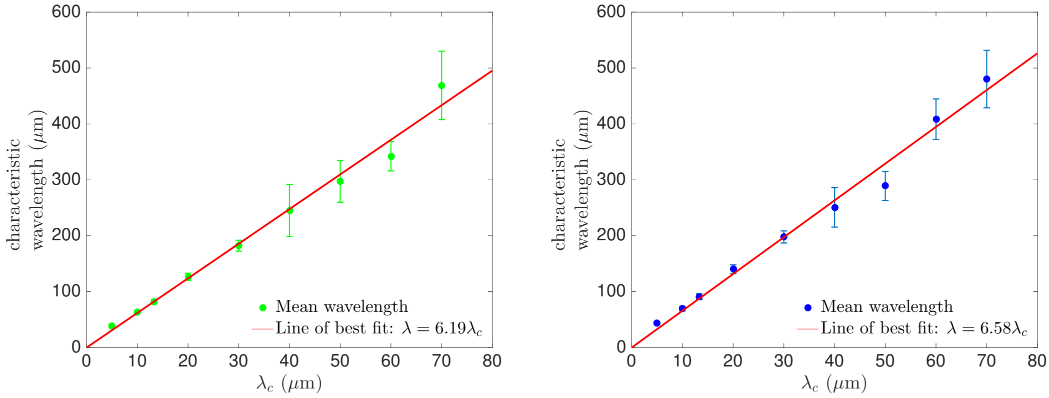

(a) characteristic wavelength of cell density ρ (b) characteristic wavelength of cell death s

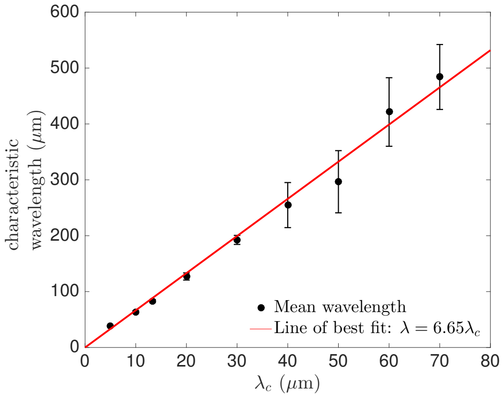

(c) characteristic wavelength of growth rate α

Figure 2.11: Plots of mean characteristic wavelengths of cell density ρ (Figure (a)), cell death s (Figure (b)) and growth rate α (Figure (c)) associated with different values of λ_c. Five different seeds were used for the initialisation of the random number generator in the calculation of the spatially correlated growth rate α. Green, blue and black circle markers show the mean characteristic wavelength calculated for specific λ_c values. Mean wavelength was calculated from the five seed initialisations used. The error bars represent one standard deviation above and below each mean value. The red line represents the line of best fit (of the mean values). Using $thv_\rho = 1.93$, $thv_s = 1.25$ and $thv_\alpha = 0.5$ the values of the corresponding slopes β were found as $\beta_\rho = 6.19$, $\beta_s = 6.58$ and $\beta_\alpha = 6.65$. Plots created in MATLAB using parameter values taken from Table 2.1 and initial conditions as specified in [6].

within a reasonable range. Choosing threshold values $thv_\rho = 1.93$ and $thv_s = 1.25$, the approximate values for the corresponding coefficients β_ρ and β_s in equation (2.27) were found to be $\beta_\rho = 6.19$ and $\beta_s = 6.58$ respectively.

Having verified the existence of a linear relationship between the parameter λ_c and the characteristic wavelength of patterns that emerge in cell density and cell death simulations, we implemented the same techniques to determine if the same relationship was evident in the random growth rate $\alpha(\mathbf{r})$. As one might anticipate, a linear relationship between characteristic wavelength and λ_c was again identified (see Figure 2.11(c)). Furthermore, through careful choice of the threshold value thv_α, it was found that the slope β_α could match the slopes β_ρ and β_s that are associated with cell density and cell death respectively.

These results confirm our hypothesis that the value of λ_c is linked to the characteristic wavelength of patterns that emerge in ρ and s in system (2.1), with smaller wavelengths arising for small values of λ_c and larger wavelengths arising for larger λ_c. However, the discovery of linear relationship between characteristic wavelength and λ_c is unexpected. The exponential term in the correlation equation (2.24) might instead be expected to bring about an exponential relationship linking characteristic wavelength and λ_c.

Overall, these findings suggest that the simulation results of system (2.1) are predetermined by the model formulation, with the spatial correlation of the growth rate chosen as the input of the model also being observed in the output. It follows that in order to obtain numerical results that are realistic and that match experimental data, it is vital to choose the correct value of the parameter λ_c.

2.7 Conclusions

The model devised by Asally et.al [6] gives a good starting point for the investigation into the mechanisms controlling patterns that are observed inside the coffee-ring structure of *B. subtilis* biofilms grown *in vitro*. The heterogeneous nature of cell density and corresponding cell death that is observed in experimental results is replicated in the numerical simulations of system (2.1) to a good extent. Analysis of the model has shown that the driving forces behind heterogeneity are the random growth rate and non-constant diffusion terms, and as such the inclusion of these terms is essential in order for patterns to be observed.

Experimental results in the paper suggest that mechanical forces cause buckling to occur in areas of localised cell death. While the model formulated in [6] appears to produce cell death patterns with a good likeness to those observed in experiments, the model does not take into account the buckling mechanism that is proposed to occur within the biofilm. As a result, the simulated cell death patterns can only give an indication as to the possible location of wrinkles within the coffee-ring region. The physical properties of the wrinkles that may arise as a result of the localisation of cell death are not considered in this model. Thus we have no indication of the physical properties of the resulting wrinkle structure.

Some other disadvantages of the model include the fact that the model proposed only takes account of wrinkling formation inside the coffee-ring, while the domain the simulations are calculated on shows the full biofilm as it grows. We suggest a circular domain with no-flux boundary conditions could provide a more suitable region for basing the simulations of this model on. We also note that the model could be made simpler by considering the carrying capacity of cell density ρ to be a constant term, as the results obtained in this case are indistinguishable from the full model in terms of the general phenotype of patterns. Another suggestion for improvement to the model is to explicitly model cell death. As it stands, cell density is only controlled by carrying capacity and there is no death term incorporated.

A significant drawback of the model is that the spatial correlation of the random growth rate α determines the degree of heterogeneity that is observed in simulation results. We can choose the most appropriate value of the parameter λ_c (and consequently the characteristic wavelength of emergent patterns) to be used in simulation results to best match experimental observations. However by doing this, we predetermine the output of the model.

Chapter 3

Cross-Diffusion Induced Pattern Formation in a Two-Species Model Representing Biofilm Formation

It was shown in the previous chapter that the PDE model of Asally et al. [6], which described bacterial cell density and corresponding cell death in a *Bacillus subtilis* biofilm, that spatial patterns could form in the presence of a random cell growth rate and density-dependent cell diffusion. In the model in [6], it was found that the wavelength of the spatial pattern that emerged was predetermined by the random growth rate used in the model formulation. Thus, patterns of any wavelength could be formed by varying the growth rate. In experimental results, however, a typical wavelength is observed in wildtype *B. subtilis* biofilms. We now investigate other PDE models describing biofilm growth to determine if they can generate spatial patterns with typical wavelengths that arise as a result of the underlying biological considerations rather than by some predetermined model input. We investigate how a two-species PDE model with different combinations of diffusion terms may generate patterns in spatially inhomogeneous systems. We focus on the effect of incorporating cross-diffusion terms, where the different components of the biofilm can move up or down concentration gradients of other components as well as their own species, into the model. The non-classic diffusion case, where self-diffusion terms are negative rather than positive, is also analysed.

3.1 Cross-Diffusion and Derivation from Random Walk

3.1.1 Cross-Diffusion Background

In Chapter 2, multi-species PDE systems consisting of reaction terms and self-diffusion terms were analysed. The self-diffusion terms described the movement of a species with respect to its own concentration gradient [153], however the systems considered did not take into account the possibility that concentration gradients in the other species could affect the movement of the original species. In reaction-diffusion systems where only self-diffusion terms exist, the generic form of the equation is

$$\frac{\partial \mathbf{u}}{\partial t} = \text{Reaction terms} + \nabla \cdot \big(D(\mathbf{u})\,\nabla \mathbf{u}\big)\,, \tag{3.1}$$

where the diffusion matrix $D = D(\mathbf{u})$ is a diagonal matrix [117]. For example, in the case of a two-species model, D takes the form

$$D = \begin{pmatrix} D_{11} & 0 \\ 0 & D_{22} \end{pmatrix}, \tag{3.2}$$

where $D_{ii} = D_{ii}(\mathbf{u})$. A standard requirement of self-diffusion terms is that coefficients $D_{ii} \geq 0$ [120, 136, 153]. These positive coefficients represent the fact that directed movement is down concentration gradients, generally resulting in a more equal distribution of species throughout the domain. A simple example of self-diffusive behaviour is Fickian diffusion, where D_{ii} is a constant.

In comparison to self-diffusion, cross-diffusion is only relevant in multi-species models. Cross-diffusion is the general term given to the situation where the concentration gradient of one species induces the flux of another species [153]. Non-diagonal elements of the diffusion matrix are called the cross-diffusion coefficients, and hence in a cross-diffusion situation at least one non-diagonal element of the diffusion matrix is non-zero [116]. A full diffusion matrix for a two-species system where the gradients of both species induce a flux in both their own species and the alternate species has the form

$$D = \begin{pmatrix} D_{11} & D_{12} \\ D_{21} & D_{22} \end{pmatrix}, \tag{3.3}$$

where all elements $D_{ij} = D_{ij}(\mathbf{u})$ are non-zero [136].

In comparison to self-diffusion coefficients which usually have the restriction $D_{ii} \geq 0$, there is no such restriction on the cross-diffusion terms D_{ij}; they can be positive, negative or zero [120]. We note that the possibility for D_{ij} to vary sign at different times and concentrations of model species also exists, however we do not deal with this case here. A cross-diffusion coefficient D_{ij}, where $i \neq j$, describes the diffusion of species i in relation to the concentration gradient of species j. D_{ij} will be negative when species i preferentially moves up concentration gradients of species j, and positive when the preferential movement is directed down concentration gradients. One condition that must be met in order for D_{ij} to be biologically relevant is that $D_{ij} = 0$ in the absence of species i. This is simply because there is no availability of species i to be directed towards or away from species j.

Cross-diffusion systems have been used to model several different scenarios in biology. Examples of cross-diffusion behaviour include the process of chemotaxis, where cells move towards or away from higher concentration gradients of molecules secreting chemical signals which attract or repel the cells (chemoattractants/chemorepellants) [153]. The Keller-Segel model is the classic example of a cross-diffusion chemotaxis model [85]. Haptotaxis is another example of cross-diffusion where cells aggregate due to their adhesion to a second species [20], which normally represents some form of underlying sticky matrix [7, 127].

3.1.2 Derivation of Cross-Diffusion from a Random Walk

To gain a better understanding of the origin of cross-diffusion terms in a two-species model, and what they mean in relation to the movement of individuals, a derivation from first principals is summarised here, following the same method as outlined in [86, 128]. The two species considered are denoted by u and v. For simplicity only the 1-D spatial case is considered here, although it is possible to extend this method to the n-D case. The derivation uses a random walk process to describe the movement of particles through a 1-D lattice with equidistant grid points and is as follows:

A standard conservation argument yields

$$\begin{pmatrix}\text{rate of change}\\ \text{of particle}\\ \text{concentration}\end{pmatrix} = \begin{pmatrix}\text{rate of entry}\\ \text{into }\Delta V\\ \text{per unit time}\end{pmatrix} - \begin{pmatrix}\text{rate of exit}\\ \text{from }\Delta V\\ \text{per unit time}\end{pmatrix} + \begin{pmatrix}\text{creation/loss}\\ \text{in }\Delta V\\ \text{per unit time}\end{pmatrix}, \quad (3.4)$$

where ΔV is the volume of a small element being considered [45].

Consider a grid point i within the lattice, and the flux of particles into and out of this location. Assume that a particle of u at location i can leave by either moving to the left or to the right, with probability P_i^- or P_i^+ respectively. Alternatively, it can also remain stationary. A particle in a neighbouring location (either $i-1$ or $i+1$) can ‘jump’ into location i either from the left with probability P_{i-1}^+ or from the right with probability P_{i+1}^-. Therefore, from the conservation equation (3.4) (where creation and loss are zero and where a change is density is considered over a small time step Δt), a master equation can be written down as:

$$u_i(t+\Delta t) = u_i + P_{i+1}^- u_{i+1} + P_{i-1}^+ u_{i-1} - \left(P_i^+ + P_i^-\right) u_i. \tag{3.5}$$

Here, u_i, u_{i-1} and u_{i+1} are the concentrations of particles at the respective locations of i, $i-1$ and $i+1$ at time t.

The next step is to define the probabilities, P, of particles jumping. In general, if the probability of jumping to a neighbouring location is density dependent on both species u and v, a general ansatz that can be considered for a two-species model is

$$\begin{aligned} P_i^\pm &= p_1(u_i, v_i) p_2(u_{i\pm 1}, v_{i\pm 1}), \\ P_{i\pm 1}^\mp &= p_1(u_{i\pm 1}, v_{i\pm 1}) p_2(u_i, v_i). \end{aligned} \tag{3.6}$$

The subscript of P denotes the location from which the particle is jumping, while the superscript indicates the direction of movement: ‘+’ describes movement in the positive x-direction (to the right) and ‘-’ describes movement in the negative x-direction (to the left). Here p_1 describes the incentive for a particle to leave its original position. On the other hand, p_2 describes the wish or need to join a neighbouring position, either location $i+1$ or $i-1$ in the case of $P_i^\pm$, or location i in the cases of $P_{i\pm 1}^\mp$. These preferences are density dependent. For example, if u was to represent a predator in a predator-prey system, the probability of u leaving its original location would be higher if more prey, v, and fewer predators, u, were in a neighbouring location.

Taylor series expansions are utilised to express $u_{i\pm 1}$ and $v_{i\pm 1}$ in terms of u_i and v_i

respectively. For example,

$$u_{i\pm1} = u_i \pm \Delta x \frac{\partial u_i}{\partial x} + \frac{(\Delta x)^2}{2} \frac{\partial^2 u_i}{\partial x^2} + \text{H.O.T.}, \tag{3.7}$$

where H.O.T. represents higher order terms and Δx is the small distance between grid points. Taylor series can also be used to describe $p_1(u_{i\pm1}, v_{i\pm1})$ and $p_2(u_{i\pm1}, v_{i\pm1})$ in terms of $p_1(u_i, v_i)$ and $p_2(u_i, v_i)$ and their derivatives with respect to u and v. For example,

$$\begin{aligned} p_1(u_{i\pm1}, v_{i\pm1}) =& p_1(u_i, v_i) + (u_{i\pm1} - u_i) \frac{\partial p_1(u_i, v_i)}{\partial u_i} + (v_{i\pm1} - v_i) \frac{\partial p_1(u_i, v_i)}{\partial v_i} \\ &+ \frac{1}{2} \left[(u_{i\pm1} - u_i)^2 \frac{\partial^2 p_1(u_i, v_i)}{\partial u_i^2} + (v_{i\pm1} - v_i)^2 \frac{\partial^2 p_1(u_i, v_i)}{\partial v_i^2} \right. \\ &\left. + 2(u_{i\pm1} - u_i)(v_{i\pm1} - v_i) \frac{\partial^2 p_1(u_i, v_i)}{\partial u_i \partial v_i} \right] + \text{H.O.T.} \end{aligned} \tag{3.8}$$

Substituting and combining these Taylor expansions into equation (3.5), and taking the limits as $\Delta t \to 0$ and $\Delta x \to 0$, such that $\Delta x^2/\Delta t \to$ constant, a continuous equation describing the rate of change of u can be found. Disregarding H.O.T., this equation is given by

$$\begin{aligned} \frac{\partial u}{\partial t} = & \left[p_1 p_2 + u \left(p_2 \frac{\partial p_1}{\partial u} - p_1 \frac{\partial p_2}{\partial u} \right) \right] \frac{\partial^2 u}{\partial x^2} + \left[u \left(p_2 \frac{\partial p_1}{\partial v} - p_1 \frac{\partial p_2}{\partial v} \right) \right] \frac{\partial^2 v}{\partial x^2} \\ & + \left[2 \frac{\partial p_1}{\partial u} p_2 + u \left(p_2 \frac{\partial^2 p_1}{\partial u^2} - p_1 \frac{\partial^2 p_2}{\partial u^2} \right) \right] \left(\frac{\partial u}{\partial x} \right)^2 \\ & + \left[u p_2 \frac{\partial^2 p_1}{\partial v^2} - u p_1 \frac{\partial^2 p_2}{\partial v^2} \right] \left(\frac{\partial v}{\partial x} \right)^2 \\ & + \left[2 \frac{\partial p_1}{\partial v} p_2 + 2u \left(p_2 \frac{\partial^2 p_1}{\partial u \partial v} - p_1 \frac{\partial^2 p_2}{\partial u \partial v} \right) \right] \frac{\partial u}{\partial x} \frac{\partial v}{\partial x}, \end{aligned} \tag{3.9}$$

where the simplified notation p and q represents $p(u,v)$ and $q(u,v)$ respectively. Equation (3.9) can be simplified to the form

$$\frac{\partial u}{\partial t} = \frac{\partial}{\partial x}\left[p_1 p_2 \frac{\partial u}{\partial x} + u\left(p_2\frac{\partial p_1}{\partial u} - p_1\frac{\partial p_2}{\partial u}\right)\frac{\partial u}{\partial x} + u\left(p_2\frac{\partial p_1}{\partial v} - p_1\frac{\partial p_2}{\partial v}\right)\frac{\partial v}{\partial x}\right], \quad (3.10)$$

which is now recognisable as a cross-diffusion equation and is comparable to equation (3.1) in 1-D, where

$$D_{11} = p_1 p_2 + u\left(p_2\frac{\partial p_1}{\partial u} - p_1\frac{\partial p_2}{\partial u}\right), \qquad D_{12} = u\left(p_2\frac{\partial p_1}{\partial v} - p_1\frac{\partial p_2}{\partial v}\right). \quad (3.11)$$

The same method as applied above can also be used to find $\partial v/\partial t$. If the probabilities with which v moves within the lattice is denoted by Q rather than P and the ansatz describing the density dependent diffusion is given by

$$\begin{aligned} Q_i^{\pm} &= q_1(u_i,v_i)q_2(u_{i\pm1},v_{i\pm1}), \\ Q_{i\pm1}^{\mp} &= q_1(u_{i\pm1},v_{i\pm1})q_2(u_i,v_i), \end{aligned} \quad (3.12)$$

then

$$\frac{\partial v}{\partial t} = \frac{\partial}{\partial x}\left[v\left(q_2\frac{\partial q_1}{\partial u} - q_1\frac{\partial q_2}{\partial u}\right)\frac{\partial u}{\partial x} + q_1 q_2\frac{\partial v}{\partial x} + v\left(q_2\frac{\partial q_1}{\partial v} - q_1\frac{\partial q_2}{\partial v}\right)\frac{\partial v}{\partial x}\right], \quad (3.13)$$

where

$$D_{21} = v\left(q_2\frac{\partial q_1}{\partial u} - q_1\frac{\partial q_2}{\partial u}\right), \qquad D_{22} = q_1 q_2 + v\left(q_2\frac{\partial q_1}{\partial v} - q_1\frac{\partial q_2}{\partial v}\right). \quad (3.14)$$

It can be seen that the choice of p_1, p_2, q_1 and q_2 as constants in equations (3.11) and (3.14) results in the recovery of the Fickian diffusion terms as given in matrix (3.2), where D_{11} and D_{22} are constant diffusion terms and no cross-diffusion terms are present. This represents random movement of both species u and v within the lattice.

3.2 Investigation of Cross-Diffusion Induced Instabilities in a Two-Species Biofilm Model

The classic Turing instability, that was investigated in Chapter 2, arises when a stable steady state in the absence of diffusion can be made unstable in the presence of self-diffusion. This classic Turing instability can result in pattern formation [107, 150]. It is also known that the stability of a steady state of a reaction-diffusion system with self-diffusion terms can be reversed if cross-diffusion terms are added into the system. That is, a steady state that is stable in either the absence of any diffusion terms or in the presence of self-diffusion alone can be destabilised when cross-diffusion terms are added into the system. This is called a ‘cross-diffusion induced instability’ [136], and may also induce pattern formation [16, 163]. On the other hand, it is possible for a stable steady state in the absence of any diffusion that becomes unstable in the presence of self-diffusion (via traditional Turing instabilities) to once again become stable in the presence of cross-diffusion. This is called ‘cross-diffusion induced stability’ [136], and prevents pattern formation.

3.2.1 Formulation of Model

We investigate if patterns with wavelengths determined by the mathematical description of biological factors can emerge in a simple biofilm model. To do this we set up a general two-species reaction-diffusion model to represent the two key components of the biofilm (cell density and extracellular matrix) and carry out stability analysis. The general non-dimensional form of the reaction-diffusion model that we consider is

$$\begin{aligned}\frac{\partial u}{\partial t} &= F(u,v) + \nabla \cdot \left[D_{11}(u,v)\nabla u + D_{12}(u,v)\nabla v\right],\\ \frac{\partial v}{\partial t} &= G(u,v) + \nabla \cdot \left[D_{21}(u,v)\nabla u + D_{22}(u,v)\nabla v\right],\end{aligned} \tag{3.15}$$

where u represents bacterial cell density, v represents extracellular matrix and $F(u,v)$ and $G(u,v)$ are general reaction terms. In this general model formulation, all diffusion terms D_{ij}, where $D_{12}(u,v)$ and $D_{21}(u,v)$ are cross-diffusion terms and $D_{11}(u,v)$ and $D_{22}(u,v)$ are self-diffusion terms, are included.

3.2.2 Model Assumptions on Reaction Terms

Before carrying out stability analysis on system (3.15), we first specify some assumptions regarding the form of reaction terms F and G. The production of bacterial cells occurs through cell proliferation so the reaction rate F must be dependent on u. It is also clear from the literature that at least one sub-population of bacterial cells produce extracellular matrix in *B. subtilis* biofilms [22, 109, 157], and so G must also be dependent on u. Matrix also plays a role in the production of both cells and matrix (we do not specify the particular role at this stage) and consequently we assume that F and G are also both dependent on v. We therefore consider the most general reaction terms $F(u,v)$ and $G(u,v)$, as specified in (3.15), in stability calculations. Further assumptions are based on what we believe to be reasonable or observable behaviour with regard to the production and decay of bacterial cells and extracellular matrix in biofilms and are as follows:

1. At least one non-trivial positive steady state, $(u,v) = (u^*,v^*)$, exists.
2. Production or degradation of bacterial cells cannot occur in the absence of cells i.e. $F(0,v) = 0$.
3. Cell proliferation is more dominant than cell death for small u while cell death dominates for $u > u^*$ i.e. $F_u^0 > 0$ and $F_u^* < 0$, where F_u^0 and F_u^* denote the derivative of F with respect to u, evaluated at the trivial steady state and positive steady state (u^*,v^*) respectively (see Figure 3.1(a)).

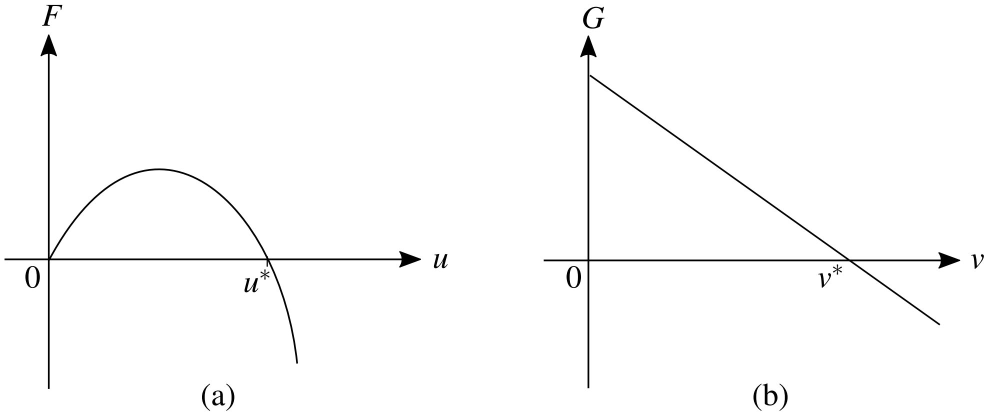

(a) (b)

Figure 3.1: Assumed possible forms of reaction terms, F (Figure (a)) and G (Figure (b)), in system (3.15) under the assumptions as listed in section 3.2.2.

4. In the absence of cells, matrix cannot be produced. The possibility of matrix degradation does however exist when no cells are present i.e. $G(0,v) \leq 0$. Matrix degradation also occurs when cells are present. As v approaches v^*, matrix degradation dominates matrix production i.e. $G_v^* < 0$, where G_v^* is the derivative of G with respect to v evaluated at the steady state (u^*, v^*) (see Figure 3.1(b)).

No assumptions about the form of the diffusion terms are made at this stage. We do however specify the combinations of diffusion terms that we will investigate. A list of these different combinations is shown in Table 3.1, with an explanation for the choice of these combinations following later. Note that an additional eight cases to those listed in Table 3.1 are also considered. These combinations, Cases A_2^0-A_9^0, correlate to equivalent Cases A_2-A_9, where $D_{11}^* = 0$.

Case	Combinations of diffusion terms
A$_1$	$D^*_{11} > 0, \quad D^*_{12} = 0, \quad D^*_{21} = 0, \quad D^*_{22} = 0$
A$_2$	$D^*_{11} > 0, \quad D^*_{12} = 0, \quad D^*_{21} > 0, \quad D^*_{22} = 0$
A$_3$	$D^*_{11} > 0, \quad D^*_{12} = 0, \quad D^*_{21} < 0, \quad D^*_{22} = 0$
A$_4$	$D^*_{11} > 0, \quad D^*_{12} > 0, \quad D^*_{21} = 0, \quad D^*_{22} = 0$
A$_5$	$D^*_{11} > 0, \quad D^*_{12} > 0, \quad D^*_{21} > 0, \quad D^*_{22} = 0$
A$_6$	$D^*_{11} > 0, \quad D^*_{12} > 0, \quad D^*_{21} < 0, \quad D^*_{22} = 0$
A$_7$	$D^*_{11} > 0, \quad D^*_{12} < 0, \quad D^*_{21} = 0, \quad D^*_{22} = 0$
A$_8$	$D^*_{11} > 0, \quad D^*_{12} < 0, \quad D^*_{21} > 0, \quad D^*_{22} = 0$
A$_9$	$D^*_{11} > 0, \quad D^*_{12} < 0, \quad D^*_{21} < 0, \quad D^*_{22} = 0$
B$_1$	$D^*_{11} = 0, \quad D^*_{12} = 0, \quad D^*_{21} = 0, \quad D^*_{22} < 0$
B$_2$	$D^*_{11} > 0, \quad D^*_{12} = 0, \quad D^*_{21} = 0, \quad D^*_{22} < 0$
B$_3$	$D^*_{11} < 0, \quad D^*_{12} = 0, \quad D^*_{21} = 0, \quad D^*_{22} < 0$

Table 3.1: Table showing the different combinations of diffusion terms that are investigated in the stability analysis of system (3.15). An additional set of cases $\mathrm{A}_2^0 - \mathrm{A}_9^0$ are also investigated and correspond to the equivalent cases $\mathrm{A}_2 - \mathrm{A}_9$, where $D^*_{11} = 0$.

3.2.3 Stability Analysis

Linear stability analysis for $\mathbf{x} \in \mathbb{R}^n$ is carried out on system (3.15) with the aim of determining if, and under what conditions, diffusion-driven instabilities and subsequent diffusion-driven pattern formation can arise for the different combinations of diffusion terms as described in Table 3.1. The method used is the same as described in Chapter 2. It is assumed that u and v take the form of $u(\mathbf{x},t) = u^* + \hat{u}(\mathbf{x},t)$ and $v(\mathbf{x},t) = v^* + \hat{v}(\mathbf{x},t)$, where $\hat{u}(\mathbf{x},t)$ and $\hat{v}(\mathbf{x},t)$ are small perturbations to the fixed point (u^*, v^*), which satisfy equation (2.6) and the eigenvalue problem described by equation (2.7) in Section 2.4.2. As in Section 2.4.2, we consider solutions with wave number k on a bounded domain with no-flux boundary conditions (which could be considered to be periodically extended in order to model the interior of the coffee-ring region).

System (3.15) is linearised around the steady state (u^*, v^*) using the above substitutions to give

$$\begin{aligned} \hat{u}_t &= \left(F_u^* - k^2 D_{11}^*\right)\hat{u} + \left(F_v^* - k^2 D_{12}^*\right)\hat{v}, \\ \hat{v}_t &= \left(G_u^* - k^2 D_{21}^*\right)\hat{u} + \left(G_v^* - k^2 D_{22}^*\right)\hat{v}, \end{aligned} \tag{3.16}$$

where * indicates evaluation at the equilibrium (u^*, v^*) and subscripts $_u$ and $_v$ denote differentiation with respect to u and v respectively. System (3.16) can be written in the form

$$\hat{\mathbf{W}}_t = J_k \hat{\mathbf{W}} \tag{3.17}$$

where $\hat{\mathbf{W}} = \begin{bmatrix} \hat{u}(\mathbf{x},t) & \hat{v}(\mathbf{x},t) \end{bmatrix}^T$ and J_k is the associated Jacobian matrix

$$J_k = \begin{pmatrix} F_u^* - k^2 D_{11}^* & F_v^* - k^2 D_{12}^* \\ G_u^* - k^2 D_{21}^* & G_v^* - k^2 D_{22}^* \end{pmatrix}. \tag{3.18}$$

In general, the characteristic polynomial in terms of the trace and determinant, and corresponding eigenvalues λ_k, are given by:

$$\begin{aligned} &\text{Characteristic polynomial:} \quad \lambda_k^2 - \mathrm{tr}(J_k)\lambda_k + \det(J_k) = 0, \\ &\text{Corresponding eigenvalue:} \quad \lambda_k^{\pm} = \frac{1}{2}\left((\mathrm{tr}(J_k))^2 \pm \sqrt{(\mathrm{tr}(J_k))^2 - 4\det(J_k)}\right). \end{aligned} \tag{3.19}$$

The notation of J_k and λ_k is used to represent the Jacobian matrix and corresponding eigenvalues in the presence of diffusion (see equations (3.18) and (3.19) respectively). In the absence of diffusion, the notation $J_k(k=0) = J_0$ will be used.

The spatially uniform non-trivial steady state (u^*, v^*) can be either stable or unstable in the absence of diffusion and therefore instabilities may arise via different mechanisms. Taking into account the assumptions for our model (3.15), we consider the classic diffusion-driven instability where (u^*, v^*) is stable in the absence of diffusion.

We determine if it is possible for (u^*, v^*) to be driven unstable in the presence of diffusion by establishing if it is possible for $\mathrm{Re}(\lambda_k^+) > 0$ for some range of wave numbers k^2 (we only consider $\mathrm{Re}(\lambda_k^+) > 0$ as $\mathrm{Re}(\lambda_k^+) > \mathrm{Re}(\lambda_k^-)$ always). First we apply stability analysis to Cases A_1-A_9 (and A_2^0-A_9^0) in Table 3.1 for the general reaction terms $F = F(u, v)$ and $G = G(u, v)$. We then move on to analyse stability in Cases B_1-B_3.

3.2.4 Cross-Diffusion Induced Instabilities (Cases A_1-A_9)

In Chapter 2 it was shown that in Case A_1, where only $D_{11}^* > 0$ was non-zero, no Turing instabilities could arise for any two-species model under our assumptions as described in section 3.2.2. We investigate the effect of the presence of cross-diffusion terms in system (3.15), by considering the cases where $D_{11} \geq 0$, $D_{12} \neq 0$, $D_{21} \neq 0$ and $D_{22} = 0$ (Cases A_2-A_9 and A_2^0-A_9^0). By ensuring $D_{11} \geq 0$ we can compare the results with those found in Chapter 2. Any bifurcation that occurs in system (3.15) for Cases A_2-A_9 and A_2^0-A_9^0 must therefore come about as a result of the presence of cross-diffusion terms, and any patterns that emerge must do so via a cross-diffusion induced instability. In all Cases A_2-A_9 and A_2^0-A_9^0, it is found that cross-diffusion induced instabilities can occur under certain conditions. An outline of the calculations for the most general cases A_5, A_6, A_8 and A_9, where $D_{11} \neq 0$, $D_{12} \neq 0$ and $D_{21} \neq 0$, are detailed here.

For $\mathrm{Re}(\lambda_0^+) > 0$ the condition $\det(J_0) = F_u^* G_v^* - F_v^* G_u^* > 0$ must hold and is therefore assumed. The determinant of J_k as given in (3.18) can be rewritten as a quadratic in k^2:

$$\det(J_k) = -k^4 D_{12}^* D_{21}^* + k^2 \left(-D_{11}^* G_v^* + D_{12}^* G_u^* + D_{21}^* F_v^*\right) + \left(F_u^* G_v^* - F_v^* G_u^*\right). \quad (3.20)$$

By solving $\det(J_k)$=0 for k^2 we can determine the values of k^2 (if any) for which the

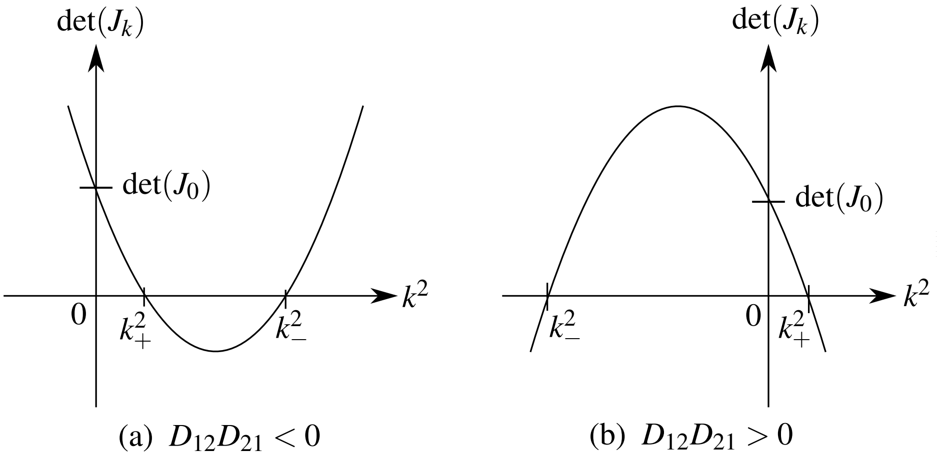

(a) $D_{12}D_{21} < 0$ (b) $D_{12}D_{21} > 0$

Figure 3.2: Possibilities for the shape of det(J_k) as k^2 varies in the cases where $D_{12}^*D_{21}^* \neq 0$ in Table 3.1 for (a) $D_{12}^*D_{21}^* < 0$ and (b) $D_{12}^*D_{21}^* > 0$. In Figure (a), det(J_k) is seen to have two real positive roots and so Turing instabilities can occur for $k^2 \in (k_+^2, k_-^2)$. In Figure (b), det(J_k) has only one real positive root and Turing instabilities can occur for $k^2 > k_+^2$.

inequality $\det(J_k) < 0$ holds. These solutions are

$$\begin{aligned} k_\pm^2 = &\frac{1}{2D_{12}^*D_{21}^*}\Big[\left(-D_{11}^*G_v^* + D_{12}^*G_u^* + D_{21}^*F_v^*\right) \\ &\pm\sqrt{\left(-D_{11}^*G_v^* + D_{12}^*G_u^* + D_{21}^*F_v^*\right)^2 + 4D_{12}^*D_{21}^*\left(F_u^*G_v^* - F_v^*G_u^*\right)}\Big], \end{aligned} \tag{3.21}$$

where k_+^2 and k_-^2 represent the solution given by the $+$ and $-$ of $\pm$ respectively. Our assumption $\det(J_0) = F_u^*G_v^* - F_v^*G_u^* > 0$ ensures that a plot of $\det(J_k)$ against k^2 crosses the positive $\det(J_k)$-axis at $k^2 = 0$. As $k \in \mathbb{R}$, only positive solutions of k^2 for which $\det(J_k) < 0$ are of interest; the possibilities for these solutions are shown in Figure 3.2.

As $k^2 \in \mathbb{R}$, equation (3.21) must have two real solutions and so the only case of interest is

$$\left(-D_{11}^*G_v^* + D_{12}^*G_u^* + D_{21}^*F_v^*\right)^2 + 4D_{12}^*D_{21}^*\left(F_u^*G_v^* - F_v^*G_u^*\right) > 0, \tag{3.22}$$

where $F_u^*G_v^* - F_v^*G_u^* > 0$.

If $D_{12}^*D_{21}^* > 0$, then condition (3.22) is always satisfied and $\det(J_k) < 0$ for all $k^2 > k_+^2$, and subsequently $\mathrm{Re}(\lambda_k^+) > 0$ for all $k^2 > k_+^2$ (see Figure 3.2(b)). Thus instabilities can occur in this case when k^2 is sufficiently large. If $D_{12}^* D_{21}^* < 0$, then $\det(J)$ has two positive real roots if $-D_{11}^* G_v^* + D_{12}^* G_u^* + D_{21}^* F_v^* < 0$ and condition (3.22) holds (see equation (3.21)). Turing instabilities can only occur for a finite range of $k^2 \in (k_+^2, k_-^2)$ in this case (see Figure 3.2(a)).

Similar calculations were carried out for the remaining cases $\mathrm{A_i}$ in Table 3.1 to determine if and when cross-diffusion instabilities could arise in equation (3.15) for $F = F(u,v)$ and $G = G(u,v)$. A summary of the results is presented here, where cases have been grouped according to the results:

$$
\begin{array}{ll}
\text{Case A}_2: & F_v^* < 0 \quad \text{and} \quad D_{21}^* F_v^* < D_{11}^* G_v^* < 0 \quad \text{and} \quad k^2 \text{ sufficiently large}\\
\text{Case A}_3: & F_v^* > 0 \quad \text{and} \quad D_{21}^* F_v^* < D_{11}^* G_v^* < 0 \quad \text{and} \quad k^2 \text{ sufficiently large}\\
\text{Case A}_4: & G_u^* < 0 \quad \text{and} \quad D_{12}^* G_u^* < D_{11}^* G_v^* < 0 \quad \text{and} \quad k^2 \text{ sufficiently large}\\
\text{Case A}_7: & G_u^* > 0 \quad \text{and} \quad D_{12}^* G_u^* < D_{11}^* G_v^* < 0 \quad \text{and} \quad k^2 \text{ sufficiently large}
\end{array}
$$

$$
\left.\begin{array}{l}
\text{Case A}_5:\\[1em]
\text{Case A}_9:
\end{array}\right\} \; k^2 \text{ sufficiently large} \tag{3.23}
$$

$$
\left.\begin{array}{l}
\text{Case A}_6:\\[1em]
\text{Case A}_8:
\end{array}\right\} \;
\begin{array}{l}
(D_{12}^* G_u^* + D_{21}^* F_v^* - D_{11}^* G_v^*)^2 > -4 D_{12}^* D_{21}^* (F_u^* G_v^* - F_v^* G_u^*)\\
\text{and} \quad D_{12}^* G_u^* + D_{21}^* F_v^* - D_{11}^* G_v^* < 0\\
\text{and} \quad k^2 \in (k_+^2, k_-^2)
\end{array}
$$

An additional requirement for instability to occur in each of the above cases is $F_u^* G_v^* - F_v^* G_u^* > 0$. It is noted that bifurcations can also arise in all Cases A_2^0-A_9^0. The conditions required for these instabilities are not explicitly stated here, but can be found by substituting $D_{11}^* = 0$ into conditions (3.23).

Despite instabilities arising in all of the above cases, only in Cases A_6 and A_8 (and the similar Cases A_6^0 and A_8^0), where $D_{12}^* D_{21}^* < 0$, can a specific wave number, $k = k_g$, be

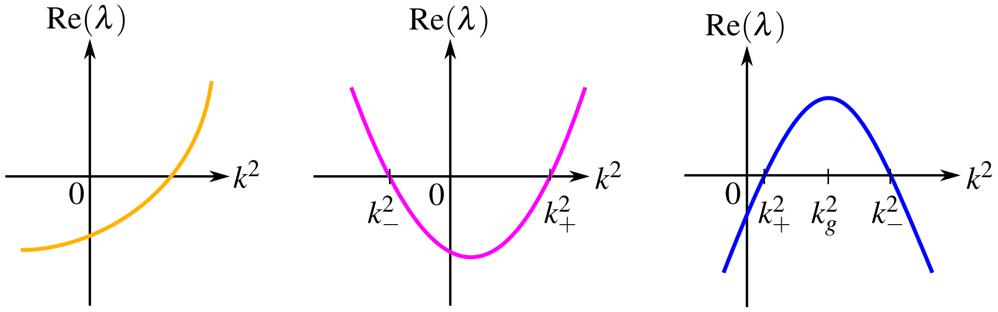

(a) Cases A_2, A_3, A_4, A_7

(b) Cases A_5 and A_9 ($D^*_{12}D^*_{21} > 0$)

(c) Cases A_6 and A_8 ($D^*_{12}D^*_{21} < 0$)

Figure 3.3: Forms of eigenvalue Re(λ^+) against k^2 where cross-diffusion induced instabilities can occur in Cases A_2-A_9 of Table 3.1 (see conditions (3.23)). Figure (a) shows the form for cases A_2, A_3, A_4 and A_7. Figure (b) shows the eigenvalue shape in Cases A_5 and A_9 where $D^*_{12}D^*_{21} > 0$. Figure (c) shows the shape for Cases A_6 and A_8 under the assumption $D^*_{12}D^*_{21} < 0$, with the fastest growing wave number, k_g^2, indicated.

preferentially chosen as the fastest growing wave number of Re(λ) > 0. In these cases, plots of Re(λ) against k^2 are positive between $k^2 \in (k_+^2, k_-^2)$ and reach a maximum at $k^2 = k_g^2$. This is illustrated in Figure 3.3(c). In the remaining cases where $D^*_{12}D^*_{21} \geq 0$, plots of Re(λ) against k^2 are positive for all k^2 sufficiently large with $\lim_{k^2 \to \infty} = \infty$ (see Figure 3.3(a) showing the cases where $D^*_{12}D^*_{21} = 0$ and Figure 3.3(b) showing the cases where $D^*_{12}D^*_{21} > 0$). In these cases diffusion can drive the system to become unstable, however all wavelengths where k^2 is sufficiently large are excitable. Thus, a specific wavelength of pattern cannot be chosen and we surmise that any patterns that do arise will not be a result of the biological features of the model.

3.2.5 Effect of a Matrix Aggregation Term (Cases B_1-B_3)

The effect of adding a negative matrix self-diffusion term, $D_{22} < 0$ (Cases B_1-B_3 in Table 3.1), into system (3.15) is now investigated. We aim to determine if the presence of the $D_{22} < 0$ term, which represents matrix aggregation, can induce pattern formation in our system (3.15). We concentrate on the case $D_{22} < 0$ rather than $D_{22} > 0$ as we hypothesise that the stickiness attributed to the matrix component makes matrix aggregation a more biologically plausible scenario than matrix diffusion. We focus only on the effect of term $D_{22} < 0$, and therefore cross-diffusion terms are neglected i.e. $D_{12} = D_{21} = 0$. As a result, any instabilities that are induced in this case must come about as a result of self-diffusion rather than cross-diffusion. We consider again a stable steady state (u^*, v^*) and the reaction terms $F(u,v)$ and $G(u,v)$ satisfying the assumptions as listed in section 3.2.2.

The steady state (u^*, v^*) is stable in the case where $\operatorname{tr}(J_0) = F_u^* + G_v < 0$ (always satisfied under our assumptions) and $\det(J_0) = F_u^* G_v^* - F_v^* G_u^* > 0$. Inspecting the trace of matrices J_k

$$\operatorname{tr}(J_k) = F_u^* + G_v^* - k^2(D_{11}^* + D_{22}^*), \tag{3.24}$$

it is clear that under the condition $D_{22}^* < 0$, $\operatorname{tr}(J_k)$ is no longer restricted to be negative and thus $\operatorname{tr}(J_k) > 0$ is a possibility in Cases B$_1$-B$_3$. In calculations similar to those as given in section 3.2.4, we find the conditions under which instabilities can occur. They are:

$$\begin{aligned} \text{Case B}_1: &\quad k^2 > \frac{F_u^* G_v^* - F_v^* G_u^*}{D_{22}^* F_u^*} \\ \text{Case B}_2: &\quad k^2 > k_{b-}^2 \\ \text{Case B}_3: &\quad k^2 > k_{b+}^2 \end{aligned} \tag{3.25}$$

where

$$k_{b\pm}^2 = \frac{(D_{11}^* G_v^* + D_{22}^* F_u^*) \pm \sqrt{(D_{11}^* G_v^* + D_{22}^* F_u^*)^2 - 4D_{11}^* D_{22}^* (F_u^* G_v^* - F_v^* G_u^*)}}{2D_{11}^* D_{22}^*}, \tag{3.26}$$

is the (positive) solution of $\det(J_k) = 0$. Once again, the additional condition $F_u^* G_v^* - F_v^* G_u^* > 0$ must also hold.

It is clear that if k^2 is sufficiently large, a bifurcation can arise for all cases B$_1$-B$_3$.

However, as before, the range of unstable wave numbers has no upper bound so the fastest growing wave number cannot be specifically chosen and patterns with wavelengths determined by the biology will not arise.

In summary, diffusion driven instabilities can occur in all cases listed in Table 3.1 under certain conditions. However, it is only when $D_{12}^{*}D_{21}^{*} < 0$ that the fastest growing wave number can be preferentially selected to determine the wavelength of any emerging patterns. In all the other cases the fastest growing wave number has no upper bound. It can be deduced that patterns with a biologically determined wavelength may therefore only form in Cases A_6, A_8, A_6^0 and A_8^0, under the corresponding conditions given by (3.23), as a result of cross-diffusion induced instabilities.

3.3 Numerical Simulation of a Simple Specific Model

The possibility for cross-diffusion induced instabilities and subsequent patterns exists for Cases A_6, A_8, A_6^0 and A_8^0 (in Table 3.1) where $D_{12}^{*}D_{21}^{*} < 0$. We consider a simple biofilm model of the form given in system (3.15). Ensuring our model assumptions are satisfied, and choosing appropriate parameters satisfying the aforementioned conditions for instabilities to arise (conditions (3.23)), numerical simulations are performed to determine if in fact spatial patterns do occur.

Logistic growth is widely used to describe the growth of bacterial cells [102, 138]. It is known that cells produce matrix but also that matrix degrading enzymes can break down polymers within the matrix [2, 33], and that some of the resulting components may be used as a nutrient source for cells throughout the biofilm [103, 114, 154]. We therefore assume that a proportion of matrix is ‘eaten’ by cells and used for their production. The reaction terms we choose for system (3.15) are

$$F = \gamma u(\mu - u) + \beta uv, \quad G = \alpha u^2 - \beta uv, \tag{3.27}$$

where γ, μ, β and α are positive constants. The trivial and semi-trivial steady states $(u^*, v^*) = (0, v)$ exist, as well as one non trivial steady state

$$(u^*, v^*) = \left(\frac{\gamma\mu}{\gamma - \alpha}, \frac{\alpha\gamma\mu}{\beta\,(\gamma - \alpha)} \right), \tag{3.28}$$

which is positive provided that $\gamma > \alpha$. For this positive steady state it can be shown that $F_u^* < 0$ and $G_v^* < 0$ as per our assumptions. We choose the default parameter values

$$\gamma = 0.1, \quad \mu = 3, \quad \beta = 0.1, \quad \alpha = 0.05, \tag{3.29}$$

for reaction terms (3.27) in system (3.15). Whilst these values have no biological significance, they result in a stable spatially homogeneous positive steady state, $(u^*, v^*) = (6, 3)$, as is required.

Cross-diffusion driven instabilities can arise in system (3.15) for a bounded range of wave numbers provided that $D_{12}^* D_{21}^* < 0$ and the corresponding conditions in (3.23) are satisfied. We focus on Case A_8 in Table 3.1 which falls into this category. Using reaction terms defined in equation (3.27), we carry out 1-D numerical simulations of system (3.15) where the diffusion terms are

$$D_{11} = D_{11c}, \quad D_{12} = -D_{12c}u, \quad D_{21c} = D_{21c}v, \quad D_{22} = D_{22c}, \tag{3.30}$$

and D_{11c}, D_{12c} and D_{21c} are positive constants and $D_{22c} = 0$. We use a small random initial condition for cell density, $u(x, 0) \in [0.1, 0.2]$, and zero initial condition for matrix, $v(x, 0) = 0$. Periodic boundary conditions are also used. Simulation results

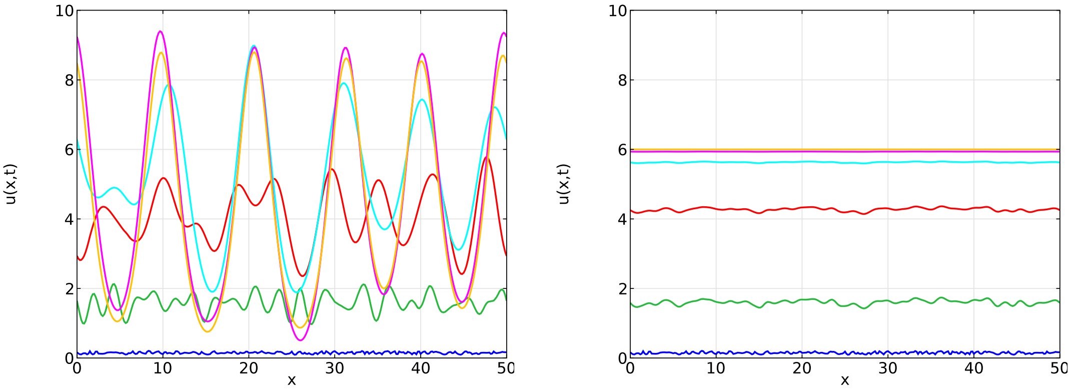

(a) Case A_8;
$D_{11} > 0, D_{12} < 0, D_{21} > 0, D_{22} = 0$

(b) Case B_2;
$D_{11} > 0, D_{12} = 0, D_{21} = 0, D_{22} < 0$

Figure 3.4: Numerical simulations of cell density $u(x,t)$ in system (3.15) with reaction terms as given in (3.27). Two different combinations of diffusion terms from Table 3.1 are shown. Figure (a) shows Case A_8 where $D_{11} = 0.01$, $D_{12} = -u$, $D_{21} = 0.1v$ and $D_{22} = 0$. Pattern formation does occur in this case. Figure (b) shows Case B_2 where $D_{11} = 0.01$, $D_{12} = 0$, $D_{21} = 0$ and $D_{22} = -0.001$. Pattern formation does not occur in this case. Times shown are $t = 0$ (blue), $t = 10$ (green), $t = 20$ (red), $t = 30$ (cyan), $t = 40$ (magenta), $t = 100$ (yellow). Parameter values are $\gamma = 0.1$, $\mu = 3$, $\beta = 0.1$ and $\alpha = 0.05$. Simulations are carried out in COMSOL with a small random initial condition $u(x,0) \in [0.1, 0.2]$, and $v(x,0) = 0$. Boundary conditions are periodic.

showing cell density in the above model can be seen in Figure 3.4(a), where the diffusion constants D_{ijc} have been chosen such that the conditions in (3.23) have been satisfied. As expected, spatial patterns with a specific wavelength corresponding to the fastest growing wave number do emerge. Figure 3.4(b) shows simulation results for $D_{11c} > 0$, $D_{12c} = D_{21c} = 0$ and $D_{22c} < 0$, which falls into the category of Case B_2, for comparison. As expected spatial patterns do not form in this case, despite the fact that instabilities arise for sufficiently large wave numbers (see conditions (3.25)).

3.4 Cross-Diffusion as a Biologically Relevant Pattern Formation Mechanism in a Biofilm Model

We have shown that cross-diffusion in a two-species model is a possible mechanism for pattern formation in a biofilm, providing that the product of cross-diffusion terms evaluated at the steady state, $D_{12}^{*}D_{21}^{*}$, is negative. We consider the biological meaning of $D_{12}^{*}D_{21}^{*} < 0$, and proceed to determine if it may apply to our biofilm model (3.15).

In Cases A_8 and A_8^0 we have $D_{12} < 0$ and $D_{21} > 0$, suggesting that cells move up concentration gradients of matrix and that matrix moves down concentration gradients of cell density. Despite there being no evidence to suggest that matrix movement is actively influenced by the presence of cells, we suggest that it is plausible that, as cells diffuse, matrix may be driven down concentration gradients as an indirect result of the movement of bacterial cells pushing on the matrix. As a result, the $D_{21} > 0$ term may have some biological significance. On the other hand, the assumption that cells move up concentration gradients suggests that either the ’stickiness’ of the matrix component traps cells at high matrix concentration, or that cells are preferentially drawn to matrix. Although the matrix is a sticky material and acts like a glue, as far as we are aware there is no evidence to suggest that cells respond haptotactically to matrix in a biofilm setting (we note, however, that in some situations, haptotaxis modelling has been implemented, for example, in modelling the migration of cancer cells [23, 24]). Similarly, evidence suggests that matrix protects cells [51, 158] and thus it may be beneficial for cells to be near matrix. However, the evidence does not extend to suggest that cells respond to matrix in a chemotactic manner. The assumption that $D_{12} < 0$ is therefore unlikely to be biologically relevant.

In Cases A_6 and A_6^0, $D_{12} > 0$ and $D_{21} < 0$, which suggests that cells move down concentration gradients of matrix and that matrix moves up concentration gradients of cell density respectively. To the best of our knowledge, there is no biological reasoning to support either of these claims, and we surmise these cases are not biologically plausible.

We note that in Cases A_6 and A_8, the assumption $D_{11} > 0$ may have some biological significance. However, as these cases are also grouped with the condition $D_{12}D_{21} < 0$, their full set of diffusion terms are not biologically relevant. We conclude that any model of the form given in equation (3.15) where $D_{12}D_{21} < 0$ has limited biological relevance. As a result, the likelihood of cross-diffusion providing a viable means of pattern formation in any two-species biofilm cell and matrix model is also limited.

3.5 Conclusions

In this chapter it has been shown that a two-species reaction diffusion model of the form (3.15) can undergo cross-diffusion induced instabilities in the case where $D_{11} \geq 0$ and $D_{22} = 0$. In particular, it was found that both cross-diffusion terms D_{12} and D_{21} must be non-zero in order for this to occur, and that an additional condition is $D_{12}D_{21} < 0$. In this case, pattern formation is found to be possible supposing other conditions relating to the reaction terms of the model are satisfied. In scenarios where these restrictions are adhered to, the wavelength of the emergent patterns can be attributed to the underlying biology behind the model, rather than a predetermined input factor as is the case in the model of Asally et al [6]. However, a lack of biological evidence supports the claim that $D_{12}D_{21} < 0$ and therefore, although cross-diffusion instabilities and subsequent pattern formation are mathematically possible, the cross-diffusion model may not be a biologically feasible way to model biofilm growth.

It has also been shown in this chapter, that the presence of a second self-diffusion term D_{22} in system (3.15) to represent matrix aggregation could in theory drive the steady state (u^*, v^*) unstable. However, this can only occur for large wave numbers, $k > k_u$. As the unstable wave numbers $k > k_u$ have no upper bound, an infinite collection of wave numbers are excitable but none are preferentially selected as the favoured pattern wavelength. Numerical simulations of these cases either choose $k = 0$ as the preferred wavelength (so no patterns form) or run into numerical computation problems. Therefore even if the idea of matrix aggregation providing a possible mechanism for pattern formation is biologically sound, we suggest it is not best modelled in a reaction-diffusion fashion. Instead, we suggest that the reasoning behind matrix aggregation could be explained by contraction within the biofilm as it begins to dry out, causing it to clump together as a result of forces accumulating within the biofilm. We therefore propose that a mechanical model that can take into account the forces that build up in the biofilm may be better able to describe the processes that occur within the biofilm as it develops.

Chapter 4

The Effect of Cell Death on the Stability of a Growing Biofilm

4.1 Introduction

In the previous two chapters of this thesis, a reaction-diffusion and cross-diffusion approach to biofilm pattern formation was investigated. Another popular biofilm modelling method implements a fluid dynamics approach to describe the development of biofilms as a moving boundary problem [7, 32, 41, 61]. This is the focus of this chapter.

Free or moving boundary (or Stefan) problems, characterised by a space and time dependent moving boundary that must be tracked throughout development as part of the solution [30], present complex mathematical challenges. Nonlinearity arising through the coupling of material and interface dynamics, and the inclusion of multiple time and length scales, contribute to the difficulties associated with these problems [100]. As a result of these complications, numerical rather than analytical techniques are generally used to determine behaviour, except in some special simplified cases [50].

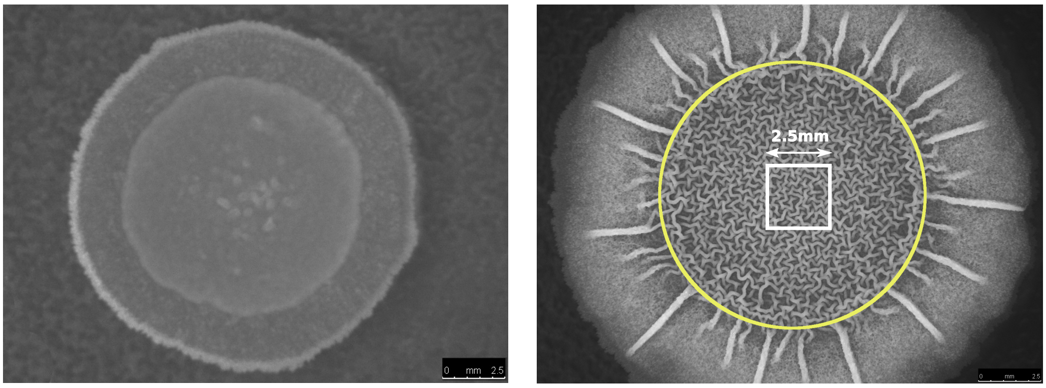

(a) wildtype *B. subtilis* biofilm at $t = 18\,\mathrm{h}$ after initial inoculation

(b) wildtype *B. subtilis* biofilm at $t = 48\,\mathrm{h}$ after initial inoculation

Figure 4.1: Morphology of wildtype *Bacillus subtilis* biofilm grown at 30°C on 1.5% agar substrate. Figure (a): Early biofilm (18 hours into growth) shows homogeneity. Figure (b): Mature biofilm (48 hours into growth) shows complex heterogeneous pattern within the coffee-ring region (yellow outline). A close-up of the intricate patterns highlighted in the white square can be seen in Figure 2.1(c). Photographs courtesy of L. Li.

Dockery and Klapper [41] presented a simple moving boundary model of a single substrate limited biofilm growing into a static aqueous environment. They deduced that the biofilm interface is linearly unstable to fingering instabilities under certain conditions. In this chapter we build on the model derived in [41] to consider the case of biofilm growth on a surface in which the growth limiting substrate is assumed to be oxygen in the air above. The growth surface represents agar in a typical laboratory experiment where penetration into the agar is minimal and nutrients within the medium are not limiting for growth (initially in any case). Under these conditions complex biofilm morphologies can be produced, particularly in mature biofilms which are often not of uniform depth and indeed can form elaborate, heterogeneous large-scale structures [6, 10, 18, 149] (see Figure 4.1). We extend the model formulated in [41] by introducing a new cell death term to represent the findings of Asally et al. [6] (the focus of Chapter 2), which stated that cell death at the base of biofilms acts as a precursor to wrinkling, specifically within the central region of the biofilm i.e. the ‘coffee-ring’ region, which can be seen in Figure 4.1(b). We examine the effect that the loss of

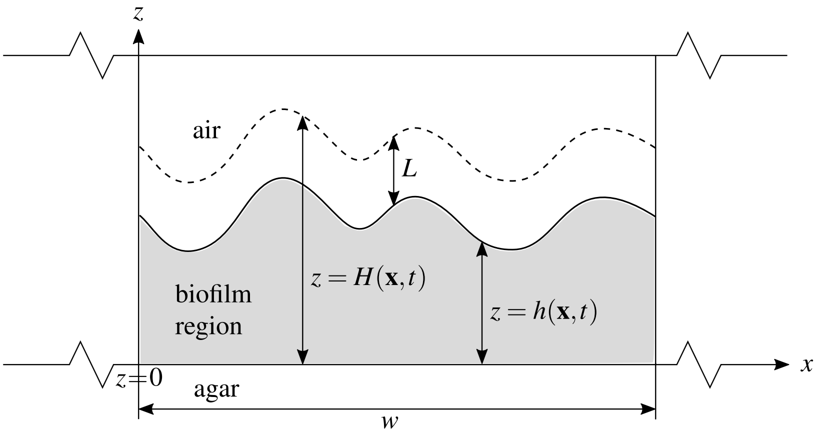

Figure 4.2: Schematic of model set-up. The biofilm grows on an agar substrate and expands vertically into the air above. The x and z-directions are labelled (y points into the page), as is the characteristic length scale w. The biofilm-agar interface is positioned at $z = 0$.

cells has on the growth of the biofilm and the heterogeneity and patterning displayed, particularly at steady state solutions.

4.2 Model Set-up

The model set-up used in this chapter follows much the same formulation as in [41]. However, rather than considering a biofilm growing into an aqueous environment, we investigate a non-submerged biofilm growing on an agar substrate into the air above. For convenience, an overview of the model set-up is described here (full details can be found in [41]), and a schematic of the set-up is shown in Figure 4.2.

The domain of interest $D \subset \mathbb{R}^3$ is an unbounded slab separated by a surface $z = h(\mathbf{x},t)$ (where $\mathbf{x} = (x,y)$), into two regions: (i) the biofilm in $0 < z < h(\mathbf{x},t)$, and (ii) the air above in $z > h(\mathbf{x},t)$. Oxygen is assumed here to be the growth limiting substrate and is denoted by $s = s(\mathbf{x},z,t)$.

In the lower region, the biofilm itself is modelled as a viscous, homogeneous, incompressible fluid with constant density, rescaled here to unity. The velocity, $\mathbf{u}$, of this fluid is related to the pressure, $p(\mathbf{x},z,t)$ (or more specifically the pressure gradient $\nabla p(\mathbf{x},z,t)$), within the biofilm via a standard relationship, namely,

$$\mathbf{u} = -\lambda \nabla p, \tag{4.1}$$

where λ is a positive constant (note that this relationship is often referred to as Darcy's Law in certain specific contexts). Cell growth and division generates a source of mass within the biofilm which is taken into account within the conservation of mass equation,

$$\nabla \cdot \mathbf{u} = g, \tag{4.2}$$

where $g = g(s)$ is some growth function that models the net production of bacteria per unit volume per unit time. Combining (4.2) with (4.1) yields a relationship between growth and resultant pressure such that

$$-\lambda \nabla^2 p = g(s). \tag{4.3}$$

Cell maintenance and growth require substrate (in this case oxygen). Substrate consumption is modelled by an expression of the form $f(s)$ and thus substrate concentration within the biofilm region is governed by the equation

$$s_t = D_2 \nabla^2 s - f(s), \tag{4.4}$$

where $D_2 > 0$ is a standard Fickian diffusion coefficient. Clearly, the growth function, g, and substrate utilisation, f, are related as will be discussed later.

Substrate concentration in the upper region, $h(\mathbf{x},t) < z < H(\mathbf{x},t)$, is again assumed to diffuse in a standard Fickian manner and is thus governed by the equation

$$s_t = D_1 \nabla^2 s, \tag{4.5}$$

where D_1 is a positive constant. It is reasonably assumed that substrate concentration far above the biofilm interface is unaffected by biofilm growth. Thus substrate is assumed to be a constant above a height denoted by $H(\mathbf{x},t)$=$h(\mathbf{x},t)+L$, where L is a constant. Finally, in the upper region, we set pressure $p \equiv 0$. In fact, we define the interface separating the upper and biofilm regions by $p = 0$.

To complete the model, boundary conditions are imposed as follows: The biofilm-agar interface ($z = 0$) is assumed impermeable to the biofilm, and therefore the z-component of velocity is zero here. Consistent with this condition, $p_z(\mathbf{x},0,t) = 0$. Similarly, the flux of substrate across the boundary is set to be zero at $z = 0$. At the biofilm surface $z = h(\mathbf{x},t)$, the pressure is assumed to be zero. Indeed this defines the location of the tracked interface via the interface equation given below. Moreover, the substrate concentration is assumed continuous at the interface $z = h(\mathbf{x},t)$, and a flux continuity condition is imposed as detailed below. Finally, the substrate concentration is set constant for $z > H(\mathbf{x},t)$. In summary, the applied boundary conditions are as follows:

$$p|_{z=h} = 0, \quad p_z|_{z=0} = 0; \tag{4.6a}$$

$$s|_{z=H} = s_\infty, \quad s_z|_{z=0} = 0; \tag{4.6b}$$

$$s|_{z=h^+} = s|_{z=h^-}; \tag{4.6c}$$

$$\mathbf{n} \cdot D_1 \nabla s|_{z=h^+} = \mathbf{n} \cdot D_2 \nabla s|_{z=h^-}, \tag{4.6d}$$

along with the interface equation

$$\frac{\partial h}{\partial t} = -\mathbf{n} \cdot \lambda \nabla p|_{z=h^-}, \tag{4.7}$$

where h^+ and h^- denote the biofilm interface approached from above and below respectively, **n** denotes the (upward pointing) normal to the interface $z = h$ and s_∞ is a positive constant representing the bulk substrate concentration.

4.3 Non-dimensionalisation

Some scaling factors are introduced to simplify the model. Wildtype biofilms of *B. subtilis* grown on agar, despite generally having much greater length than height, appear to develop spatial features with a characteristic length of pattern, denoted w, which are repeated throughout the domain. Experimental observations show that both the characteristic length of patterns and biofilm height are of the same order of approximately $10^2\mu$m (see for example [161, 173]). Hence, for computational purposes, a domain of fixed height, $\bar{H}$, and width, w, can be employed on which periodic boundary conditions in the x and y-directions can be imposed for the pressure and substrate variables. A time-scale, T, associated with biofilm growth can also be introduced. By setting

$$\bar{\mathbf{x}} = \frac{\mathbf{x}}{w}, \quad \bar{z} = \frac{z}{w}, \quad \bar{h} = \frac{h}{w}, \quad \bar{H} = \frac{H}{w}, \quad \bar{L} = \frac{L}{w}, \quad \bar{t} = \frac{t}{T}, \quad S = \frac{s}{s_\infty},$$

$$\bar{f}(s) = \frac{f(s)}{f(s_\infty)}, \quad \bar{g}(s) = g(s)T, \quad P = \frac{\lambda T}{w^2}p,$$

the non-dimensional system can be obtained after dropping bars for simplicity:

$$\varepsilon_1 S_t - \nabla^2 S = 0, \qquad h(\mathbf{x},t) < z < H(\mathbf{x},t) \tag{4.8}$$

$$\begin{cases} \varepsilon_2 S_t - \nabla^2 S = -Gf(S); \\ \nabla^2 P = -g(S); \end{cases} \qquad 0 < z < h(\mathbf{x},t) \tag{4.9}$$

with the evolution equation

$$h_t = -\mathbf{n}\cdot\nabla P|_{z=h^-}, \tag{4.10}$$

where $G = \frac{w^2}{s_\infty D_2} f(s_\infty)$, $\varepsilon_i = \frac{w^2}{D_i T}$ and a new non-dimensional variable $\hat{g}$ is defined such that $\bar{g}(Ss_\infty) = \hat{g}(S)$. Similarly the new non-dimensional variable $\hat{f}$ is defined such that $\bar{f}(Ss_\infty) = \hat{f}(S)$. The hat notation has also been dropped for simplicity. Note the (periodically repeating) domain is rescaled such that $(x,y) \in (0,1)\times(0,1)$.

Substituting the desired forms of non-dimensional variables into the boundary conditions (4.6) yields the corresponding dimensionless boundary conditions:

$$P|_{z=h} = 0, \quad P_z|_{z=0} = 0; \tag{4.11a}$$

$$S|_{z=H} = 1, \quad S_z|_{z=0} = 0; \tag{4.11b}$$

$$S|_{z=h^+} = S|_{z=h^-}; \tag{4.11c}$$

$$\mathbf{n}\cdot K\nabla S|_{z=h^+} = \mathbf{n}\cdot\nabla S|_{z=h^-}, \tag{4.11d}$$

where $K = D_1/D_2$. As oxygen diffuses more readily through air than the porous medium of the biofilm [31, 140], it can be reasonably assumed that $D_2 < D_1$. Hence, throughout this chapter, $K > 1$. It is also assumed that ε_1 and ε_2 are small up to observable biofilm length scales ω [41], thus $\varepsilon_i \ll 1$. As noted in [41], the parameter G, referred to as the *growth number*, has a particular meaning: $G = w^2/l_s^2$ where $l_s = \sqrt{D_2 s_\infty / f(s_\infty)}$ measures the *penetration depth* of substrate into the biofilm i.e. a depth scale over which the diffusible substrate can penetrate before it is consumed. The region $h - l_s < z < h$ is referred to as the active layer of the biofilm, therefore the quantity $1/\sqrt{G}$ is a measure of the active layer depth which can alternatively be thought of as a measure of the efficiency of substrate utilisation.

Finally, the functional forms for f and g must be set. Following [41] we take the simplest, reasonable form for f, namely $f(S) = S$, and use this throughout the chapter as a viable approximation to more complete descriptions of appetite-limited substrate utilisation in non-saturated conditions. It is well known that bacterial death occurs in the biofilm [133, 166, 167] and of particular relevance here is recent work that has highlighted the role that cell death plays in mediating heterogeneous growth [6]. Asally et al. [6] highlighted the role of cell death in generating pattern formation in bacterial biofilms grown in laboratory conditions represented by the model set-up considered here. In particular, in [6], it was shown that cell death occurred at the base of *Bacillus subtilis* biofilms (at the biofilm-agar interface). Specifically, it was hypothesised that the resulting cell death pattern within the central coffee-ring region (highlighted in Figure 4.1(b)), acts as a pre-pattern for the striking growth patterns of the type illustrated in Figure 2.1(c). To model this phenomenon, it is necessary to introduce a death term into the bacterial growth function g i.e. (in non-dimensional form) $g(S) = f(S) - d(S)$ where $d = d(S)$ represents the death of cells, which can be thought of as being associated with cell removal or shrinkage. In [41], most of the analysis considers the case $d \equiv 0$. In this chapter we investigate the role of cell death in more detail. In particular we examine two cases: cell death at a constant rate (discussed briefly in [41]) and substrate dependent cell death, motivated by [6]. We therefore consider both $d(S) := \mu$ and $d(S) := \mu(1 - S)$ in turn. The former is the standard constant death term. The latter is a simple model for the phenomenon discussed in [6], where death rate increases with decreasing substrate concentration (corresponding to increasing distance below the biofilm-air interface) and approaches the constant death rate μ below the active layer region. Thus $g(S) = S - \mu$ and $g(S) = (1 + \mu)S - \mu$, respectively. In both cases we present an analysis of the effects of cell death on the development of the biofilm and pattern formation.

In conclusion, setting $\varepsilon_1 = \varepsilon_2 = 0$ (a standard analytical approach in the solution of moving boundary problems) and employing the growth and utilisation functions detailed above yields a quasi-static description of equations (4.8) and (4.9)

$$\nabla^2 S = 0; \qquad h(\mathbf{x},t) < z < H(\mathbf{x},t) := h(\mathbf{x},t) + L, \tag{4.12}$$

$$\begin{cases} \nabla^2 S = GS; \\ \\ \nabla^2 P = -D_\mu S + \mu; \end{cases} \qquad 0 < z < h(\mathbf{x},t) \tag{4.13}$$

that is to be solved in conjunction with the interface evolution equation (4.10) and boundary conditions (4.11). Here

$$D_\mu = \begin{cases} 1, & d(S) := \mu, \\ \\ 1+\mu, & d(S) := \mu(1-S), \end{cases} \tag{4.14}$$

where μ is a positive constant. As an aside we note that setting $D_\mu = 1$ and $\mu = 0$ in equation (4.13) recovers the case where no cell death occurs ($d \equiv 0$), which is the main focus in [41].

The chapter is organised as follows. Planar solutions to equations (4.12)-(4.13) are found and differences between behaviour at the steady states in the different cases of cell death are noted. Following this, the corresponding non-planar solutions are derived and the possibility of pattern formation occurring at steady states is investigated in both ‘shallow’ and ‘deep’ biofilms (as explained later).

4.4 Planar Solutions

First, we consider the effects of cell death on planar solutions. From (4.12)-(4.13), planar solutions $S_0(z,t), P_0(z,t)$ and $h_0(t)$ must satisfy

$$S_{0_{zz}} = 0 \qquad h_0(t) < z < H_0(t) := h_0(t) + L. \tag{4.15}$$

$$\begin{cases} S_{0_{zz}} = GS_0; \\ P_{0_{zz}} = -D_\mu S_0 + \mu; \end{cases} \qquad 0 < z < h_0(t) \tag{4.16}$$

where the boundary conditions for planar solutions are

$$P_0\big|_{z=h_0} = 0\,, \quad P_{0_z}\big|_{z=0} = 0; \tag{4.17a}$$

$$S_0\big|_{z=H_0} = 1, \quad S_{0_z}\big|_{z=0} = 0; \tag{4.17b}$$

$$S_0\big|_{z=h_0^+} = S_0\big|_{z=h_0^-}; \tag{4.17c}$$

$$KS_{0_z}\big|_{z=h_0^+} = S_{0_z}\big|_{z=h_0^-}, \tag{4.17d}$$

and the interface evolution equation is

$$h_0'(t) = -P_{0_z}|_{z=h_0}. \tag{4.18}$$

Solving (4.15)-(4.16) with the above boundary conditions, it follows that the planar solution for the substrate is

$$S_0(z,t) = \begin{cases} 1 - \bar{S}K^{-1}\sqrt{G}\tanh(\sqrt{G}h_0)(H_0 - z), & h_0(t) < z < H_0(t); \\ \\ \bar{S}\dfrac{\cosh(\sqrt{G}z)}{\cosh(\sqrt{G}h_0)}, & 0 < z < h_0(t); \end{cases} \tag{4.19}$$

where

$$\bar{S} = \left[1 + LK^{-1}\sqrt{G}\tanh(\sqrt{G}h_0)\right]^{-1}$$

is the value of the substrate at the interface $z = h_0$. Substituting the second expression in (4.19) into the second expression of (4.16), integrating twice and implementing the boundary conditions yields

$$P_0(z,t) = \frac{D_\mu \bar{S}}{G}\left[1 - \frac{\cosh(\sqrt{G}z)}{\cosh(\sqrt{G}h_0)}\right] + \frac{\mu}{2}(z^2 - h_0^2). \tag{4.20}$$

Finally, substitution of (4.20) into the interface evolution equation (4.18) yields

$$h_0'(t) = \frac{D_\mu \bar{S}}{\sqrt{G}}\tanh(\sqrt{G}h_0) - \mu h_0. \tag{4.21}$$

We now examine the effects of cell death on the planar development of the biofilm by focussing on the biofilm-substratum interface $h_0(t)$ and referring to equation (4.21). A closed form solution for equation (4.21) cannot be obtained, however it is informative to consider the qualitative structure of the solution in each case of cell death. We are only interested in non-negative solutions and it follows directly from standard arguments that solutions of (4.21) with non-negative initial data remain non-negative.

To distinguish between solutions h_0 in the different cases of cell death, the notation h_{0a}, h_{0c} and h_{0s} is used to denote planar solutions in the absence of death (where $D_\mu = 1$ and $\mu = 0$), with constant death (where $D_\mu = 1$) and with substrate dependent death (where $D_\mu = 1 + \mu$), respectively. Immediately, it can be seen that for any given $h_0(t)$,

$$h_{0a}'(t) > h_{0s}'(t) > h_{0c}'(t), \tag{4.22}$$

representing the fact that biofilm growth at a specific planar height will be fastest when no cell death is present, as one might anticipate. For each fixed value of μ, growth at h_0 will also be faster in the case of substrate dependent death compared to constant cell death. Further qualitative details can be found by examining the different death cases in turn.

Firstly, in the case of no cell death, it is clear from (4.21) that for any non-negative $h_0(t)$, $h'_{0a}(t) > 0$ and

$$\lim_{h_{0a}\to\infty} \bar{S} = \frac{1}{1+K^{-1}L\sqrt{G}} \implies \lim_{h_{0a}\to\infty} h'_{0a}(t) = \frac{1}{\sqrt{G}+K^{-1}LG}.$$

Thus, given any non-negative initial biofilm height $h_{0a}(0)$, the biofilm is predicted to increase in height (thickness) without bound. Moreover, the terminal velocity of the growth rate is a decreasing function of the growth number, G, and the length scale, L, of the far-field substrate concentration. The terminal velocity is also an increasing function of K, a measure of the relative density of the biofilm. These relationships have very natural consequences in that they predict efficient growth or a closer far-field substrate will induce faster growth, whilst a biofilm more impervious to substrate (smaller K) will grow more slowly.

In the case of positive death rates, $\mu > 0$, it is straightforward to verify from equation (4.21) that

$$\begin{aligned} h'_0(t) &\leq \frac{D_\mu \tanh(\sqrt{G}h_0)}{\sqrt{G}} - \mu h_0 \\ &\leq \frac{D_\mu}{\sqrt{G}}\sqrt{G}h_0 - \mu h_0 \\ &= (D_\mu - \mu)h_0, \end{aligned} \tag{4.23}$$

and hence a sufficient condition for monotonic die-back of the biofilm is $D_\mu < \mu$. Hence, in the case of constant cell death, complete die-back will occur for $\mu > 1$. In the case of substrate dependent cell death, condition (4.23) simplifies to $h'_{0s}(t) \leq h_{0s}(t)$, and therefore (4.23) fails to define any necessary or sufficient conditions to ensure the die-back of a biofilm in the presence of substrate dependent death. Rather, (4.23) simply states that growth in this case can be no faster than exponential.

Considering the interface equation (4.21) in isolation and following standard arguments, it is clear that at least one real steady state, the trivial steady state, exists in both the absence and presence of cell death. While the trivial steady state $h_0^* = 0$ is the singular fixed point in the absence of death and the presence of constant cell death with $\mu > 1$, a second steady state $h_0^* = h_0^*(\mu)$ given implicitly by

$$h_0^*(\mu) = \frac{D_\mu \bar{S}^*}{\mu\sqrt{G}} \tanh\left(\sqrt{G} h_0^*\right), \tag{4.24}$$

where * denotes evaluation at this steady state, exists in the case of constant cell death where $\mu < 1$ and all cases of substrate dependent death. An examination of extreme parameter cases contributes to a better understanding of steady state behaviour in the presence of cell death. It is clear that as $\mu \to 0$, $h_0^* \to \infty$. It can also be seen that

$$\begin{aligned} \lim_{\mu \to 0} h'_{0c}(t) = \lim_{\mu \to 0} h'_{0s}(t) = & \frac{\tanh(\sqrt{G} h_0)}{\sqrt{G}\left(1 + LK^{-1}\sqrt{G}\tanh(\sqrt{G} h_0)\right)} \\ = & h'_{0a}(t), \end{aligned} \tag{4.25}$$

therefore as $\mu \to 0$, biofilm growth in the presence of death is expected to follow the same evolutionary behaviour as that in the absence of death, with the biofilm growing without bound. On the other hand, if $\mu \to \infty$, then $h'_{0c} < 0$ and $h^*_{0c} = 0$, while

$$h^*_{0s} \to \frac{\tanh(\sqrt{G} h^*_{0s})}{\sqrt{G}\left(1 + LK^{-1}\sqrt{G}\tanh(\sqrt{G} h^*_{0s})\right)}. \tag{4.26}$$

Moreover, it can be shown by rearrangement of equation (4.24) and implementation of the chain, product and quotient rules, that both $\partial h^*_{0c}/\partial \mu < 0$ and $\partial h^*_{0s}/\partial \mu < 0$. Hence, as may be expected, an increase in cell death results in thinner biofilms overall, regardless of whether death is constant or substrate dependent. Similarly, $\partial h^*_{0c}/\partial G < 0$ and $\partial h^*_{0s}/\partial G < 0$, and thus decreasing substrate penetration depth l_s, where $l_s = 1/\sqrt{G}$, has the effect of decreasing steady state biofilm height.

Standard methods for dynamical systems applied to the interface equation (4.21) in isolation suggest that the singular trivial steady state $h_0^* = 0$ will be unstable in the absence of death, and stable in the presence of constant death where $\mu > 1$. In the case of constant death with $\mu < 1$ and all cases of substrate dependent death, similar arguments imply that the trivial steady state will be unstable, while the second non-trivial steady state $h_0^*(\mu)$ will be stable to linear perturbations. As a result, it is predicted that in contrast to constant cell death, complete biofilm die-back will never occur in the case of substrate dependent cell death; even for large μ, the biofilm height will stabilise at a positive value.

In conclusion, a planar analysis of the model predicts that in the absence of cell death, a biofilm with planar surface limited only by substrate diffusion increases in thickness without bound with a terminal velocity determined by the value of the growth parameters. In the case of constant cell death, the model predicts that for sufficiently small death rates ($\mu < 1$) planar height will tend to a steady state with value $h_{0c}^* = h_{0c}^*(\mu)$. For constant cell death at super-threshold levels $(\mu > 1)$, biofilm collapse is induced. In the case of a substrate-dependent death rate, the model predicts that the planar height will always tend to a steady state with value $h_{0s}^* = h_{0s}^*(\mu)$, regardless of the value of μ. In the following section, we discuss stability of the interface to non-planar perturbations and the role of cell death in this process.

4.5 Non-planar Growth

4.5.1 General Formulation

Next, in order to investigate the stability of the planar solutions to non-planar perturbations, we follow a similar method as described in [41] and consider solutions of (4.10), (4.12), (4.13) of the form

$$
\begin{aligned}
S(\mathbf{x},z,t) &= S_0(z,t) + S_1(z,t)\exp(i\mathbf{k}\cdot\mathbf{x}),\\
P(\mathbf{x},z,t) &= P_0(z,t) + P_1(z,t)\exp(i\mathbf{k}\cdot\mathbf{x}),\\
h(\mathbf{x},t) &= h_0(t) + h_1(t)\exp(i\mathbf{k}\cdot\mathbf{x}),
\end{aligned}
\tag{4.27}
$$

where S_0, P_0 and h_0 are as defined in section 4.4, where $|S_1| \ll 1$, $|S_{1_z}| \ll 1$, $|P_1| \ll 1$, $|P_{1_z}| \ll 1$, $|h_1| \ll 1$, $|h_1'(t)| \ll 1$ and where $\mathbf{k}$ is the 2-D wave number $\mathbf{k} = (k_1, k_2)$ with $|\mathbf{k}| = k$. Note that the variable separation in (4.27) is possible because we consider a finite, periodically repeating component (with periodic boundary conditions) of the original infinite $\mathbf{x}$ domain. As in [41], we set $H(\mathbf{x},t) = h_0(t) + L$ for simplicity (recall that L is the distance above the biofilm-air interface where substrate concentration can be assumed to be unaffected by biofilm growth). On substitution into (4.10), (4.12), (4.13), and after following standard arguments, it can be shown that the perturbations $S_1(z,t)$ and $P_1(z,t)$ must satisfy

$$
S_{1_{zz}} - k^2 S_1 = 0; \qquad h_0(\mathbf{x},t) < z < H_0(t) \tag{4.28}
$$

$$
\begin{cases}
S_{1_{zz}} - (k^2+G)S_1 = 0; \\
P_{1_{zz}} - k^2 P_1 = -D_\mu S_1;
\end{cases}
\qquad 0 < z < h_0(\mathbf{x},t) \tag{4.29}
$$

and the interface perturbation $h_1(t)$ satisfies

$$
h_1' = -h_1 P_{0_{zz}}|_{h_0} - P_{1_z}|_{h_0}. \tag{4.30}
$$

[This last equation follows from substitution into (4.10) and on using the second equation in (4.16)]. The corresponding boundary conditions for the small perturbations S_1,

P_1 and h_1 are

$$h_1 P_{0_z}|_{h_0} + P_1|_{h_0} = 0, \quad P_{1_z}|_0 = 0; \tag{4.31a}$$

$$S_1|_{h_0+L} = 0, \quad S_{1_z}|_0 = 0; \tag{4.31b}$$

$$h_1 S_{0_z}|_{h_0^+} + S_1|_{h_0^+} = h_1 S_{0_z}|_{h_0^-} + S_1|_{h_0^-}; \tag{4.31c}$$

$$K\left(h_1 S_{0_{zz}}|_{h_0^+} + S_{1_z}|_{h_0^+}\right) = h_1 S_{0_{zz}}|_{h_0^-} + S_{1_z}|_{h_0^-}. \tag{4.31d}$$

[Note that all of the above expressions neglect higher order terms]. Solving for $S_1(z,t)$ in (4.28) and (4.29) and using the boundary conditions (4.31b)-(4.31d) yields:

$$S_1(z,t) = \begin{cases} A_1 \bar{S} h_1 \sqrt{G} \dfrac{\sinh[k(H_0 - z)]}{\cosh[k(H_0 - h_0)]}, & h_0(\mathbf{x},t) < z < H_0(t), \\ B_1 \bar{S} h_1 \sqrt{G} \dfrac{\cosh[\sqrt{k^2+G}z]}{\cosh[\sqrt{k^2+G}h_0]}, & 0 < z < h_0(\mathbf{x},t), \end{cases} \tag{4.32}$$

where $A_1 = A_1(t)$ and $B_1 = B_1(t)$ are constants (w.r.t. z) of integration, that after some algebra can be expressed as

$$\begin{aligned} A_1 &= \frac{(K-1)\sqrt{k^2+G}\tanh(\sqrt{G}h_0)\tanh(\sqrt{k^2+G}h_0) - \sqrt{G}K}{K\left(\sqrt{k^2+G}\tanh(kL)\tanh(\sqrt{k^2+G}h_0) + Kk\right)}, \\ B_1 &= -\left(\frac{k(K-1)\tanh(\sqrt{G}h_0) + \sqrt{G}\tanh(kL)}{\sqrt{k^2+G}\tanh(kL)\tanh(\sqrt{k^2+G}h_0) + Kk}\right). \end{aligned} \tag{4.33}$$

Using (4.32), the second equation in (4.29) yields

$$P_1(z,t) = h_1\left[E_1 e^{kz} + F_1 e^{-kz} - \frac{D_\mu B_1 \bar{S}}{\sqrt{G}} \frac{\cosh(\sqrt{k^2+G}z)}{\cosh(\sqrt{k^2+G}h_0)}\right]. \tag{4.34}$$

Applying the boundary condition (4.31a) and substituting the expression for P_0 given in (4.20) results in $E_1 = F_1$ where

$$E_1 = \frac{1}{2\cosh(kh_0)}\left[\frac{D_\mu \bar{S}}{\sqrt{G}}(B_1 + \tanh(\sqrt{G}h_0)) - \mu h_0\right]. \tag{4.35}$$

Finally, an expression for the first order correction to the interface evolution equation is obtained. On substitution of the expression for $S_0(z,t)$ for $0 < z < h(x,t)$ given in (4.19) into (4.30) and using (4.34), it follows that

$$\begin{aligned} h_1'(t) =& h_1 \Bigg[(kh_0 \tanh(kh_0) - 1)\mu + D_\mu \bar{S}\left(1 - \frac{k\tanh(kh_0)}{\sqrt{G}}B_1\right) - \\ & D_\mu \bar{S}\left(\frac{k\tanh(kh_0)\tanh(\sqrt{G}h_0)}{\sqrt{G}} - \frac{\sqrt{k^2+G}}{\sqrt{G}}\tanh(\sqrt{k^2+G}h_0)B_1\right)\Bigg], \end{aligned} \tag{4.36}$$

where $B_1 = B_1(h_0^*) < 0$, and is given in (4.33). It is noted that (4.36) is of the form $h_1'(t) = \omega(k,t)h_1(t)$, where $\omega(k,t)$ is the *dispersive coefficient* of system (4.12)-(4.13) about the planar solutions (4.19)-(4.21). It is clear that the sign of $\omega(k,t)$ varies depending on the choice of the wave number k and other parameter values. Therefore, the evolving planar solution of system (4.12)-(4.13) is potentially unstable to non-planar perturbations with certain wave numbers.

Notice also that the above linearisation is around a general $h_0 = h_0(t)$, and is therefore valid for all values of h_0. Linearisation around the uniform steady state h_0^*, such that $P_0(z,t) = P_0(z)$ and $S_0(z,t) = S_0(z)$, results in the same system and solutions as defined in equations (4.32)-(4.36) (where h_0 is replaced by h_0^*) due to the fact that the quasi-static description of equations (equations (4.12)-(4.13)) is considered. On substitution of the steady state expression (4.24) into equation (4.36), a specific expression for the evolution of $h_1(t)$ at $h_0 = h_0^*$ in the presence of cell death is found as $h_1^{*'}(t) = h_1(t)\omega^*$, where

$$\omega^* = \mu \left[\frac{h_0^*}{\tanh(\sqrt{G} h_0^*)} \left(\sqrt{G} - k \tanh(k h_0^*) B_1^* + \sqrt{k^2+G} \tanh(\sqrt{k^2+G} h_0^*) B_1^* \right) - 1 \right], \tag{4.37}$$

and the superscript * denotes evaluation at the non-trivial steady state h_{0c}^* or h_{0s}^*. Expression (4.37) is the same for both constant and substrate dependent cell death, though recall that the steady state $h_0^* > 0$ only exists for constant cell death if $\mu < 1$, and $h_{0c}^* < h_{0s}^*$ for a fixed value of μ.

4.5.2 Relevant Perturbations and Values of k

We note that the above expressions $A_1(t)$ and $B_1(t)$ and thus the derived non-planar solutions $S_1(z,t)$, $P_1(z,t)$ and $h_1'(t)$ in section 4.5.1 are undefined at $k = 0$. However, non-planar solutions in this special case can be found by substitution of $k = 0$ into the equations (4.28)-(4.29) and perturbations (4.27) and solving as above. Comparing the solutions with $k = 0$ and $k > 0$, it can be seen that

$$\begin{aligned} S_1(k=0,z,t) &= \lim_{k \to 0} S_1(z,t), \\ P_1(k=0,z,t) &= \lim_{k \to 0} P_1(z,t), \\ h_1'(k=0,t) &= \lim_{k \to 0} h_1'(t). \end{aligned} \tag{4.38}$$

Also, at the steady state h_0^*,

$$\omega^*(k=0,t) = \mu \left[\sqrt{G} h_0^* \left(\frac{1}{\tanh(\sqrt{G} h_0^*)} + \hat{B}_1^* \right) - 1 \right] = \lim_{k \to 0} \omega^*(k,t), \tag{4.39}$$

where * again denotes evaluation at the non-trivial steady state h_0^* and

$$\hat{B}_1^* = -\left(\frac{(K-1)\tanh(\sqrt{G}h_0^*) + \sqrt{G}L}{\sqrt{G}L\tanh(\sqrt{G}h_0^*) + K}\right) = \lim_{k\to 0} B_1^*. \tag{4.40}$$

It is therefore clear that all solutions can be evaluated at, and are continuous at, $k = 0$. We use this limiting case later.

Recall that we are interested in periodic solutions. In addition we restrict our attention to perturbations satisfying a zero-mass assumption (no addition or loss of material), and therefore the applicable values of k are $k = 2n\pi$, where $n \in \mathbb{N}$. Moreover, it is possible to choose the rescaling in order that the perturbation represented by any relevant wave number $k = 2n\pi$, where $n \geq 2$, can be scaled to represent the cosine function over a single wavelength (where $k = 2\pi$) on the chosen domain (recall the non-dimensionalisation in section 4.3). Thus the only relevant wave number is $k = 2\pi$.

4.6 The Role of Cell Death on Pattern Formation

Having found expressions for planar and non-planar biofilm growth, focus is turned to determining the effect of different death terms on the growth of the biofilm. The role of cell death in the evolution of patterns is of particular interest and is now investigated.

It can be seen from equation (4.36) that in the absence of cell death, the dispersion relation $\omega(k,t)$ reduces to

$$\begin{aligned}\omega_a = \bar{S}\Bigg(1 - \frac{k\tanh(kh_0)}{\sqrt{G}}B_1 - \frac{k\tanh(kh_0)\tanh(\sqrt{G}h_0)}{\sqrt{G}} \\ + \frac{\sqrt{k^2+G}}{\sqrt{G}}\tanh(\sqrt{k^2+G}h_0)B_1\Bigg).\end{aligned} \tag{4.41}$$

In the presence of constant and substrate dependent cell death, the respective expressions for the dispersion relations at a specific h_0 are given by $\omega_c = (kh_0 \tanh(kh_0) - 1)\mu + \omega_a$ and $\omega_s = (kh_0 \tanh(kh_0) - 1 + \omega_a)\mu + \omega_a$.

At first glance it appears that the term $(kh_0 \tanh(kh_0) - 1)\mu$ in ω_c represents the effect of the bacterial death in the constant cell death case, suggesting that for kh_0 small enough, the introduction of $\mu > 0$ contributes an extra negative term in ω_c, which switches to an extra positive term as h_0 increases. Therefore the model seems to predict that at the early stage of biofilm growth (where h_0 is small), a constant rate of bacterial death will stabilise the planar height growth to heterogeneous perturbations while at the mature stage of biofilm growth (where h_0 is large), constant bacterial death will destabilise the planar height growth. These observations suggest constant bacterial death facilitates spatial pattern formation in mature biofilms. However, recalling that $h_0 = h_0(\mu)$, it is clear that ω_a is also dependent on μ, and thus the effect of cell death is not incorporated solely within the expression $(kh_0 \tanh(kh_0) - 1)\mu$, but rather within all terms in ω_c. Similar arguments follow for substrate dependent cell death: cell death is present in all terms in ω_s. As a result, a comparison of the planar solutions and behaviour of the dispersion relations ω_c and ω_s with respect to cell death is not as straightforward as appears at first sight. In order to investigate the behaviour of non-planar growth further, we now carry out a closer inspection at some extreme values in order to quantify certain qualitative features.

4.6.1 Shallow Biofilms

The first case considered assumes biofilm height at steady state is much less than the depth of the active layer, l_s, and thus substrate concentration is plentiful (a characteristic of early biofilms [141]) and approaching S_∞ throughout the entire biofilm depth.

Recalling that $G = w^2/l_s^2$, it is clear that in the non-dimensional setting, the approximation $h_0^* \ll 1/\sqrt{G}$ can be used to represent this situation, and thus we refer to the biofilm as being 'shallow'. In this case the substrate dependent death term $d(S) \approx \mu(1 - S_\infty)$, and therefore cell death remains approximately constant at its minimum rate everywhere in the biofilm.

Using $h_0^* \ll 1/\sqrt{G}$, the substitution of $\tanh(\sqrt{G}h_0^*) \simeq \sqrt{G}h_0^*$ can be made in equation (4.24) in order to find the non-trivial steady states h_{0c}^* and h_{0s}^* of shallow biofilms. The steady states are given by

$$h_{0c}^* = \frac{K(1-\mu)}{\mu GL}, \quad h_{0s}^* = \frac{K}{\mu GL}. \tag{4.42}$$

Note that in order to satisfy the shallow biofilm assumption, the value of the death parameters μ_c (in the case of constant cell death) and μ_s (in the case of substrate dependent cell death) must be sufficiently high, specifically

$$\mu_c \gg \frac{K}{K + L\sqrt{G}}, \quad \mu_s \gg \frac{K}{L\sqrt{G}}. \tag{4.43}$$

Using equation (4.42), the dependence of ω^* on μ can be explicitly defined in the case of shallow biofilms. Substitution of either h_{0c}^* or h_{0s}^* from equation (4.42) into ω^* (equation (4.37)) yields

$$\begin{aligned} \omega^* &= -B_{1S}^* \frac{\mu}{\sqrt{G}} \left(k \tanh(kh_0^*) - \sqrt{k^2+G} \tanh(\sqrt{k^2+G}h_0^*) \right) \\ &< 0, \end{aligned} \tag{4.44}$$

where

$$B_{1S}^* = -\sqrt{G} \left(\frac{k(K-1)h_0^* + \tanh(kL)}{Kk + \sqrt{k^2+G} \tanh(\sqrt{k^2+G}h_0^*) \tanh(kL)} \right) < 0. \tag{4.45}$$

As $\omega^* < 0$ for all wave numbers, it is clear that perturbations will not grow in shallow biofilms in either case of cell death. Therefore, in the long term, it is predicted that shallow biofilms will display no pattern formation.

4.6.2 Deep Biofilms

In comparison to 'shallow' biofilms, we refer to 'deep' biofilms in the instances where the depth of the biofilm far exceeds the depth of the active layer, and represent this by assuming $h_0^* \gg 1/\sqrt{G}$. In this case, a large part of the biofilm is subjected to substrate deprivation, with the bottom region being the most adversely affected. This is indicative of mature biofilms [141]. A consequence of the assumption $h_0^* \gg 1/\sqrt{G}$ is that the approximation $\tanh(\sqrt{G}h_0^*) \simeq 1$ can be made. The non-trivial steady states for deep biofilms in the presence of cell death are found from equation (4.24) and are given by

$$h_{0c}^* = \frac{K}{\mu\sqrt{G}(K+L\sqrt{G})}, \quad h_{0s}^* = \left(1+\frac{1}{\mu}\right)\frac{K}{\sqrt{G}(K+L\sqrt{G})}, \tag{4.46}$$

which are again explicitly dependent on μ, where μ must be sufficiently small, specifically

$$\mu_c \ll \frac{K}{K+L\sqrt{G}}, \quad \mu_s \ll \frac{K}{L\sqrt{G}}, \tag{4.47}$$

to be consistent with the condition $h_0^* \gg 1/\sqrt{G}$. In this case,

$$\begin{aligned} \omega_c^* &= \eta_c^* - \mu \\ \omega_s^* &= \eta_s^*(1+\mu) - \mu \end{aligned} \tag{4.48}$$

for $\eta_c^* = \eta(h_{0c}^*)$ and $\eta_s^* = \eta(h_{0s}^*)$, where

$$\eta(h) = \frac{K}{K+L\sqrt{G}}\left(1 - \frac{B_{1L}}{\sqrt{G}}\left(k\tanh(kh) - \sqrt{k^2+G}\right)\right), \tag{4.49}$$

and

$$B_{1L} = -\frac{k(K-1)+\sqrt{G}\tanh(kL)}{Kk+\sqrt{k^2+G}\tanh(kL)} < 0, \tag{4.50}$$

(note that B_{1L} is independent of μ, h_0 and h_0^*, and that $|B_{1L}| < 1$).

As noted previously, it is clear that an increase in μ decreases the steady states h_{0c}^* and h_{0s}^*, which in turn lowers η^* (see equations (4.46) and (4.49)). It is therefore apparent from equation (4.48) that $\partial\omega_c^*/\partial\mu < 0$, and thus increased (constant) cell death has a stabilising effect on non-planar perturbations to h_{0c}^*. Since $\eta < 1$, it can also be shown that $\partial\omega_s^*/\partial\mu < 0$, and therefore it can be said that, overall, an increase in μ has a stabilising effect on non-planar perturbations to h_{0s}^*.

Recalling section 4.5.2, it is clear that in order to investigate the possibility of pattern formation occuring in deep biofilms satisfying our specified boundary conditions, behaviour of the dispersion relations ω_c^* and ω_s^* must be analysed at the relevant wave number, $k = 2\pi$. Therefore, substitution of $k = 2\pi$ and h_{0c}^* and h_{0s}^* from equation (4.46) into equations (4.48)-(4.50) give the values of $\eta(h)$, B_{1L} and subsequently ω^* that must be considered:

$$\eta(h_{0c}^*, k=2\pi) = \frac{K}{K+L\sqrt{G}}\left(1-\frac{B_{1L}}{\sqrt{G}}\left(2\pi\tanh\left(\frac{2\pi K}{\mu\sqrt{G}(K+L\sqrt{G})}\right)-\sqrt{4\pi^2+G}\right)\right), \tag{4.51a}$$

$$\eta(h_{0s}^*, k=2\pi) = \frac{K}{K+L\sqrt{G}}\left(1-\frac{B_{1L}}{\sqrt{G}}\left(2\pi\tanh\left(\frac{2\pi K(1+\mu)}{\mu\sqrt{G}(K+L\sqrt{G})}\right)-\sqrt{4\pi^2+G}\right)\right), \tag{4.51b}$$

where

$$B_{1L}(k=2\pi) = -\frac{2\pi(K-1)+\sqrt{G}\tanh(2\pi L)}{2\pi K+\sqrt{4\pi^2+G}\tanh(2\pi L)} < 0. \tag{4.52}$$

As both $\partial \omega_c^*/\partial \mu < 0$ and $\partial \omega_s^*/\partial \mu < 0$ for any fixed k and any h_0^*, it follows that in the case of deep biofilms, the maximum values of $\omega_c^*(k=2\pi)$ and $\omega_s^*(k=2\pi)$ can be found by taking the limits as $\mu \to 0$. We find that

$$\begin{aligned}
\lim_{\mu\to 0} \omega_c^*(k=2\pi) &= \lim_{\mu\to 0} \eta(h_{0c}^*, k=2\pi) \\
&= \frac{K}{K+L\sqrt{G}}\left(1-\frac{B_{1L}(k=2\pi)}{\sqrt{G}}\left(2\pi-\sqrt{4\pi^2+G}\right)\right) \\
&\geq \frac{K}{K+L\sqrt{G}}\left(1+B_{1L}(k=2\pi)\right) \\
&> 0.
\end{aligned} \tag{4.53}$$

Similarly, it is found that

$$\lim_{\mu\to 0} \omega_s^*(k=2\pi) = \lim_{\mu\to 0} \omega_c^*(k=2\pi) > 0. \tag{4.54}$$

Thus, in both regimes of cell death, the wave number $k=2\pi$ becomes unstable to perturbations as $\mu \to 0$.

In the case of constant cell death, the condition $\partial \omega_c^*/\partial \mu < 0$ holds. Also, as $\lim_{\mu\to 0} \omega_c^*(k=2\pi) > 0$, it follows that as μ transits some critical value μ_c^{crit}, the stability of the wave number $k=2\pi$ changes. This critical value is defined implicitly by the equation

$$\omega_c^*(\mu_c^{crit}, k=2\pi) = \eta(h_{0c}^*(\mu_c^{crit}), k=2\pi) - \mu_c^{crit} = 0. \tag{4.55}$$

We have:

$$\omega_c^* > 0 \text{ (growing perturbations) for } k=2\pi \text{ if } \mu < \mu_c^{crit}, \tag{4.56a}$$

$$\omega_c^* < 0 \text{ (decaying perturbations) for } k=2\pi \text{ if } \mu > \mu_c^{crit}, \tag{4.56b}$$

(see Figure 4.3(a)).

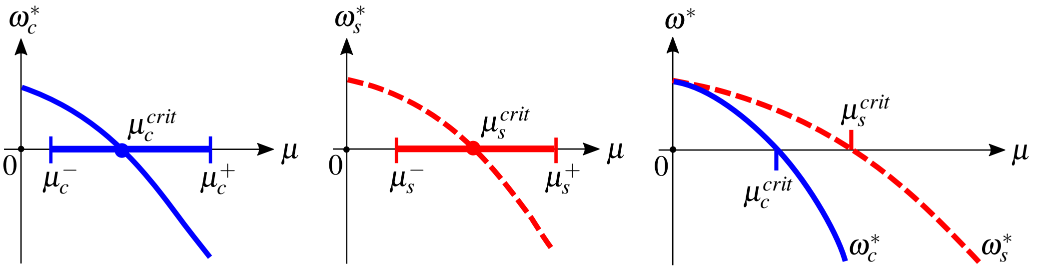

(a) $\omega_c^*(k=2\pi)$ (b) $\omega_s^*(k=2\pi)$ (c) ω_c^* (blue) and ω_s^* (red)

Figure 4.3: Schematic representation of dispersion relations $\omega^*(k=2\pi)$ as functions of μ, in the case of $\sqrt{Gh_0^*} \gg 1$. Figure (a): Plot showing ω_c^*, which passes through μ_c^{crit}, where $\mu_c^- < \mu_c^{crit} < \mu_c^+$. Figure (b): Plot showing ω_s^*, which passes through μ_s^{crit}, where $\mu_s^- < \mu_s^{crit} < \mu_s^+$. Figure (c): Schematic showing both ω_c^* (blue solid line) and ω_s^* (red dashed line), where the relative positions of μ_c^{crit} and μ_s^{crit} are labelled.

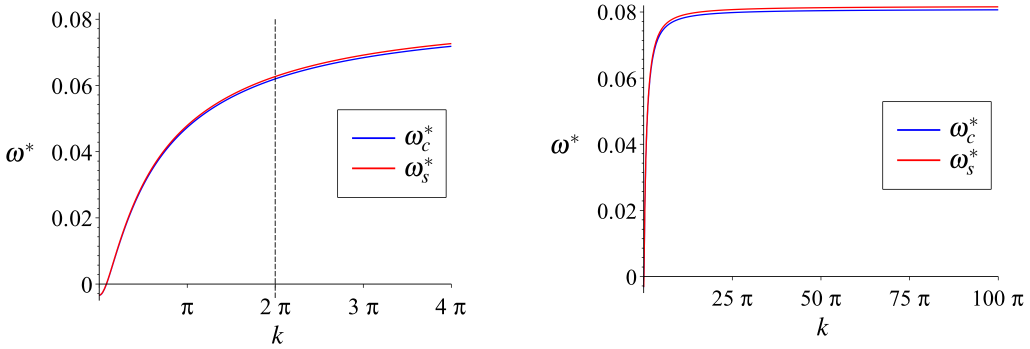

(a) (b)

Figure 4.4: An example plot of ω_c^* (blue) and ω_s^* (red) against k in the case of deep biofilms ($\sqrt{Gh_{0c}^*} \gg 1$ and $\sqrt{Gh_{0s}^*} \gg 1$ respectively). It can be seen that both $\partial\omega_c^*/\partial k > 0$ and $\partial\omega_s^*/\partial k > 0$. Figure (a) shows the interval $k \in (0, 4\pi)$ with the relevant value $k = 2\pi$ highlighted by a dashed line. Figure (b) shows $k \in (0, 100\pi)$. Parameter values are $G = 100$, $L = 5$, $K = 5$, $\mu = 0.01$. Steady states are $h_{0c}^* \approx 0.909$ and $h_{0s}^* \approx 0.918$. Plot created in Maple.

It is possible to find an interval in which the implicitly defined value μ_c^{crit} lies by considering other aspects of the problem as follows. It can be shown that $\partial\omega_c^*/\partial k > 0$ (an example plot of ω_c^* as a function of k, using specific parameter values, is shown in blue in Figure 4.4), and as such the limits as $k \to 0$ and $k \to \infty$ give the threshold values of μ, denoted μ_c^- and μ_c^+, for which all wave numbers $k > 0$ in ω_c^* can be said to be unstable or stable respectively. We have $\omega_c^* > 0$ for all $k > 0$ if $\mu < \mu_c^-$ and $\omega_c^* < 0$ for all $k > 0$ if $\mu > \mu_c^+$, where

$$\mu_c^- = \frac{K}{(K + L\sqrt{G})^2}, \quad \mu_c^+ = \frac{K}{K + L\sqrt{G}}. \tag{4.57}$$

Thus it is clear that μ_c^{crit} must lie in the interval defined by

$$\mu_c^- < \mu_c^{crit} < \mu_c^+, \tag{4.58}$$

(again see Figure 4.3(a)). Recalling condition (4.47), it can be seen that for any value of $\mu > \mu_c^+$, the assumption of deep biofilms ($h_{0c}^* \gg 1/\sqrt{G}$) does not hold. Therefore any $\mu > \mu_c^+$ is irrelevant in our analysis of deep biofilms subject to constant cell death.

In the case of substrate dependent cell death, the conditions $\partial\omega_s^*/\partial\mu < 0$ and $\lim_{\mu\to 0}\omega_s^*(k = 2\pi) > 0$ hold. As in the case of constant cell death it follows that, as μ transits some critical value, denoted μ_s^{crit}, the sign of ω_s^* changes. Again we note that while the critical death parameter μ_s^{crit} cannot be defined explicitly, it is implicitly defined by

$$\omega_s^*(\mu_s^{crit}, k = 2\pi) = \eta(h_{0s}^*(\mu_s^{crit}), k = 2\pi) \cdot (1 + \mu_s^{crit}) - \mu_s^{crit} = 0, \tag{4.59}$$

and the following conditions are true:

$$\omega_s^* > 0 \text{ (growing perturbations) for } k = 2\pi \text{ for } \mu < \mu_s^{crit}, \tag{4.60a}$$

$$\omega_s^* < 0 \text{ (decaying perturbations) for } k = 2\pi \text{ for } \mu > \mu_s^{crit}. \tag{4.60b}$$

Using a similar method as described in the case of constant cell death, we use the fact that $\partial\omega_s^*/\partial k > 0$ (an example plot of ω_s^* against k is shown in red in Figure 4.4), and take the limits of ω_s^* as $k \to 0$ and $k \to \infty$, to define the threshold values of μ, denoted μ_s^- and μ_s^+, for which all wave numbers $k > 0$ in ω_s^* can be said to be unstable or stable respectively. We have $\omega_s^* > 0$ for all $k > 0$ if $\mu < \mu_s^-$ and $\omega_s^* < 0$ for all $k > 0$ if $\mu > \mu_s^+$, where

$$\mu_s^- = \frac{K}{(K + L\sqrt{G})^2 - K}, \quad \mu_s^+ = \frac{K}{L\sqrt{G}}. \tag{4.61}$$

Clearly μ_s^{crit} lies in the interval

$$\mu_s^- < \mu_s^{crit} < \mu_s^+, \tag{4.62}$$

(see Figure 4.3(b)). Once again it follows from condition (4.47), that the assumption $h_{0s}^* \gg 1/\sqrt{G}$ does not hold for $\mu > \mu_s^+$. Therefore analysis of deep biofilms subject to substrate dependent cell death, and the corresponding dispersion relation ω_s^*, bears no significance when $\mu > \mu_s^+$.

Comparing the cases of constant and substrate dependent cell death it is clear that, for any fixed $k > 0$ and a fixed set of parameter values, $\omega_c^* < \omega_s^*$. As a result, $\mu_c^{crit} < \mu_s^{crit}$ (as shown in Figure 4.3(c)). Thus it is possible that, for a fixed set of parameter values, a single value of μ satisfying both $h_{0c}^* \gg 1/\sqrt{G}$ and $h_{0s}^* \gg 1/\sqrt{G}$ may be chosen such that the condition

$$\mu_c^{crit} < \mu < \mu_s^{crit} \tag{4.63}$$

holds. In this special case, it is clear that $\omega_c^*(k = 2\pi) < 0$ and $\omega_s^*(k = 2\pi) > 0$. Thus, the wave number $k = 2\pi$ is unstable to perturbations in the case of substrate dependent cell death but is stable in the case of constant cell death. As a result, it is predicted that for values of μ in the interval defined by condition (4.63), patterning may occur in the case of substrate dependent cell death but will not occur in the case of constant cell death.

It is noted that the above analysis considering the wave number $k = 2\pi$ allows us to determine the existence of instabilities and patterns at the smallest relevant wave number (recall Section 4.5.2). As both $\partial \omega_c^*/\partial k > 0$ and $\partial \omega_s^*/\partial k > 0$, it is not possible to find a specific wave number for which instabilities will be fastest growing and so a specific wavelength of pattern cannot be found. It may be possible that the inclusion of additional biological or physical phenomena, e.g. surface tension, in the system described in Section 4.2 may allow a fastest growing wave number to be chosen and thus a specific wavelength of pattern may emerge. However, we do not consider this case here.

4.7 Conclusions

In this chapter we introduced an extension of the model of Dockery and Klapper [41] to investigate the role of cell death in biofilm growth and wrinkle formation. It was found that the existence of a non-trivial steady state in the presence of both constant and substrate dependent cell death limits biofilm growth. While sufficiently high death rate, μ, was found to induce complete biofilm die-back in the case of constant cell death, complete biofilm collapse was precluded, independent of the size of μ, in the case of substrate dependent cell death. In the instances where complete die-back did not occur, it was found that cell death played a key role in determining steady state biofilm height. As one might anticipate, the steady state biofilm depth was predicted

	Shallow biofilms ($\sqrt{G}h_0^* \ll 1$)	Deep biofilms ($\sqrt{G}h_0^* \gg 1$)
Constant cell death	no patterning	possibility of patterning for $\mu < \mu_c^{crit}$
Substrate dependent cell death	no patterning	possibility of patterning for $\mu < \mu_s^{crit}$

Table 4.1: Table summarising the analytical results of Sections 4.6.1 and 4.6.2. When the possibility of patterning exists, the necessary conditions for patterning to occur are stated.

to decrease with increasing cell death rate.

In addition to determining the effect of cell death on biofilm height, our analysis also revealed the role of cell death in pattern formation (a summary of our results is given in Table 4.1). By analysing the evolution of non-planar perturbations to the non-trivial steady state, it was found that there is potential for spatial patterns to arise in deep biofilms, characterised by low levels of either constant or substrate dependent cell death. Moreover, the possibility of patterns evolving in shallow (early-stage) biofilms was ruled out. Experimental results have shown that during development, wildtype *B. subtilis* biofilms initially grow in height until reaching a critical thickness at which point vertical growth slows in lieu of horizontal expansion [134, 173]. It is also commonly observed that patterning occurs in mature (deep) biofilms [6, 18, 149]. Thus our analysis is in accordance with observed biological results.

Recent experimental observations by Asally et al. [6] showed that cell death focussed at the base of biofilms can induce patterning in biofilms. Interestingly, our analysis shows that biofilms subject to substrate dependent cell death at a certain rate μ could potentially exhibit pattern formation, whereas biofilms subject to constant cell death at the same rate are predicted to exhibit no pre-patterning behaviour. In summary, our analysis predicts that cell death focussed at the base of the biofilm is more likely to generate patterns, and is thus in line with the results of [6].

In conclusion, we propose that cell death may act as a precursor to patterning in biofilms by generating an instability within the biofilm. As in [6], we suggest that this patterning is likely to be further acted upon by other mechanisms at work in the biofilm in order to generate large-scale wrinkles. Biofilm models incorporating additional biological (in particular the role of EPS [59]) and mechanical processes, following similar approaches as explored in e.g. [48, 149], may provide a complementary understanding of biofilm pattern formation.

Chapter 5

An Elastic-Viscoelastic Approach to Wrinkle Formation

It is clear from experimental results that the physical and mechanical properties of biofilms play an important role in determining how biofilms develop. In the previous chapters, we neglected to include any mechanical properties in our description of biofilms and instead focussed on the specific biological processes that may instigate wrinkle formation, most notably cell death. In this chapter, the mechanics that are at play during biofilm formation is at the forefront of our investigation. Our aim is to determine whether an existing wrinkling model, which considers a purely mechanical approach to wrinkling and which is observed to give rise to remarkably similar patterns as observed within the coffee-ring structure of *Bacillus subtilis* biofilms, can be reasonably and realistically applied to the biofilm context.

5.1 Motivation of a Mechanical Approach to Biofilm Wrinkling

Deformation of materials occurs when they are subject to spatial constraints, intrinsic growth or external forces. Many different types of deformations are known to occur both in nature and in synthetic materials. For example, vehicles crumple in response to large impacts and the skin of apples wrinkle as the flesh dries out [21, 155].

We are interested in the wrinkling patterns that are observed in the coffee-ring structures of *Bacillus subtilis* biofilms. It is proposed that wrinkling patterns occur as a result of mechanical forces within the biofilm. The hypothesis is that as the bacterial cells multiply and the biofilm grows, stress builds up due to compression and must be relieved in some way. In Asally et al. [6], it was hypothesised, and backed up by experimental observations, that a buckling mechanism within the central coffee-ring of biofilms leads to the formation of wrinkles in this area. However, the model formulated did not take any physical mechanisms into account. Nevertheless, in recent years, several models describing the development of biofilms in terms of their physical and mechanical properties have been published. For example, see [1, 48, 149]. Wrinkling mechanisms in thin sheets have been more widely studied [21, 35, 74]. The wrinkling patterns that have been shown to develop in some cases are representative of the wrinkling patterns that emerge in biofilms. In particular, in some cases the wrinkling patterns that emerge in thin sheets lying on top of soft substrates closely resemble those wrinkles that develop in biofilms grown on agar. In some respects biofilms are physically comparable to thin sheets subject to external and internal forces. In particular we note that the height of both biofilms and thin sheets is small compared to other dimensions.

In this chapter we introduce a mechanical model presented by Huang and Im [76] and investigate whether it has any relevance to the biofilm wrinkling problem. We first summarise the analytical results presented by the authors. We then discuss parameter values describing the mechanical properties of biofilms. Finally we consider how the model set-up may relate to the biofilm structure and its growth conditions. We investigate how the wrinkling patterns observed in numerical simulations of different representations of the biofilm differ, and we compare the results with experimental observations to determine their varying degrees of accuracy in comparison to experimental results.

5.2 Model Set-up and Summary

Several papers by Huang and Im et. al investigate and describe the emergence and evolution of wrinkles in thin elastic sheets of thickness h_f, lying on top of softer substrates of height H, which in turn lie on rigid surfaces. In all cases, the elastic sheet is bonded to the softer substrate and the two layers are considered together as one single bilayer [75–79]. Note the bottom of the bilayer is bonded to the rigid surface upon which it lies. The models formulated describe the deformation of the bilayer as the thin elastic film is subjected to a constant compressive (negative) stress.

Numerical simulations of one model in particular showed striking similarities to the wrinkling patterns observed in the coffee-ring structures of *B. subtilis* biofilms. In [76, 79], the model formulated describes the soft substrate of height H as a viscoelastic material, and thus the bilayer is an elastic-viscoelastic bilayer. A schematic showing a cross-section of the model set-up can be seen in Figure 5.1.

In order to model the evolution of the bilayer in response to the compressive stress, the elastic and viscoelastic layers are considered separately. As the bilayer is bonded at the elastic-viscoelastic interface, the forces and displacements across this interface

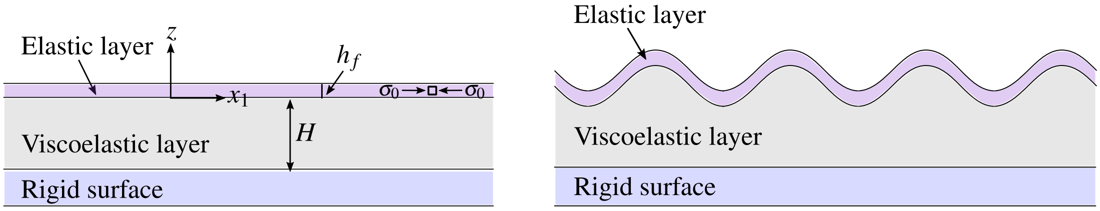

(a) Initial model set-up (b) Bilayer in a wrinkled state

Figure 5.1: Schematic of model set-up as described in [76, 79], where an elastic-viscoelastic bilayer is subject to compressive stress σ_0. Figure (a) shows the elastic-viscoelastic bilayer in the reference state. Figure (b) shows a possible wrinkle state occurring as a result of the applied compressive stress σ_0. H and h_f are the heights of the viscoelastic and elastic layers respectively.

must be continuous. This fact can then be used to couple the equations modelling the behaviour in the two separate layers into a single model which describes the deformation of the bilayer as a whole. A brief description of the equations used to describe the deformation in each of the two bilayer components is given below. A more detailed mechanical background describing elastic and viscoelastic materials and their governing equations can be found in Appendices A and B respectively, and thus we refer the reader here for further information.

5.2.1 Modelling of a Thin Elastic Film

The deformation of the thin elastic layer is modelled using the Föppl-von Kármán equations which describe the deformation of a plate lying in the x_1x_2-plane under an applied distributed lateral force, q, acting in the positive z-direction (see Appendix A.3 for more information about the derivation and meaning of these equations). In the case of pure bending, where only lateral loads (see Figure A.5(a)) are present and the deformation is so small that the middle plane of the plate can be considered to be unstressed and undeformed, the equation describing the lateral deflection of the plate is

$$
\begin{aligned}
& \frac{\partial^4 w}{\partial x_1^4} + \frac{\partial^4 w}{\partial x_2^4} + 2\frac{\partial^4 w}{\partial x_1^2 \partial x_2^2} = \frac{q}{D_f}, \\
\Longrightarrow \quad & \nabla^4 w(x_1, x_2) = \frac{q}{D_f} \quad \text{with} \quad D_f = \frac{E_f h_f^3}{12(1-\nu_f^2)},
\end{aligned}
\tag{5.1}
$$

where w is the out-of-plane displacement of the middle plane in the z-direction [147]. D_f is defined as the flexural rigidity of the plate which takes into account the physical properties, E_f (Young's modulus) and ν_f (Poisson's ratio), of the elastic film. High values of D_f correspond to plates that are more difficult to bend than those with lower values of D_f. An alternative constant to describe the physical properties of the plate is the shear modulus, $\mu_f = 6D_f(1-\nu_f)/h_f^3 = E_f/2(1+\nu_f)$, which is often denoted by G in the literature. The shear modulus is another measure of stiffness, and it can again be seen that higher values of μ_f corresponds to stiffer plates. The derivatives in equation (5.1) arise from strain equations measuring the elongations of the plate in the x_1 and x_2 (in-plane) directions as it bends, which in turn are measured using the curvature of the middle plane (see Appendix A.3.4).

Under axial stress, the middle plane of the elastic plate can no longer be assumed to remain unstressed and the resulting in-plane stresses of the middle plane must be incorporated into the plate equations (see [147] and Appendix A.3.6 for further details). Both normal ($\sigma_{\alpha\alpha}$) and shear ($\sigma_{\alpha\beta}$) in-plane stresses are considered (α and β take on the values of the in-plane coordinates, 1 and 2). Balancing these normal and shear stresses in the x_1 and x_2-directions, and taking into account their projection on the

w	out-of-plane displacement (deflection of plate in z-direction)
$\mathbf{u}$	in-plane displacement (u_i is displacement in the x_i-direction)
D_f	flexural rigidity of plate
q	normal traction at elastic-viscoelastic interface
N	in-plane membrane force
E_f	Young' modulus
ν_f	Poisson's ratio for elastic layer
h_f	height of elastic layer
$\varepsilon_{\alpha\beta}$	strain (non-linear to account for the relatively large deformations)
$\sigma^0_{\alpha\beta}$	initial stress applied to elastic layer (compressive stress $\therefore \sigma^0_{\alpha\beta} < 0$)

Table 5.1: Table of parameters and variables relevant to equations describing the deformation of elastic sheets (system (5.2)).

z-axis, the full equations for describing the deflection of the elastic sheet are:

$$\begin{aligned}
q &= -D_f\nabla^2\nabla^2 w^4 + N_{\alpha\beta}\frac{\partial^2 w}{\partial x_\alpha x_\beta} + \frac{\partial N_{\alpha\beta}}{\partial x_\beta}\frac{\partial w}{\partial x_\alpha}, \\
D_f &= \frac{E_f h_f^3}{12(1-\nu_f^2)}, \quad \left(\mu_f = \frac{6D_f(1-\nu_f)}{h_f^3}\right), \\
\sigma_{\alpha\beta} &= \sigma^0_{\alpha\beta} + \frac{E_f}{1-\nu_f^2}\left[(1-\nu_f)\varepsilon_{\alpha\beta} + \nu_f\varepsilon_{\gamma\gamma}\delta_{\alpha\beta}\right], \\
\varepsilon_{\alpha\beta} &= \frac{1}{2}\left(\frac{\partial u_\alpha}{\partial x_\beta} + \frac{\partial u_\beta}{\partial x_\alpha}\right) + \frac{1}{2}\frac{\partial w}{\partial x_\alpha}\frac{\partial w}{\partial x_\beta},
\end{aligned} \tag{5.2}$$

where $N_{\alpha\beta} = \sigma_{\alpha\beta}h_f$. The meaning of the parameters and variables used in system (5.2) are defined in Table 5.1. The subscripts α and β take on the values of the in-plane coordinates i.e. 1 or 2. The repeated Greek subscript γ represents summation over 1 and 2. The Kronecker delta, $\delta_{\alpha\beta}$, is defined by

$$\delta_{ij} = \begin{cases} 0 & \text{if } i \neq j, \\ 1 & \text{if } i = j. \end{cases}$$

Thus $\varepsilon_{\gamma\gamma}\delta_{12} = \varepsilon_{\gamma\gamma}\delta_{21} = 0$ and $\varepsilon_{\gamma\gamma}\delta_{11} = \varepsilon_{\gamma\gamma}\delta_{22} = \varepsilon_{11} + \varepsilon_{22}$.

Equations (5.2) are the Föppl-von Kármán equations which describe relatively large deflections in thin plates [93]. The deformation of an elastic plate under compression is, in general, difficult to analyse. However, it is possible that in the simplest cases of plate bending, where the in-plane forces $N_{\alpha\alpha}$ and $N_{\alpha\beta}$ are considered constant, the critical values of forces at which the flat equilibrium becomes unstable may be found [147]. The methods used to find these critical values and the corresponding buckling modes are similar to those used to determine buckling in beam-columns, described in Appendix A.2.

5.2.2 The Viscoelastic Component

The viscoelastic layer displays properties of both viscous and elastic materials on different time-scales. Unlike an elastic material, a viscoelastic material subjected to a constant applied stress over a period of time will display viscoelastic creep, with strain increasing in a time-dependent manner rather than remaining constant. On short time-scales the material can be thought of as behaving in an elastic manner, while on long time-scales the behaviour is more comparable to that of a viscous material [156]. The Kelvin model of linear viscoelasticity and a thin-layer approximation of the viscoelastic layer (where H^2 is considered negligible) is used to derive equations to describe the behaviour of the thin viscoelastic layer.

The normal and shear forces at the elastic-viscoelastic interface ($z = 0$) must be consistent; the normal stress $\sigma_{zz} = S_z$ while the shear stresses $\sigma_{z\alpha} = S_\alpha$, where S is the traction in the viscoelastic layer at $z = 0$. Similarly, the lower surface of the viscoelastic substrate is bonded to the rigid surface and therefore the displacements $u_\alpha(z = -H) = 0$

w	out-of-plane displacement (deflection of plate in z-direction)
$\mathbf{u}$	in-plane displacement (u_i is displacement in the x_i-direction)
$\mathbf{S}$	traction in the viscoelastic layer at $z = 0$
μ_R	shear modulus for viscoelastic layer at rubbery limit (long time-scales)
ν	Poisson's ratio for viscoelastic layer
η	viscosity of viscoelastic layer
H	height of viscoelastic layer

Table 5.2: Table of parameters relevant to equations (5.3) which describe the behaviour of a thin viscoelastic layer.

and $w(z=-H)=0$. The equations to describe the viscoelastic layer are derived as

$$\begin{aligned}\frac{\partial \mathbf{u}}{\partial t} &= \frac{H}{\eta}\mathbf{S} - \frac{\mu_R}{\eta}\mathbf{u},\\ \frac{\partial w}{\partial t} &= \frac{1-2\nu}{2(1-\nu)}\frac{H}{\eta}S_z - \frac{\mu_R}{\eta}w.\end{aligned} \tag{5.3}$$

Descriptions of the relevant parameters and variables are given in Table 5.2.

It is noted that μ_R, ν and η describe the physical properties of the viscoelastic layer. In particular, the rubbery modulus μ_R is the shear relaxation modulus at the long term rubbery limit, which gives a measure of the magnitude of stress required to maintain a constant deformation in a viscoelastic material at long time-scales. Large μ_R represents a stiff material, while small μ_R describes more flexible and compliant materials. A purely viscous material has $\mu_R = 0$ [156]. A viscoelastic material behaviour under compression will deform until reaching the rubbery state, at which point the material has reached its compliance limit.

5.2.3 The Coupling Of Layers To Form An Elastic-viscoelastic Bilayer

Combining the equations for the elastic and viscoelastic layer (equations (5.2) and (5.3)), and using the assumption of continuous traction and displacements at $z = 0$ and $z = -H$, the final equations used to describe the bilayer can be found as

$$\begin{aligned}
\frac{\partial w}{\partial t} &= \frac{1-2\nu}{2(1-\nu)}\frac{Hh_f}{\eta}\left[-\frac{\mu_f h_f^2}{6(1-\nu_f)}\nabla^2\nabla^2 w + \nabla\cdot(\sigma\cdot\nabla w)\right] - \frac{\mu_R}{\eta}w,\\
\frac{\partial \mathbf{u}}{\partial t} &= \frac{Hh_f}{\eta}\nabla\cdot\sigma - \frac{\mu_R}{\eta}\mathbf{u},\\
\sigma_{\alpha\beta} &= \sigma^0_{\alpha\beta} + 2\mu_f\left[\varepsilon_{\alpha\beta} + \frac{\nu_f}{1-\nu_f}\varepsilon_{\gamma\gamma}\delta_{\alpha\beta}\right],\\
\varepsilon_{\alpha\beta} &= \frac{1}{2}\left(\frac{\partial u_\alpha}{\partial x_\beta}+\frac{\partial u_\beta}{\partial x_\alpha}\right)+\frac{1}{2}\frac{\partial w}{\partial x_\alpha}\frac{\partial w}{\partial x_\beta}.
\end{aligned} \tag{5.4}$$

Descriptions of the relevant parameters and variables are given in Table 5.3. The same notation as described in Section 5.2.1 is used.

w	out-of-plane displacement (deflection in z-direction)
$\mathbf{u}$	in-plane displacement (u_i is displacement in the x_i-direction)
μ_f	shear modulus of elastic layer
ν_f	Poisson's ratio for elastic layer
μ_R	shear modulus for viscoelastic layer
ν	Poisson's ratio for viscoelastic layer at rubbery limit
η	viscosity of viscoelastic layer
H	height of viscoelastic layer
h_f	height of elastic layer
$\varepsilon_{\alpha\beta}$	in-plane strain components (non-linear)
$\sigma_{\alpha\beta}$	in-plane stress components
$\sigma^0_{\alpha\beta}$	stress applied to elastic layer (compressive stress $\therefore \sigma^0_{\alpha\beta} < 0$)

Table 5.3: Table of parameters relevant to equations (5.4) which describe the behaviour of an elastic-viscoelastic bilayer in response to a compressive stress, σ_0, applied to the elastic layer.

In general we comment on the fact that the time derivatives in the model stem from the viscoelastic assumptions applied to the bottom layer, while the space derivatives arise as a consequence of the elastic plate equations describing relatively large deformations i.e. the Föppl-von Kármán equations. Thus the presence of the viscoelastic component allows the evolution of the bilayer to be tracked.

5.2.4 Non-dimensionalisation

On the application of an appropriate non-dimensionalisation, the number of controlling parameters in system (5.4) can be reduced. By setting

$$W = \frac{w}{h_f}, \quad \mathbf{U} = \frac{\mathbf{u}}{h_f}, \quad \mathbf{X} = \frac{\mathbf{x}}{h_f}, \quad T = \frac{\mu_f}{\eta} t, \quad \bar{\sigma} = \frac{\sigma}{\mu_f},$$

and introducing the parameter groupings

$$h_{rat} = \frac{H}{h_f}, \quad \mu_{rat} = \frac{\mu_R}{\mu_f},$$

system (5.4) can be rewritten in the following non-dimensional form:

$$\begin{aligned}
\frac{\partial W}{\partial T} &= \frac{1-2\nu}{2(1-\nu)} h_{rat} \left[-\frac{1}{6(1-\nu_f)} \nabla^2 \nabla^2 W + \nabla \cdot (\bar{\sigma} \cdot \nabla W) \right] - \mu_{rat} W, \\
\frac{\partial \mathbf{U}}{\partial T} &= h_{rat} \nabla \cdot \bar{\sigma} - \mu_{rat} \mathbf{U}, \\
\bar{\sigma}_{\alpha\beta} &= \bar{\sigma}^0_{\alpha\beta} + 2 \left[\bar{\varepsilon}_{\alpha\beta} + \frac{\nu_f}{1-\nu_f} \bar{\varepsilon}_{\gamma\gamma} \delta_{\alpha\beta} \right], \\
\bar{\varepsilon}_{\alpha\beta} &= \frac{1}{2} \left(\frac{\partial U_\alpha}{\partial X_\beta} + \frac{\partial U_\beta}{\partial X_\alpha} \right) + \frac{1}{2} \frac{\partial W}{\partial X_\alpha} \frac{\partial W}{\partial X_\beta}.
\end{aligned} \tag{5.5}$$

The parameter grouping h_{rat} measures the ratio of the height of the viscoelastic layer in comparison to the height of the elastic layer. In the model set-up it is assumed that

$H > h_f$, and thus $h_{rat} > 1$. The ratio of the rubbery modulus to the shear modulus of the elastic layer is given by μ_{rat}. This value provides a comparative measure of the stiffnesses of the viscoelastic and elastic layers, assuming the viscoelastic layer is at its maximum possible compliance, and thus can be thought of as giving a measure of the substrate elasticity.

5.3 Stages of Wrinkle Development: Analytical Results

Through the use of a scaling analysis approach, Huang and Im [76] identified that the evolution of wrinkles described by equation (5.4) could be split into three distinct stages; initial growth of wrinkles, coarsening of wrinkles, and finally equilibration of wrinkles. We outline their findings here, and use their results in our consideration of the biofilm context later.

5.3.1 Initial Growth

The initial growth stage considers the case where the in-plane stress in the elastic layer can be approximated by its initial (non-dimensional) value, $\bar{\sigma}_0$. At this early stage in the wrinkling process, the relaxation of stresses has only just commenced. A linear perturbation analysis, assuming a small sinusoidal perturbation in the thin elastic layer, allows both a critical and fastest growing (non-dimensional) wrinkle wavelength to be calculated, $\bar{\lambda}_c$ and $\bar{\lambda}_m$ respectively. In order that the elastic film becomes unstable, it is required that the wavelength of developing wrinkles, $\bar{\lambda}$, satisfies the condition $\bar{\lambda} > \bar{\lambda}_c$. Substrate elasticity, taken into account in the value of μ_{rat}, plays a role in suppressing the wrinkling instability by restricting the amount of compliance that the viscoelastic layer can exhibit. A (non-dimensional) critical stress, $\bar{\sigma}_c$, determines the value at which stress dominates and overpowers the substrate elasticity, and therefore it is expected that wrinkles may form for $\bar{\sigma}_0 > \bar{\sigma}_c$. The values of the (non-dimensional) critical stress, $\bar{\sigma}_c$, and critical wavelength, $\bar{\lambda}_c$, are:

$$\begin{aligned} \bar{\sigma}_c &= -\sqrt{\frac{4(1-\nu)}{3(1-2\nu)(1-\nu_f)}\frac{\mu_{rat}}{h_{rat}}}, \\ \bar{\lambda}_c &= 2\pi\sqrt{\frac{-1}{6(1-\nu_f)\bar{\sigma}_0}}. \end{aligned} \tag{5.6}$$

It is important to note that in this initial stage of development the stress within the elastic film is relaxed solely by increasing wrinkle amplitude; wrinkle wavelength remains constant.

5.3.2 Coarsening of Wrinkles

The second stage of wrinkle development that occurs in model (5.5) is coarsening. This describes the stage where wrinkles have reached an amplitude comparable to the thickness of the film. In this phase of development the linear approximation, as used in the initial growth stage, is no longer valid and thus the non-linear effects of the large deflections must be considered. If the substrate can be considered as viscous ($\mu_R = 0$), it is found that a spatially uniform (non-dimensional) stress, $\bar{\sigma}_k$, in the elastic film is inversely proportional to the square of the wrinkle wavelength (see equation (5.7)). Therefore an increase in wavelength, $\bar{\lambda}$, can help to decrease the stress within the film and relax it. This increase in the wrinkle wavelength is called coarsening. The corresponding (non-dimensional) wrinkle amplitude at this stage is given by $\bar{A}_k$ (see equation (5.7)) where $\bar{\lambda}_c$ is defined from equation (5.6). We have:

$$\begin{aligned} \bar{\sigma}_k &= -\frac{2\pi^2}{3(1-\nu_f)\bar{\lambda}^2}, \\ \bar{A}_k &= \sqrt{\frac{1}{3}\left(\frac{\bar{\lambda}^2}{\bar{\lambda}_c^2}-1\right)}. \end{aligned} \tag{5.7}$$

It can be seen that in this stage of development, wrinkle wavelength and amplitude both grow over time. This differs from the initial gowth stage where it was shown, by Huang and Im [76], that amplitude increased but wavelength remained constant.

5.3.3 Wrinkle Equilibrium

The final stage of wrinkle evolution only occurs in cases where the substrate elasticity is not equal to zero ($\mu_R \neq 0$). At this stage the viscoelastic layer has reached its relaxation limit and is as soft and compliant as is possible. The amplitude and wavelength of the wrinkles that can form in the bilayer are therefore limited. Energy minimisation calculations show that at this stage of development, stress in the bilayer becomes stabilised at an equilibrium wavelength, $\bar{\lambda}_{eq}$, and a corresponding equilibrium amplitude, $\bar{A}_{eq}$. As a result, on reaching the equilibrium stage, wrinkles no longer evolve. Expressions for the (non-dimensional) equilibrium wavelength, $\bar{\lambda}_{eq}$ and amplitude, $\bar{A}_{eq}$, are

$$\begin{aligned} \bar{\lambda}_{eq} &= 2\pi \left(\frac{(1-2\nu)}{12(1-\nu)(1-\nu_f)} \frac{h_{rat}}{\mu_{rat}} \right)^{1/4}, \\ \bar{A}_{eq} &= \sqrt{\frac{2}{3}\left(\frac{\bar{\sigma}_0}{\bar{\sigma}_c} - 1\right)}, \end{aligned} \tag{5.8}$$

where $\bar{\sigma}_c$ is defined by equation (5.6). We find

$$\frac{\partial \bar{\lambda}_{eq}}{\partial \nu} < 0, \quad \frac{\partial \bar{\lambda}_{eq}}{\partial \nu_f} > 0, \quad \frac{\partial \bar{\lambda}_{eq}}{\partial h_{rat}} > 0, \quad \frac{\partial \bar{\lambda}_{eq}}{\partial \mu_{rat}} < 0, \tag{5.9}$$

and

$$\frac{\partial \bar{A}_{eq}}{\partial \nu} < 0, \quad \frac{\partial \bar{A}_{eq}}{\partial \nu_f} < 0, \quad \frac{\partial \bar{A}_{eq}}{\partial h_{rat}} > 0, \quad \frac{\partial \bar{A}_{eq}}{\partial \mu_{rat}} < 0, \quad \frac{\partial \bar{A}_{eq}}{\partial |\bar{\sigma}_c|} < 0, \quad \frac{\partial \bar{A}_{eq}}{\partial |\bar{\sigma}_0|} > 0. \tag{5.10}$$

It is noted that a viscous substrate does not have a rubbery limit ($\mu_R = 0$) and as such stores no elastic energy. Therefore, wrinkles in an elastic-viscous bilayer continue to evolve in the coarsening phase [78]. Wrinkle amplitude is, however, limited by height H. Where wrinkles exceed amplitude H, the viscous substrate no longer remains bonded to the rigid surface, and thus the model is no longer valid.

5.4 Wrinkling Morphologies

Before applying system (5.5) to the biofilm context, we briefly describe some of the different wrinkling morphologies that have been demonstrated to arise from model (5.5). Some examples of the different types of patterning that may develop are shown in Figure 5.2. In all numerical simulations of system (5.5) we implement periodic boundary conditions and a small random initial condition on W (the non-dimensional height of wrinkles).

5.4.1 Uniaxial Stress Patterns

Uniaxial stress describes the case where only one component of normal stress acts along two opposite sides of the elastic film (the other two edges of the film are free from normal stress). For a compressive stress acting normal to the X_1-axis this corresponds to $\bar{\sigma}_{11} < 0$, with all other stress components set to zero. In this case, energy is minimised by stress being relieved in only one in-plane direction (the X_1-direction). Consquently, wrinkles develop perpendicular to the direction of the applied normal stress in a stripe formation (see Figure 5.2(a)).

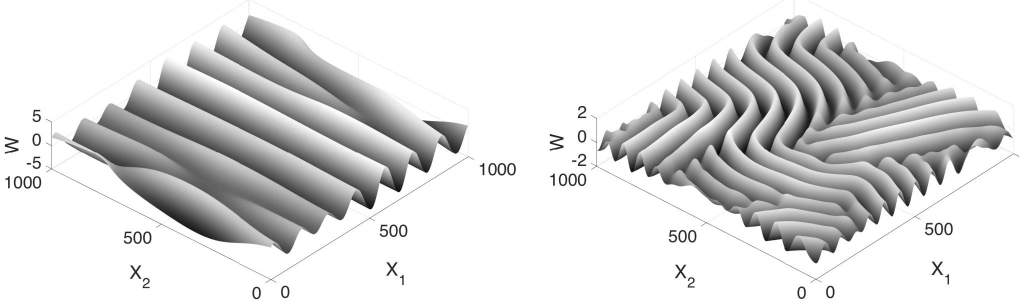

(a) Uniaxial stress stripe pattern

(b) Equibiaxial stress labyrinth pattern

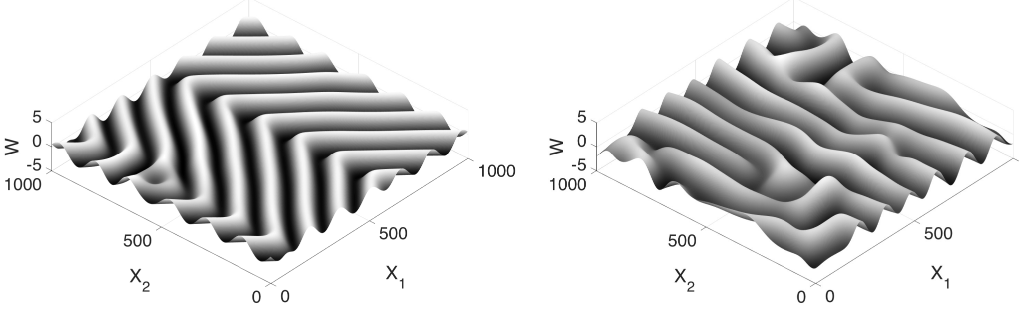

(c) Herringbone pattern

(d) Biased axial stress pattern

Figure 5.2: Examples of the different wrinkling morphologies produced by numerical simulation of the bilayer described by system (5.5), under different stress conditions. Figure (a): Stripe formation at $T = 10^7$. Parameter values are $\nu = 0.45$, $\nu_f = 0.3$, $h_{rat} = 10$, $\mu_{rat} = 0$, $\bar{\sigma}_{11}^0 = -0.01$, $\bar{\sigma}_{22}^0 = 0$, $\bar{\sigma}_{12}^0 = \bar{\sigma}_{21}^0 = 0$. Figure (b): Labyrinth at $T = 10^8$. Parameter values are $\mu_{rat} = 10^{-5}$, $\bar{\sigma}_{11}^0 = \bar{\sigma}_{22}^0 = -0.005$. Figure (c): Herringbone pattern at $T = 10^8$, with $\nu = 0.2$, $\nu_f = 0.45$, $\mu_{rat} = 10^{-5}$. Figure (d): Biased biaxial stress pattern at $T = 10^7$ for $\bar{\sigma}_{11}^0 = -0.005$ and $\bar{\sigma}_{22}^0 = -0.002$. In Figures (b)-(d), parameter values that are not explicitly defined are the same as used in Figure (a). Periodic boundary conditions are implemented, and a small random initial condition is applied to W. All other initial conditions are set to zero. Numerical simulations were run in COMSOL and data exported to MATLAB for plotting.

5.4.2 Equibiaxial Stress Patterns

Equibiaxial stress describes the case where equal stress is applied in the normal direction along all four edges of the bilayer, i.e. $\bar{\sigma}_{11} = \bar{\sigma}_{22} \neq 0$. Where the normal stresses are compressive, the energy in the plate is minimised by relieving the stress in both the X_1 and X_2-directions as well as the Z-direction. The resulting wrinkle pattern is a maze-like configuration of wrinkles called a labyrinth pattern (see Figure 5.2(b)).

A bilayer as described in the model set-up can in some cases of equibiaxial stress display zig-zag-like wrinkle patterns called herringbone patterns, as seen in Figure 5.2(c). Like labyrinth patterns, herringbones relieve compression in both directions. In fact both patterns contain the same amount of energy, and thus it may be said that a herringbone is really just an ordered arrangement of the more common labyrinth configuration [78].

5.4.3 Biased Axial Stress Patterns

In the case of normal compressive stress that is biased in one direction i.e. $|\bar{\sigma}_{11}| > |\bar{\sigma}_{22}|$, stress is relieved in both the X_1 and X_2-directions. However the amount of stress relaxation that occurs in each direction is unequal. Where $|\bar{\sigma}_{11}| \gg |\bar{\sigma}_{22}|$, a stripe pattern with nearly parallel stripes forms perpendicular to the X_2-axis. As the difference between $\bar{\sigma}_{11}$ and $\bar{\sigma}_{22}$ decreases, a more labyrinth-like unbiased wrinkle pattern forms. The wrinkling pattern that is established is therefore a balance between the pattern that develops for uniaxial stress in the X_1-direction (see Figure 5.2(a)) and the labyrinth pattern that develops for equibiaxial stress (see Figure 5.2(b)). An overall pattern of stripes perpendicular to the X_2-axis can be observed, however the domain displays some regions where the patterning is more disordered and labyrinth like. Figure 5.2(d) shows an example of the wrinkling pattern that may be produced in the presence of biased biaxial stress.

5.4.4 The Resemblance of Wrinkling Morphologies to Patterns Observed in Biofilms

In relation to the biofilm problem, it can be seen that the wrinkling patterns displayed in labyrinth patterns of equibiaxially stressed films show remarkable similarities to the wrinkling patterns observed in the coffee-rings of *B. subtilis* biofilms (compare, for example, Figures 2.1(c) and 5.2(b)). It seems plausible that a biofilm left to grow on an agar substrate without the addition of any external pressures would be subject to approximately equal stresses throughout. We hypothesise that these stresses would be directed towards the centre of the biofilm, as compressive forces accumulate in the coffee-ring region as a result of the biofilm growing and the bacterial cells becoming more spatially constrained. We suggest that this hypothesis may be particularly relevant within the coffee-ring region for two reasons. Firstly, we suggest that contraction within the biofilm as it begins to dry may result in a focussing of forces directed towards the centre. Secondly, the coffee-ring appears to act as a barrier between the two regions inside and outside of it. Thus we assume spatial constraints are greater inside the coffee-ring, compared to outside, as movement of bacteria is limited. Patterning resulting from the presence of compressive equibiaxial normal forces are our focus in the next part of this chapter.

As an aside, we note that other types of patterns developing in bilayers subject to different types of compression are also observed to show some similarities to biofilms grown in different conditions. Specifically, we note that the stripe formation in uniaxially compressed bilayers share similar characteristics with the radial wrinkles observed in *B. subtilis* biofilms in the region outside of the coffee-ring (see Figure 2.1(b)). In

[149], the wrinkling patterns of *B. subtilis* pellicles in confined geometries is investigated. It is found that rectangular pellicles confined at two opposite ends form wrinkles approximately parallel to the direction of confinement, similar to those observed in the case of biaxial compression as seen in Figure 5.2(d). Indeed in this paper, the authors implement a mechanical approach, similar to that described in section 5.2.1, to model the pellicle as an elastic sheet under compression.

5.5 Application of Model to the Biofilm Context

Having summarised the model set-up, derivation and resulting wrinkle morphologies that may arise as a result of the model proposed by Huang and Im [76], we now investigate whether this model may be a useful tool to model wrinkling in biofilms, specifically those grown on agar. We discuss the relevance of the model in two different representative scenarios: (1) the elastic-viscoelastic bilayer representing a thin elastic biofilm growing on a thicker viscoelastic substrate and (2) the elastic-viscoelastic bilayer representing two different component parts of the biofilm.

5.5.1 Parameter Estimates of Biofilms

First, in order that we may relate the model to the biofilm context, it is necessary to compile a list of known mechanical and physical properties of biofilms and agar substrates. The subscripts $_b$ and $_a$ in this section are used to denote typical values in biofilms and agar respectively.

Experimental results have shown that the typical height of a mature wildtype *B. subtilis* biofilm is of the order $10^2\,\mu\text{m}$ [161, 162, 168, 173]. Furthermore, experimental results have also shown that during development, wildtype *B. subtilis* biofilms initially grow in height until reaching a critical thickness upon which EPS production is increased due to a lack of nutrients, at which point vertical growth slows in lieu of horizontal expansion [134, 173]. As our analysis considers the central coffee-ring region of the biofilm (which is far from the expanding outer edge in mature biofilms), we assume that biofilm height in this region remains approximately constant upon the triggering of horizontal expansion and thus reaches a quasi-steady state.

As previously noted in Chapter 4, biofilm height and the characteristic length of patterns are generally of the same order of approximately $10^2\,\mu\text{m}$. For a more accurate measurement of the characteristic wavelength of wrinkles in the types of biofilms we are focussed on, we use ImageJ software to highlight (see Figure 5.3) and measure the approximate wrinkle width of *B. subtilis* biofilms grown on 1.5% agar, from a series of photographs. Each photograph shows a biofilm of the same bacterial strain grown in identical environmental conditions, and each measurement is taken from a wrinkle located in the coffee-ring region. The mean wrinkle width in a mature wildtype biofilm is calculated to be approximately $150\,\mu\text{m}$. Assuming that the wrinkle wavelength is double the wrinkle width, we estimate the typical wrinkle wavelength in mature *B. subtilis* biofilms as $\lambda_{av} \approx 300\,\mu\text{m}$, which is in good agreement with the estimate given above.

The mechanical properties relating to biofilms can be more problematic to ascertain. Nevertheless, the literature does provide us with some estimates of these values. Recall in Chapter 4, we considered the biofilm as a perfectly incompressible material with Poisson's ratio $\nu_b = 0.5$. In [8, 94, 132, 149], estimates for Poisson's ratio of biofilms range from $\nu_b = 0.4$ to $\nu_b = 0.5$.

Biofilms have, in the literature, been described as both elastic and viscoelastic materials. For example, in [149], biofilm pellicles are described as behaving like 'growing elastic plates' while in [88], biofilms are described in a viscoelastic manner. Estimates

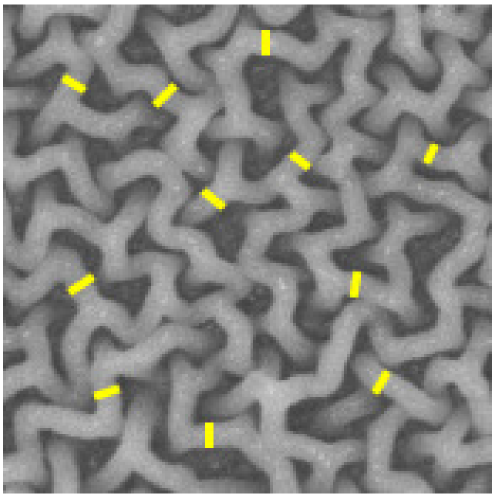

Figure 5.3: Example of typical width of wrinkles in coffee-ring area of a mature $(t = 48\,\mathrm{h})$ *B. subtilis* biofilm grown on agar. Examples of several widths are highlighted in yellow. Each highlighted width was measured using ImageJ software, and the mean width was calculated. The area of the biofilm region shown is $2.5\,\mathrm{mm} \times 2.5\,\mathrm{mm}$. Photograph courtesy of L. Li.

for the Young's modulus of biofilms vary hugely, differing by several orders of magnitude (estimated values vary from order $10-10^5$ Pa [66]). In [6], it is estimated that wildtype *B. subtilis* biofilms (grown on agar) have a Young's modulus towards the upper end of this scale, with measurements suggesting $E_b \approx 25\,\mathrm{kPa}$. Estimates for the viscosity and shear modulus of biofilms grown *in vitro* are also highly variable: viscosity, η_b, and shear modulus, G_b, of the biofilm range from 10^1-10^5 Pa s and 10^5-10^8 Pa respectively [68].

In comparison to biofilms, which have in different contexts been interpreted as both elastic and viscoelastic materials, it is generally accepted that agar displays viscoelastic behaviour [118]. The mechanical properties of the agar vary depending on the agar composition [48]. For example, as agar concentration increases the substrate becomes stiffer (higher Young's modulus and shear modulus) [108]. Typical reported values of Young's moduli range from $E_a = 27\,\mathrm{kPa} - 52\,\mathrm{kPa}$, while typical reported values of Poisson's ratio range from $\nu_a = 0.32 - 0.5$ [48].

Another relevant parameter is the height of the agar substrate used in experiments. Standard laboratory practice for growing bacterial cultures involves filling petri dishes with agar to a depth of a few millimetres, and thus we assume agar height is of O(1 mm).

5.5.2 Biofilm/Agar as an Elastic-viscoelastic Bilayer

In our first application of system (5.5) to the biofilm context, we assume the elastic-viscoelastic bilayer set-up represents an elastic biofilm growing on a viscoelastic agar substrate. As noted in section 5.5.1, the elastic properties of biofilms and the viscoelastic properties of agar have been documented. In addition, it has been shown in laboratory experiments that a biofilm may be separated from the agar substrate on which it grows by gently peeling it away. Upon the biofilm's removal, it is observed that a shallow but detailed imprint remains in the agar surface [168]. The presence of this agar deformation indicates that biofilm development alters and affects the structure of the agar, and thus it seems reasonable that we treat the bioilm and agar as a bilayer that is bonded continuously across their shared interface.

As an initial test to determine if the above assumptions may be realistic, we consider the wavelengths of patterns that form in biofilms of different stiffnesses. Increasing values of μ_f and decreasing values of μ_{rat} characterise biofilms of increasing stiffness. As $\partial\bar{\lambda}_{eq}/\partial\mu_{rat} < 0$, this corresponds to stiffer biofilms showing increased wavelengths at equilibrium. This is in agreement with results in [6], that show a positive correlation between biofilm stiffness and wrinkle wavelength exists.

In our investigation of the relevance of system (5.5) to a biofilm-agar complex, we consider four separate cases in turn (see Figure 5.4). These cases are:

1. The elastic-viscoelastic bilayer consists of the complete depth of the biofilm and

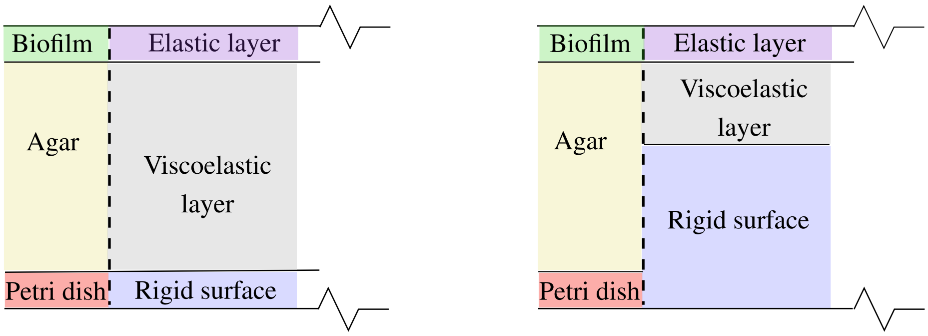

(a) Case A set-up

(b) Case B set-up

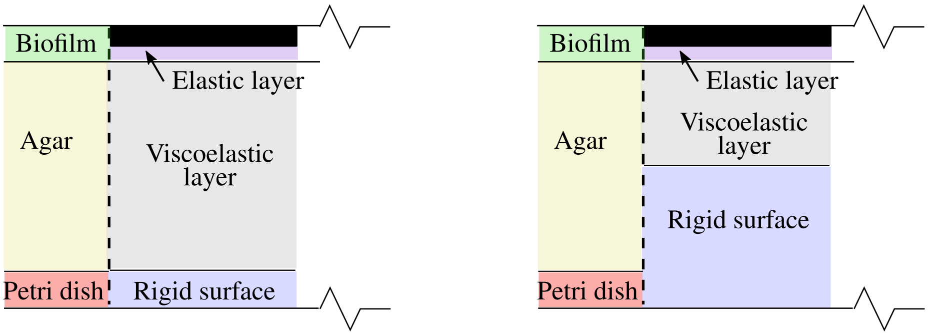

(c) Case C set-up

(d) Case D set-up

Figure 5.4: Schematic showing the different set-ups considered in relation to the application of an elastic-viscoelastic bilayer used to describe a biofilm growing on an agar substrate. Figures (a)-(d) represent Cases A-D as described in section 5.5.2, respectively. The left of each figure shows a cross-section of the biofilm-agar complex. The right of each figure shows the depth scales over which we consider each of the component parts of the bilayer to cover. The black areas representing the top parts of the biofilm in Figures (c) and (d) are ignored in our consideration of these cases.

the complete depth of the agar (see Figure 5.4(a)).

2. The elastic-viscoelastic bilayer represents the complete depth of the biofilm (elastic layer), but only a partial depth of the agar (viscoelastic) layer (see Figure 5.4(b)).

3. The elastic component of the bilayer represents the bottommost slice of a biofilm, while the viscoelastic layer represents the complete depth of the agar substrate (see Figure 5.4(c)).

4. The elastic-viscoelastic substrate is represented by only partial segments of the agar and biofilm (see Figure 5.4(d)).

Case A:

The first case considered assumes that the full depth of agar substrate is affected by biofilm growth and development, and that the complete depth of the biofilm exhibits elastic behaviour. This set-up is illustrated in Figure 5.4(a). Referring to parameter values in section 5.5.1, it can be seen that biofilm height and wrinkle wavelength are of the same order of magnitude. This creates a complication by throwing into doubt the suitability of system (5.5) to model this biological set-up. In general, the Föppl-von Kármán equations are applied to thin plates undergoing relatively large deformations that are not small in comparison to the plate's height but that are small in comparison to the plate's length. In addition, the wavelength of patterns that accompany deformations are assumed to be large in comparison to the height of the plate. For wavelengths of the same order of magnitude of the height, the usefulness of the Föppl-von Kármán equations is limited [101]. Indeed, the wavelength of wrinkles that emerge in numerical simulations (not shown here) using biologically relevant parameters is greatly overestimated in comparison to the wrinkle wavelengths observed in experimental results. Thus we conclude that it is ineffectual to use system (5.5) to describe the biological set-up in this case.

Case B:

In [168] it was noted that the imprint left by a biofilm on an agar substrate was shallow. We use this fact to conjecture that only the topmost section of the agar substrate contributes to, and is affected by, the wrinkling process that occurs during the growth of biofilms. Accordingly, we take into account only the upper segment of agar (nearest the biofilm-agar interface) in our representation of the problem (see Figure 5.4(b)). The rest of the agar is considered to be physically unaffected by biofilm growth, showing no relaxation, deformation or displacement, and may be thought of as being part of the rigid surface to which the viscoelastic layer is attached. As in Case A, height h_f and wrinkle wavelength observed in biofilms are of the same order of magnitude. Thus we question the model's ability to produce accurate results in this case. Simulation results (not included here) again show that wrinkle wavelength is significantly overestimated by the model, in comparison to experimental results.

Case C:

In [149], a mechanical model implementing the Föppl-von Kármán plate equations was used to model wrinkling in *B. subtilis* pellicles. It was noted by the authors, that the proposed model in this paper overestimated the wavelength of wrinkle patterns in comparison to those observed in real life. In order that patterns on a true length scale could be observed, it was necessary to assume that only a thin layer within the pellicle was governed by the specified plate equations. We use this hypothesis in the next case we consider. We assume that only a thin elastic layer within the biofilm is involved in the mechanical response to stress, and that this layer lies at the bottom of the biofilm at the biofilm-agar interface. While the top portion of the biofilm responds to the displacements in the bottom layer to which it is bonded, it is not actively involved in the relaxation of stresses. Under these assumptions, h_f is decreased in comparison to H (i.e. h_{rat} is greater than in Cases A and B above). As the height of the effective elastic plate is reduced while the observed wrinkle wavelength remains the same, the suitability of the application of the Föppl-von Kármán equations to describe the biofilm layer is restored. For example, assuming that $h_f = 10\,\mu\text{m}$, wrinkle wavelengths of the desired order $\lambda = O(100\,\mu\text{m})$ can reasonably be described using the elastic plate equations. However, as h_{rat} is increased the thin layer approximation used to describe the viscoelastic layer begins to break down. Assuming the partial segment of biofilm considered is of order $h_f = \mathrm{O}(10\,\mu\text{m})$, and the depth of the agar of order $H = \mathrm{O}(1\,\text{mm})$, then $h_{rat} = \mathrm{O}(100)$. The thin layer viscoelastic assumption will no longer hold at these values and thus system (5.5) cannot be reasonably applied to this case.

Case D:

In this case we use a combination of the assumptions specified in Cases B and C above, and consider the elastic-viscoelastic bilayer as only a partial component of the biofim-agar complex. We suggest that a small elastic layer at the bottom of the biofilm bonded to the top of the agar substrate constitutes the mechanical bilayer that controls the wrinkling process (see Figure 5.4(d)). Assuming the ratio of biofilm to agar depth in the active bilayer remains the same as in the real life set-up we take $h_{rat} = \mathrm{O}(10)$. While it is difficult to make assumptions as to the depth of this active bilayer, we know that the plate equations best describe deformations up to the same order of magnitude as the plate's height. Similarly we know that wrinkle wavelength should be an order of magnitude higher than the height of the elastic layer. Using these guidelines, we assume $h_f = \mathrm{O}(10\,\mu\text{m})$, $H = \mathrm{O}(100\,\mu\text{m})$ and $\lambda = \mathrm{O}(100\,\mu\text{m})$. Numerical simulation results, implementing periodic boundary conditions to represent the repeating nature of the biofilm patterning, show that biologically realistic results can arise when implementing model (5.5) to describe wrinkling in Case D. For example, compare the results shown in Figure 5.5, particularly Figure 5.5(d), with the wrinkle pattern observed on an equivalent domain shown in Figure 5.3. Measurement of wrinkles in ImageJ determines an approximate simulation wrinkle width of $90\,\mu\text{m}$, and wrinkle wavelength of $180\,\mu\text{m}$.

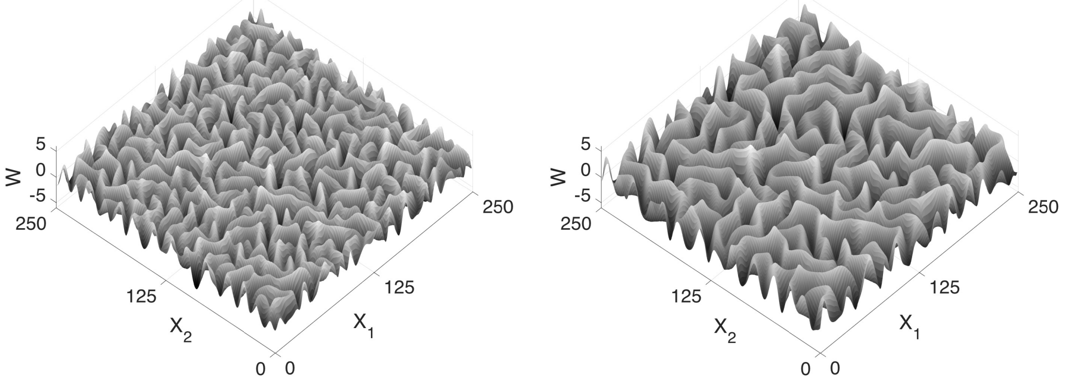

(a) $T = 100$ (side-view)

(b) $T = 500$ (side-view)

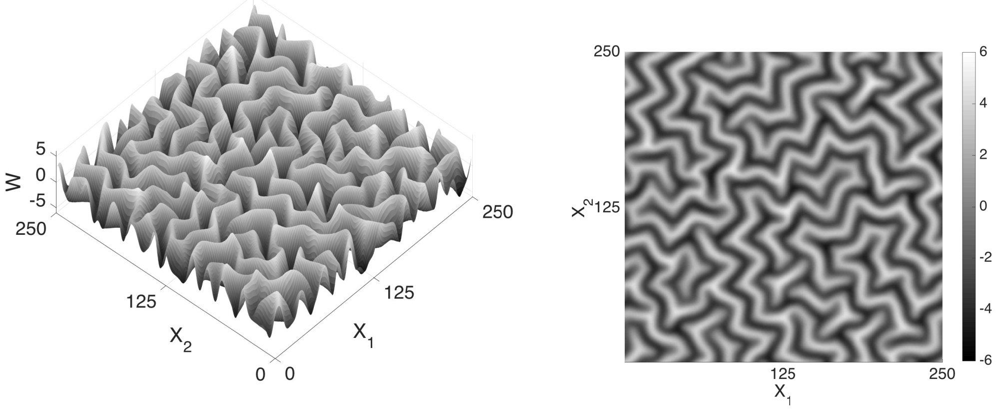

(c) $T = 5000$ (side-view)

(d) $T = 5000$ (top-view)

Figure 5.5: Numerical simulation of the evolution of an elastic-viscoelastic bilayer (equation (5.5)) representing Case D: a partial component of the biofilm-agar complex. Domain represents a square measuring $2.5\,\mathrm{mm} \times 2.5\,\mathrm{mm}$, as seen in Figure 5.3. Figures (a)-(c) show side-views of wrinkling patterns (deflection W) at times $T = 100, 500, 5000$ respectively. Figure (d) shows top-view of wrinkling pattern (deflection W) at $T = 5000$, when equilibrium has been reached. Parameters values are $h_{rat} = 10$, $\mu_{rat} = 0.01$, $\nu_f = 0.45$, $\nu = 0.4$, $\bar{\sigma}^0_{11} = \bar{\sigma}^0_{22} = -0.7$. Periodic boundary conditions and a small random initial condition for W are used.

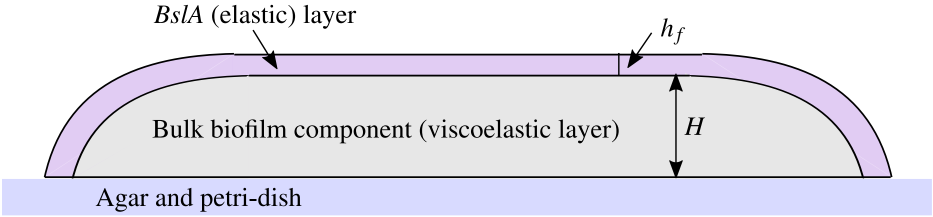

Figure 5.6: Schematic showing the set-up for system (5.5) applied to a biofilm represented by a bulk viscoelastic component coated with a thin *BslA* elastic layer.

In all of the above cases it has been assumed that the biofilm remains bonded to the agar throughout development. However, it has been shown in [168] that channels form under the wrinkles, and it is hypothesised that these channels contain water drawn from the agar substrate. Thus in the above cases, our assumption of a bonded interface between the agar and biofilm must also assume that the water channels and agar act as a single component. While it is true that the composition of agar is mostly water, it is unclear whether the differing mechanical properties of water and agar make this a realistic assumption. However, if we do not assume that the agar and water act as a single component, then it follows that the elastic-viscoelastic bilayer becomes delaminated at the rigid surface, and thus model (5.5) cannot be applied.

5.5.3 *BslA* Coating as an Elastic Layer on a Viscoelastic Biofilm

It is clear that the representation of a biofilm-agar complex as an elastic-viscoelastic bilayer has some drawbacks. As an alternative approach we now consider that the bilayer may describe two different component parts of the biofilm structure. The recent discovery of a hydrophobic coating at the interfaces of *B. subtilis* biofilms has been found to contribute to their non-wetting properties [72]. The coating, referred to as a 'hydrophobic cap' or 'raincoat' in the literature, is composed of a small secreted protein, *BslA* (or Biofilm Surface Layer protein A), and surrounds the bacterial cells preventing external material such as water and biocides from penetrating into the bacterial community [5, 72].

Experimental imaging has shown that this hydrophobic protective layer extends from the outer periphery of the biofilm into a depth of around 4 µm [72]. In addition the material properties of the layer suggest that it is an elastic film [72]. Recalling the viscoelastic properties of biofilms (see Section 5.5.1), and noting the elastic properties of the *BslA* layer, we suggest that the deformation of an elastic-viscoelastic bilayer set-up, as shown in Figure 5.1, could potentially describe the deformation of a biofilm grown on agar if the biofilm is considered as comprising a viscoelastic bulk, of height H, coated by a thin elastic *BslA* layer of height h_f (see Figure 5.6). While experimental imaging has shown that *BslA* forms at both the cell-air and agar-cell interfaces on a *B. subtilis* biofilm grown on agar, the protein has been determined as being more concentrated at the cell-air interface [72]. For this reason we assume that the less concentrated *BslA* layer at the agar-cell interface behaves more like the bulk viscoelastic biofilm, with which it is interspersed, rather than a separate elastic component. We note that in this set-up we assume that the rigid surface, upon which the elastic-viscoelastic bilayer lies, comprises both the petri-dish and the agar substrate upon which the biofilm is grown.

Assuming a biofilm depth of approximately 100 µm, of which the topmost *BslA* layer constitutes approximately 5 µm, we set $h_{rat} = 20$. Choosing parameters within the biologically relevant ranges summarised in Section 5.5.1, we find that wrinkling patterns with the same physical properties as observed in *B. subtilis* biofilms can arise from system (5.5), as seen in Figure 5.7 (note that periodic boundary conditions are again implemented to represent the repeating nature of the biofilm patterning). For example, measuring the wavelength from the numerical simulation results seen in Figure 5.7 (again using ImageJ software) we find that patterns have a wrinkle width and wavelength of approximately 120 µm and 240 µm respectively, which is in reasonable agreement with the real life measurements of wrinkle width ≈ 150 µm and $\lambda_{av} \approx 300$ µm. In

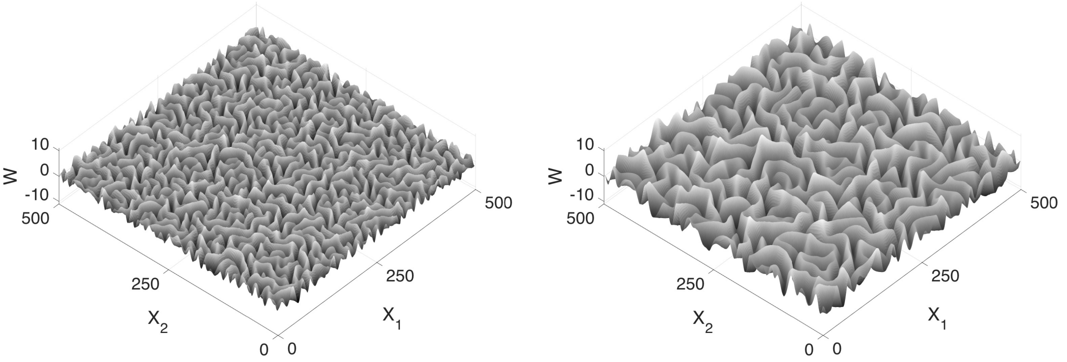

(a) $T = 100$ (side-view)

(b) $T = 500$ (side-view)

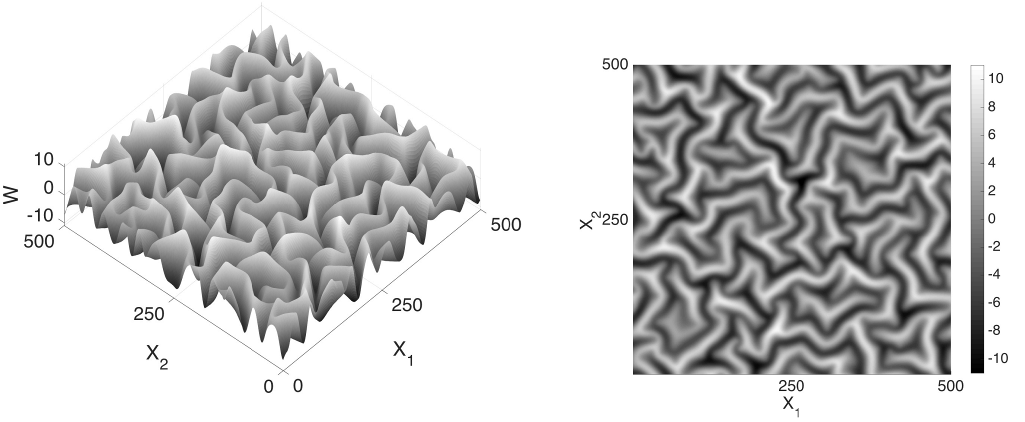

(c) $T = 5000$ (side-view)

(d) $T = 5000$ (top-view)

Figure 5.7: Numerical simulation of the evolution of an elastic-viscoelastic bilayer representing a biofilm coated with *BslA* (equation (5.5)). Domain represents a square measuring 2.5 mm × 2.5 mm, as seen in Figure 5.3. Figures (a)-(c) show side-view of wrinkling pattern (deflection W) at times $T = 100$, 500, 5000 respectively. Figure (d) shows top-view of wrinkling pattern (deflection W) at $T = 5000$, when equilibrium has been reached. Parameters values are $h_{rat} = 20$, $\mu_{rat} = 0.001$, $\nu_f = 0.45$, $\nu = 0.4$, $\bar{\sigma}^0_{11} = \bar{\sigma}^0_{22} = -0.5$. Periodic boundary conditions and a small random initial condition for W are used.

addition, wrinkle amplitude is of the same order as biofilm depth, as is observed experimentally. Thus, the elastic-viscoelastic bilayer model applied to the *BslA* covered biofilm can produce biologically relevant results. However, it appears that wrinkles emerge and reach their equilibrium height in numerical simulations much faster than they do in real life.

In order that the time-scales of wrinkling in biofilms and numerical simulations are reasonably matched, we suggest that the wrinkling of the bilayer does not come into play immediately, but rather when the biofilms have reached a sufficient height. Accordingly, by delaying the implementation of the model until later on during biofilm development, there is also an increased chance that the critical stress, σ_c, is transcended by initial stress, σ_0, as the growing bacterial population are subject to more spatial constraints later in development.

5.5.4 Model Applied on a Circular Domain

In Sections 5.5.2 and 5.5.3, numerical simulations of the elastic-viscoelastic bilayer model of system (5.5) representing both a biofilm-agar complex and a biofilm coated with a *BslA* layer were carried out on a square domain representing a small central square (dimensions 2.5 mm × 2.5 mm, as seen in Figure 5.3) located within the coffee-ring region of the biofilm. These simulation results can be seen in Figures 5.5 and 5.7. While these results give us a good representation of the patterning observed in a zoomed in region of the coffee-ring of biofilms, they do not allow us to observe the full coffee-ring region.

In order that we may observe the full coffee-ring region we carried out numerical simulations on a domain representing a circle of radius 5 mm, which when compared with the yellow highlighted region in Figure 2.1(b) can be seen to be the approximate

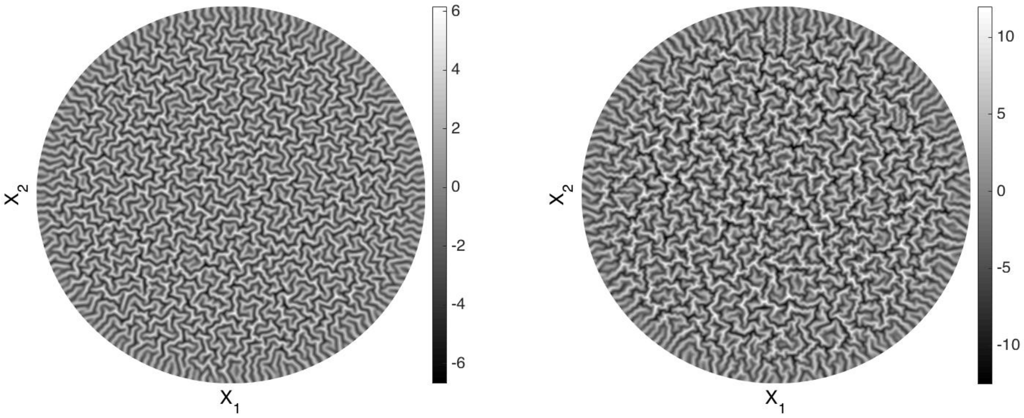

(a) biofilm-agar bilayer (Case D) at $T = 5000$ (top-view)

(b) *BslA* coated biofilm at $T = 5000$(top-view)

Figure 5.8: Numerical simulation of system (5.5), showing wrinkles in the coffee-ring region of a biofilm. Results are shown when the system is in equilibrium (T=5000). Domain represents the coffee-ring region, a circle of radius 5 mm. Figure (a) represents the case where the elastic-viscoelastic bilayer represents a partial component of the biofilm-agar complex (see Case D in Section 5.5.2), and uses the same parameter values as implemented in Figure 5.5. Figure (b) represents the case where the elastic-viscoelastic bilayer represents a biofilm coated with *BslA* (see Section 5.5.3), and uses the same parameter values as implemented in Figure 5.7. Both figures show a top-view of the biofilm, where the colour-bar represents deflection W. Zero-flux boundary conditions and a small random initial condition for W are used.

radius of the coffee-ring region. Numerical simulations representing both the biofilm-agar complex as described by Case D in Section 5.5.2 and the *BslA* coated biofilm as described in Section 5.5.3 were carried out and can be seen in Figure 5.8, which show a top-view of the biofilm coffee-ring region when the system is in equilibrium. Parameter values used in Figures 5.8(a) and 5.8(b) are the same as those used in the creation of Figures 5.5 and 5.7 respectively.

It can be seen that the wrinkling patterns in the full coffee-ring region show a good phenotypic similarity to those observed in experimental results (compare Figure 5.8 with the coffee-ring region highlighted in yellow in Figure 2.1(b)). The amplitude and wavelength of the wrinkles at equilibrium are also of the same order as expected, and are very similar to the amplitude and wavelength of the wrinkles observed in the corresponding simulations carried out on the smaller square domain (this can be seen by a comparison of Figure 5.5(d) with Figure 5.8(a), and Figure 5.7(d) with Figure 5.8(b)). The wrinkles observed at the boundary of the circular domain also show some similarities to those observed experimentally. In particular, note the radial direction of wrinkles at the edge of the coffee-ring seen in Figure 2.1(b). These wrinkles are comparable to the radially directed wrinkles seen near the boundary in the numerical simulations of Figure 5.8.

5.6 Comparison of Analytical and Numerical Results

In section 5.3, some analytical results obtained by Huang and Im in [76] were presented. These results gave estimates for some of the physical properties of the wrinkling patterns that emerge in numerical simulations of the elastic-viscoelastic bilayer described by system (5.5) at different stages of wrinkle development. We now make some comparisons of these analytical results with the results of numerical simulations to determine the accuracy of some of these estimates. We are particularly interested in the wavelength of wrinkling patterns that are reached at equilibrium, and as such we specifically focus on this stage and the analytical results presented in Section 5.3.3.

It can be seen from equation (5.8), that the analytical estimate for equilibrium wavelength, $\bar{\lambda}_{eq}$, of the wrinkling patterns resulting from system (5.5) is a function of the non-dimensional parameters ν, ν_f, h_{rat} and μ_{rat}. Interestingly, the absence of the applied initial stress $\bar{\sigma}_0$ in the equation for $\bar{\lambda}_{eq}$ suggests that, providing $\bar{\sigma}_0$ is large enough that wrinkles can emerge ($\bar{\sigma}_0 > \bar{\sigma}_c$), $\bar{\sigma}_0$ does not have any impact on the wavelength of pattern. Indeed, numerical simulations (not included here) comparing the wavelength of patterns for varying $\bar{\sigma}_0$ values where all other parameters are held constant appear

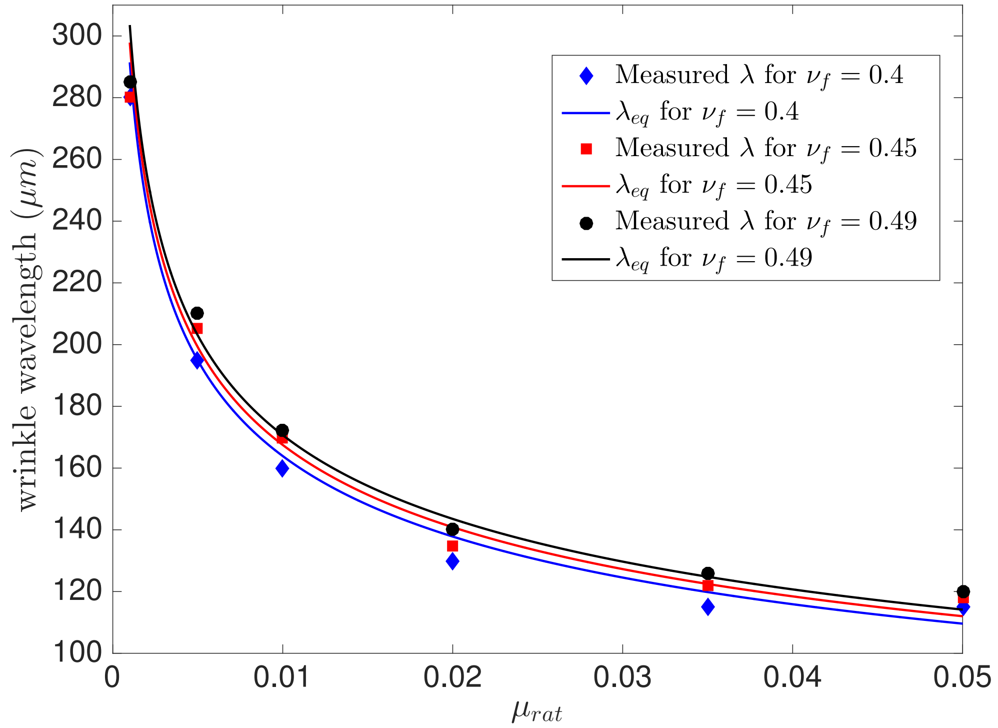

Figure 5.9: Plot showing equilibrium wrinkle wavelength as a function of μ_{rat}. Results for three different values of ν_f are shown. They are $\nu_f = 0.4$ (blue), $\nu_f = 0.45$ (red) and $\nu_f = 0.49$ (black). Diamond, square, and circle markers show approximate dimensional (equilibrium) wavelength measurements from simulation results of system (5.5). Measurements were made using ImageJ software. The corresponding coloured solid lines show the function λ_{eq} (dimensional form of equation (5.8)). Other parameter values are $h_{rat} = 10$, $\nu = 0.4$, $\bar{\sigma}_{11}^0 = \bar{\sigma}_{22}^0 = -0.4$. Figure plotted in MATLAB.

to agree with this suggestion.

One parameter which does appear to influence the wavelength of patterns is μ_{rat}, which as described in Section 5.2.4, provides a comparative measure of the stiffnesses of the viscoelastic and elastic layers. For example, a higher μ_{rat} value suggests a comparatively stiffer viscoelastic substrate than a lower μ_{rat} value. As seen from equation (5.9), $\partial\bar{\lambda}_{eq}/\partial\mu_{rat} < 0$. This suggests that as the viscoelastic layer becomes stiffer, the wavelength of wrinkles at equilibrium is expected to decrease. Indeed, a plot showing some measurements of equilibrium wavelengths (dimensional form) from numerical simulations results appears to confirm this (see Figure 5.9). In addition, the analytical approximation to dimensional wavelength at equilibrium (given by $\lambda_{eq} = h_f\bar{\lambda}_{eq}$), is in good agreement with the observed numerical results (again see Figure 5.9). We note again that while the magnitude of $\bar{\sigma}_0$ has no effect on the wavelength of pattern exhibited in these simulations, we choose a $\bar{\sigma}_0$ large enough such that $\bar{\sigma}_0 > \bar{\sigma}_c$ for the range of μ_{rat} investigated. Thus, for all parameter values investigated and implemented in the creation of Figure 5.9, wrinkle formation does occur and wrinkle wavelength can be measured.

As an aside we note from the analytical results of equation (5.9), that $\partial\bar{\lambda}_{eq}/\partial\nu_f > 0$. Again, this is confirmed in Figure 5.9, which shows plots for three different values of ν_f which indeed show that an increase in ν_f leads to an increase in equilibrium wrinkle wavelength. Again, $\bar{\sigma}_0$ is chosen to be large enough such that wrinkles can emerge for the parameter range investigated.

5.7 Conclusions

In this section we introduced a physical model formulated by Huang and Im [76] that describes the evolution of wrinkling patterns arising in an elastic-viscoelastic substrate subject to axial compression. Having noted the similarity between patterns arising in biofilms and numerical simulations of the model given in [76], we investigated the potential application of the model to describe wrinkling formation in biofilms.

Two different representations of the model in relation to the biofilm context were considered. The first representation assumed that a biofilm and its agar substratum could be modelled as an elastic-viscoelastic bilayer. By comparing the magnitudes of the physical properties of biofilm and agar, and considering the limitations of the model, it was found that a biofilm-agar complex could not generally realistically be modelled by an elastic-viscoelastic bilayer. However, in cases where only a small subsection of the biofilm-agar complex (situated at the biofilm-agar interface) was considered, some biologically relevant results could be obtained. In the second case considered, it was assumed that the biofilm could be split into two separate regions; a bulk viscoelastic component that was covered by an elastic coating that represented the hydrophobic *BslA* cap. In this case, it was found that biologically realistic wrinkling patterns could emerge upon utilisation of model (5.5).

We conclude that the model propsed by Huang and Im in [76] may prove to be a useful tool in the modelling of wrinkling in biofilms. However, as the model considers a purely mechnical approach to wrinkling there are obvious limitations in its application to biological materials such as biofilms, which are ever evolving inhomogeneous materials. We suggest that a modelling approach that combines both physical and biological elements may provide a better description of bacterial biofilms. Indeed these types of model are explored in [48, 149].

Chapter 6

Conclusions and Future Work

6.1 Conclusions and Discussion

In this thesis we investigated and presented different mathematical modelling techniques in order to better understand the mechanisms controlling wrinkle formation in biofilms. We considered a continuum approach, specifically partial differential equation models, and have discussed some of the different aspects encompassed within each model that may contribute to pattern formation.

Some biological processes that are hypothesised to contribute to the heterogeneous structure of biofilms were incorporated in the mathematical models in order to determine their effect on biofilm development. In the first of our approaches we considered the possibility that mathematical models describing the interaction of extracellular matrix with bacterial cells could produce patterning. The biological process of cell death was also considered as a potential means of inducing pattern formation in biofilms. Finally we considered the effect of mechanical processes on the stucture of biofilms.

In Chapter 2, we investigated an existing reaction-diffusion model by Asally et al. [6], that described the heterogeneous nature of cell density and cell death observed within the coffee-ring structures of wildtype *Bacillus subtilis* biofilms. Experimental results presented in the paper suggested that localised cell death acted as a precursor to wrinkling patterns in *B. subtilis* biofilms by creating a weakness in the biofilm which could then be acted upon by mechanical forces, causing a buckling mechanism. A model proposed by the authors predicted heterogeneous cell density and cell death patterns in numerical simulations, which appeared to be in agreement with experimental results. However, the mathematical component causing heterogeneity in numerical simulations was not immediately obvious. Our aim was to identify the driving force of the spatial patterning that was observed in the model results.

Through a combination of stability analysis and analysis of numerical simulation results, we determined that two model features were crucial in the instigation of spatial heterogeneity: (i) a non-constant diffusion term and (ii) a spatially correlated random bacterial growth rate. Interestingly we found that the spatial correlation assigned to the growth rate could be observed in the cell density and cell death patterns through the entirety of the simulation time. Furthermore, we found that it was possible to control the wavelength of the spatial patterning observed in simulations by changing a single parameter, λ_c, included in the expression determining the spatial correlation of growth rate, $\alpha(\mathbf{r})$. We therefore concluded that the spatial characteristics of the patterning observed in the model was not an emergent property due to some underlying mathematical or biological feature, but rather a direct consequence of the model input.

In Chapter 3, a cross-diffusion approach to biofilm modelling was investigated. We aimed to determine if a simple biofilm model, that described the interaction of bacterial cells with the surrounding extracellular matrix, could exhibit heterogeneity. In particular, we explored the possibility that concentration gradients in each of the two different biofilm components could affect the movement of the other. A generic two-species cross-diffusion model was formulated and analysed. We noted that in Chapter 2, the possibility of patterns arising in a similarly formulated model describing only the self-diffusion of bacteria had been ruled out. Stability analysis applied to the cross-diffusion model determined that patterns could only occur in the cases where both cross-diffusion terms were present. An additional requirement suggested that patterning could only occur when the two cross-diffusion terms were of opposite signs i.e. $D_{12}D_{21} < 0$. On consideration of the biological meaning of $D_{12}D_{21} < 0$, we determined that, due to lack of evidence in the literature, it was unlikely this condition could hold in the proposed context.

In addition to cross-diffusion, the effect of a matrix aggregation term was also investigated in Chapter 3. While linear stability analysis suggested that this aggregation term could result in an instability arising, the absence of a preferred wavelength of pattern led us to determine that it was not a suitable method for modelling pattern formation in biofilms.

In Chapter 4 we considered an alternative approach to modelling biofilms, by assuming that biofilm expansion occurs as a result of cell growth rather than diffusion. We described the growth of a biofilm growing on agar into the air above (oxygen was assumed to be the growth limiting substrate) by following the approach presented in Dockery and Klapper [41]. The model set-up implemented a reaction-diffusion equation to describe substrate concentration, and implemented Darcy's Law to describe movement of bacterial cells. Thus it was assumed that cell growth induces a pressure gradient in the biofilm. The evolution of the biofilm-air interface was tracked by assuming pressure was equal to zero at the biofilm surface.

We were particularly interested in determining the effect of cell death on biofilm development. Thus we extended the model of [41] to include two different cell death terms: (i) constant cell death and (ii) substrate dependent cell death (motivated by the observation that cell death occurs at the bottom of biofilms [6]). Planar analysis of solutions identified different behaviour in each of the different cases of cell death. While unbounded growth of biofilms was found to occur in the absence of any cell death, biofilm height stabilised in the presence of cell death. Furthermore, constant cell death at sufficiently high levels was found to induce complete biofilm collapse. This die-back was not observed in the case of substrate dependent cell death.

Analysis of non-planar perturbations at the non-trivial steady state (where it existed) revealed a link between biofilm height and the emergence of patterning. While the potential for patterning to occur in deep biofilms (characterised by low levels of cell death) did exist, it was found that no patterning could arise in shallow biofilms (characterised by high levels of cell death). This result was in agreement with experimental observations that show pattern formation in biofilms occurs at later time stages (mature, deep biofilms) rather than in the early stages of growth (shallow biofilms).

Chapter 5 considered a mechanical approach to wrinkling. A purely physical model formulated by Huang and Im [76], that described wrinkle formation in an elastic-viscoelastic bilayer, was explored. Some of the different wrinkle morphologies that are known to arise in numerical simulations of the model were presented, as were some previously derived analytical results that describe the physical properties of the simulated wrinkles. We noted that wrinkles in the central coffee-ring of *B. subtilis* biofilms were similar to those observed in simulation results of the model in [76], and thus we considered if the model could be applied to the biofilm context.

First we explored the possibility that the elastic-viscoelastic bilayer could represent an elastic biofilm growing on a viscoelastic agar substrate. We determined that it was unlikely the model could accurately recreate biologically realistic wrinkles unless only a partial segment of the biofilm-agar complex was assumed as being represented by the bilayer. If this assumption was not taken into account, the wavelength of wrinkles arising would be greatly overestimated in comparison to their real life values. Our second consideration determined whether the elastic-viscoelastic bilayer may represent two different components of the biofilm. We suggested the viscoelastic substrate may constitute the bulk of the biofilm situated near the agar interface, while the elastic component may constitute a *BslA* layer located towards the surface of the biofilm. We found that numerical simulations of wrinkle morphologies in this case did predict realistic biofilm wrinkling on a suitable length scale, on the substitution of appropriate parameter values.

6.2 Future Work

In this thesis we have investigated several different mechanisms by which heterogeneity may arise in bacterial biofilm formation. However, there are still many unknowns surrounding the formation of wrinkle structures in biofilms.

In the first part of this thesis we investigated cellular processes that may occur within the biofilm and lead to the initiation of pattern formation. While the mathematical modelling techniques that we used allowed us to determine the conditions under which patterns may be observed to occur, no information relating to the physical features of the wrinkles could be inferred. Contrastingly, in the latter part of the thesis a mechanical approach to wrinkling allowed us to explore the specific physical features that could be attributed to wrinkles observed within the coffee-ring structure of *B. subtilis* biofilms. However, none of the biological processes and mechanisms that govern the observed wrinkle features were incorporated in the model. We suggest that a model approach that takes into account both the biology and physical properties of biofilms (and their surrounding environment) may be a more realistic method of modelling biofilm wrinkling.

6.2.1 Inclusion of Biofilm Growth in an Elastic-Viscoelastic Model

One example of a mechanical approach to wrinkling in biofilms that incorporates some biological factors is given in [149]. This model, formulated to describe wrinkling in spatially constrained bacterial pellicles, describes pellicles as elastic sheets. The equation describing the deflection of the elastic plate remains unchanged from the traditional plate bending equations. However, the biological nature of the pellicles are taken into account within the equations describing the stress and strain within the plate (or biofilm) by the introduction of a single parameter described as the cumulative growth rate. The parameter, which increases throughout biofilm development, acts to increase the magnitude of the strain that occurs in biofilms. Thus, in comparison to the absence of a growth term, increased stress is fed into the plate bending equation. We suggest that a similar growth rate may be incorporated within the stress and strain equations describing the evolution of an elastic-viscoelastic bilayer as described in Chapter 5 (see equation 5.4). This may allow a possible link between the biofilm development factors and the physical properties of wrinkle structures to be made.

6.2.2 Biofilms as Annular Sheets

The majority of our investigations into the wrinkling of biofilms as described in Chapter 5 considered a square domain representing a small section of the coffee-ring region, subject to applied normal axial stresses. In reality, an unrestricted biofilm grown on agar is circular in shape. Whilst a circular domain was briefly considered in Section 5.5.4, it may be of interest to carry out some more in-depth investigations to determine if the proposed model (5.4) holds any further biological significance on a more realistic biofilm domain.

We suggested in Chapter 5 that the contraction of a biofilm, specifically in the coffee-ring region, could cause compressive forces to accumulate, which in turn could cause wrinkling to occur, provided certain conditions were adhered to. We suggest that if this is indeed the case, then compressive forces on the inside of the coffee-ring may act to pull the outer region in towards the centre of the biofilm, causing a tension in the region of biofilm outside of the coffee-ring. In [27, 35], models describing wrinkling in annular thin sheets have been formulated. In both set-ups, the annulus is considered to be subjected to tensile radial forces on both the short inner edge and longer outer edge. Radial wrinkling patterns are found to form at the inner edge as a result of a typical buckling instability. This is demonstrated in Figure 6.1, which shows a plastic sheet, in the shape of an annular segment, subject to an applied tensile force on both the inner and outer edges. The patterns exhibited on the annular domains as described share some similarities with biofilms, as the radial wrinkles extend from the perimeter of the coffee-ring towards the outer edge.

In [21, 74] the concept of penetration depth, which describes how far into the bulk a wrinkle persists, is used to characterise wrinkles. We suggest that this measurement may also be an appropriate method of characterising different wrinkling patterns that appear in biofilms, as not all patterns extend to the outer rim of the biofilm surface (see Figure 1.2(a)). Overall, it would be interesting to investigate if a model describing tension applied to an annular domain (in conjunction with some biological factor such as the growth term as described in section 6.2.1) could realistically recreate wrinkling patterns as observed in biofilms grown on agar.

Figure 6.1: Wrinkle configuration exhibited in a stretched annular segment of a plastic bag. Tensile stress is applied radially outwards along the inner and outer edges. Wrinkles form at the inner edge of the annular segment, and different penetration depths can be observed for individual wrinkles i.e. some wrinkles extend further into the domain than others.

6.2.3 Hybrid Models

In this thesis we have considered only a continuum approach to modelling wrinkling in biofilms. However, as noted in section 1.2.1, many biofilm models also implement discrete methods. In [48] a hybrid approach, using both PDEs and a cellular automaton, was implemented to model the wrinkling in biofilms. This model produced some very good results that accurately captured the characteristics of both the radial wrinkles at the edge of the biofilm and the cluster of wrinkles in the centre of the biofilm. We suggest a similar type of hybrid model that incorporates localised cell death at the microscopic scale (described by discrete methods), in conjunction with PDEs that describe the collective behaviour and response of cells and other biofilm components, may provide a useful tool for modelling biofilm wrinkling. In particular, it may provide us with more information about how the different length scales interact, and explain more about why and how the biofilm exhibits multicelluar behaviour.

Appendix A

Mechanical background

A background describing some of the key concepts used in the mechanical approach to wrinkling as described in Chapter 5 is presented here.

A.1 Force Concepts

It is important for us to have a basic understanding of fundamental solid mechanics. Some essential concepts are described here. Further details of these can be found in references [15, 58, 69, 151], which are good introductory references for the mechanics of materials.

Equilibrium:
A particle is in equilibrium when the resultant of all forces acting on that particle is zero, i.e.

$$\sum F_x = 0, \quad \sum F_y = 0, \quad \text{and} \quad \sum F_z = 0, \tag{A.1}$$

where F_x, F_y and F_z are forces acting in the x, y and z Cartesian directions respectively, and the sum considers all forces acting on the particle in question. Note that positive

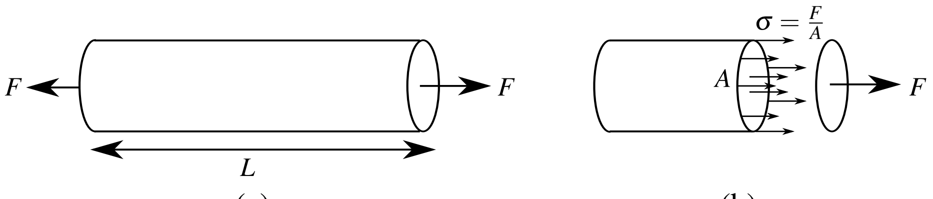

(a) (b)

Figure A.1: Normal stress acting on a cylindrical body of length L: Figure (a) shows a bar under an applied concentrated axial force, F, while Figure (b) shows the resulting stress in the bar which is distributed over the exposed cross-sectional area, A.

forces act in the positive axis direction, while negative forces act in the negative axis direction. The unit of force is the Newton (N).

Moment:

Moments measure the propensity of a rigid body to rotate about some axis under force [82]. The moment, M_0, of a force, F, about an axis through a point O is defined as the product of the magnitude of F times the perpendicular distance, d, from the location of F to the axis O, i.e.

$$M_0 = F\,d. \tag{A.2}$$

The unit for moment is the Newton-metre (N m). At equilibrium the moments on either side of the element must balance. Bending and twisting moments measure the tendency of a body to bend and twist respectively [151].

A.1.1 Basic Stress and Strain

Normal (or Direct) Stress (σ):

Stress is defined as the intensity of force (force per unit area). A material body subjected to an applied external force, F, acting perpendicular to a cross-sectional surface of the body, will result in a normal (also called direct or axial) stress, σ, in the same direction (normal to the cross-section) as F (see Figure A.1). Normal or direct stress

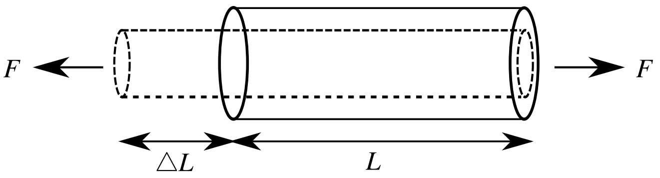

Figure A.2: The effect of normal strain in a bar of length L. An applied tensile axial force, F, induces a deformation in the bar, extending the bar by a length $\triangle L$.

is therefore expressed as

$$\sigma = \frac{F}{A}, \tag{A.3}$$

where A is the cross-sectional area of the body. Units are $\mathrm{N\,m^{-2}}$ (or Pascals, Pa).

Normal (or Direct) Strain (ε):

The magnitude of deformation of a material due to normal stress is called normal (or direct or axial strain), ε. Normal strain is expressed as

$$\text{strain} = \frac{\text{change in length}}{\text{original length}} \quad \left(\varepsilon = \frac{\triangle L}{L}\right), \tag{A.4}$$

where the lengths L and $\triangle L$ are the original length and the change in length of the material respectively (see Figure A.2). As strain is a ratio it has no units.

In order to distinguish between the different effects that an applied force can have on the body it is acting on the sign convention for stress and strain is defined such that positive stress and strain results in tension and consequently extension of a material. Contrastingly, contraction in a material is a result of negative strain caused by negative compressive stress.

Shear (or Tangential) Stress (τ):

Shear or tangential stress, τ, occurs when a material is subjected to an external shear

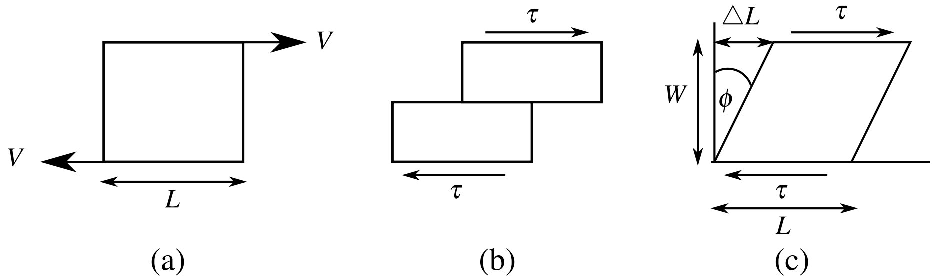

(a) (b) (c)

Figure A.3: Figure showing the effect of shear stress and strain on an element of length L. Figure (a) shows a shear force V acting tangential to the top and bottom surfaces of a small element, while Figure (b) shows the resulting shear stresses τ. Figure (c) shows the angle, ϕ, and change in length, $\triangle L$, used in the measurement of shear strain, γ (see equation (A.6)).

force, V, acting tangential to an axis or surface (see Figure A.3). Shear stress is expressed as

$$\text{shear stress} = \frac{\text{shear load}}{\text{area resisting shear load}} \quad \left(\tau = \frac{V}{A}\right). \tag{A.5}$$

An example of shear force is friction.

Shear (or Tangential) Strain (γ):

Shear strain, γ, is a measure of angular distortion due to shear stress, τ. Shear strain is measured in radians, and is the displacement of the shear plane relative to the plane distance W away (see Figure A.3(c)):

$$\gamma = \frac{\triangle L}{W} = \tan(\phi). \tag{A.6}$$

A.1.2 Elastic Materials

In this section the concept of elastic materials and their governing laws are introduced. A material is defined as elastic if, having been subject to stress and resultant strain, it returns to its original unloaded dimensions when stress is removed [69]. Elastic materials have a limit of elasticity reached at a certain stress level. As stress exceeds this level, the behaviour of the material can no longer be considered elastic and an irreversible deformation of the material will occur [58].

Hooke's Law:

For linear elastic materials within the limits of elasticity, Hooke's Law states that normal stress is directly proportional to normal strain [69] i.e.

$$\frac{\sigma}{\varepsilon} = E \quad \text{(constant)}. \tag{A.7}$$

The constant E is the Young's modulus (or modulus of elasticity) with units $\mathrm{N\,m^{-2}}$, and is a measure of the stiffness of the material [151]. The corresponding Hooke's Law in shear states that

$$G = \frac{\tau}{\gamma}, \tag{A.8}$$

where G is the modulus of rigidity (or shear modulus of elasticity), and τ and γ are shear stress and strain respectively [151]. Note that these are the simplest versions of Hooke's Law that apply only to the simplest cases of uniaxial stress (i.e. stress acting in only one direction along the longitudinal axis of the structure); they are unsuitable for use in more complex cases of stress.

Poisson's Ratio:

Poisson's ratio describes the negative ratio of lateral to longitudinal strain, of a material within elastic limits [151]. This is displayed in Figure A.4 which shows a rectangular bar of length L under a tensile axial load, F. An extension in the axial (longitudinal) direction is accompanied by a reduction in lateral dimensions, breadth b and depth d, due to conservation of mass. Longitudinal and lateral strains, ε_L and ε_{lat}, are defined as

$$\varepsilon_L = \frac{\triangle L}{L}, \quad \varepsilon_{lat} = -\frac{\triangle b}{b} = -\frac{\triangle d}{d}. \tag{A.9}$$

respectively where $\triangle L$, $\triangle b$ and $\triangle d$ are the changes in respective dimensions (see

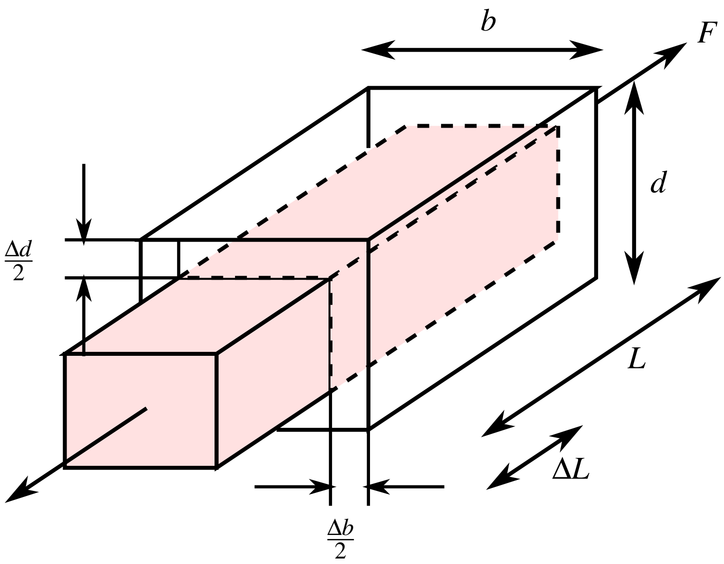

Figure A.4: Poisson's effect in a rectangular bar of length L , breadth b and depth d. An axial tensile load F applied to the bar has the effect of extending the bar in the longitudinal direction by a length ΔL. As a result a contraction in the breadth and depth of the bar, Δb and Δd, also occurs.

Figure A.4). Poisson's ratio, ν, is thus defined by

$$\text{Poisson's ratio} = -\frac{\text{lateral strain}}{\text{longitudinal strain}}, \quad \text{i.e.} \quad \nu = -\frac{\varepsilon_{lat}}{\varepsilon_L}. \tag{A.10}$$

[69]. Poisson's ratio is positive for most materials. The upper limit of $\nu = 0.5$ describes incompressible materials (for example, the value of Poisson's ratio for rubber is close to $\nu = 0.5$) [151] . Contrastingly, the Poisson's ratio for cork is close to $\nu = 0$ [58].

A.2 Fundamentals of Beam Bending

Having introduced some key mechanical concepts, our next step is to consider the simplest cases of bending in elastic beams. A beam is defined as a 3-D structure where one dimension is much larger than the other two [9], and as such is considered mathematically as a 1-D structure. Under different loading conditions it is useful to describe

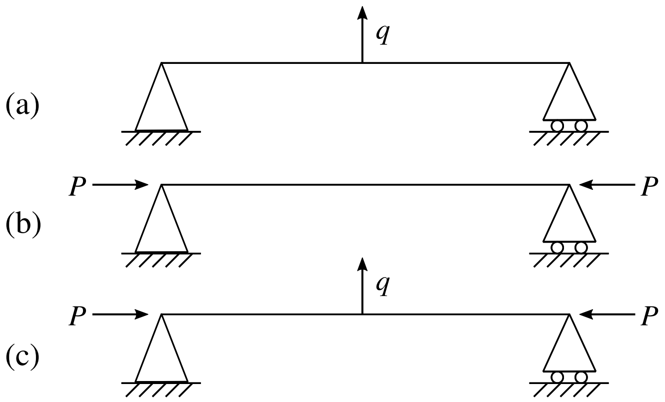

Figure A.5: Figure showing 1-D structures under three different types of loading. Figure (a) shows a beam with an applied lateral (transverse) load q, Figure (b) shows a column under an applied compressive axial load P and Figure (c) shows a beam-column under both an applied lateral load q and an applied compressive axial load P.

such a structure with different names. A beam under transverse (or lateral) load (force vectors perpendicular to axis of bar [58]) is simply called a beam. Under axial load (load directed along axis of member [58]) is called a column. Under both transverse and axial loads simultaneously it is called a beam-column [147]. These differences are shown in Figure A.5. As we are particularly interested in axial compression and stretching, we focus on the column and beam-column set-up.

Many different mathematicians have been involved in the development of beam bending theory over several centuries. Two notable mathematicians in this area of work were Jacob Bernoulli and Leonard Euler. In the seventeenth century, Bernoulli was the first to look at the deformed shapes of elastic beams and calculate their deflection. Leonard Euler further developed Bernoulli's theory and methods into a form that is recognisable and still used today [145]. This is Euler-Bernoulli beam theory which, although using some of the simplest ideas and assumptions, is still widely used today.

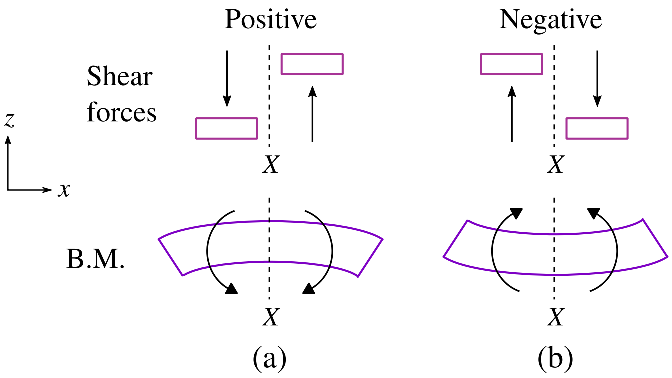

Figure A.6: Chosen sign convention for positive and negative shearing forces and bending moments (B.M.) in the xz-plane. Figure (a) shows the sign convention for positive shear forces and bending moments about a point X, while Figure (b) shows the sign convention for negative shear forces and bending moments.

A.2.1 Sign Convention

We investigate the bending of physical structures in an attempt to determine if any of the mechanics behind the wrinkle formation in biofilms can be explained using beam (1-D analysis), and later plate (2-D analysis), bending equations. As the problem that is tackled in this thesis looks into the wrinkling of biofilms grown on agar we choose a sign-convention for the beam and plate bending equations that we feel best represents our problem. We suppose that a biofilm grown on an agar substrate will preferentially buckle upwards as the agar will obstruct the downwards deflection of the biofilm. As such we use a traditional 2-D axis orientation of an xz-plane with positive x-axis directed to the right and the positive z-axis oriented upwards. Our chosen sign-convention for bending moments and shearing forces (as described in section A.1) about a point X are shown in Figure A.6.

It should be noted that the sign convention as outlined above differs from the most commonly used convention described in reference texts. However, provided it is used consistently in the derivation of equations, the sign-convention chosen is largely irrelevant. Throughout this thesis we use the sign convention as described in Figure A.6

unless explicitly stated otherwise.

A.2.2 Derivation of Beam Bending

In this section we derive the beam bending equations, using our chosen sign convention. The beam bending equations describe the behaviour of a beam under a variety of applied loads. A straight beam initially free from any load and lying in the *xz*-plane deforms into a shape called the deflection curve as load is applied [151], and the deflection measures the displacement of any point along the beam from its original position [58]. Axial displacement, u, measures displacement in the horizontal x-direction while lateral displacement, w, measures vertical displacement in the z-direction. As displacement is a vector, the displacement components u and w are signed. For example, if the beam bends upwards from the initial position ($z = 0$), the displacement w has positive value along the length of the beam.

A key concept in the theory of beam bending is that of the neutral axis, first proposed by Mariotte [145]. A beam subjected to bending moment will elongate and contract on opposite sides along its longitudinal axis x [58]. In our sign convention, the top of the beam (where the z-coordinate is positive) is subject to tension and is extended while the bottom of the beam (where z is negative) is under compression and contracts for positive bending moment (see Figure A.7(a)). Therefore stress at the top edge of the beam is positive while stress at the bottom edge of the beam is negative. It follows that somewhere along the z-direction of the beam stress must equal zero [69]. The locus of all these points with stress equal to zero is called the neutral axis (N.A.), and occurs along the middle axis, halfway between the top and bottom, of the beam. The neutral axis is neither stretched or shortened but has the same length as the undeformed beam [58] and can be seen highlighted in red in Figure A.7(a).

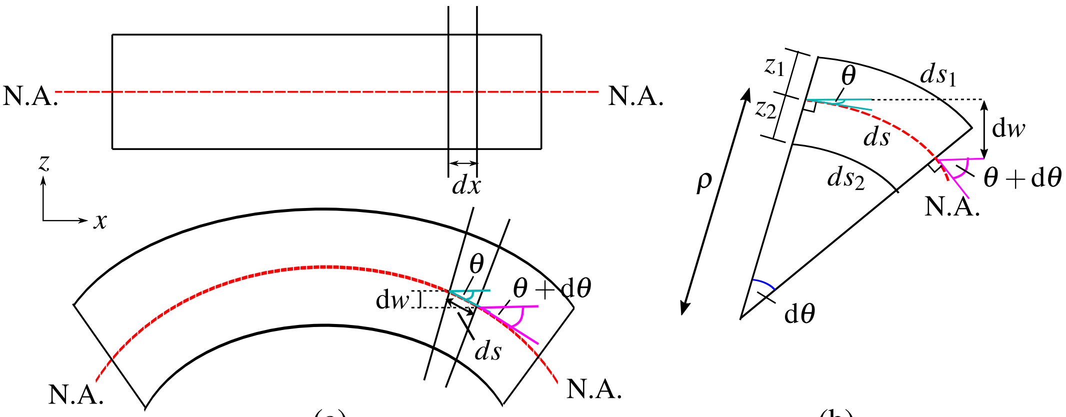

(a) (b)

Figure A.7: The deformation of a beam. Figure (a) shows the initial configuration of a beam (top image) that is then bent out of shape (bottom image). The neutral axis is highlighted in red. The relationship between the angle of rotation, θ, and the deflection, w, is also shown. Figure (b) shows a close up of the small segment of length dx highlighted in Figure (a), to demonstrate the relationship between radius of curvature, ρ, and arc length, ds. The neutral axis is again highlighted in red.

The beam bending equations are expressed in terms of lateral and axial displacement (w and u respectively). We consider a small section of a beam, with length dx, that, under the action of applied forces, deforms into the shape shown in Figure A.7(a). As the beam bends the neutral axis remains unstressed and unstrained. Tangents to the curve in the element make an angle of θ and $\theta + d\theta$ with the positive x-axis at opposite ends of the element, where θ is the angle of rotation and is positive when measured in an anticlockwise direction for our axis configuration (see again Figure A.7(a)) . Extending lines normal to the tangents at the left and right hand ends produces a circular segment with an angle of $d\theta$ between normals, and radius of curvature equal to ρ [58], as shown in Figure A.7(b). The arc length of the small segment of length dx shown in Figures A.7(a) and A.7(b) is denoted by ds. As part of the neutral axis, the length ds is unstressed and is therefore equal in length to the undeformed element, i.e. $ds \approx dx$. The arc lengths ds_1 and ds_2 are the arc lengths of the deformed segment at heights of z_1 and z_2 above and below the neutral axis respectively. Notice z_1 and z_2 are simply lengths and so have positive values. The arc-lengths of ds can be expressed in terms of the radius of the curvature of the neutral axis, ρ, by

$$ds = \rho \, d\theta \tag{A.11}$$

[58]. Similarly the lengths ds_1 and ds_2 can be expressed by

$$\begin{aligned} ds_1 &= (\rho + z_1)\, d\theta = \rho \, d\theta + z_1 \, d\theta = ds + z_1 \, d\theta, \\ ds_2 &= (\rho - z_2)\, d\theta = \rho \, d\theta - z_2 \, d\theta = ds - z_2 \, d\theta. \end{aligned} \tag{A.12}$$

Using equation (A.4) the strain can be expressed in terms of z and ρ:

$$\begin{aligned} \varepsilon_1 &= \frac{ds_1 - ds}{ds} = \frac{ds + z_1 \, d\theta - ds}{ds} = \frac{z_1 \, d\theta}{\rho \, d\theta} = \frac{z_1}{\rho} > 0 \quad \text{(elongation)}, \\ \varepsilon_2 &= \frac{ds_2 - ds}{ds} = \frac{ds - z_2 \, d\theta - ds}{ds} = -\frac{z_2 \, d\theta}{\rho \, d\theta} = -\frac{z_2}{\rho} < 0 \quad \text{(contraction)}. \end{aligned} \tag{A.13}$$

We note that ε_1 is positive (representing elongation on the top fibres of the segment) and ε_2 is negative (representing contraction in bottom fibres of the segment). Hooke's Law (A.7) yields:

$$\sigma_1 = E \, \varepsilon_1 = E \frac{z_1}{\rho}, \qquad \sigma_2 = E \, \varepsilon_2 = -E \frac{z_2}{\rho}, \tag{A.14}$$

where σ_1 and σ_2 denote the direct stress at distances z_1 above and z_2 below the neutral axis respectively.

Consider now the curvature, κ, which measures how sharply a beam bends [58]. It is expressed as $\kappa = 1/\rho$, where ρ is the radius of curvature as shown in Figure A.7(b). As only small displacements are considered the approximation of $ds = dx$ can be made as above and equation (A.11) can be rearranged to find an expression for curvature:

$$\kappa = \frac{1}{\rho} = \frac{d\theta}{ds} \simeq \frac{d\theta}{dx} \quad \text{(for small displacements)}. \tag{A.15}$$

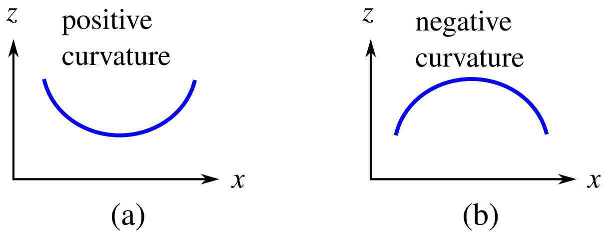

Figure A.8: Signed curvature. Figure (a) shows a curve with positive curvature. Figure (b) shows a curve with negative curvature.

Signed curvature is defined by axis orientation. For the orientation used here, positive curvature is concave upward and negative curvature is concave down (see Figure A.8).

From Figure A.7(b) it is also possible to identify the angle of rotation, θ, in terms of vertical displacement, w. The assumption of small displacements and rotations is adhered to, allowing the approximation $\tan(\theta) \simeq \theta$ to be made [58]. From Figure A.7 it can be seen that for small deflections and rotations the slope of the deflection curve of the small section dx is $\dfrac{dw}{dx} < 0$. The expression

$$\tan(\theta) = \frac{dw}{dx} \quad \implies \quad \theta \simeq \frac{dw}{dx} \tag{A.16}$$

therefore holds. Combining equations (A.15) and (A.16) gives

$$\frac{1}{\rho} = \pm \frac{d^2w}{dx^2}, \tag{A.17}$$

[151] where the sign depends on the chosen sign convention. Comparing Figure A.6 and Figure A.8 it can be seen that positive curvature corresponds to negative bending moment and vice versa. Therefore signed curvature for positive bending moment is given by

$$\kappa = \frac{1}{\rho} = -\frac{d^2w}{dx^2}. \tag{A.18}$$

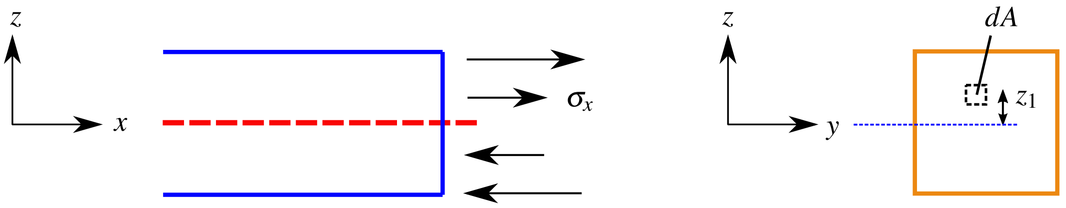

(a) (b)

Figure A.9: Figure showing the cross-section of a beam in two different planes. Figure (a) shows the xz-plane, with a positive tensile stress σ_x acting along the top fibres of the beam and a negative compressive stress σ_x acting along the bottom fibres of the beam. The neutral axis is shown in red. Figure (b) shows a cross-section of the yz-plane where an element dA, a height z_1 above the neutral axis, is highlighted.

The concept of bending moment can be further linked to the curvature by considering a cross-section of the beam, as seen in Figure A.9. Referring to equation (A.2), the bending moment acting over a small element dA within the cross-section, positioned a distance z_1 above or below the neutral axis (as seen in Figure A.9), is given by

$$dM = \sigma z_1 \, dA \tag{A.19}$$

[58]. From equations (A.19) and (A.14), it follows that the bending moment acting over the full cross-sectional area of the beam is

$$M = \int_A \sigma z dA = \frac{E}{\rho} \int_A z^2 dA = \frac{E}{\rho} I, \tag{A.20}$$

where $I = \int_A z^2 dA$ is the moment of inertia of the cross-section of the beam [58]. A final substitution of equation (A.17) into (A.20) gives the relation for bending moment in terms of deflection w:

$$M = -EI \frac{d^2 w}{dx^2} \tag{A.21}$$

[147]. A quick inspection of the expected signs in relation (A.21) allows us to

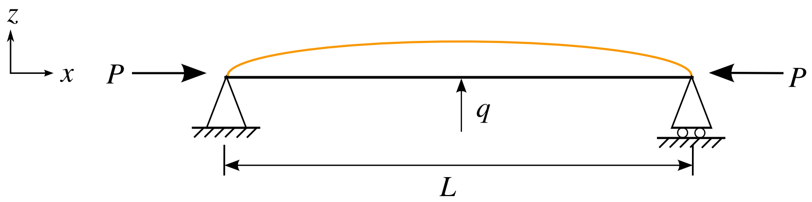

Figure A.10: Beam-columnn of length L under applied axial compression, P, and concentrated lateral load, q. The z-direction is directed upwards. The orange curve shows the deflection curve after deformation.

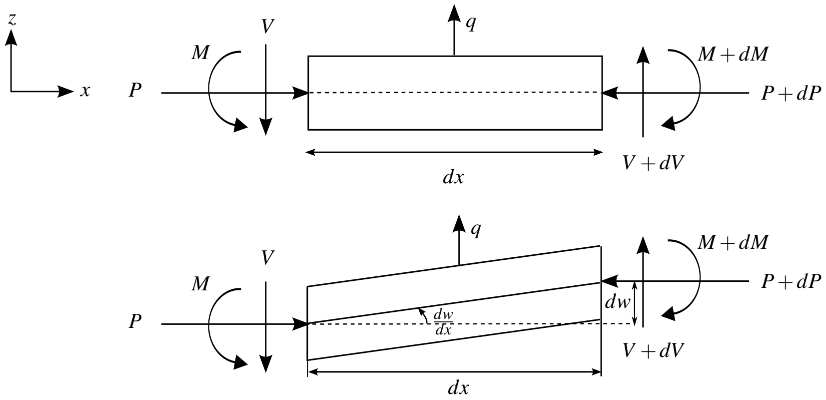

Figure A.11: Equilibrium of segment of length dx: M and $M + dM$ are the bending moments, V and $V + dV$ are the shearing forces, q is lateral load and P and $P + dP$ are axial loads.

check these derivations are correct. Recall from Figure A.8 that positive curvature $\left(d^2w/dx^2 > 0\right)$ results in negative bending moment and negative curvature $\left(d^2w/dx^2 < 0\right)$ results in positive bending moment. This is in agreement with equation (A.21) as required.

Using relation (A.21), the well known Euler-Bernoulli beam bending equations can be derived. The derivation described here follows that given in [147]. The deformation of a beam under a distributed lateral load q is considered as shown in Figure A.10 (setting $P = 0$ for the time being). Taking a small segment of the beam of length dx (see Figure A.11, again ignoring axial loads P), and considering shearing forces V at the left and $V + dV$ at the right of the segment, forces within the beam can be equilibrated. Balancing forces in the z-direction gives

$$\begin{aligned} -V+(V+dV)+q\,dx&=0 \\ \implies \frac{dV}{dx}&=-q. \end{aligned} \tag{A.22}$$

Bending moments, represented by M and $M+dM$ in Figure A.11, at opposite ends of the beam are also taken into account in the equilibration of moments. Summing moments around the left hand end of the neutral axis in segment dx gives

$$\begin{aligned} M&=(M+dM)-(V+dV)\,dx-q\frac{dx}{2}\,dx \\ \implies V&=\frac{dM}{dx}, \end{aligned} \tag{A.23}$$

where higher order terms (H.O.T.) are ignored. Substituting equation (A.21) into equations (A.22) and (A.23) gives

$$EI\frac{d^4w}{dx^4}=q, \tag{A.24}$$

for E and I constant. Equation (A.24) is the Euler-Bernoulli beam bending equation, which describes the deflection of a beam under a lateral load q. It is valid only for long, thin, isotropic elastic beams under small rotations and deflections [9, 15]. Assumptions of the model are that cross-sections of the beam are rigid and do not deform [58] and also, during deformation, cross-sections remain normal to the neutral axis [9]. Because the column is long and thin, axial displacement u (displacement in the x-direction) is small compared to lateral displacement w (displacment in the z-direction). As the equations only hold for small lateral displacement, axial displacement is considered negligible and can be ignored. The results using these assumptions are accurate for long thin isotropic beams but begin to break down when one or more of the assumptions are not satisfied.

If a compressive axial force, P, is also applied to the beam (as seen in Figures A.10 and A.11), the relation (A.23) linking shearing force and moment must be altered to include P:

$$\begin{aligned} M &= (M+dM)-(V+dV)dx-q\frac{dx}{2}dx-(P+dP)\frac{dw}{dx}dx \\ \implies V &= \frac{dM}{dx}-P\frac{dw}{dx}. \end{aligned} \tag{A.25}$$

Equation (A.25) therefore replaces (A.23) when axial load P is included. Combining equations (A.21) and (A.22) with (A.25), the beam bending equation for beam-columns under axial and lateral load becomes

$$EI\frac{d^4w}{dx^4}+P\frac{d^2w}{dx^2}=q. \tag{A.26}$$

The simplest beam equation for a column with only a compressive axial load, P, is therefore

$$EI\frac{d^4w}{dx^4}+P\frac{d^2w}{dx^2}=0. \tag{A.27}$$

A.2.3 Buckling of Beam-columns

Buckling in a beam-column is failure by lateral movement [58]. For a column under axial compression (as considered in Figure A.10, where load q is ignored), buckling occurs when the axial compression P reaches a critical value above which the column is no longer in equilibrium and is unstable, causing the column to displace laterally [58]. The equation describing column deflection in this case can be rearranged from (A.27) into a dimensionless form giving

$$\frac{d^4w}{dx^4}+k^2\frac{d^2w}{dx^2}=0, \quad \text{where} \quad k^2=\frac{P}{EI}, \tag{A.28}$$

which has the general solution

$$w(x)=A\cos(kx)+B\sin(kx)+Cx+D, \tag{A.29}$$

where A, B, C and D are constants [147]. When coupled with appropriate boundary conditions equation (A.28) becomes an eigenvalue problem that can be solved to find multiple eigenvalues k and corresponding eigenfunctions w, which give the different possibilities for the shape of the deflection curve i.e. mode shapes [15].

From equation (A.28), it is seen that axial load satisfying the eigenvalue problem is $P = EIk^2$. The critical load P_{cr} is defined as the smallest load $P = EIk^2 \neq 0$, for eigenvalues k satisfying the eigenvalue problem as described above. A column that is initially straight and in equilibrium will therefore remain straight and in stable equilibrium, returning to its original position if disturbed laterally, for $P < P_{cr}$ [147]. At $P = P_{cr}$ the column is at the boundary between stability and instability [15]. If axial compression exceeds the critical load ($P > P_{cr}$), the column is unstable and is displaced laterally i.e. the column buckles [58]. As columns buckle at P_{cr} (the lowest non-zero force P satisfying equation (A.28)), the eigenfunctions w corresponding to different eigenvalues k where P is larger do not get the chance to be observed, unless some lateral supports are provided at intermediate points in the column [58].

As mentioned previously, the boundary conditions enforced on a column determine the deflection curve observed. The most common types of supports and their corresponding boundary conditions [58] are listed here:

1. A pinned (or simply supported) end of the column allows rotation of the beam but prevents any translation in the vertical or horizontal directions. The corresponding boundary conditions are zero lateral deflection ($w = 0$) and zero bending moment, $M = 0 \left(\frac{\partial^2 w}{\partial x^2} = 0 \right)$.
2. A roller support is similar to pinned-support but allows horizontal movement. Again, the beam is free to rotate. The boundary conditions are the same as in 1 above.

3. A fixed (or clamped) support prevents the end of the beam from moving both horizontally and vertically, and from rotating. The boundary conditions for a clamped end are zero vertical deflection ($w = 0$) and also zero derivative of the deflection in the vertical direction $\left(\frac{\partial w}{\partial x} = 0\right)$.
4. A free end of a beam is not restrained from any movement in any direction, and is free to rotate and translate without restriction. The boundary conditions in this case are zero bending moment $\left(\frac{\partial^2 w}{\partial x^2} = 0\right)$ and zero shearing force.

A summary of results of the eigenvalue problem in equation (A.28) for an axially compressed column of length L as seen in Figure A.10 for some common boundary conditions are given here (see [15, 58, 147] for further details). Specifically, the critical axial forces P_{cr} are given along with the corresponding eigenfunctions $w(x)$:

- Simply supported column

  A column that is simply supported at both ends ($x = 0$ and $x = L$) has boundary conditions given by $w(0) = w(L) = 0$ and $w_{xx}(0) = w_{xx}(L) = 0$. The deflection curve $w(x)$ at the critical loading force P_{cr} is found to be

  $$w(x) = B \sin\left(\frac{\pi x}{L}\right) \quad \text{when} \quad P_{cr} = \frac{\pi^2 EI}{L^2}. \tag{A.30}$$

  A schematic representing this case can be seen in Figure A.12(a) while the mode shape corresponding to $P = P_{cr}$ can be seen in Figure A.12(e) (black curve).

- Clamped-clamped column

  A column clamped at both ends ($x = 0$ and $x = L$) has boundary conditions $w(0) = w(L) = 0$ and $w_x(0) = w_x(L) = 0$. The critical loading force P_{cr} and corresponding deflection curve $w(x)$ are found to be

  $$w(x) = A\left(\cos\left(\frac{2\pi}{L}x\right) - 1\right) \quad \text{when} \quad P_{cr} = 4\frac{\pi^2 EI}{L^2}. \tag{A.31}$$

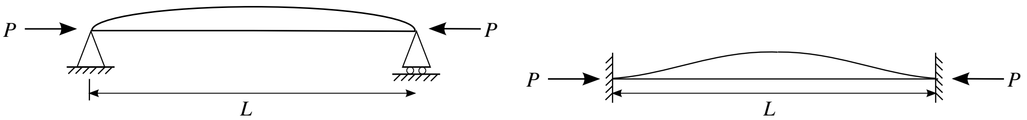

(a) Simply supported column schematic (b) Clamped column schematic

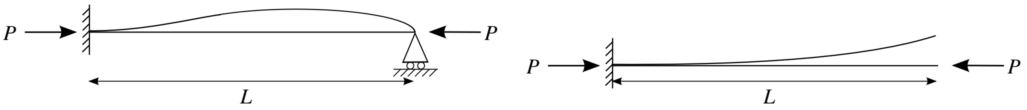

(c) Clamped-pinned column schematic (d) Clamped-free column schematic

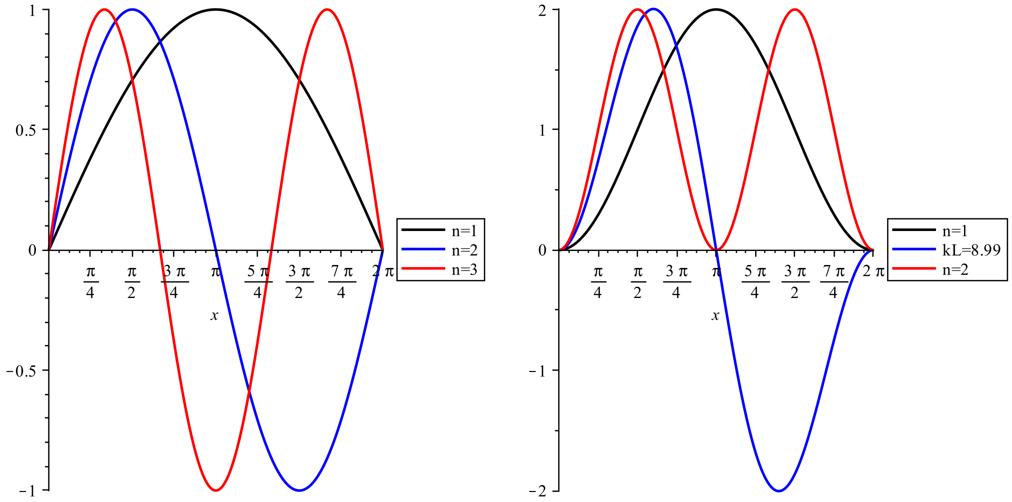

(e) Simply supported column deflection (f) Clamped column deflection

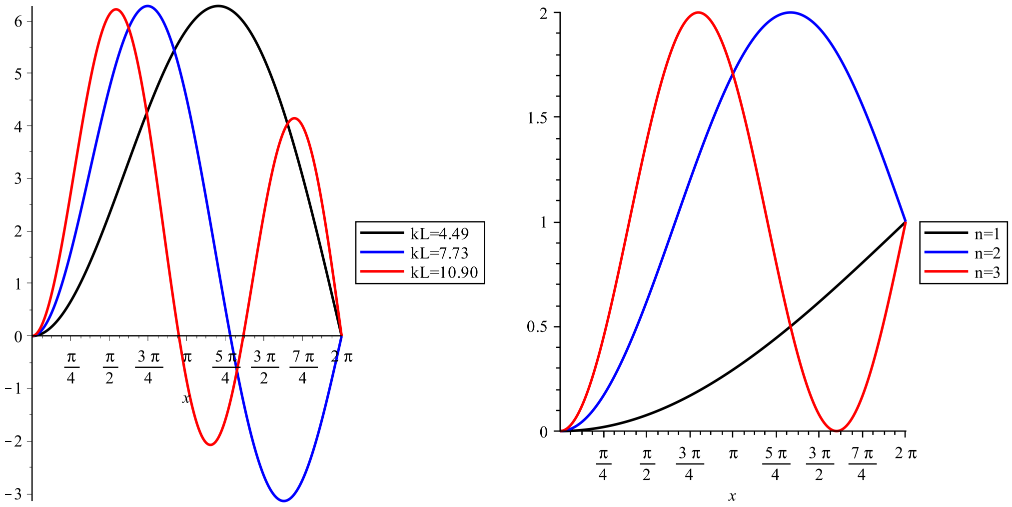

(g) Clamped-pinned column deflection (h) Clamped-free column deflection

Figure A.12: Schematics and corresponding deflection curves for columns of length L undergoing axial compression P under different boundary conditions. Figures A.12(a)-A.12(d) shows schematic representations of columns with different end supports. Figures A.12(e)-A.12(h) show the corresponding deflection curves for each case. In Figures A.12(e)-A.12(h) the black line represents the deflection curve corresponding to the smallest eigenvalue k and $P = P_{cr}$. The blue and red curves correspond to the second and third eigenvalues respectively. Deflection curves simulated in Maple.

Figure A.12(b) shows a schematic representing this set-up while the black line in Figure A.12(f) shows the deflection curve for $P = P_{cr}$.

- Clamped-pinned column

  For a column clamped at one end ($x = 0$) and simply supported at the other ($x = L$), the boundary conditions are $w(0) = w(L) = 0$, $w_x(0) = 0$ (zero derivative of deflection at clamped end) and $w_{xx}(L) = 0$ (zero bending moment at the simply supported end). The critical loading is

  $$P_{cr} = 2.04\frac{\pi^2 EI}{L^2} \tag{A.32}$$

  and the eigenfunction for the column deflection at P_{cr} is

  $$w(x) = B(\sin(kx) - kL\cos(kx) + k(L-x)) \tag{A.33}$$

  where $k \approx 4.49/L$, the smallest eigenvalue satisfying $kL = \tan(kL)$. A schematic representation of this set-up can be seen in Figure A.12(c) while the deflection corresponding to $P = P_{cr}$ is shown in Figure A.12(g) (black curve).

- Clamped-free column

  A column clamped at one end ($x = 0$) and free at the other ($x = L$) has boundary conditions $w(0) = 0$, $w_x(0) = 0$, $w_{xx}(L) = 0$ and $w_{xxx}(L) + k^2 w_x(L) = 0$. The last condition here represents zero shearing force at the free end. The critical loading force P_{cr} and corresponding deflection curve $w(x)$ are

  $$w(x) = A\left(\cos\left(\frac{\pi x}{2L}\right) - 1\right) \quad \text{when} \quad P_{cr} = \frac{\pi^2}{4}\frac{EI}{L^2}. \tag{A.34}$$

  Figure A.12(d) shows a schematic representing this set-up while the black curve in Figure A.12(h) shows the deflection when $P = P_{cr}$.

A.3 Plate Bending

In this section we extend the theory of beam structures and apply it to plates. The plates are assumed to be flat and thin (small thickness compared to axial dimensions), have uniform thickness and be linear elastic following Hooke's Law. First the basic mechanical concepts and force expressions are derived for plates undergoing deformation. The plate bending equations themselves are then derived.

A.3.1 Pure Bending of Plates

We consider the pure bending of plates, where the assumption is that the middle plane of the plate, which lies halfway between the two faces of the plate on the xy-plane, remains strain-free after deformation and can therefore be considered as the neutral surface, equivalent to the neutral axis in the corresponding beam theory [148]. It is also assumed that plane sections that are initially perpendicular to the middle plane of the plate remain perpendicular after deformation i.e. normals to the neutral surface remain normal [147, 148].

It is conventional to use the xyz-plane for this set-up, where the neutral surface lies along the xy-plane at $z = 0$. Once again z is directed in the positive upwards direction, normal to the undeformed plate, and vertical displacement is represented by w. Lateral deflection in the x and y directions are denoted by u and v respectively. As in Euler beam theory, the components of lateral displacement in the middle plane are small relative to w and so are neglected [147]. However, only the neutral plane of the plate is assumed to remain strain-free after deformation, therefore lateral displacement must be incorporated into displacement vectors when deflection is not measured from the neutral surface [13, 147]. To compare these two different scenarios consider two different points on an initially undeformed plate: point $O(x_1, y_1, 0)$ lying on the xy-plane

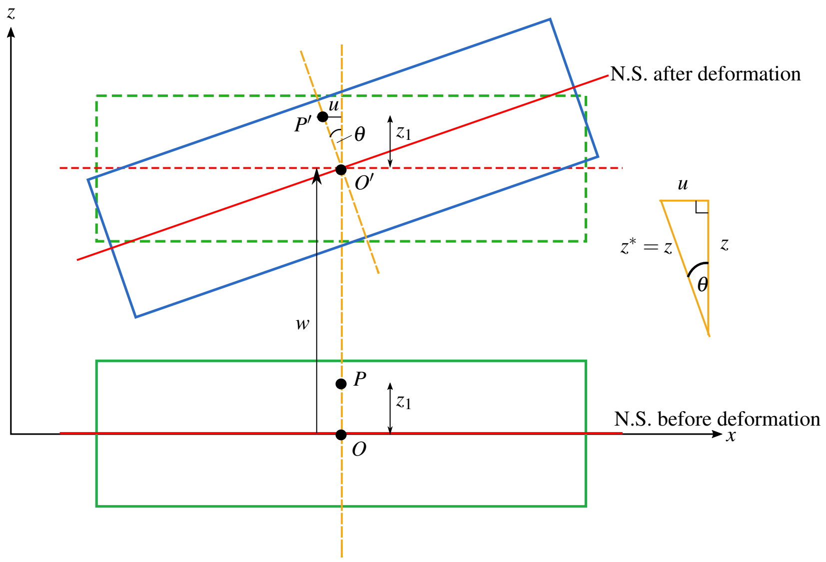

Figure A.13: Figure showing the method of measuring the axial deflection of plates. Axial deflection, u, in the x-direction is shown, where the green solid rectangle represents a cross-section of a plate before deformation and the blue rectangle shows the cross-section after deformation. Points O and P in the original element can be tracked to points O' and P' in the deformed element. The orange triangle shows the angle of rotation θ and axial deflection u. The abbreviation N.S. indicates the neutral surface of the plate.

and point $P(x_1, y_1, z_1)$ located a positive distance z_1 directly above it (see Figure A.13, which shows the cross-section of a plate deforming along its x-axis in the z-direction). After deformation these two points are displaced to the corresponding points of O' and P' which have new coordinates

$$\begin{aligned} O'(x,y,z) = &\quad (x',y',z') = (x_1, y_1, w(x,y)), \\ P'(x,y,z) = &\quad (x'',y'',z'') = (x_1 + u(x,y,z), y_1 + v(x,y,z), z_1 + w(x,y)). \end{aligned} \tag{A.35}$$

Thus it can be seen that point P has been displaced both vertically and laterally, whereas O has been displaced only vertically.

A.3.2 Stress/Strain Relations in Plates

We consider plates to be 3-D structures, where one dimension (the height or thickness, h) is much smaller than the other two dimensions. Because of the increased dimensions compared to beams, more components of stress and strain are present. Specifically, three axial stress (σ_{xx}, σ_{yy}, σ_{zz}) and axial strain components (ε_{xx}, ε_{yy}, ε_{zz}) exist. Additionally, six shear stress (τ_{xy}, τ_{xz}, τ_{yx}, τ_{yz}, τ_{zx}, τ_{zy}) and shear strain components (γ_{xy}, γ_{yx}, γ_{yx}, γ_{yz}, γ_{zx}, γ_{zy}) also exist. However, if the assumptions of plane stress, where forces in the z-direction are regarded as negligible, are applied then some of these terms can be neglected ($\sigma_z = 0$, $\tau_{xz} = \tau_{yz} = 0$, $\gamma_{xz} = \gamma_{yz} = 0$) [70, 146]. A final assumption states there is no change in thickness, h, of the plate, therefore $\varepsilon_z = 0$ [13]. The equations relating each of the remaining stress and strain components are as follows:

$$\begin{aligned}
\sigma_{xx} &= \frac{E}{(1-\nu^2)}\left(\varepsilon_{xx} + \nu\varepsilon_{yy}\right), & \sigma_{yy} &= \frac{E}{(1-\nu^2)}\left(\varepsilon_{yy} + \nu\varepsilon_{xx}\right), \\
\varepsilon_{xx} &= \frac{1}{E}\left(\sigma_{xx} - \nu\sigma_{yy}\right), & \varepsilon_{yy} &= \frac{1}{E}\left(\sigma_{yy} - \nu\sigma_{xx}\right), \\
\tau_{xy} &= G\gamma_{xy} = \frac{E}{2(1+\nu)}\gamma_{xy}, & &
\end{aligned} \tag{A.36}$$

where E is Young's modulus, ν is Poisson's ratio and G is the shear modulus [70]. Equations (A.36) stem from the 3-D derivation of Hooke's Law which assumes that each stress relation considers a superposition of two effects: elongation (or contraction) in the normal direction, and consequent contraction (or elongation) in the remaining two axial directions.

A.3.3 Strain-Displacement Equations

As previously noted, horizontal deflection cannot be ignored in the case of pure bending if the deflection is measured from any point not lying on the neutral surface. Thus,

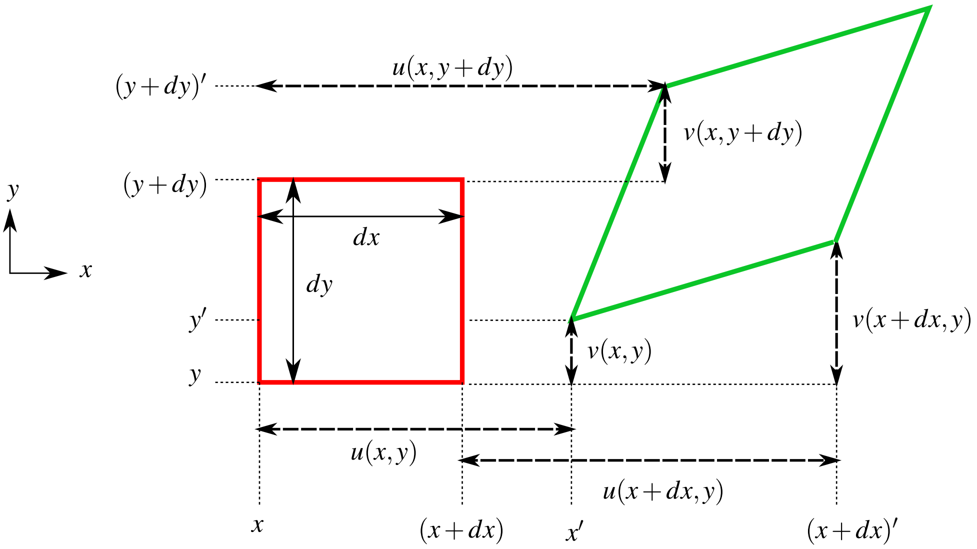

Figure A.14: Figure explaining the derivation of normal and shear strain relations in terms of lateral deflections u and v. Figure shows a bird's-eye view of a small plate element of area $\mathrm{d}x\mathrm{d}y$ as it is deformed in the xy-plane. Lateral deflection in the x-direction and y-directions are represented by u and v respectively.

horizontal deflection must be incorporated in these cases, and in the cases where pure bending assumptions are not adhered to, via strain-displacement equations. Consider the movement and deformation of a small plate element of length dx and breadth dy as seen in Figure A.14. The expression for strain [69] is given as:

$$\text{strain} = \frac{\text{change in length}}{\text{original length}} = \varepsilon \text{ or } \gamma \quad (\varepsilon = \text{axial (normal) strain}, \gamma = \text{shear strain}). \tag{A.37}$$

The expression for axial (normal) strain ε_{xx} can therefore be determined by

$$\begin{aligned} \varepsilon_{xx} &= \frac{\text{deformed length - original length}}{\text{original length}} \\ &= \frac{((x+dx)' - x') - dx}{dx} \\ &= \frac{u(x+dx) - u(x)}{dx} \\ &= \frac{\partial u}{\partial x}. \end{aligned} \tag{A.38}$$

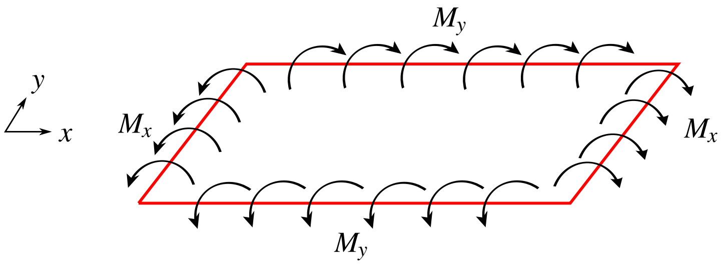

Figure A.15: Chosen sign convention for plate bending moments M_x and M_y.

Contrastingly, the expression for shear strain is

$$\begin{aligned}\gamma_{xy} &= \frac{\text{deformed breadth-original breadth}}{\text{original length}} + \frac{\text{deformed length-original length}}{\text{original breadth}} \\ &= \frac{v(x+dx,y)-v(x,y)}{dx} + \frac{u(x,y+dy)-u(x.y)}{dy} \\ &= \frac{\partial v}{\partial x} + \frac{\partial u}{\partial y}.\end{aligned} \tag{A.39}$$

Similarly, it can be shown that

$$\varepsilon_{yy} = \frac{\partial v}{\partial y}, \quad \gamma_{yx} = \gamma_{xy} = \frac{\partial v}{\partial x} + \frac{\partial u}{\partial y}. \tag{A.40}$$

A.3.4 Relationship between Stress, Strain and Curvature

In a similar way as considered in the Section A.2.1 for beam bending, the sign-convention we choose for plate bending results in the top surface of the plate being stretched (positive stress and strain) in both the x and y-directions while the bottom surface is compressed (negative stress and strain). Positive bending moments M_x and M_y for this set-up are shown in Figure A.15, which correspond to negative curvature in both the x and y-directions. Relating the curvature and deflection w, an argument similar to that described in section A.2.2 determines that

$$\frac{1}{\rho_x} = -\frac{\partial^2 w}{\partial x^2}, \quad \frac{1}{\rho_y} = -\frac{\partial^2 w}{\partial y^2}, \tag{A.41}$$

where ρ_x and ρ_y are the radii of curvature in the x and y directions respectively [147]. The relations linking strain and curvature are

$$\varepsilon_{xx} = \frac{z}{\rho_x}, \quad \varepsilon_{yy} = \frac{z}{\rho_y}, \tag{A.42}$$

[148] where z is signed. Equations (A.41) and (A.42) can be combined to find the strain-displacement equations

$$\varepsilon_{xx} = -z\frac{\partial^2 w}{\partial x^2}, \quad \varepsilon_{yy} = -z\frac{\partial^2 w}{\partial y^2}. \tag{A.43}$$

Shear strain can also be expressed as a function of w using equation (A.39) and referring to Figure A.13. The angle θ in Figure A.13 can be shown to equal $\frac{\partial w}{\partial x}$, therefore

$$u = -z\frac{\partial w}{\partial x}. \tag{A.44}$$

Similarly,

$$v = -z\frac{\partial w}{\partial y}. \tag{A.45}$$

Combining equation (A.39) with (A.44) and (A.45) , it can be shown that

$$\gamma_{xy} = -2z\frac{\partial^2 w}{\partial x \partial y}, \tag{A.46}$$

where $\frac{\partial^2 w}{\partial x \partial y}$ is called the twist of the surface with respect to the x and y-axes [148]. Recall the direction of the bending moments from Figure A.15. In addition to the bending moments M_x and M_y, twisting moments M_{xy} and M_{yx} must also be incorporated in plate deformations. The chosen sign convention for twisting moments is shown in Figure A.16, which also shows the directions for axial and shear stresses σ_{xx}, σ_{yy}, τ_{xy}

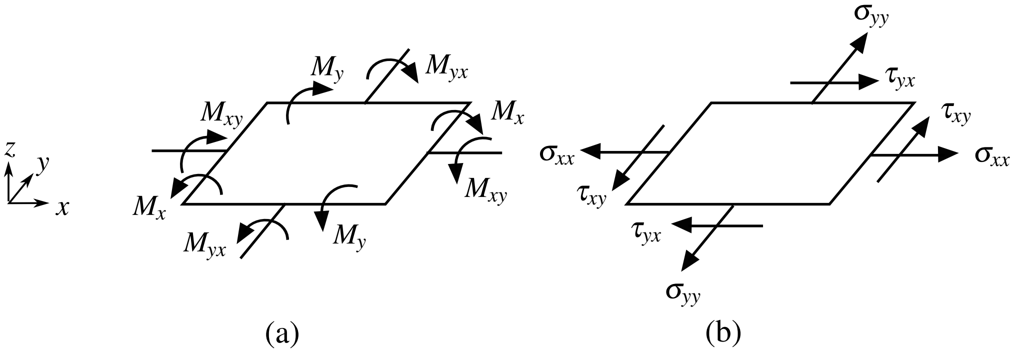

Figure A.16: Sign convention for positive bending and twisting moments and shear stress. Figure (a) shows a small element of the plate with area dxdy and the chosen directions for positive bending moments M_x and M_y and twisting moments M_{xy} and M_{yx}. Figure (b) shows the usual sign convention for axial stresses σ_{xx} and σ_{yy} and shear stresses τ_{xy} and τ_{yx}.

and τ_{yx}. The formulae for bending and twisting moments [147] are

$$M_\alpha = \int \sigma_{\alpha\alpha} z \,\mathrm{d}z, \quad M_{\alpha\beta} = \int \tau_{\alpha\beta} z \,\mathrm{d}z. \tag{A.47}$$

The bending moment M_x is therefore found as

$$\begin{aligned} M_x &= \int_{-\frac{h}{2}}^{\frac{h}{2}} \sigma_{xx} z \,\mathrm{d}z \\ &= \frac{E}{1-\nu^2} \int_{-\frac{h}{2}}^{\frac{h}{2}} \left(\varepsilon_{xx} + \nu \varepsilon_{yy}\right) \mathrm{d}z \\ &= -\frac{E}{1-\nu^2} \left(\frac{\partial^2 w}{\partial x^2} + \nu \frac{\partial^2 w}{\partial y^2} \right) \int_{-\frac{h}{2}}^{\frac{h}{2}} z^2 \,\mathrm{d}z \\ &= -\frac{Eh^3}{12(1-\nu^2)} \left(\frac{\partial^2 w}{\partial x^2} + \nu \frac{\partial^2 w}{\partial y^2} \right) \\ &= -D \left(\frac{\partial^2 w}{\partial x^2} + \nu \frac{\partial^2 w}{\partial y^2} \right) \end{aligned} \tag{A.48}$$

where $D = (Eh^3)/(12(1-\nu^2))$ is the flexural rigidity of the plate and h is the height (or thickness) of the plate [147]. Similarly,

$$M_y = -D\left(\frac{\partial^2 w}{\partial y^2} + \nu\frac{\partial^2 w}{\partial x^2}\right), \quad M_{xy} = D(1-\nu)\frac{\partial^2 w}{\partial x \partial y}, \quad M_{yx} = -D(1-\nu)\frac{\partial^2 w}{\partial x \partial y}. \tag{A.49}$$

Notice that $M_{xy} = -M_{yx}$, a consequence of the chosen sign convention for positive and negative twisting moments in relation to the positive sign convention for shear stresses τ_{xy} and τ_{yx} as seen in Figure A.16 (i.e. $M_{xy} = -\int \tau_{xy} z\, \mathrm{d}z$ and $M_{yx} = \int \tau_{yx} z\, \mathrm{d}z$). It is noted that a plate bent in only one direction, for example in the x-direction, like a beam will have $M_y = 0$ and $M_x = -D\frac{\partial^2 w}{\partial x^2}$, which is comparable to equation (A.21) describing beam behaviour.

A.3.5 Bending of Plates by Distributed Lateral Load

Having extended the basic mechanical concepts of the beam to the plate structure, derivations of the plate bending equations can be examined. First we consider the bending of a plate by a distributed lateral load acting perpendicular to the neutral surface of the plate. The method followed is the same as described in [147]. The presence of the load, q, produces vertical shearing forces τ_{xz} and τ_{yz}. The variation of τ_{xz} and τ_{yz} along small distances dx and dy can be neglected and therefore τ_{xz} and τ_{yz} can be incorporated into the plate bending equations by the introduction of concentrated forces Q_x and Q_y, which pass through the centroids of the sides of the elements as seen in Figure A.17(b). We therefore have:

$$\begin{array}{lll} \text{Vertical shearing forces (per unit length)}: & Q_x = \int_{-\frac{h}{2}}^{\frac{h}{2}} \tau_{xz}\, dz, & Q_y = \int_{-\frac{h}{2}}^{\frac{h}{2}} \tau_{yz}\, dz; \\ \text{Bending Moments (per unit area)}: & M_x = \int_{-\frac{h}{2}}^{\frac{h}{2}} \sigma_x z\, dz, & M_y = \int_{-\frac{h}{2}}^{\frac{h}{2}} \sigma_y z\, dz; \\ \text{Twisting Moments (per unit area)}: & M_{xy} = -\int_{-\frac{h}{2}}^{\frac{h}{2}} \tau_{xy} z\, dz, & M_{yx} = \int_{-\frac{h}{2}}^{\frac{h}{2}} \tau_{yx} z\, dz; \end{array} \tag{A.50}$$

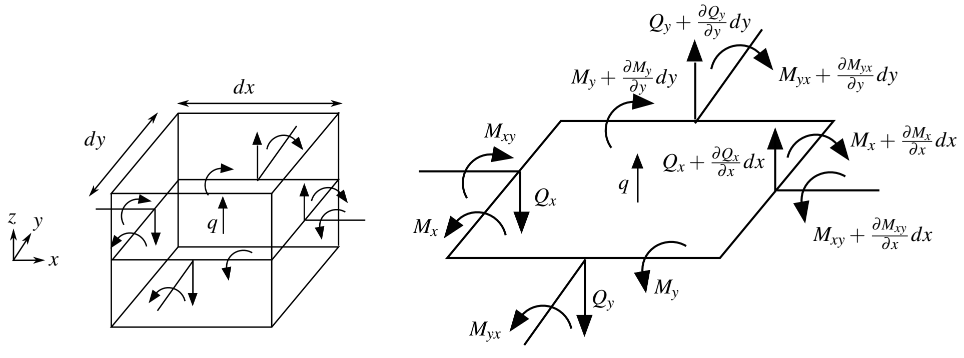

(a) (b)

Figure A.17: Forces and bending and twisting moments considered in the pure bending of plates. Figure (a) shows a small plate element of length dx and breadth dy and the directions of the forces and moments that are required to derive the plate bending equation, where q is an applied vertical load. Figure (b) shows a more detailed representation of the neutral surface of the plate with labelled forces and moments.

where h is the height of the plate.

The plate bending equation is essentially derived from force-balance equations, where higher order terms (H.O.T) are neglected. Forces acting on the z-axis are first balanced:

$$-Q_x dy + \left(Q_x + \frac{\partial Q_x}{\partial x}\right) dy - Q_y dx + \left(Q_y + \frac{\partial Q_y}{\partial y}\right) dx + q\, dx\, dy = 0, \tag{A.51}$$

which can be simplified to

$$\frac{\partial Q_x}{\partial x} + \frac{\partial Q_y}{\partial y} + q = 0. \tag{A.52}$$

Moments of forces acting on the element with respect to the y-axis can be equilibrated:

$$\begin{aligned} M_x dy &= \left(M_x + \frac{\partial M_x}{\partial x} dx\right) dy - M_{yx} dy + \left(M_{yx} + \frac{\partial M_{yx}}{\partial y} dy\right) dx \\ &\quad - \left(Q_x + \frac{\partial Q_x}{\partial x} dx\right) dx\, dy \qquad \text{(A.53)} \\ \Longrightarrow \qquad 0 &= \frac{\partial M_x}{\partial x} dx\, dy + \frac{\partial M_{yx}}{\partial y} dx\, dy - Q_x dx\, dy + \text{H.O.T}, \end{aligned}$$

which reduces to

$$\frac{\partial M_x}{\partial x} + \frac{\partial M_{yx}}{\partial y} = Q_x. \tag{A.54}$$

Similarly, the moments of forces acting on the element with respect to the x-axis are equilibrated:

$$\frac{\partial M_y}{\partial y} - \frac{\partial M_{xy}}{\partial x} = Q_y. \tag{A.55}$$

Substitution of equations (A.54) and (A.55) into (A.52) gives:

$$\begin{aligned} \frac{\partial}{\partial x}\left(\frac{\partial M_{yx}}{\partial y} + \frac{\partial M_x}{\partial x}\right) + \frac{\partial}{\partial y}\left(-\frac{\partial M_{xy}}{\partial x} + \frac{\partial M_y}{\partial y}\right) + q =& 0 \\ \implies \quad \frac{\partial^2 M_{yx}}{\partial x \partial y} + \frac{\partial^2 M_x}{\partial x^2} - \frac{\partial^2 M_{xy}}{\partial x \partial y} + \frac{\partial^2 M_y}{\partial y^2} =& -q. \end{aligned} \tag{A.56}$$

Simplifying this equation using equations (A.48) and (A.49) gives:

$$\begin{aligned} -D\left(\frac{\partial^4 w}{\partial x^4} + \nu \frac{\partial^4 w}{\partial x^2 \partial y^2} + \frac{\partial^4 w}{\partial y^4} + \nu \frac{\partial^4 w}{\partial x^2 \partial y^2}\right) - 2D(1-\nu)\frac{\partial^4 w}{\partial x^2 \partial y^2} &= -q \\ \implies \frac{\partial^4 w}{\partial x^4} + \frac{\partial^4 w}{\partial y^4} + 2\frac{\partial^4 w}{\partial x^2 \partial y^2} &= \frac{q}{D} \\ \implies \nabla^4 w(x,y) &= \frac{q}{D}, \end{aligned} \tag{A.57}$$

which is the equation for the pure bending of plates.

A.3.6 Combined Bending and Tension or Compression in Plates

In pure bending plate theory it is assumed bending occurs by lateral loads, and deflections are so small that the stretching of the middle plane can be neglected so it is regarded as a neutral surface of the plate. However, if in addition to lateral loads there are forces acting in the middle plane of the plate, stretching or compression of the middle plane occurs [147]. If the stresses in the middle plane are sufficiently large, their effect on the bending of the plate cannot be ignored and must be considered. Again, the derivation follows that described in [147].

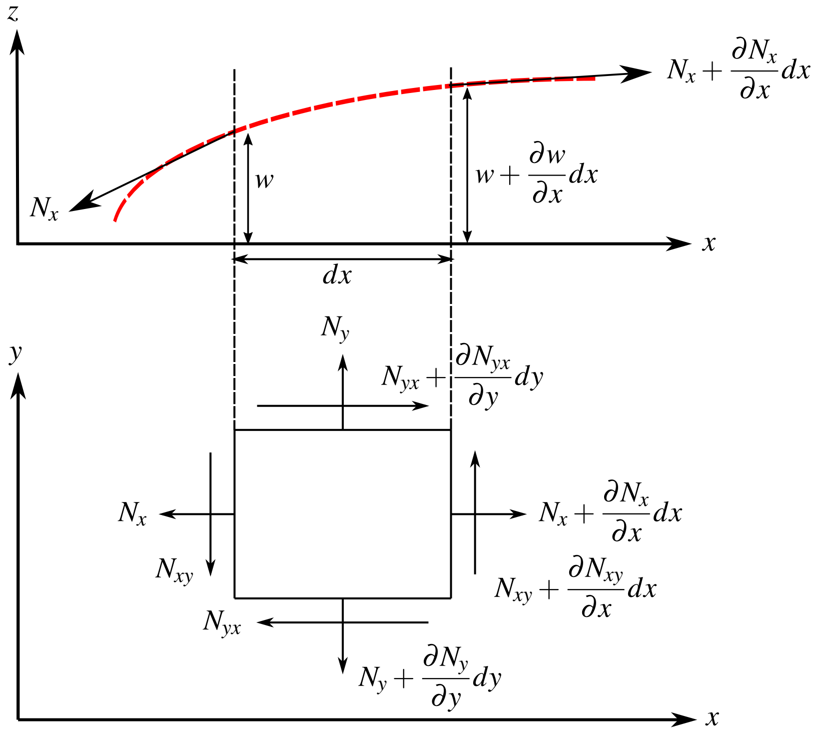

Figure A.18: The directions of tensile force components in the extension of the middle plane of a plate element as seen from two different viewpoints. Both a cross-section of the xz-plane (above) and xy-plane (below) are displayed for an element of area $\mathrm{d}x\mathrm{d}y$. N represents the in-plane forces of the middle plane.

Consider the equilibrium of a small element of the plate. In addition to the moments and forces considered previously (see Figure A.17), forces, N, acting in the middle plane of the plate are also considered (see Figure A.18, where notation shown is per unit length and $N_{xy} = N_{yx}$). The forces N can be incorporated into the plate bending equation by finding their projection on the positive z-axis and adding this to load q in equation (A.57), which also acts in the positive z-direction, as seen in Figure A.17. Projecting the forces on the x and y-axes gives the following equations of equilibrium:

$$\frac{\partial N_x}{\partial x} + \frac{\partial N_{yx}}{\partial y} = 0 \quad \text{and} \quad \frac{\partial N_y}{\partial y} + \frac{\partial N_{xy}}{\partial x} = 0. \tag{A.58}$$

The projection of forces on the z-axis must also be considered by taking into account the vertical deflection of the plate. Owing to the curvature of the plate in the xz-plane (as seen in Figure A.18), the projection of the normal forces N_x along the positive z-axis is:

$$\begin{aligned}
&-N_x dy \frac{\partial}{\partial x}(w) + \left(N_x + \frac{\partial N_x}{\partial x} dx\right) dy \frac{\partial}{\partial x}\left(w + \frac{\partial w}{\partial x} dx\right) \\
=&-N_x \frac{\partial w}{\partial x} dy + \left(N_x + \frac{\partial N_x}{\partial x} dx\right)\left(\frac{\partial w}{\partial x} + \frac{\partial^2 w}{\partial x^2} dx\right) dy \\
=&N_x \frac{\partial w^2}{\partial x^2} dx dy + \frac{\partial N_x}{\partial x}\frac{\partial w}{\partial x} dx dy + \frac{\partial N_x}{\partial x}\frac{\partial^2 w}{\partial x^2} dx^2 dy.
\end{aligned} \tag{A.59}$$

Again neglecting H.O.T, this gives the z-projection of the normal forces N_x as:

$$N_x \frac{\partial w^2}{\partial x^2} dx dy + \frac{\partial N_x}{\partial x}\frac{\partial w}{\partial x} dx dy. \tag{A.60}$$

Similarly the projection of the normal forces N_y along the positive z-axis is:

$$N_y \frac{\partial w^2}{\partial y^2} dx dy + \frac{\partial N_y}{\partial y}\frac{\partial w}{\partial y} dx dy. \tag{A.61}$$

The projection of the shearing forces N_{xy} and N_{yx} on the z-axis are also considered and it is found that:

$$\begin{aligned}
\text{Projection of } N_{xy} &= N_{xy} \frac{\partial^2 w}{\partial x \partial y} dx dy + \frac{\partial N_{xy}}{\partial x}\frac{\partial w}{\partial y} dx dy, \\
\text{Projection of } N_{yx} &= N_{yx} \frac{\partial^2 w}{\partial x \partial y} dx dy + \frac{\partial N_{yx}}{\partial y}\frac{\partial w}{\partial x} dx dy.
\end{aligned} \tag{A.62}$$

The total projection of all the normal and shearing forces (in the element) on the z-axis can be found by adding together the expressions in equations (A.60-A.62). This can be further simplified by recalling the equality $N_{xy} = N_{yx}$, and the final expression for the projection of forces on the z-axis on the small element as shown in Figure A.18 is:

$$N_x \frac{\partial^2 w}{\partial x^2} dx dy + N_y \frac{\partial^2 w}{\partial y^2} dx dy + 2N_{xy} \frac{\partial^2 w}{\partial x \partial y} dx dy. \tag{A.63}$$

Adding expression (A.63) to the load q acting on the pure bending element in equation (A.57) it is found that:

$$\frac{\partial^4 w}{\partial x^4} + 2\frac{\partial^4 w}{\partial x^2 \partial y^2} + \frac{\partial^4 w}{\partial y^4} = \frac{1}{D}\left(q + N_x \frac{\partial^2 w}{\partial x^2} + N_y \frac{\partial^2 w}{\partial y^2} + 2N_{xy}\frac{\partial^2 w}{\partial x \partial y}\right). \tag{A.64}$$

This equation can be used to determine the deflection of a plate when in-plane forces N_x, N_y and N_{xy} are not small in comparison with the critical values of these forces i.e. the forces required to buckle the plate.

In the case of large deformations of a plate, both the stresses and strain in the middle surface must be considered. In this case, the deflection of the plate can be described using an equation of the same form as equation (A.64). In this case however, the in-plane forces N now depend on both the external forces applied in the xy-plane and the strain in the neutral surface (caused by bending). Strain is now taken to be non-linear and as such can be described by:

$$\begin{aligned} \varepsilon_{xx} &= \frac{\partial u}{\partial x} + \frac{1}{2}\left(\frac{\partial^2 w}{\partial x^2}\right), \quad \varepsilon_{yy} = \frac{\partial v}{\partial y} + \frac{1}{2}\left(\frac{\partial^2 w}{\partial y^2}\right), \\ \tau_{xy} = \tau_{yx} &= \frac{\partial u}{\partial y} + \frac{\partial v}{\partial x} + \frac{1}{2}\left(\frac{\partial w}{\partial x}\frac{\partial w}{\partial y}\right). \end{aligned} \tag{A.65}$$

After some algebra the equation describing large deformations in plates can be derived. It is given by:

$$\frac{\partial^4 w}{\partial x^4} + 2\frac{\partial^4 w}{\partial x^2 \partial y^2} + \frac{\partial^4 w}{\partial y^4} = \frac{1}{D}\left(q + \frac{\partial}{\partial x}\left(N_x \frac{\partial w}{\partial x} + N_{xy}\frac{\partial w}{\partial y}\right) + \frac{\partial}{\partial y}\left(N_y \frac{\partial w}{\partial y} + N_{xy}\frac{\partial w}{\partial x}\right)\right). \tag{A.66}$$

Equations (A.65) and (A.66) together form the Föppl-von Kármán equations which describe the large deflections of plates.

Appendix B

Linear Viscoelastic Materials

A background describing some viscoelastic material properties and behaviour is described here. The concept of viscoelasticity is explored in Chapter 5.

B.1 Viscoelasticity

Viscoelasticity describes materials exhibiting properties found in both elastic and viscous substances [65]. As already noted, an elastic solid in shear is described by the constitutive equation

$$\tau = G\gamma, \tag{B.1}$$

where τ and γ are the shear stress and strain , and G is the modulus of rigidity (sometimes also called the modulus of elasticity in shear, or the shear modulus) [146]. In elastic materials, the compliance J is the inverse of G i.e. $J = 1/G$, and can be thought of as the opposite of stiffness.

In contrast to elastic materials, the description of viscous materials includes time as

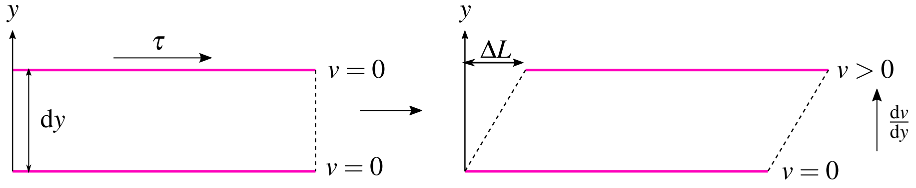

(a) (b)

Figure B.1: Illustration of Newton's Law of Viscosity. A velocity gradient, $\mathrm{d}v/\mathrm{d}y$, is induced in the fluid between the two plates (as shown in pink) on application of a shear force, τ, to the top plate (see Figure (a)). Velocity is larger at the top of the fluid, thus the velocity gradient is directed upwards (in the positive y-direction) as seen in Figure (b).

a variable. The concept of viscosity can be explained by considering two plates suspended in a fluid and separated by a small distance, $\mathrm{d}y$. On setting one of the plates (for example, the top plate) in motion via an applied shear stress, τ, the fluid in the layer closest to the moving plate begins to move. Over time, fluid further from the moving plate also begins to move, and a velocity gradient, $\mathrm{d}v/\mathrm{d}y$, is induced across the two plates (see Figure B.1(b)). Newton's Law of Viscosity describes how the applied shear stress and resulting velocity gradient induced in the fluid are directly proportional. The law states that

$$\tau = \eta \frac{\mathrm{d}v}{\mathrm{d}y} \tag{B.2}$$

where η is the viscosity of the fluid, and $\mathrm{d}v/\mathrm{d}y$ is the velocity gradient [156].

Recalling the equation describing shear strain (A.6) and comparing Figure A.3(c) with Figure B.1, we find that

$$\tau = \eta \frac{\mathrm{d}v}{\mathrm{d}y} = \eta \frac{\mathrm{d}}{\mathrm{d}y}\left(\frac{\mathrm{d}u}{\mathrm{d}t}\right) = \eta \frac{\mathrm{d}}{\mathrm{d}t}\left(\frac{\mathrm{d}u}{\mathrm{d}y}\right) = \eta \frac{\mathrm{d}}{\mathrm{d}t}\left(\frac{\mathrm{d}\Delta L}{\mathrm{d}W}\right), \tag{B.3}$$

where $u \equiv \Delta L$ are the shear displacements at the top plate (see Figure B.1(b)). Using equation (A.6) we can therefore rewrite the constitutive equation (B.2) in the equivalent form

$$\tau = \eta \frac{\mathrm{d}\gamma}{\mathrm{d}t}, \tag{B.4}$$

where $\mathrm{d}\gamma/\,\mathrm{d}t$ is the shear rate and t represents time dependence. The units of viscosity are $\mathrm{kg\,m^{-1}\,s^{-1}}$ (or Pa s).

The combination of both elastic and viscous components can be seen in the behaviour of a deformed viscoelastic material. On the removal of an applied force, the material will return to its original dimensions (a result of the elastic component), however, rather than occuring immediately, the response will occur over some time (a result of the viscous component) [156].

It is noted that only linear viscoelastic materials, where stress and strain are linearly related by a function of time [49], are considered here. The Boltzmann Superposition Principle can therefore be implemented. It states that the response of a linear viscoelastic material will be a function of its entire mechanical history [156] and that each single mechanical effect contributes a linearly additive response in the material [49].

B.1.1 Experimental Responses in Viscoelastic Materials and Measures of Viscoelasticity

The behaviour of viscoelastic (VE) materials can be described by analysing the response of the material during different experiments which measure either the stress or strain in the material through time. In stress-relaxation experiments, stress within the material is measured while strain, $\gamma = \gamma_0$, is held constant throughout [80]. Through time the stress within the VE material will decrease (see Figure B.2(a)) and the resulting behaviour may be expressed through the shear stress relaxation function (or modulus) $G(t)$ [49], where

$$\tau(t) = \gamma_0 G(t). \tag{B.5}$$

The stress relaxation modulus $G(t)$ is larger at early time-steps, indicating that the material is stiffer and thus less compliant. At later time-steps, $G(t)$ is lower and the

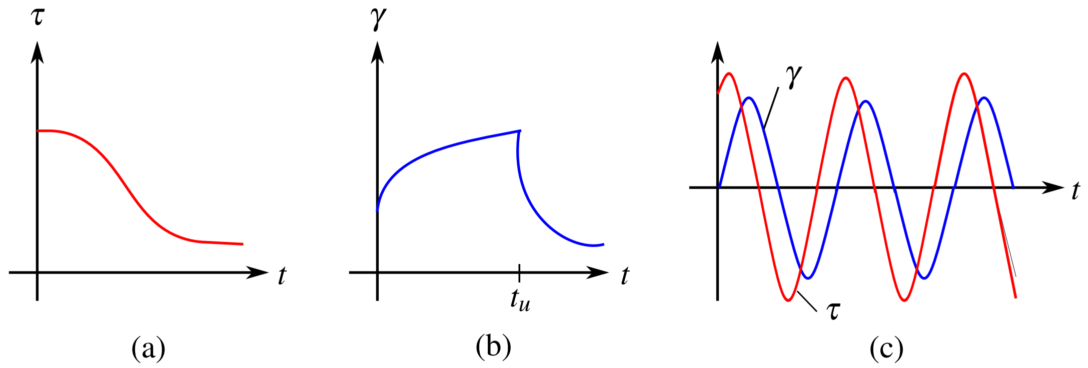

Figure B.2: Experimental responses of a viscoelastic material in response to deformation. Figure (a) shows the stress response in a stress-relaxation experiment while Figure (b) shows the strain response in a creep experiment where t_u represents the time that load is removed. Figure (c) shows the results of a dynamic experiment, where blue represents applied strain, γ (varied periodically), and red represents the resulting stress, τ.

material can be described as more compliant. At the long-term time limit the stress relaxation modulus is said to be at its rubbery limit and the material is as flexible as it can possibly be. The material is at its ‘glassy modulus’ when it is at its least compliant early on in the experiments [156].

Contrastingly, creep experiments describe the response of a VE material subject to an applied constant stress, $\tau = \tau_0$, through time [156]. The deformation in the VE material increases as time progresses, thus strain increases (as seen in Figure B.2(b)). The equation describing the strain is

$$\gamma(t) = \tau_0 J(t), \tag{B.6}$$

where $J(t)$ is the compliance function, a non-decreasing function of t. Note that while in an elastic material $J(t) = J = 1/G$, in a VE material $J(t) \neq 1/G(t)$ [49]. At early time-steps the compliance of a material is low, but becomes greater at later times. Thus the value of $J(t)$ at its glassy limit is low, while at its rubbery limit is high [156].

Dynamic (or periodic) experiments measuring the response of a VE material subject to stress or strain oscillating periodically with frequency ω may also be carried out [80]. An elastic material subject to a sinusoidal strain with maximum amplitude γ_0 will be perfectly in-phase with the resultant stress [156], however a linear VE material will be out-of-phase such that

$$\begin{aligned}\tau =&\gamma_0 \sin(\omega t+\delta)\\ =&\gamma_0 \left(\sin(\omega t)\cos(\delta)+\cos(\omega t)\sin(\delta)\right)\\ =&\gamma_0 \left(\sin(\omega t)G'+\cos(\omega t)G''\right),\end{aligned} \tag{B.7}$$

where δ is the phase angle between the stress and strain response [49] (see Figure B.2(c)). The amount of energy stored and recovered per unit cycle is measured by $G'(\omega)$ which is the storage modulus (the stress in-phase with strain). Conversely, the loss modulus $G''(\omega)$ measures the energy lost per unit cycle and is the stress 90° out-of-phase [49]. Note an elastic material (perfectly in-phase) has a loss modulus $G''(\omega)=0$ as no energy is lost through time.

B.1.2 Mechanical models of viscoelasticity

For the purposes of mechanical modelling, elasticity is represented by Hookean springs while viscous elements are represented by dashpots (which may be thought of as pistons moving in oil) [49]. As viscoelastic materials display some elastic and some viscous behaviour, they may be represented by a combination of both springs and dashpots [156], each with their own elastic or viscosity coefficient (G or η). The two simplest mechnanical models for viscoelasticity are the Maxwell element, where a linear spring and linear dashpot are connected in series as shown in Figure B.3(a), and the Kelvin-Voight element, where they are connected in parallel as shown in Figure B.3(b) [80]. Descriptions of both set-ups are given below (more details can be found in [49, 80, 156]):

Maxwell element (Figure B.3(a)):

The stress in both the viscous and elastic element is equal $(\tau = \tau_1 = \tau_2)$, however the total strain is the sum of the strains contributed by the separate elements, $\gamma = \gamma_1 + \gamma_2$. Each of the separate elements can be described by the following:

$$\begin{aligned} \text{Hookean spring:} \quad \tau_1 = G\gamma_1 \quad &\Longrightarrow \quad \frac{\mathrm{d}\tau_1}{\mathrm{d}t} = G\frac{\mathrm{d}\gamma_1}{\mathrm{d}t}, \\ \text{Newtonian dashpot:} \quad \tau_2 = \eta\frac{\mathrm{d}\gamma_2}{\mathrm{d}t} \quad &\Longrightarrow \quad \frac{\mathrm{d}\gamma_2}{\mathrm{d}t} = \frac{1}{\eta}\tau_2. \end{aligned} \tag{B.8}$$

Strains are additive in this case and thus the equation describing this system is found to be

$$\frac{\mathrm{d}\gamma}{\mathrm{d}t} = \frac{1}{G}\frac{\mathrm{d}\tau}{\mathrm{d}t} + \frac{\tau}{\eta}. \tag{B.9}$$

In a stress-relaxation experiment strain is held constant at γ_0. Assuming that $\mathrm{d}\gamma/\,\mathrm{d}t = 0$ and that initial strain is $\gamma(0) = \gamma_0$ the solution to equation (B.9) is found to be

$$\tau = \gamma_0\, G \exp\left(-\frac{t}{\tau_r}\right) = \gamma_0\, G(t), \tag{B.10}$$

where $G(t)$ is the stress-relaxation function and $\tau_r = G/\eta$ is the relaxation time i.e. the time required for stress relaxation to occur [49].

Kelvin-Voight element (Figure B.3(b)):

The strain in both model elements is equal $(\gamma = \gamma_1 = \gamma_2)$, while the total stress is the sum of the stresses contributed by the separate elements $(\tau = \tau_1 + \tau_2)$. Referring to equation (B.8), the constitutive equation for the system is

$$\tau = G\gamma + \eta\,\frac{\mathrm{d}\gamma}{\mathrm{d}t}. \tag{B.11}$$

Creep experiments hold stress constant at τ_0 while observing the effect on strain. On integration of equation (B.11), using the assumption that initial strain is $\tau(0) = \tau_0$, the

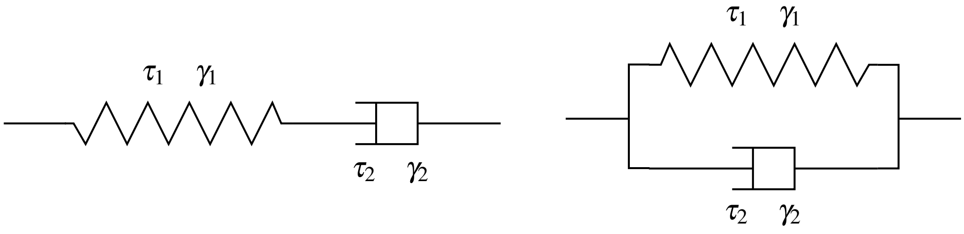

(a) Maxwell element (b) Kelvin-Voight element

Figure B.3: Mechanical models for modelling viscoelasticity. Figure (a) shows a Maxwell element consisting of an elastic spring and viscous dashpot connected in series and Figure (b) shows a Kelvin-Voight element consisting of an elastic spring and viscous dashpot connected in parallel. τ_1 and τ_2 are the stresses contributed to the systems by the spring and dashpot respectively, while γ_1 and γ_2 are the strain contributions.

solution is found as

$$\gamma = \frac{\tau_0}{G}\left(1 - \exp\left(-\frac{t}{\tau_c}\right)\right) = \tau_0 J\left(1 - \exp\left(-\frac{t}{\tau_c}\right)\right) = \tau_0 J(t), \tag{B.12}$$

where $J(t)$ is the compliance function and $\tau_c = \eta/G$ is the retardation time i.e. a measure of the time the dashpot delays spring extension to equilibrium length [49].

The Maxwell and Kelvin-Voight elements give limited results in terms of describing the behaviour of real viscoelastic materials, partly due to the fact that the Maxwell element is unsuitable for measuring creep while the Kelvin-Voight element is unsuitable for use in the measurement of stress-relaxation [156]. More realistic models can be built using different combinations of several Maxwell and Kelvin-Voight elements. In general, the most useful models consist of numerous Maxwell elements connected in parallel or Kelvin-Voight elements connected in series [156]. Mathematically, the constitutive equations describing models comprising numerous elements are more complicated than equations (B.9) and (B.11), and the implementation of the Laplace transform method may assist in the derivation of their solutions [67]. The resulting compliance and stress-relaxation functions, $J(t)$ and $G(t)$, are also more complex.

Appendix C

Numerical Simulations: Software Settings and Codes

C.1 MATLAB Files

C.1.1 pdepe - Direction of Flow

MATLAB code used to plot Figure 2.6, and thus illustrate the effect of term c_1 in equation (2.21). The code implements MATLAB's pdepe solver.

```
%%%%%%%%%%%%%%%%%%%%%%%%%%%%%%%%%%%%%%%%%%%%%%%%%%%%%%%%%%%%%%%%%%%%

%Investigate the effect of the varying diffusion part of the RD
   equation with non-constant diffusion term
m = 0;
x = linspace(-4,4,801);
t = linspace(0,0.5,11);

%Apply MATLAB's pdepe solver to differential equations in
   conjunction with corresponding initial and boundary conditions
sol = pdepe(m,@non_const_diff_PDE,@non_const_diff_IC,
   @non_const_diff_BC,x,t);
% Extract solution
```

```
u = sol(:,:,1);

%Plot solution at first and last time-steps
figure;
plot(x,u(1,:),'red');
hold on
plot(x,u(end,:),'blue');
legend('IC','Solution at last time step',0);
xlabel('Distance x');
ylabel('u(x,2)');
%--------------------------------------------------------------------

%Function to define partial differential equation
function [c,f,s] = anon_const_diff_PDE(x,t,u,DuDx)

c = 1;  %time derivative coefficient
f = 0*0.0000001;  %flux term
s = -1*DuDx+0*u*(1-1*u); %source term
%--------------------------------------------------------------------

%Function to define initial conditions
function u0 = non_const_diff_IC(x)
u0 = 0.1*(sin(pi*x/2))^2;
%--------------------------------------------------------------------

%No flux boundary conditions
function [pl,ql,pr,qr] =non_const_diff_BC(xl,ul,xr,ur,t)
pl = 0;
ql = 1;
pr = 0;
qr = 1;

%%%%%%%%%%%%%%%%%%%%%%%%%%%%%%%%%%%%%%%%%%%%%%%%%%%%%%%%%%%%%%%%%%%%
```

C.1.2 pdepe - Effect of Non-constant Diffusion

MATLAB code used to visualise the effect of non-constant diffusion on system (2.23), and plot Figure 2.7. The code implements MATLAB's pdepe solver.

```
%%%%%%%%%%%%%%%%%%%%%%%%%%%%%%%%%%%%%%%%%%%%%%%%%%%%%%%%%%%%%%%%%%%

%Investigate the effect of the varying diffusion part of the RD
   equation with non-constant diffusion term
m = 0;
x = linspace(-2,2,801);
```

```
t = linspace(0,3,11);

%Apply MATLAB's pdepe solver to differential equations in
   conjunction with corresponding initial and boundary conditions
sol = pdepe(m,@non_const_diff_PDE,@non_const_diff_IC,
   @non_const_diff_BC,x,t);
% Extract solutions
u1 = sol(:,:,1);  % u1=rho (cell density)
u2 = sol(:,:,2);  % u2=m (extracellular matrix)

%Plot solutions at first and last time-steps
figure;
plot(x,u1(1,:),'blue');
hold on
plot(x,u1(end,:),'red');
legend('t=0','t=3');
xlabel('Distance x');
ylabel('u1');
%---------------------------------------------------------------------
%Function to define two partial differential equations (in non-
   dimensional terms)
function [c,f,s] = non_const_diff_PDE(x,t,u,DuDx)

km=0.05;
k0=5;
alpha=1;
nm=2;
lambdam=10;
m_scaling=lambdam/alpha;  % dimensional form of M
h=km/k0;

c = [1;1];  % time derivative coefficient
f = [0.0000001;0]; %flux term
s = [1*exp(u(2)*m_scaling)*DuDx(2).*DuDx(1)+1e-6+0.2*u(1)*(1-h*u(1))
   ;(u(1)^nm)/(1+(u(1)^nm))];  %source term
%---------------------------------------------------------------------
%Function to define initial conditions
function u0 = non_const_diff_IC(x)
u0 = [0.1*(sin(pi/2*x))^2;0];
%---------------------------------------------------------------------
%Function to define no-flux boundary conditions
function [pl,ql,pr,qr] =non_const_diff_BC(xl,ul,xr,ur,t)
pl = [0;0];
ql = [1;1];
pr = [0;0];
qr = [1;1];

%%%%%%%%%%%%%%%%%%%%%%%%%%%%%%%%%%%%%%%%%%%%%%%%%%%%%%%%%%%%%%%%%%%%%%
```

C.1.3 Mean Wavelength Calculation Code

Code used to extract data from C code output (see Section C.2) and plot spatial variation in cell densities and cell death as seen in Figure 2.10, for different values of λ_c. The code also calculates mean wavelengths corresponding to different values of λ_c, and is used to plot Figure 2.11.

```
%%%%%%%%%%%%%%%%%%%%%%%%%%%%%%%%%%%%%%%%%%%%%%%%%%%%%%%%%%%%%%%%%%%%%%%%

%Extract data from C code output:
%Open '.pat' file, read data and reshape cell density data into
   suitable array (dimensions 500x500x81 representing 500x500 domain
    and 81 time-steps).

x=linspace(0,5,500);

wt_orig_u=fopen('.../output/wt_ict2500_rcol1.5_rring125_orig_u.pat')
   ;
stat_wt_orig_u=fseek(wt_orig_u,8,'bof');
Wt_orig_u=fread(wt_orig_u,inf,'double');
WT_orig_u=reshape(Wt_orig_u,250001,81);
WT_orig_u_3D=reshape(WT_orig_u(2:250001,:),500,500,81);

%Extract data for t=40hrs
WTorigu40=WT_orig_u_3D(:,:,81);

%Reduce size of matrix to focus in on central area (coffeering)
%- Interested in central 35% of domain:
%0.35*500=175 so interested in central square of 175*175 grid points
cs_length=0.35*length(x);
cs_position_xleft=(length(x)-cs_length)/2;
cs_position_xleft_int = floor(cs_position_xleft);
cs_position_xright=(length(x)+cs_length)/2;
cs_position_xright_int = ceil(cs_position_xright);
WTorigu40_ca=WTorigu40(cs_position_xleft_int:cs_position_xright_int,
   cs_position_xleft_int:cs_position_xright_int);

%Set threshold value for u to be considered a peak
thv=1.928;

%Plot cell density in central square region
figure(1)
surf(WTorigu40_ca,'Edgecolor','none')
colorbar
view(2)

%Replace all matrix values less than threshold value with 0 (sparse
   matrix) and plot cell density
```

```
WTorigu40_ca(WTorigu40_ca<thv)=0;
%Identify regional maximums in sparse matrix by comparing values of
   each matrix element with 8 neighbouring values
WTorigu40_ca_peaks=imregionalmax(WTorigu40_ca,8);  %  =a1
%Plot location of regional max elements
figure(2)
spy(WTorigu40_ca_peaks)
view(0,-90)
%Find number and location of peaks (non-zero elements) :  i gives
   row number and j gives column number working from left to right
[iWTorigu40_ca_peaks jWTorigu40_ca_peaks] = find(WTorigu40_ca_peaks)
   ;
WTorigu40_ca_no_of_peaks=size(iWTorigu40_ca_peaks);

%Create matrix where each element denotes the distance from one peak
    to another
%- Build square lower triangular matrix (moved down one row).
   Matrix has length=no.of peaks.
%- Calculate Euclidean distance from each non-zero element to every
   other non-zero element and insert in LT
%- Build symmetric matrix (with zeros on diagonal) representing the
   Euclidean distance from non-zero element of a1 to every other
   nonzero element of a1
%E.g: Diag(3,1)=Diag(1,3) is the Euclidean distance from element (i1
   ,j1) to (i3,j3)
%     Diag(4,4)=0 is the Euclidean distance from (i4,j4) to (i4,j4)
LT_WTorigu40 = tril(ones(numel(iWTorigu40_ca_peaks)),-1);  % LT
   matrix moved down one row (gives distance)
LT_WTorigu40(LT_WTorigu40~=0) = hypot(pdist(iWTorigu40_ca_peaks),
   pdist(jWTorigu40_ca_peaks));
Diag_WTorigu40=LT_WTorigu40+transpose(LT_WTorigu40);
%Replace zeros on diagonal with inf and find minimum in each column:
    Resultant matrix Diag_min returns a row vector with the first
   element (1,1) giving the min distance of (i1,j1) to its nearest
   neighbouring peak, (2,2) giving the min distance of (i2,j2) to
   its nearest neighbouring peak, etc.
Diag_WTorigu40(~Diag_WTorigu40)=inf;
Diag_WTorigu40_min=min(Diag_WTorigu40);

%Find median and mean distances between non-zero elements of a1
Median_Diag_WTorigu40=median(Diag_WTorigu40_min)
Mean_Diag_WTorigu40=mean(Diag_WTorigu40_min)

%Repeat method to find mean distances between regional peaks for
   other values of agrcl.

%-----------------------------------------------------------------


%Create row vector: entries determine the mean distance between
   peaks for different values of agrcl (in ascending order of agrcl
   value)
Mean_wavelength_for_diff_agrcl_values=[...,Mean_Diag_WTorigu40,...];
```

```
%  Create row vectors containing different values of agrcl  (in
   ascending order of agrcl value) and lambdac
agrcl_values=[...0.05,...];
lambdac_values=1./agrcl_values;

%In dimensional terms distance between grid points is 10um
%Square encasing central coffeering domain size=177x177 mesh points
   therefore central coffeering domain=1770um*1770um
%Multiply mean length by 10 to get dimensional wavelength (in
   microns)
Dimensional_mean_wavelength_um=Mean_wavelength_for_diff_agrcl_values
   *10;

%Plot Diensional_mean_wavelength_um against lambdac
figure(3)
plot(lambdac_values,Dimensional_mean_wavelength_um)
xlabel(’lambdac’)
ylabel(’wavelength (\mu m)’)
%Find curve of best fit for constant gamma with lambda=gamma*lambdac
    (lambda is real mean wavelength)
wavelength_alpha_fit = fittype(’gamma*lambdac’,’dependent’,’
   Real_mean_wavelength_um’,’independent’,’lambdac’,’coefficients’,’
   gamma’)
wavelength_alpha_fit = fit(lambdac_values’,
   Dimensional_mean_wavelength_um’,wavelength_alpha_fit)

%Plot line of best fit
plot(wavelength_alpha_fit,lambdac_values,
   Dimensional_mean_wavelength_um)
xlabel(’lambdac (\mu m)’)
ylabel(’wavelength (\mu m)’)
legend(’Location’,’southeast’,’Orientation’,’vertical’)

%%%%%%%%%%%%%%%%%%%%%%%%%%%%%%%%%%%%%%%%%%%%%%%%%%%%%%%%%%%%%%%%%%%%%%
```

C.2 C Code

C-code (courtesy of the authors of [6]) used to solve system (2.1). Calls on a '.par' file (not included here), which contains a list of the system's parameter values.

```
#include "sptk.h"
double *xrn;

int main(int argc, char *argv[])
{
  double aux;
  int i,j,i2,j2,i3;
  int ij,it,seed,L,N,Lh,Mh,nst,nme,ict,npat;
  /* Integration parameters */
  double tt,t,st,dx,dt,dth,r2;
  double cx,cy;
  /* Initial conditions */
  double umin,umax,rcol,rring;
  int *n1,*n2,*n3,*n4;
  /* Model parameters */
  double agr0,agrcl,agrcp;
  double x0;
  double xrn_avg, xrn2_avg, xrn_std;
  double am,km,lbd,nh,ikm,akm,gd,kd,ph;
  double aw,lbdw;
  double as,ks,lbds,ns,iks,aks;
  double *Du,fD,fD1,diffpref;
  double epsK,Kmax0, Kmin, lbdK, kk, nk,ikk;
  double Kmax,Kmaxi, u_avg,ui_avg, reac_Kmax, reac_Kmaxi;
  /* Integrator variables */
  double K, Ki;
  double *u,*ui,*agr,*mtx,*mtxi,*w,*wi,*s,*si;
  double *reac_u,*reac_ui;
  double *reac_m,*reac_mi;
  double *reac_w,*reac_wi;
  double *reac_s,*reac_si;
  double *diff_u,*diff_ui;
  double *diff_u2,*diff_u2i;
  double mn,mx;
  /* GSL rng stuff */
  const gsl_rng_type * type = gsl_rng_default;
  gsl_rng * rng;
  /* File handling */
  char name1[60],name3[60];
  FILE *input,*outdat;
  /* Fourier space */
  double ki,kj,dk,*k2vec;
  /* FFTW stuff */
```

```
  fftw_plan plan_u1f,plan_u1b;
  fftw_complex *xrn_ft;
  double complex *Cu1;
  int flag_save_u,flag_save_m,flag_save_w,flag_save_s;

/**********  INPUT DATA  **********/
  strcpy(name1,argv[1]);

  sprintf(name3,"parfiles/%s.par",name1);
  input = fopen(name3,"r");
  fscanf(input,"%lg",&agr0);      next_line(input);
  fscanf(input,"%lg",&agrcl);     next_line(input);
  fscanf(input,"%lg",&agrcp);     next_line(input);
  fscanf(input,"%lg",&Kmax0);     next_line(input);
  fscanf(input,"%lg",&Kmin);     next_line(input);
  fscanf(input,"%lg",&lbdK);     next_line(input);
  fscanf(input,"%lg",&epsK);     next_line(input);
  fscanf(input,"%lg",&kk);     next_line(input);
  fscanf(input,"%lg",&nk);     next_line(input);
  fscanf(input,"%lg",&am);        next_line(input);
  fscanf(input,"%lg",&km);     next_line(input);
  fscanf(input,"%lg",&lbd);    next_line(input);
  fscanf(input,"%lg",&nh);        next_line(input);
  fscanf(input,"%lg",&aw);        next_line(input);
  fscanf(input,"%lg",&lbdw);    next_line(input);
  fscanf(input,"%lg",&as);        next_line(input);
  fscanf(input,"%lg",&ks);     next_line(input);
  fscanf(input,"%lg",&lbds);   next_line(input);
  fscanf(input,"%lg",&ns);        next_line(input);
  fscanf(input,"%lg",&gd);        next_line(input);
  fscanf(input,"%lg",&kd);        next_line(input);
  fscanf(input,"%lg",&ph);        next_line(input);
  fscanf(input,"%lg",&umin);  next_line(input);
  fscanf(input,"%lg",&umax);  next_line(input);
  fscanf(input,"%i", &ict);   next_line(input);
  fscanf(input,"%lg",&rcol);  next_line(input);
  fscanf(input,"%lg",&rring);  next_line(input);
  fscanf(input,"%i",&L);      next_line(input);
  fscanf(input,"%lg",&tt);    next_line(input);
  fscanf(input,"%lg",&st);    next_line(input);
  fscanf(input,"%lg",&dx);    next_line(input);
  fscanf(input,"%lg",&dt);    next_line(input);
  fscanf(input,"%i",&seed);   next_line(input);
  fscanf(input,"%i",&flag_save_u);   next_line(input);
  fscanf(input,"%i",&flag_save_m);   next_line(input);
  fscanf(input,"%i",&flag_save_w);   next_line(input);
  fscanf(input,"%i",&flag_save_s);   next_line(input);
  fclose(input);

  sprintf(name3,"output/%s_gr.prof",name1);
  outdat = fopen(name3,"w");
  fwrite(&L,sizeof(int),1,outdat);
  fclose(outdat);
```

```
  if (flag_save_u) {
    sprintf(name3,"output/%s_u.pat",name1);
    outdat = fopen(name3,"w");
    fwrite(&L,sizeof(int),1,outdat);
    npat = (int)(tt/st+0.5);
    fwrite(&npat,sizeof(int),1,outdat);
    fclose(outdat);
  }
  if (flag_save_m) {
    sprintf(name3,"output/%s_m.pat",name1);
    outdat = fopen(name3,"w");
    fwrite(&L,sizeof(int),1,outdat);
    npat = (int)(tt/st+0.5);
    fwrite(&npat,sizeof(int),1,outdat);
    fclose(outdat);
  }
  if (flag_save_w) {
    sprintf(name3,"output/%s_w.pat",name1);
    outdat = fopen(name3,"w");
    fwrite(&L,sizeof(int),1,outdat);
    npat = (int)(tt/st+0.5);
    fwrite(&npat,sizeof(int),1,outdat);
    fclose(outdat);
  }
  if (flag_save_s) {
    sprintf(name3,"output/%s_s.pat",name1);
    outdat = fopen(name3,"w");
    fwrite(&L,sizeof(int),1,outdat);
    npat = (int)(tt/st+0.5);
    fwrite(&npat,sizeof(int),1,outdat);
    fclose(outdat);
  }

/**********  SIMULATION CONSTANTS  **********/
  N = L*L;
  Lh = L/2;
  Mh = L*(Lh+1);
  nst = (int)(st/dt+0.5);
  nme = (int)(tt/dt+0.5);
  dth = dt*0.5;
  fD = 1/(dx*dx);
  fD1 = 1/(4*dx*dx);
  dk=2.0*M_PI/((double)L * dx);
  akm = am/pow(km,nh);
  ikm = 1/pow(km,nh);
  aks = as/pow(ks,ns);
  iks = 1/pow(ks,ns);
  ikk = 1/pow(kk,nk);
  mn = 0;
  mx = 0;

  /* Memory allocation */
```

```
  u = (double *)calloc(N,sizeof(double));
  ui = (double *)calloc(N,sizeof(double));
  reac_u = (double *)calloc(N,sizeof(double));
  reac_ui = (double *)calloc(N,sizeof(double));
  mtx = (double *)calloc(N,sizeof(double));
  mtxi = (double *)calloc(N,sizeof(double));
  reac_m = (double *)calloc(N,sizeof(double));
  reac_mi = (double *)calloc(N,sizeof(double));
  w = (double *)calloc(N,sizeof(double));
  wi = (double *)calloc(N,sizeof(double));
  reac_w = (double *)calloc(N,sizeof(double));
  reac_wi = (double *)calloc(N,sizeof(double));

  s = (double *)calloc(N,sizeof(double));
  si = (double *)calloc(N,sizeof(double));
  reac_s = (double *)calloc(N,sizeof(double));
  reac_si = (double *)calloc(N,sizeof(double));
  diff_u = (double *)calloc(N,sizeof(double));
  diff_ui = (double *)calloc(N,sizeof(double));
  diff_u2 = (double *)calloc(N,sizeof(double));
  diff_u2i = (double *)calloc(N,sizeof(double));
  agr=(double *)calloc(N,sizeof(double));
  k2vec=(double *)calloc(N,sizeof(double));
  Du=(double *)calloc(N,sizeof(double));
  xrn=(double *)calloc(N,sizeof(double));
  xrn_ft =(fftw_complex *) fftw_malloc(L*(L/2+1)*sizeof(fftw_complex
     ));
  Cu1 = (double complex *)calloc(Mh,sizeof(double complex));

  n1 = (int *)calloc(N,sizeof(int));
  n2 = (int *)calloc(N,sizeof(int));
  n3 = (int *)calloc(N,sizeof(int));
  n4 = (int *)calloc(N,sizeof(int));

  for (i=0;i<L;i++)
    for (j=0;j<L;j++) {
      ij=ncord(L,i,j,0,0);
      n1[ij]=ncord(L,i,j,1,0);
      n2[ij]=ncord(L,i,j,0,1);
      n3[ij]=ncord(L,i,j,-1,0);
      n4[ij]=ncord(L,i,j,0,-1);
    }

/* FFT Plans */
  plan_u1f = fftw_plan_dft_r2c_2d(L,L,xrn,xrn_ft,FFTW_MEASURE);
  plan_u1b = fftw_plan_dft_c2r_2d(L,L,xrn_ft,xrn, FFTW_MEASURE);

/**********  RNG initialisation  **********/
  gsl_rng_env_setup();
  rng = gsl_rng_alloc (type);
  gsl_rng_set (rng, seed);

/**********  Growth rate heterogeneity  **********/
```

```
for(ij=0;ij<N;ij++)
  xrn[ij]=gsl_ran_gaussian(rng,1.0);

for(i=0;i<L;i++) {
  if(i<Lh) ki=dk*(double)i;
  else ki=dk*(double)(i-L);
  for(j=0;j<Lh+1;j++) {
    ij=j+(Lh+1)*i;
    kj=dk*(double)j;
    k2vec[ij]=ki*ki+kj*kj;
  }
}
for (ij=0;ij<Mh;ij++) {
  Cu1[ij]=exp(-pow(k2vec[ij]/(2*agrcl*agrcl),agrcp));
}
fftw_execute(plan_u1f);
for (ij=0;ij<Mh;ij++) {
  xrn_ft[ij]*=Cu1[ij];
}
fftw_execute(plan_u1b);
for (ij=0;ij<N;ij++) {
  xrn[ij]=xrn[ij]/(double)N;
}

// normalize xrn
xrn_avg=0;
xrn2_avg=0;

for (ij=0;ij<N;ij++) {
  xrn_avg+=(xrn[ij]-xrn_avg)/(((double) ij+1));
  xrn2_avg+=(xrn[ij]*xrn[ij]-xrn2_avg)/(((double) ij+1));
}
xrn_std=sqrt(xrn2_avg-xrn_avg*xrn_avg);
//printf("%g %g\n",xrn_avg, xrn_std);

for (ij=0;ij<N;ij++) {
  xrn[ij]=(xrn[ij]-xrn_avg)/xrn_std;
}
// now xrn is approximately distributed as a standard normal
   distrib.


x0 = log(agr0);
for (ij=0;ij<N;ij++) {
      agr[ij] = agr0*(0.25+0.75/(1.0+exp(-1 -xrn[ij])));
}

sprintf(name3,"output/%s_gr.prof",name1);
outdat = fopen(name3,"a");
t = 0;
fwrite(agr,sizeof(double),N,outdat);
fclose(outdat);
```

```
/**********  INITIAL CONDITIONS  **********/
  Kmax=Kmax0;
  Kmaxi=Kmax0;

  for (ij=0;ij<N;ij++) {
     u[ij]=0.0;
     mtx[ij]=0.0;
     w[ij]=0.0;
         //K[ij]=Kmax;
     s[ij]=0.0;
  }

/**** I.C.: random spatially uncorrelated noise ****/
  if (ict==0) {
    for (i=0;i<L;i++)
      for (j=0;j<L;j++) {
        ij=ncord(L,i,j,0,0);
        u[ij]=fabs(gsl_ran_flat(rng,umin,umax));
      }
  }

/**** I.C.: random punctual perturbation in the center ****/
  if (ict==1) {
        i=L/2;
        j=L/2;
        for (i2=0;i2<L;i2++)
                for (j2=0;j2<L;j2++) {
                        r2 = sqrt(pow(i2-i,2.0)+pow(j2-j,2.0));
                        if (r2<5) {
                                ij=ncord(L,i2,j2,0,0);
                        u[ij]+=umax;
                        }
                }
  }


/**** I.C.: random coffee ring ****/
  if (ict>1) {
        for(i3=0; i3<ict;i3++) {
          aux=gsl_ran_flat(rng,0,2*M_PI);
          //if(gsl_ran_bernoulli(rng,0.025)) {
          if(gsl_ran_bernoulli(rng,0.05)) {
                do {
                  cx=gsl_ran_flat(rng,0,L);
                  cy=gsl_ran_flat(rng,0,L);
                  r2=sqrt(pow(cx-Lh,2.0)+pow(cy-Lh,2.0));
                } while(r2>rring);
          }
          else {
            r2=gsl_ran_exponential(rng,0.005);
            if(r2>1) continue;
            cx=Lh+rring*(1-r2)*cos(aux);
            cy=Lh+rring*(1-r2)*sin(aux);
```

```
          }
          i=(int) cx;
          j=(int) cy;
          for (i2=(i-10);i2<(i+10);i2++)
                for (j2=(j-10);j2<(j+10);j2++) {
                  r2 = sqrt(pow(i2-cx,2.0)+pow(j2-cy,2.0));
                  if (r2<rcol) {
                        ij=ncord(L,i2,j2,0,0);
                        u[ij]+=umax;
                  }
                }
    }
  }

/**********  SIMULATION  **********/
  for (it=0;it<=nme;it++) {
        if (it%nst==0) {
      t=dt*(double)it;
          printf("%g ",t);
      if (flag_save_u) {
        sprintf(name3,"output/%s_u.pat",name1);
        outdat = fopen(name3,"a");
        fwrite(&t,sizeof(double),1,outdat);
        fwrite(u,sizeof(double),N,outdat);
        fclose(outdat);
          }
      if (flag_save_m) {
        sprintf(name3,"output/%s_m.pat",name1);
        outdat = fopen(name3,"a");
        fwrite(&t,sizeof(double),1,outdat);
        fwrite(mtx,sizeof(double),N,outdat);
        fclose(outdat);
          }
      if (flag_save_w) {
        sprintf(name3,"output/%s_w.pat",name1);
        outdat = fopen(name3,"a");
        fwrite(&t,sizeof(double),1,outdat);
        fwrite(w,sizeof(double),N,outdat);
        fclose(outdat);
          }
      if (flag_save_s) {
        sprintf(name3,"output/%s_s.pat",name1);
        outdat = fopen(name3,"a");
        fwrite(&t,sizeof(double),1,outdat);
        fwrite(s,sizeof(double),N,outdat);
        fclose(outdat);
          }
    }

    /* Heun method in time - FD in space */

    u_avg=0;
    for (ij=0;ij<N;ij++)
```

```
  u_avg+=u[ij];
u_avg/=(double)N;
reac_Kmax=-lbdK*u_avg;
Kmaxi=Kmax+dt*reac_Kmax;
for (ij=0;ij<N;ij++) {
  Du[ij] = gd*exp(-mtx[ij]/kd);
  K=(Kmax+Kmin*ikk*pow(w[ij],nk))/(1+ikk*pow(w[ij],nk));
      reac_u[ij]=agr[ij]*u[ij]*(1-u[ij]/K);
      diff_u[ij]=fD*Du[ij]*(u[n1[ij]]+u[n2[ij]]+u[n3[ij]]+u[n4[
         ij]]-4*u[ij]);
      diffpref = -fD1*Du[ij]/kd;
      diff_u2[ij]= diffpref*((u[n1[ij]]-u[n3[ij]])*(mtx[n1[ij]]-
         mtx[n3[ij]])+(u[n2[ij]]-u[n4[ij]])*(mtx[n2[ij]]-mtx[n4[
         ij]]));
  ui[ij]=u[ij]+dt*(reac_u[ij]+diff_u[ij]+diff_u2[ij]);
      reac_m[ij]=akm*pow(u[ij],nh)/(1+ikm*pow(u[ij],nh))-lbd*mtx
         [ij];
  mtxi[ij]=mtx[ij]+dt*reac_m[ij];
  reac_w[ij]=aw*u[ij]-lbdw*w[ij];
  wi[ij]=w[ij]+dt*reac_w[ij];

  reac_s[ij]=aks*pow(u[ij],ns)/(1+iks*pow(u[ij],ns))-lbds*s[ij];
  si[ij]=s[ij]+dt*reac_s[ij];
}
    if (it%nst==0) {
            printf(" (%g, %g) ",u_avg, Kmax);
            mn=1e10;
            mx=0;
            for (ij=0;ij<N;ij++) {
                    if (mn>u[ij]) mn=u[ij];
                    if (mx<u[ij]) mx=u[ij];
            }
            printf("%g %g %g | ", mn,mx,u[0]);
            mn=1e10;
            mx=0;
            for (ij=0;ij<N;ij++) {
                    if (mn>w[ij]) mn=w[ij];
                    if (mx<w[ij]) mx=w[ij];
            }
            printf("%g %g\n", mn,mx);


    }

    ui_avg=0;
for (ij=0;ij<N;ij++)
  ui_avg+=ui[ij];
ui_avg/=(double)N;
reac_Kmaxi=-lbdK*ui_avg;
Kmax=Kmax+dth*(reac_Kmax+reac_Kmaxi);
for (ij=0;ij<N;ij++) {
  Du[ij] = gd*exp(-mtxi[ij]/kd);
  Ki=(Kmaxi+Kmin*ikk*pow(wi[ij],nk))/(1+ikk*pow(wi[ij],nk));
```

```
    reac_ui[ij]=agr[ij]*ui[ij]*(1-ui[ij]/Ki);
        diff_ui[ij]=fD*Du[ij]*(ui[n1[ij]]+ui[n2[ij]]+ui[n3[ij]]+ui
           [n4[ij]]-4*ui[ij]);
        diffpref = -fD1*Du[ij]/kd;
        diff_u2i[ij]= diffpref*((ui[n1[ij]]-ui[n3[ij]])*(mtxi[n1[
           ij]]-mtxi[n3[ij]])+(ui[n2[ij]]-ui[n4[ij]])*(mtxi[n2[ij
           ]]-mtxi[n4[ij]]));
    aux=u[ij]+dth*(reac_u[ij]+reac_ui[ij]+diff_u[ij]+diff_ui[ij]+
       diff_u2[ij]+diff_u2i[ij]);
        u[ij]=aux;
    reac_mi[ij]=akm*pow(ui[ij],nh)/(1+ikm*pow(ui[ij],nh))-lbd*mtxi
       [ij];
    mtx[ij]=mtx[ij]+dth*(reac_m[ij]+reac_mi[ij]);
    reac_wi[ij]=aw*ui[ij]-lbdw*wi[ij];
    w[ij]=w[ij]+dth*(reac_w[ij]+reac_wi[ij]);
    reac_si[ij]=aks*pow(ui[ij],ns)/(1+iks*pow(ui[ij],ns))-lbds*si[
       ij];
    s[ij]=s[ij]+dth*(reac_s[ij]+reac_si[ij]);
  }
}

/**** writing final configuration to a file ****/

if (flag_save_u) {
  sprintf(name3,"output/%s_u.fc",name1);
  outdat = fopen(name3,"w");
  fwrite(&L,sizeof(int),1,outdat);
  fwrite(u,sizeof(double),N,outdat);
  fclose(outdat);
}
if (flag_save_m) {
  sprintf(name3,"output/%s_m.fc",name1);
  outdat = fopen(name3,"w");
  fwrite(&L,sizeof(int),1,outdat);
  fwrite(mtx,sizeof(double),N,outdat);
  fclose(outdat);
}
if (flag_save_w) {
  sprintf(name3,"output/%s_w.fc",name1);
  outdat = fopen(name3,"w");
  fwrite(&L,sizeof(int),1,outdat);
  fwrite(w,sizeof(double),N,outdat);
  fclose(outdat);
}
if (flag_save_s) {
  sprintf(name3,"output/%s_s.fc",name1);
  outdat = fopen(name3,"w");
  fwrite(&L,sizeof(int),1,outdat);
  fwrite(s,sizeof(double),N,outdat);
  fclose(outdat);
}
printf("\nQuitting.\n\n");
```

```
  return 0;
}
```

C.3 COMSOL Multiphysics Settings

Given below are general mesh and solver settings used in COMSOL setup when solving systems (2.1) and (5.5). Settings were the same for all simulations with the obvious exception of domain geometry and model equations, both of which can be set up by following COMSOL documentation.

1. Modules Used
    - Equations for ρ, m, w, s in system (2.1): General Form PDE (g)
    - Equations for W, X_1, X_2 in system (5.5): General Form PDE (g)
2. Boundary Condition Types Used
    - Boundary conditions for ρ, m, w, s in system (2.1): 'No Flux' system
    - Boundary conditions for w, X_1, X_2 in (5.5): 'Periodic Condition'
3. Mesh Settings
    - Sequence Type: 'Physics-controlled Mesh'
    - Element size for solving system (2.1): 'Extra Fine'
    - Element size for solving system (5.5): 'Extremely fine'
4. Time Dependent Solver
    - Absolute Tolerance:
        - Global Method: 'Scaled'
    - Time Stepping
        - Method: 'BDF'
        - Steps taken by solver: 'Free'

  - Maximum BDF order: 5
  - Minimum BDF order: 1
  - Event Tolerance: 0.01
- Output
  - Store reaction forces: ‘On’
  - Store time-derivatives: ‘On’
  - Store solution out-of-core: ‘On’
- Advanced
  - Error estimation: ‘Include algebraic’

Bibliography

[1] M. B. Amar and M. Wu. Patterns in biofilms: From contour undulations to fold focussing. *EPL (Europhysics Letters)*, 108(3):38003, 2014.

[2] H. Antelmann, H. Tjalsma, B. Voigt, S. Ohlmeier, S. Bron, J. M. van Dijl, and M. Hecker. A proteomic view on genome-based signal peptide predictions. *Genome Research*, 11(9):1484–1502, 2001.

[3] M. Ardré, H. Henry, C. Douarche, and M. Plapp. An individual-based model for biofilm formation at liquid surfaces. *Physical Biology*, 12(6):066015, 2015.

[4] J. Armitano, V. Méjean, and C. Jourlin-Castelli. Gram-negative bacteria can also form pellicles. *Environmental microbiology reports*, 6(6):534–544, 2014.

[5] S. Arnaouteli, C. E. MacPhee, and N. R. Stanley-Wall. Just in case it rains: building a hydrophobic biofilm the bacillus subtilis way. *Current Opinion in Microbiology*, 34:7–12, 2016.

[6] M. Asally, M. Kittisopikul, P. Rué, Y. Du, Z. Hu, T. Çağatay, A. B. Robinson, H. Lu, J. Garcia-Ojalvo, and G. M. Süel. Localized cell death focuses mechanical forces during 3d patterning in a biofilm. *Proceedings of the National Academy of Sciences*, 109(46):18891–18896, 2012.

[7] B. P. Ayati and I. Klapper. A multiscale model of biofilm as a senescence-structured fluid. *Multiscale Modeling & Simulation*, 6(2):347–365, 2007.

[8] M. Baniasadi, Z. Xu, L. Gandee, Y. Du, H. Lu, P. Zimmern, and M. Minary-Jolandan. Nanoindentation of *Pseudomonas aeruginosa* bacterial biofilm using atomic force microscopy. *Materials Research Express*, 1(4):045411, 2014.

[9] O. A. Bauchau and J. I. Craig. *Structural analysis: with applications to aerospace structures*, volume 163. Springer Science & Business Media, 2009.

[10] M. M. Baum, A. Kainović, T. O'Keeffe, R. Pandita, K. McDonald, S. Wu, and P. Webster. Characterization of structures in biofilms formed by a *Pseudomonas fluorescens* isolated from soil. *BMC microbiology*, 9(1):103, 2009.

[11] E. Ben-Jacob, I. Cohen, I. Golding, and Y. Kozlovsky. Modeling branching and chiral colonial patterning of lubricating bacteria. In *Mathematical models for biological pattern formation*, pages 211–253. Springer, 2001.

[12] E. Ben-Jacob and H. Levine. Self-engineering capabilities of bacteria. *Journal of The Royal Society Interface*, 3(6):197–214, 2006.

[13] W. B. Bickford. *Advanced mechanics of materials*. Addison-Wesley, 1998.

[14] S. S. Branda, J. E. González-Pastor, S. Ben-Yehuda, R. Losick, and R. Kolter. Fruiting body formation by *Bacillus subtilis*. *Proceedings of the National Academy of Sciences*, 98(20):11621–11626, 2001.

[15] D. O. Brush and B. O. Almroth. Buckling of bars, plates, and shells. 1975.

[16] M. A. Budroni, L. Lemaigre, A. De Wit, and F. Rossi. Cross-diffusion-induced convective patterns in microemulsion systems. *Physical Chemistry Chemical Physics*, 17(3):1593–1600, 2015.

[17] M. Burmølle, T. R. Thomsen, M. Fazli, I. Dige, L. Christensen, P. Homøe, M. Tvede, B. Nyvad, T. Tolker-Nielsen, M. Givskov, et al. Biofilms in chronic infections–a matter of opportunity–monospecies biofilms in multispecies infections. *FEMS Immunology & Medical Microbiology*, 59(3):324–336, 2010.

[18] L. S. Cairns, L. Hobley, and N. R. Stanley-Wall. Biofilm formation by *Bacillus subtilis*: new insights into regulatory strategies and assembly mechanisms. *Molecular microbiology*, 93(4):587–598, 2014.

[19] K. D. Carpenter, C. R. Czuba, C. S. Magirl, M. D. Marineau, S. Sobieszczyk, J. A. Czuba, and M. K. Keith. *Geomorphic Setting, Aquatic Habitat, and Water-Quality Conditions of the Molalla River, Oregon, 2009–10*. US Department of the Interior, US Geological Survey, 2012.

[20] S. B. Carter. Haptotaxis and the mechanism of cell motility. *Nature*, 213:256–260, 1967.

[21] E. Cerda and L. Mahadevan. Geometry and physics of wrinkling. *Physical review letters*, 90(7):074302, 2003.

[22] Y. Chai, F. Chu, R. Kolter, and R. Losick. Bistability and biofilm formation in *Bacillus subtilis*. *Molecular microbiology*, 67(2):254–263, 2008.

[23] M. A. Chaplain and G. Lolas. Mathematical modelling of cancer cell invasion of tissue: The role of the urokinase plasminogen activation system. *Mathematical Models and Methods in Applied Sciences*, 15(11):1685–1734, 2005.

[24] M. A. Chaplain and G. Lolas. Mathematical modelling of cancer invasion of tissue: dynamic heterogeneity. *NHM*, 1(3):399–439, 2006.

[25] F. Clarelli, C. Di Russo, R. Natalini, and M. Ribot. A fluid dynamics model

of the growth of phototrophic biofilms. *Journal of mathematical biology*, 66(7):1387–1408, 2013.

[26] N. Cogan. Effects of persister formation on bacterial response to dosing. *Journal of theoretical biology*, 238(3):694–703, 2006.

[27] C. Coman and D. Haughton. Localized wrinkling instabilities in radially stretched annular thin films. *Acta Mechanica*, 185(3-4):179–200, 2006.

[28] J. W. Costerton, Z. Lewandowski, D. E. Caldwell, D. R. Korber, and H. M. Lappin-Scott. Microbial biofilms. *Annual Reviews in Microbiology*, 49(1):711–745, 1995.

[29] J. W. Costerton, P. S. Stewart, and E. Greenberg. Bacterial biofilms: a common cause of persistent infections. *Science*, 284(5418):1318–1322, 1999.

[30] J. Crank. *Free and moving boundary problems*. Clarendon press Oxford, 1984.

[31] E. L. Cussler. *Diffusion: mass transfer in fluid systems*. Cambridge university press, 2009.

[32] B. D'Acunto, L. Frunzo, and M. Mattei. Qualitative analysis of the moving boundary problem for a biofilm reactor model. *Journal of Mathematical Analysis and Applications*, 438(1):474–491, 2016.

[33] M. Dahl, T. Msadek, F. Kunst, and G. Rapoport. The phosphorylation state of the degu response regulator acts as a molecular switch allowing either degradative enzyme synthesis or expression of genetic competence in *Bacillus subtilis*. *Journal of Biological Chemistry*, 267(20):14509–14514, 1992.

[34] M. E. Davey and G. A. O'toole. Microbial biofilms: from ecology to molecular genetics. *Microbiology and molecular biology reviews*, 64(4):847–867, 2000.

[35] B. Davidovitch, R. D. Schroll, D. Vella, M. Adda-Bedia, and E. A. Cerda. Prototypical model for tensional wrinkling in thin sheets. *Proceedings of the National Academy of Sciences*, 108(45):18227–18232, 2011.

[36] S. Dawar, S. Wahab, M. Tariq, and M. J. Zaki. Application of *Bacillus species* in the control of root rot diseases of crop plants. *Archives of Phytopathology and plant protection*, 43(4):412–418, 2010.

[37] R. D. Deegan, O. Bakajin, T. F. Dupont, G. Huber, S. R. Nagel, and T. A. Witten. Capillary flow as the cause of ring stains from dried liquid drops. *Nature*, 389(6653):827–829, 1997.

[38] C. Degering, T. Eggert, M. Puls, J. Bongaerts, S. Evers, K.-H. Maurer, and K.-E. Jaeger. Optimization of protease secretion in *Bacillus subtilis* and *Bacillus licheniformis* by screening of homologous and heterologous signal peptides. *Applied and environmental microbiology*, 76(19):6370–6376, 2010.

[39] N. DeLeon-Rodriguez, T. L. Lathem, L. M. Rodriguez-R, J. M. Barazesh, B. E. Anderson, A. J. Beyersdorf, L. D. Ziemba, M. Bergin, A. Nenes, and K. T. Konstantinidis. Microbiome of the upper troposphere: Species composition and prevalence, effects of tropical storms, and atmospheric implications. *Proceedings of the National Academy of Sciences*, 110(7):2575–2580, 2013.

[40] L. E. Dietrich, C. Okegbe, A. Price-Whelan, H. Sakhtah, R. C. Hunter, and D. K. Newman. Bacterial community morphogenesis is intimately linked to the intracellular redox state. *Journal of bacteriology*, 195(7):1371–1380, 2013.

[41] J. Dockery and I. Klapper. Finger formation in biofilm layers. *SIAM Journal on Applied Mathematics*, 62(3):853–869, 2002.

[42] J. D. Dockery and J. P. Keener. A mathematical model for quorum sensing in *Pseudomonas aeruginosa*. *Bulletin of mathematical biology*, 63(1):95–116, 2001.

[43] R. M. Donlan. Biofilms: Microbial life on surfaces. *Emerging infectious diseases*, 8(9):881–890, 2002.

[44] H. J. Eberl, D. F. Parker, and M. Van Loosdrecht. A new deterministic spatio-temporal continuum model for biofilm development. *Computational and Mathematical Methods in Medicine*, 3(3):161–175, 2001.

[45] L. Edelstein-Keshet. *Mathematical models in biology*, volume 46. Siam, 1988.

[46] S. Elias and E. Banin. Multi-species biofilms: living with friendly neighbors. *FEMS microbiology reviews*, 36(5):990–1004, 2012.

[47] A. K. Epstein, T.-S. Wong, R. A. Belisle, E. M. Boggs, and J. Aizenberg. Liquid-infused structured surfaces with exceptional anti-biofouling performance. *Proceedings of the National Academy of Sciences*, 109(33):13182–13187, 2012.

[48] D. Espeso, A. Carpio, and B. Einarsson. Differential growth of wrinkled biofilms. *Physical Review E*, 91(2):022710, 2015.

[49] J. Ferry. *Viscoelastic properties of polymers*. New York [etc.]: Wiley, 1970.

[50] A. S. Fleischer. *Thermal Energy Storage Using Phase Change Materials: Fundamentals and Applications*. Springer, 2015.

[51] H.-C. Flemming and J. Wingender. The biofilm matrix. *Nature Reviews Microbiology*, 8(9):623–633, 2010.

[52] H.-C. Flemming, J. Wingender, U. Szewzyk, P. Steinberg, S. A. Rice, and S. Kjelleberg. Biofilms: an emergent form of bacterial life. *Nature Reviews Microbiology*, 14(9):563–575, 2016.

[53] M. R. Frederick, C. Kuttler, B. A. Hense, and H. J. Eberl. A mathematical model of quorum sensing regulated eps production in biofilm communities. *Theoretical Biology and Medical Modelling*, 8(8):1–29, 2011.

[54] H. Fujikawa. Diversity of the growth patterns of *Bacillus subtilis* colonies on agar plates. *FEMS microbiology ecology*, 13(3):159–167, 1994.

[55] H. Fujikawa and M. Matsushita. Fractal growth of *Bacillus subtilis* on agar plates. *Journal of the physical society of japan*, 58(11):3875–3878, 1989.

[56] R. A. Gatenby and E. T. Gawlinski. A reaction-diffusion model of cancer invasion. *Cancer research*, 56(24):5745–5753, 1996.

[57] S. L. Gellatly and R. E. Hancock. *Pseudomonas aeruginosa*: new insights into pathogenesis and host defenses. *Pathogens and disease*, 67(3):159–173, 2013.

[58] J. Gere and S. Timoshenko. *Mechanics of Materials*. PWS-Kent Pub. Co., 4th ed edition, 1997.

[59] J. Gerwig, T. B. Kiley, K. Gunka, N. Stanley-Wall, and J. Stülke. The protein tyrosine kinases epsb and ptka differentially affect biofilm formation in *Bacillus subtilis*. *Microbiology*, 160(4):682–691, 2014.

[60] M. Ginovart, D. López, J. Valls, and M. Silbert. Individual based simulations of bacterial growth on agar plates. *Physica A: Statistical Mechanics and its Applications*, 305(3):604–618, 2002.

[61] C. Giverso, M. Verani, and P. Ciarletta. Branching instability in expanding bacterial colonies. *Journal of The Royal Society Interface*, 12(104):20141290, 2015.

[62] I. Golding, Y. Kozlovsky, I. Cohen, and E. Ben-Jacob. Studies of bacterial branching growth using reaction–diffusion models for colonial development. *Physica A: Statistical Mechanics and its Applications*, 260(3):510–554, 1998.

[63] J. E. González-Pastor, E. C. Hobbs, and R. Losick. Cannibalism by sporulating bacteria. *Science*, 301(5632):510–513, 2003.

[64] A. E. Goodman and K. C. Marshall. Genetic responses of bacteria at surfaces. In H. M. Lappin-Scott and J. W. Costerton, editors, *Microbial Biofilms*, pages 80–98. Cambridge University Press, 1995. Cambridge Books Online.

[65] B. Gross. *Mathematical structure of the theories of viscoelasticity*, volume 1190. Hermann, 1953.

[66] T. Guélon, J.-D. Mathias, and P. Stoodley. Advances in biofilm mechanics. In *Biofilm Highlights*, pages 111–139. Springer, 2011.

[67] D. Gutierrez-Lemini. *Engineering viscoelasticity*. Springer.

[68] L. Hall-Stoodley, J. W. Costerton, and P. Stoodley. Bacterial biofilms: from the natural environment to infectious diseases. *Nature reviews microbiology*, 2(2):95–108, 2004.

[69] E. J. Hearn. *Mechanics of materials 1: an introduction to the mechanics of elastic and plastic deformation of solids and structural components*. Butterworth-Heinemann, 1997.

[70] E. J. Hearn. *Mechanics of Materials 2: The mechanics of elastic and plastic deformation of solids and structural materials*. Butterworth-Heinemann, 1997.

[71] L. Hobley, C. Harkins, C. E. MacPhee, and N. R. Stanley-Wall. Giving structure to the biofilm matrix: an overview of individual strategies and emerging common themes. *FEMS microbiology reviews*, 39(5):649–669, 2015.

[72] L. Hobley, A. Ostrowski, F. V. Rao, K. M. Bromley, M. Porter, A. R. Prescott, C. E. MacPhee, D. M. Van Aalten, and N. R. Stanley-Wall. Bsla is a self-assembling bacterial hydrophobin that coats the bacillus subtilis biofilm. *Proceedings of the National Academy of Sciences*, 110(33):13600–13605, 2013.

[73] H. Horn and S. Lackner. Modeling of biofilm systems: a review. In *Productive Biofilms*, pages 53–76. Springer, 2014.

[74] J. Huang, B. Davidovitch, C. D. Santangelo, T. P. Russell, and N. Menon. Smooth cascade of wrinkles at the edge of a floating elastic film. *Physical review letters*, 105(3):038302, 2010.

[75] R. Huang. A kinetics approach to surface wrinkling of elastic thin films. In *Mechanical Self-Assembly*, pages 69–109. Springer, 2013.

[76] R. Huang and S. H. Im. Dynamics of wrinkle growth and coarsening in stressed thin films. *Physical Review E*, 74(2):026214, 2006.

[77] R. Huang and Z. Suo. Wrinkling of a compressed elastic film on a viscous layer. *Journal of Applied Physics*, 91(3):1135–1142, 2002.

[78] Z. Huang, W. Hong, and Z. Suo. Evolution of wrinkles in hard films on soft substrates. *Physical Review E*, 70(3):030601, 2004.

[79] S. Im and R. Huang. Evolution of wrinkles in elastic-viscoelastic bilayer thin films. *Journal of applied mechanics*, 72(6):955–961, 2005.

[80] F. Irgens. *Continuum mechanics*. Springer Science & Business Media, 2008.

[81] S. James, P. Nilsson, G. James, S. Kjelleberg, and T. Fagerström. Luminescence control in the marine bacterium *Vibrio fischeri*: an analysis of the dynamics of lux regulation. *Journal of molecular biology*, 296(4):1127–1137, 2000.

[82] I. Jong and B. Rogers. *Engineering Mechanics: Statics*. Oxford University Press, USA, 1990.

[83] H. Kanematsu and D. M. Barry. *Biofilm and Materials Science*. Springer, 2015.

[84] K. Kawasaki, A. Mochizuki, M. Matsushita, T. Umeda, and N. Shigesada. Modeling spatio-temporal patterns generated by *Bacillus subtilis*. *Journal of Theoretical Biology*, 188(2):177–185, 1997.

[85] E. F. Keller and L. A. Segel. Initiation of slime mold aggregation viewed as an instability. *Journal of Theoretical Biology*, 26(3):399–415, 1970.

[86] H. Khassehkhan, T. Hillen, and H. J. Eberl. A nonlinear master equation for a degenerate diffusion model of biofilm growth. In *Computational Science–ICCS 2009*, pages 735–744. Springer, 2009.

[87] S. Kitsunezaki. Interface dynamics for bacterial colony formation. *Journal of the Physical Society of Japan*, 66(5):1544–1550, 1997.

[88] I. Klapper, C. Rupp, R. Cargo, B. Purvedorj, and P. Stoodley. Viscoelastic fluid description of bacterial biofilm material properties. *Biotechnology and Bioengineering*, 80(3):289–296, 2002.

[89] J. Kreft and J. Wimpenny. Modelling biofilms with extracellular polymeric substances. *Biofilm community interactions: chance or necessity*, pages 191–199, 2001.

[90] J.-U. Kreft, G. Booth, and J. W. Wimpenny. Bacsim, a simulator for individual-based modelling of bacterial colony growth. *Microbiology*, 144(12):3275–3287, 1998.

[91] J.-U. Kreft, C. Picioreanu, J. W. Wimpenny, and M. C. van Loosdrecht. Individual-based modelling of biofilms. *Microbiology*, 147(11):2897–2912, 2001.

[92] J.-U. Kreft and J. Wimpenny. Effect of EPS on biofilm structure and function as revealed by an individual-based model of biofilm growth. *Water Science and Technology*, 43(6):135–135, 2001.

[93] L. D. Landau and E. Lifshitz. Theory of elasticity, vol. 7. *Course of Theoretical Physics*, 3:109, 1986.

[94] C. Laspidou, L. Spyrou, N. Aravas, and B. Rittmann. Material modeling of biofilm mechanical properties. *Mathematical biosciences*, 251:11–15, 2014.

[95] C. S. Laspidou and B. E. Rittmann. Modeling the development of biofilm density including active bacteria, inert biomass, and extracellular polymeric substances. *Water Research*, 38(14):3349–3361, 2004.

[96] Z. Lewandowski. *Biofilms: recent advances in their study and control*, pages 1–17. Harwood Academic Publishers, 2000.

[97] K. Lewis. Riddle of biofilm resistance. *Antimicrobial agents and chemotherapy*, 45(4):999–1007, 2001.

[98] K. Lewis. Persister cells, dormancy and infectious disease. *Nature Reviews Microbiology*, 5(1):48–56, 2007.

[99] K. Lewis. Persister cells. *Annual review of microbiology*, 64:357–372, 2010.

[100] B. Q. Li. *Discontinuous finite elements in fluid dynamics and heat transfer*. Springer Science & Business Media, 2005.

[101] A. Libai and J. G. Simmonds. *The nonlinear theory of elastic shells*. Cambridge university press, 2005.

[102] B. Liu, M. B. Allen, H. Kojouharov, B. Chen, et al. Finite-element solution of reaction-diffusion equations with advection. *Computational methods in water resources XI*, 1:3–12, 1996.

[103] D. López and R. Kolter. Extracellular signals that define distinct and coexisting cell fates in *Bacillus subtilis*. *FEMS microbiology reviews*, 34(2):134–149, 2010.

[104] D. López, H. Vlamakis, and R. Kolter. Biofilms. *Cold Spring Harbor perspectives in biology*, 2(7):a000398, 2010.

[105] D. López, H. Vlamakis, R. Losick, and R. Kolter. Cannibalism enhances biofilm development in *Bacillus subtilis*. *Molecular microbiology*, 74(3):609–618, 2009.

[106] A. Mai-Prochnow, F. Evans, D. Dalisay-Saludes, S. Stelzer, S. Egan, S. James, J. S. Webb, and S. Kjelleberg. Biofilm development and cell death in the marine bacterium *Pseudoalteromonas tunicata*. *Applied and environmental microbiology*, 70(6):3232–3238, 2004.

[107] P. Maini, K. Painter, and H. P. Chau. Spatial pattern formation in chemical and biological systems. *Journal of the Chemical Society, Faraday Transactions*, 93(20):3601–3610, 1997.

[108] K. Manickam, R. R. Machireddy, and S. Seshadri. Characterization of biomechanical properties of agar based tissue mimicking phantoms for ultrasound

stiffness imaging techniques. *Journal of the mechanical behavior of Biomedical Materials*, 35:132–143, 2014.

[109] V. L. Marlow, M. Porter, L. Hobley, T. B. Kiley, J. R. Swedlow, F. A. Davidson, and N. R. Stanley-Wall. Phosphorylated degu manipulates cell fate differentiation in the *Bacillus subtilis* biofilm. *Journal of bacteriology*, 196(1):16–27, 2014.

[110] M. Matsushita and H. Fujikawa. Diffusion-limited growth in bacterial colony formation. *Physica A: Statistical Mechanics and its Applications*, 168(1):498–506, 1990.

[111] M. Matsushita, J. Wakita, H. Itoh, K. Watanabe, T. Arai, T. Matsuyama, H. Sakaguchi, and M. Mimura. Formation of colony patterns by a bacterial cell population. *Physica A: Statistical Mechanics and its Applications*, 274(1):190–199, 1999.

[112] G. Meral. Solution of density dependent nonlinear reaction-diffusion equation using differential quadrature method. *World Academy of Science, Engineering and Technology*, 41:1178–1183, 2010.

[113] M. Mimura, H. Sakaguchi, and M. Matsushita. Reaction–diffusion modelling of bacterial colony patterns. *Physica A: Statistical Mechanics and its Applications*, 282(1):283–303, 2000.

[114] T. Msadek. When the going gets tough: survival strategies and environmental signaling networks in *Bacillus subtilis*. *Trends in microbiology*, 7(5):201–207, 1999.

[115] J. Murray. Mathematical biology. 1989. *C271*.

[116] J. D. Murray. *Mathematical Biology. II Spatial Models and Biomedical Applications {Interdisciplinary Applied Mathematics V. 18}*. Springer-Verlag New York Incorporated, 2001.

[117] J. D. Murray. *Mathematical Biology I: An Introduction, vol. 17 of Interdisciplinary Applied Mathematics*. Springer, New York, NY, USA,, 2002.

[118] V. Nayar, J. Weiland, C. Nelson, and A. Hodge. Elastic and viscoelastic characterization of agar. *Journal of the mechanical behavior of biomedical materials*, 7:60–68, 2012.

[119] Y. Ni, D. Yang, and L. He. Spontaneous wrinkle branching by gradient stiffness. *Physical Review E*, 86(3):031604, 2012.

[120] A. Okubo and S. A. Levin. *Diffusion and ecological problems: modern perspectives*, volume 14. Springer Science & Business Media, 2013.

[121] G. O'Toole, H. Kaplan, and R. Kolter. Biofilm formation as microbial development. *Annu Review of Microbiology*, 54:49–79, 2000.

[122] O. E. Petrova and K. Sauer. Sticky situations: key components that control bacterial surface attachment. *Journal of bacteriology*, 194(10):2413–2425, 2012.

[123] C. Picioreanu, J.-U. Kreft, M. Klausen, J. A. J. Haagensen, T. Tolker-Nielsen, and S. Molin. Microbial motility involvement in biofilm structure formation–a 3D modelling study. *Water science and technology*, 55(8-9):337–343, 2007.

[124] C. Picioreanu, J.-U. Kreft, and M. C. van Loosdrecht. Particle-based multidimensional multispecies biofilm model. *Applied and environmental microbiology*, 70(5):3024–3040, 2004.

[125] C. Picioreanu, M. van Loosdrecht, and J. Heijnen. *Multidimensional modeling of biofilm structure*.

[126] J. Pommerville et al. *Fundamentals of microbiology: Body systems edition*. Jones & Bartlett Publishers, 2014.

[127] N. J. Popławski, A. Shirinifard, M. Swat, and J. A. Glazier. Simulation of single-species bacterial-biofilm growth using the glazier-graner-hogeweg model and the CompuCell3D modeling environment. *Mathematical biosciences and engineering: MBE*, 5(2):355, 2008.

[128] K. A. Rahman, R. Sudarsan, and H. J. Eberl. A mixed-culture biofilm model with cross-diffusion. *Bulletin of Mathematical Biology*, 77(11):2086–2124, 2015.

[129] P. H. Rampelotto. Extremophiles and extreme environments. *Life*, 3(3):482–485, 2013.

[130] U. Römling and C. Balsalobre. Biofilm infections, their resilience to therapy and innovative treatment strategies. *Journal of internal medicine*, 272(6):541–561, 2012.

[131] S. T. Rutherford and B. L. Bassler. Bacterial quorum sensing: its role in virulence and possibilities for its control. *Cold Spring Harbor Perspectives in Medicine*, 2(11):a012427, 2012.

[132] A. Safari, Z. Tukovic, M. Walter, E. Casey, and A. Ivankovic. Mechanical properties of a mature biofilm from a wastewater system: from microscale to macroscale level. *Biofouling*, 31(8):651–664, 2015.

[133] D. Schultz, P. G. Wolynes, E. B. Jacob, and J. N. Onuchic. Deciding fate in adverse times: sporulation and competence in *Bacillus subtilis*. *Proceedings of the National Academy of Sciences*, 106(50):21027–21034, 2009.

[134] A. Seminara, T. E. Angelini, J. N. Wilking, H. Vlamakis, S. Ebrahim, R. Kolter, D. A. Weitz, and M. P. Brenner. Osmotic spreading of *Bacillus subtilis* biofilms driven by an extracellular matrix. *Proceedings of the National Academy of Sciences*, 109(4):1116–1121, 2012.

[135] X. Shen, C.-M. Ho, and T.-S. Wong. Minimal size of coffee ring structure. *The Journal of Physical Chemistry B*, 114(16):5269–5274, 2010.

[136] J. Shi, Z. Xie, and K. Little. Cross-diffusion induced instability and stability in reaction-diffusion systems. *J. Appl. Anal. Comput*, 1(1):95–119, 2011.

[137] R. Singh, D. Paul, and R. K. Jain. Biofilms: implications in bioremediation. *Trends in microbiology*, 14(9):389–397, 2006.

[138] D. Stanescu and B. M. Chen-Charpentier. Random coefficient differential equation models for bacterial growth. *Mathematical and Computer Modelling*, 50(5):885–895, 2009.

[139] T. Stein. *Bacillus subtilis* antibiotics: structures, syntheses and specific functions. *Molecular microbiology*, 56(4):845–857, 2005.

[140] P. S. Stewart. Diffusion in biofilms. *Journal of bacteriology*, 185(5):1485–1491, 2003.

[141] P. S. Stewart and M. J. Franklin. Physiological heterogeneity in biofilms. *Nature Reviews Microbiology*, 6(3):199–210, 2008.

[142] C. D. Sumi, B. W. Yang, I.-C. Yeo, and Y. T. Hahm. Antimicrobial peptides of the genus *Bacillus*: a new era for antibiotics. *Canadian journal of microbiology*, 61(2):93–103, 2014.

[143] Y. Tang and A. J. Valocchi. An improved cellular automaton method to model multispecies biofilms. *Water research*, 47(15):5729–5742, 2013.

[144] S. Timmusk and E. G. H. Wagner. The plant-growth-promoting rhizobacterium *Paenibacillus polymyxa* induces changes in arabidopsis thaliana gene expression: a possible connection between biotic and abiotic stress responses. *Molecular Plant-Microbe Interactions*, 12(11):951–959, 1999.

[145] S. Timoshenko. *History of strength of materials: with a brief account of the history of theory of elasticity and theory of structures*. Courier Corporation, 1953.

[146] S. Timoshenko, J. Goodier, and H. N. Abramson. Theory of elasticity. *Journal of Applied Mechanics*, 37:888, 1970.

[147] S. P. Timoshenko and J. M. Gere. Theory of elastic stability, second edition, 1961.

[148] S. P. Timoshenko and S. Woinowsky-Krieger. *Theory of plates and shells*. McGraw-hill, 1959.

[149] M. Trejo, C. Douarche, V. Bailleux, C. Poulard, S. Mariot, C. Regeard, and E. Raspaud. Elasticity and wrinkled morphology of *Bacillus subtilis* pellicles. *Proceedings of the National Academy of Sciences*, 110(6):2011–2016, 2013.

[150] A. M. Turing. The chemical basis of morphogenesis. *Philosophical Transactions of the Royal Society of London B: Biological Sciences*, 237(641):37–72, 1952.

[151] A. Ugural. *Mechanics of materials*. McGraw Hill, New York, 1991.

[152] J. van Dijl and M. Hecker. *Bacillus subtilis*: from soil bacterium to super-secreting cell factory. *Microbial cell factories*, 12(1):1, 2013.

[153] V. K. Vanag and I. R. Epstein. Cross-diffusion and pattern formation in reaction–diffusion systems. *Physical Chemistry Chemical Physics*, 11(6):897–912, 2009.

[154] J.-W. Veening, W. K. Smits, and O. P. Kuipers. Bistability, epigenetics, and bet-hedging in bacteria. *Annu. Rev. Microbiol.*, 62:193–210, 2008.

[155] R. Vetter, N. Stoop, F. K. Wittel, and H. J. Herrmann. Simulating thin sheets: Buckling, wrinkling, folding and growth. In *Journal of Physics: Conference Series*, volume 487, page 012012. IOP Publishing, 2014.

[156] J. Vincent. *Structural biomaterials*. Princeton University Press, 2012.

[157] H. Vlamakis, C. Aguilar, R. Losick, and R. Kolter. Control of cell fate by the formation of an architecturally complex bacterial community. *Genes & development*, 22(7):945–953, 2008.

[158] H. Vlamakis, Y. Chai, P. Beauregard, R. Losick, and R. Kolter. Sticking together: building a biofilm the *Bacillus subtilis* way. *Nature Reviews Microbiology*, 11(3):157–168, 2013.

[159] B. Vu, M. Chen, R. J. Crawford, and E. P. Ivanova. Bacterial extracellular polysaccharides involved in biofilm formation. *Molecules*, 14(7):2535–2554, 2009.

[160] Q. Wang and T. Zhang. Review of mathematical models for biofilms. *Solid State Communications*, 150(21):1009–1022, 2010.

[161] X. Wang, S. A. Koehler, J. N. Wilking, N. N. Sinha, M. T. Cabeen, S. Srinivasan, A. Seminara, S. Rubinstein, Q. Sun, M. P. Brenner, et al. Probing phenotypic growth in expanding *Bacillus subtilis* biofilms. *Applied microbiology and biotechnology*, 100(10):4607–4615, 2016.

[162] X. Wang, G. Wang, and M. Hao. Modeling of the *Bacillus subtilis* bacterial biofilm growing on an agar substrate. *Computational and mathematical methods in medicine*, 2015, 2015.

[163] Y. Wang, J. Wang, and L. Zhang. Cross diffusion-induced pattern in an SI model. *Applied Mathematics and Computation*, 217(5):1965–1970, 2010.

[164] J. P. Ward and J. R. King. Thin-film modelling of biofilm growth and quorum sensing. *Journal of Engineering Mathematics*, 73(1):71–92, 2012.

[165] J. P. Ward, J. R. King, A. Koerber, P. Williams, J. Croft, and R. Sockett. Mathematical modelling of quorum sensing in bacteria. *Mathematical Medicine and Biology*, 18(3):263–292, 2001.

[166] J. S. Webb, M. Givskov, and S. Kjelleberg. Bacterial biofilms: prokaryotic adventures in multicellularity. *Current opinion in microbiology*, 6(6):578–585, 2003.

[167] J. S. Webb, L. S. Thompson, S. James, T. Charlton, T. Tolker-Nielsen, B. Koch, M. Givskov, and S. Kjelleberg. Cell death in *Pseudomonas aeruginosa* biofilm development. *Journal of bacteriology*, 185(15):4585–4592, 2003.

[168] J. N. Wilking, V. Zaburdaev, M. De Volder, R. Losick, M. P. Brenner, and D. A. Weitz. Liquid transport facilitated by channels in *Bacillus subtilis* biofilms. *Proceedings of the National Academy of Sciences*, 110(3):848–852, 2013.

[169] J. W. Wimpenny and R. Colasanti. A unifying hypothesis for the structure of microbial biofilms based on cellular automaton models. *FEMS Microbiology Ecology*, 22(1):1–16, 1997.

[170] T. K. Wood, S. J. Knabel, and B. W. Kwan. Bacterial persister cell formation and dormancy. *Applied and environmental microbiology*, 79(23):7116–7121, 2013.

[171] J. B. Xavier, C. Picioreanu, and M. Van Loosdrecht. A framework for multidimensional modelling of activity and structure of multispecies biofilms. *Environmental microbiology*, 7(8):1085–1103, 2005.

[172] N. Zelver. What are biofilms? *http://www.biofilm.montana.edu/node/2390*.

[173] W. Zhang, A. Seminara, M. Suaris, M. P. Brenner, D. A. Weitz, and T. E. Angelini. Nutrient depletion in *Bacillus subtilis* biofilms triggers matrix production. *New Journal of Physics*, 16(1):015028, 2014.

[174] X. Zhang, X. Wang, K. Nie, M. Li, and Q. Sun. Simulation of *Bacillus subtilis* biofilm growth on agar plate by diffusion–reaction based continuum model. *Physical Biology*, 13(4):046002, 2016.